NEAR-SURFACE TORNADO WIND FIELD ESTIMATION USING DAMAGE PATTERNS

BY

DANIEL MINKEE RHEE

DISSERTATION

Submitted in partial fulfillment of the requirements
for the degree of Doctor of Philosophy in Civil Engineering
in the Graduate College of the
University of Illinois Urbana-Champaign, 2021

Urbana, Illinois

Doctoral Committee:

Assistant Professor Franklin T. Lombardo, Chair and Director of Research
Professor James M. LaFave
Professor Robert J. Trapp
Assistant Professor Eun Jeong Cha

ABSTRACT

Tornadoes are considered the most violent and dangerous wind hazards and are emerging as a major public concern, causing a significant amount of property loss and casualties in the past decades. In response, the engineering community in the United States is implementing tornado-based design in codes and standards. To ensure robust tornado-based design, an accurate estimate of the near-surface (10 m above ground level) wind field is essential. However, the near-surface wind field of a tornado is not well understood due to lack of in-situ measurements and limitations of the wind speed estimation from structural damage. As a result, a method of estimating the near-surface wind field of a tornado using tree damage, known as tree-fall analysis, is often used as an independent wind speed estimation method. Tree-fall analysis is exceptionally useful in forested areas where structural damage is limited. In addition, field observations showed similar fall patterns from other damage indicators (e.g., crops, traffic signs). In this dissertation, the foundation and applications of tree-fall analysis using different damage indicators are presented with an overarching goal of improving and accurately estimating the near-surface wind field of tornadoes using damage patterns. This dissertation covers the following topics: 1) documenting tornado damage, 2) improving tree-fall analysis, 3) analyzing failure wind speed of cantilever-like damage indicators and tornado wind field models, 4) apply tree-fall analysis to different tornadoes.

Post-storm damage from a total of nine tornadoes was documented in detail both on the ground and in the air. To rapidly collect the tree-fall directions of a large-scale tornado from aerial photographs, a new method that can automatically detect tree damages and obtain tree-fall patterns is developed using an image-processing technique. The method shows a 95% accuracy of detecting

downed trees and 74% of the downed trees have less than 45 degrees difference in median fall-direction from the traditional method (manually "tagging" trees).

Tree-fall analysis analyzes the characteristics of a tornado by examining the tree-fall pattern generated by simulating a translating idealized Rankine vortex. Different types of tree-fall patterns are examined and a method to compare the simulated pattern to the observed pattern and calibrate the vortex parameters is introduced. Herein, the critical wind speed of a cantilever-like damage indicator is used as an input parameter to simulate fall patterns. Thus, the different influential factors and methods to estimate the critical wind speed are also examined. In addition, the validity of different idealized vortex models and feasibility of incorporating into tree-fall analysis are investigated. Possible techniques to modify the idealized vortex models to accommodate external effects (e.g., RFD surge, topographic effects) are presented.

The parameters of real tornadoes are then estimated and the near-surface wind field is recreated using the estimated parameters. The estimated wind speeds are compared with independent wind speed estimates using other methods and other damage indicators. In particular, the near-surface wind field of the Naplate, IL tornado was estimated using different damage indicators (residential buildings, trees, signs). The general agreement in wind speed estimation supports the application of any subset of the methods. The near-surface wind field of Sidney, IL, and Bondurant, IA tornadoes were estimated using tree-fall analysis applied to crops. Both cases are possible evidence of the EF Scale method underrating the tornado intensity due to no structures present in the vicinity. The tree-fall patterns of Tuscaloosa, AL, and Alonsa, MB tornado show a general pattern of increase in tornado intensity, size, and tangential flow over time. Finally, empirical fragility curves of structures and trees are also established using the estimated wind fields, which quantify the vulnerability of structure and trees to tornadoes.

All glory to God

ACKNOWLEDGMENTS

"I can do all things through Christ who strengthens me." – Philippians 4:13. First and foremost, I would like to praise and thank God who has made everything possible and given me the strength to finish this work. I dedicate this dissertation to God, my Lord, and Savior.

I express my deep gratitude to my advisor, Dr. Frank Lombardo, for giving me the opportunity to pursue this research and faithfully believing in me from beginning to end. He has helped me tremendously in developing my academic competence and becoming an independent researcher through his genuine passion for wind engineering. I would also like to thank my doctoral committee members, Dr. James LaFave, Dr. Robert Trapp, and Dr. Eun Jeong Cha, for the insightful comments and advice on my research. The VORTEX-SE and the Northern Tornado Project are gratefully acknowledged for the financial support during my tenure.

I would also like to express my sincere gratitude to my family and my wife, Sohee Kim, for their constant prayer and unconditional love throughout all my ups and downs. Without their continuous support and encouragement, I would have never been able to achieve this accomplishment. I am truly grateful to all the members of the Wind Engineering Research Laboratory, Antonio Zaldivar, Justin Nevill, Alex Zickar, Rishabh Moorjani, Guangzhao Chen, Jason Lopez, and Zach Wienhoff, for many valuable discussions. They have truly made an enjoyable and positive working environment. I would also like to thank David Kang, my mentor and a great friend, who taught me the purpose of life. Special thanks go to all my friends in Champaign for many laughs and tears we had together, to my friends and relatives back in South Korea who still supported me from far away, and to the members of CEEKSA, Ecclesia, KIFA All-star, for making a meaningful and joyful student life outside of school.

TABLE OF CONTENTS

CHAPTER 1: INTRODUCTION

1.1 Problem Statement

Severe windstorm is a dangerous atmospheric phenomenon and a significant natural hazard throughout the world. In particular, tornado is considered the most violent severe windstorm (Davies-Jones et al., 2001) that can cause a tremendous amount of property damage and casualties. Because of their violent nature, tornadoes have caused significant loss and causalities in the United States. During 1996–2019, the annual total loss of property and crop damage is estimated at $1.5 billion (NOAA, 2019), and the cumulative number of casualties from tornadoes has reached nearly 1,800 (NOAA, 2020a). The significant amount of loss and number of casualties alarmed the engineering community and accelerated the implementation of tornado-based design in codes and standards (Prevatt et al., 2012a; van de Lindt et al., 2013; ASCE, 2016).

An accurate estimate of the near-surface wind field of these extreme wind events is an essential part of the tornado-based design. A considerable error can be produced in the wind-induced load calculation as the pressure is proportional to the square of wind speed (ASCE, 2016). However, obtaining in-situ measurements of the near-surface wind field of a tornado is extremely difficult due to the destructive nature and the low predictability of tornado occurrence (Folger, 2013). Not only the chance of capturing a tornado is slim, but it is also extremely dangerous to get a direct measurement of the near-surface wind speed. Moreover, most wind instruments (anemometers) are not designed to record wind speeds exceeding 150 mph (67 m/s) (R.M. Young, 2020). In fact, only a few studies on a full-scale in-situ direct measurement of a tornado are available (Lombardo, 2017; Karstens et al., 2010). Although portable radar instruments, such as DOW (Doppler On Wheels), have been able to provide full-scale wind measurements (Bluestein

et al., 2019; Kosiba and Wurman, 2013; Refan et al., 2017; Wakimoto et al., 2018), the number of DOWs are limited and the near-surface wind field, at the elevation (above ground level less than 50 m) where most engineers are interested in, are often neglected because of underlying noise in the measurements and beam blockage (Wurman et al., 2013; Wurman et al., 2014). As a result, the prevailing method for estimating the tornado wind field near the surface has been the analysis of data gathered in damage assessments (Edwards et al., 2013).

A common method of estimating the near-surface wind field of a tornado is the Enhanced Fujita Scale (EF Scale). The method classifies a tornado mostly based on structural damage (McDonald and Mehta, 2006) and is widely used in practice by engineers and meteorologists (Edwards et al., 2013). Although the structural damage and wind speed certainly have a positive correlation, estimating an accurate near-surface wind field based on structural damage is much more complicated due to the variability and subjective judgment in construction quality and type, different aerodynamic effects on the shape of the structure, etc. (Doswell, 2003; Edwards et al., 2013). As stated by Doswell and Burgess (1988), "the F-scale is a damage scale, not an intensity (or windspeed) scale." Furthermore, most of the world's tornadoes occur in rural areas where the population and structure density are low (Guyer and Moritz, 2003) and damage indicators (DIs) are lacking, making the EF-scale estimation difficult and often leading to an underrating of tornado intensity (Edwards et al., 2013). Structural damage indeed possesses valuable information on tornadoes, but the near-surface wind field should not be estimated solely based on structural damage if possible. Independent methods of estimating the near-surface wind field of tornadoes are needed to increase confidence in the near-surface wind field estimate.

1.2 Research Objectives

Oftentimes, a large volume of trees or crops is damaged during a tornado event, especially in rural areas. Tree damage can range from thousands to millions of trees with a very limited number of structures, especially in forested regions (Bech et al., 2009; Beck and Dotzek, 2010; Blanchard, 2013; Fujita, 1989; Godfrey and Peterson, 2017; Hall and Brewer, 1959), and the EF-scale estimation becomes difficult with a small number of structures. Although the current EF Scale method can provide a wind speed estimate using single tree damage (DI-27, 28) and may allow near-surface wind field estimate of a tornado to some extent, the wind speed estimate based on the damage of single trees is confined to the maximum load resistance of the tree. The maximum wind speed estimate that the EF-scale of trees can provide is 74.6 m/s (167 mph), incapable of rating intensity of EF 4 or greater tornadoes. The maximum near-surface wind speed of the tornado still remains in question.

Edwards et al. (2013) suggest that the near-surface wind field of a tornado should be estimated in the context of a surrounding forest instead of single tree damages. As a result, a method of estimating the near-surface wind field of a tornado using tree damages and looking at the tree-fall directions or patterns as a whole rather than individual DIs as a prominent method in recent years (Bech et al., 2009; Beck and Dotzek, 2010; Karstens et al., 2013; Lombardo et al., 2015). Godfrey and Peterson (2017) and Sills et al. (2021) also uses tree damage to estimate the EF-scale within certain areas based on the percentage of trees blown down, independent of tree-fall directions.

The frequent strike of tornadoes and the lack of structures in the rural area have inspired researchers to investigate tornadoes in crop fields (Baker et al., 2020; Fujita, 1993). Particularly, Fujita stresses the reliability and importance of crop damage patterns in his study of the Plainfield,

IL tornado of 28 August 1990 where multiple aerial photographs of various crop damage patterns are exhibited (Fujita, 1993). Examples of a tree-fall and corn-fall pattern after a tornado are shown in Figure 1.1(a) and Figure 1.1(b), respectively. The tree-fall and corn-fall patterns display a coherent damage pattern, which represents the airflow pattern of the tornado (Fujita, 1989; Karstens et al., 2013). The width of the damage and damage pattern of trees and crops contains important information on tornado characteristics (e.g., core size, amount of inflow, and rotation).

(a) tree-fall pattern (b) corn-fall pattern

Figure 1.1. Aerial photographs of (a) tree-fall pattern of Joplin, MO tornado and (b) corn-fall pattern of Bondurant, IA tornado. The fall directions of individual tree or a group of corns are annotated in arrows.

The tornado wind speed at a specific location can also be estimated using forensic analysis, a method where structural capacity is evaluated to calculate the wind load required for the observed failure. Boughton et al. (2012) applied forensic analysis to failed and non-failed road signs to

estimate the peak gust of the Yasi tropical cyclone. With a sufficient number of road or traffic signs, the same method can be applied to tornadoes and estimate the near-surface wind field of a tornado.

The primary focus of this study is to broaden the knowledge of near-surface wind field estimation of a tornado using damage patterns by improving existing methods and understanding the characteristics of tornadoes and damage indicators. To accomplish this research problem, tree-fall analysis, a method that analyzes fall directions and damage swath using an idealized vortex model and critical wind speed of tree, is further improved (see Chapter 4), and the critical wind speed of cantilever-like damage indicators (e.g. trees, crops, signs) is investigated (see Chapter 5). The improved method is then applied to different tornadoes using different damage indicators, and the near-surface wind field of these tornado events is estimated and compared to other methods to examine the validity of the proposed method (Chapter 7). The author aspires to benefit the engineering community and advance the tornado-based design eventually by providing a better understanding of the near-surface wind field of a tornado and filling the gaps of the current wind speed estimation methods. The following main objectives will be addressed in the proposed dissertation:

1) Documentation of tornado damage.
2) Improve the existing method of estimating of near-surface wind field of tornadoes using tree-fall patterns.
3) Accurately estimate the critical wind speed of tree/crop/sign fall to be used in the tree-fall analysis.

4) Analyze different wind field models to be used in the tree-fall analysis and the effects of topography.

5) Apply tree-fall analysis and determine the feasibility and accuracy of the method and evaluate the probability of structure and tree failure using empirical data.

1.3 Document Outline

The document is broken into chapters with tasks that will be carried out to accomplish the objectives. The following highlights each chapter.

Chapter 2 discusses methods and the significance of data collection used in the analysis. The "conventional" damage survey (e.g., EF Scale method) and the Wind Engineering Research Laboratory (WERL) damage assessment for necessary for wind field estimation are reviewed. The process of damage survey and aerial photos converted into usable data is introduced in this chapter.

Chapter 3 presents an automated method of tree damage and pattern identification from aerial photos. A new method using image processing tools is proposed and its application on Alonsa, MB tornado is presented in this chapter.

Chapter 4 introduces the history of "tree-fall" analysis and the development of the improved tree-fall analysis.

Chapter 5 discusses the investigation of bending moment capacity of trees, corn, and signs from experimental tests and analytical solutions. The critical wind speed of the three damage indicators that will be used in the tree-fall analysis can be found in this chapter.

Chapter 6 gives a detailed review on different idealized vortex models and examines the application of each model to tree-fall analysis. In addition, the topographic effect on vortex model is investigated.

Chapter 7 presents the application of the improved tree-fall analysis to multiple tornadoes to estimate their near-surface wind speeds. The estimates are compared to the estimates from other damage indicators. Empirical fragility curves of residential buildings using the estimated near-surface wind field are also developed in this chapter.

Chapter 8 presents the conclusions of this study.

Chapter 9 presents the future directions and research to further improve the tree-fall analysis.

CHAPTER 2: TORNADO DAMAGE ASSESSMENT

2.1 Introduction

Due to the lack of situ wind speed measurements near ground, a post-damage survey is often conducted and used to estimate the near-surface wind field of tornadoes. The damage inflicted by the tornado contains relevant information that correlates to the near-surface wind speed and direction. Thus, detailed documentation of the post-tornado damage is an essential part and the very first step of the near-surface wind field estimation of a tornado. In this chapter, a typical damage survey is briefly reviewed and the Wind Engineering Research Laboratory (WERL) damage survey is presented in detail. The WERL damage survey largely consists of two parts: ground-based survey and aerial survey. The primary focus of this chapter is to present the process of documenting tornado damage and compiling the collected damage information into a comprehensive damage map and com, which will be used in later chapters to estimate the near-surface wind field of tornadoes.

2.2 Conventional Damage Survey

2.2.1 Enhanced Fujita Scale (EF Scale)

The EF Scale method is commonly used to categorize the intensity of the tornado, a method developed to rate tornadoes based on written descriptions of damage (McDonald and Mehta, 2006). A Degree of Damage (DOD) is determined based on the damage state, which has an associated wind speed range. Then, the tornado is "rated" with a number and an associated range of 3-sec wind gust speed (McDonald and Mehta, 2006). The EF rating and its associated 3-sec wind gust speed are summarized in Table 2.1. The current EF Scale method includes a total of 28

damage indicators (DIs). In general, the 'official' EF Scale ratings of tornadoes occurred in the United States are rated by the National Weather Service (NWS), a weather service agency of the United States federal government. An NWS personnel identifies one or more than one of the 28 DIs and assigns an EF Scale rating based on the highest wind speed that occurred within the damage path (NWS, 2020).

Table 2.1. EF Scale rating with associated wind speed ranges.

EF scale	**3-Second Gust Speed in mph (m/s)**
EF0	65-85 mph (29-38 m/s)
EF1	86-110 mph (38-49 m/s)
EF2	111-135 mph (50-60 m/s)
EF3	136-165 mph (61-74 m/s)
EF4	166-200 mph (74-89 m/s)
EF5	Over 200 mph (over 89 m/s)

2.2.2 One- and Two-family Residences (FR12)

In common practice, the damage state and the location of the damaged one- and two-family residences (DI 2) are documented. The damage description of each DOD and its associated wind speed (expected, lower bound, and upper bound) for FR12 is summarized in Table 2.2. DI 2 is one of the most widely used DIs in wind speed estimation because of its abundance across the United States. As shown in Table 2.2, the DOD of FR12 also covers a wide range of wind speeds from 53 mph (24 m/s) to 198 mph (89 m/s). However, only several damaged FR12s are typically investigated and given a DOD rating (typically EF-2 or weaker). Figure 2.1 shows an image of a typical damage survey of the Naplate-Ottawa, IL tornado and the EF rating by the NWS retrieved

from the Damage Assessement Toolki, which is an website operated by the NWS to archive the damage survey and general information of tornado (e.g., date and time, number of injuries and fatalities) and share the information to the public. Each triangle represents a survey point from an NWS personnel using the EF-scale method. Although the Damage Assessment Toolkit is a great tool to obtain general information of a tornado and provides an EF rating and may provide the maximum wind speed of the tornado, there are still gaps and it is insufficient for engineering design purpose that requires a more detailed estimate of near-surface wind field of a tornado.

Table 2.2. Degree of Damage of FR12 (DI 2) with associated wind speed.

DOD	Damage Description	EXP[a]	LB[b]	UB[c]
1	Threshold of visible damage	65 (29)	53 (24)	80 (34)
2	Loss of roof covering material (<20%), gutters and/or awning; loss of vinyl or metal siding	79 (35)	63 (28)	97 (43)
3	Broken glass in doors and windows	96 (43)	79 (35)	114 (51)
4	Uplift of roof deck and loss of significant roof covering material (>20%); collapse of chimney; garage doors collapse inward or outward; failure of porch or carport	79 (35)	81 (36)	116 (52)
5	Entire house shifts off foundation	121 (54)	103 (46)	141 (63)
6	Large sections of roof structure removed; most walls remain standing	122 (55)	104 (47)	142 (64)
7	Top floor exterior walls collapsed	132 (59)	113 (51)	153 (68)
8	Most interior walls of top story collapsed	148 (66)	128 (57)	173 (77)
9	Most walls collapsed in bottom floor, except small interior rooms	152 (68)	127 (57)	178 (80)
10	Total destruction of entire building	170 (76)	142 (64)	198 (89)

[a] Expected wind speed in mph (m/s)
[b] Lower bound wind speed in mph (m/s)
[c] Upper bound wind speed in mph (m/s)

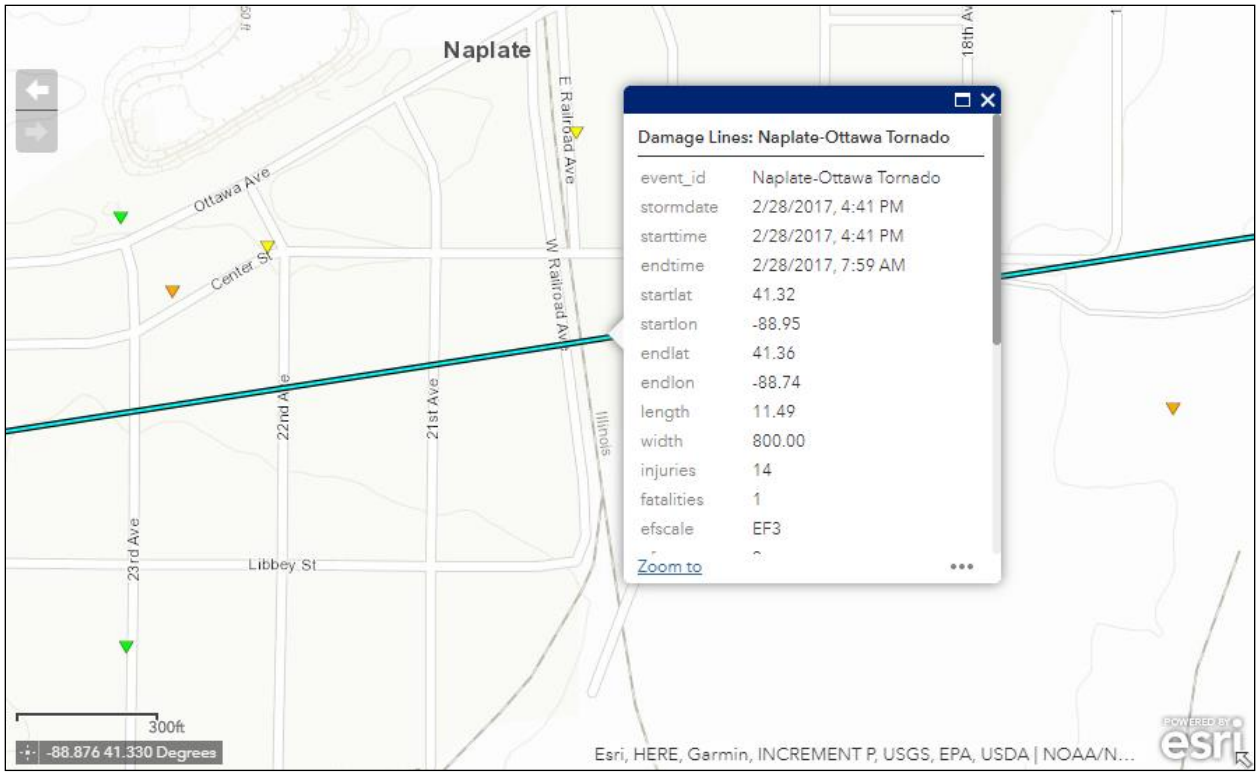

Figure 2.1. Image of a typical damage survey in Naplate, IL by the NWS (image retrieved from https://apps.dat.noaa.gov/StormDamage/DamageViewer/).

2.3 WERL Damage Survey

2.3.1 Ground-based Survey

Despite the various types of DI in the EF scale method, gaps do exist and the structural integrity between nearby DIs is still questionable. Edwards et al., (2013) suggest that more damage indicators need to be explored and other methods should be incorporated in estimating near-surface wind speed. The Wind Engineering Research Laboratory (WERL) at the University of Illinois Urbana-Champaign conducts damage surveys that collect damage information other than just the EF scale DIs. In addition to residential houses, detailed information on trees, crops, and traffic signs are collected during the damage survey. Not only the failed ones but also the non-failed ones are collected as non-failed DIs can provide information on the upper bound wind speed of the

tornado at given locations. Documenting the location of the DI is important because the near-surface wind speed varies between the location relative to the center of the tornado. A convenient and prevailing method to obtain the geolocated photographs is taking a photo using a GPS camera.

2.3.1.1 Residential buildings

For residential buildings, it is important to document the damaged structures from different angles and capture different views to avoid losing information. Multiple images of damaged residences are carefully examined, and the DOD rating that matches the damage description (Table 2.2) the most is assigned. Example images of damaged FR12s and their DOD rating rated by the WERL researchers are shown in Figure 2.2 (Figure 2.2 only shows one image that best displays the DOD rating). For the WERL damage survey, the DOD ratings are assigned to each building based on consensus between researchers who surveyed the location. First, each researcher rates all the damaged structures independently by examining the photos without discussing with another. Then, the researchers discuss their DOD ratings and reach a consensus for any discrepancies. The residential building in Figure 2.2(a), which had more than 20% loss of roof covering, was rated a DOD 4 by all researchers (Table 2.2). The DOD 6 rated building in Figure. 2.2(b) is an example where researchers had to come to a consensus: the removed lower section of the gambrel roof serves as a sidewall for the habitable space but is treated as a roof structure based on construction. The consensus method is intended to reduce the subjectivity of rating the damaged structure.

(a) DOD 4 (b) DOD 6

Figure 2.2. Image of residential buildings with DOD rating after the tornado in Naplate, IL: (a) DOD 4 and (b) DOD 6.

Once the rating is complete, the ratings of the damaged buildings are mapped on a geographic information system (GIS), using GPS coordinates. A damage survey map can help to visualize the damage extent and the gradient of damage, which can be used to estimate the characteristics of a tornado (e.g., damage width, tornado center, radius of maximum wind speed) (Lombardo et al., 2015; Prevatt et al., 2012b; Roueche and Prevatt, 2013). As an example, a total of 152 buildings were surveyed and assigned DOD ratings throughout the village of Naplate, IL as represented on the map of Figure. 2.3. The tornado center can be estimated based on the locations of the residences that took the most damage (red line in Figure. 2.3), and an evident damage gradient is shown where the DOD rating decreases further away from the estimated tornado center. The estimated damage width is approximately 0.35 miles (550 m) with the highest damage rating of DOD 8 where the exterior walls of the structure were collapsed except for some interior rooms (Table 2.2). However, it was suspected that the building failed at a lower wind speed because it had unreinforced masonry foundation walls. Thus, a lower bound wind speed of DOD 8 was assigned (more discussion in Chapter 7). Figure 2.4 shows the DOD 8 structure with

unreinforced masonry foundation walls. This example demonstrates the importance of a ground-based survey. As opposed to an aerial survey (section 2.3.3), a great level of detail, such as the construction type, can be obtained from the ground.

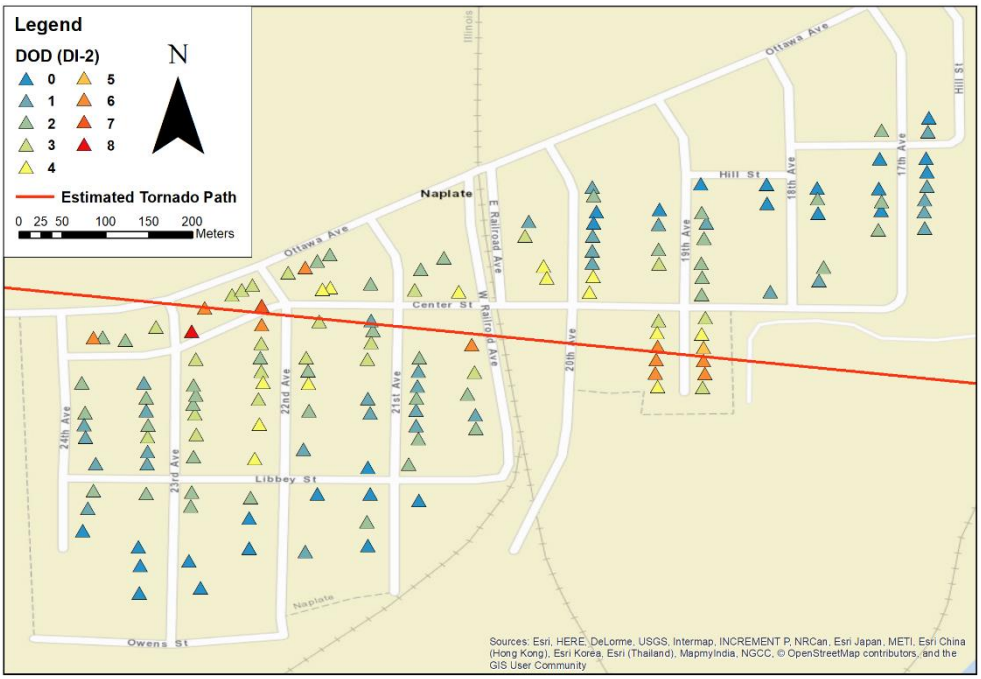

Figure 2.3. Map of damaged residential buildings in Naplate, IL on ArcGIS with estimated tornado path (red line). Residential buildings (triangles) are color-coded according to its DOD rating.

Figure 2.4. Residential rated DOD 8 due to unreinforced masonry foundation walls.

2.3.1.2 Trees

Just as the residential buildings, a ground survey is important in tree damage because valuable information related to obtaining wind speed, but unattainable from the air, can be identified from the ground. In the conventional damage survey, only the tree type (Hardwood or softwood) and the damaged state are identified, and the wind speed is assigned according to the EF Scale. In the WERL damage survey, the photograph of the tree is taken standing at the root and aligning with the trunk as shown in Figure 2.5, in which the geographic coordinates and the direction of the tree-fall are recorded. Examining the directions as a whole, the fallen trees tend to form a pattern displaying the flow pattern of a tornado. A more detailed analysis of tree-fall patterns (tree-fall analysis) is discussed later in Chapter 4. In addition, the diameter at breast height (DBH), species of the tree, and the failure mode (e.g., snapped at the stem, uprooted) were documented as these tree properties have a close relationship with tree-fall risk (Cannon et al., 2015; Cucchi et al., 2004; Peltola et al., 2000; Peterson, 2007; Peterson and Claassen, 2013). More detailed discussion regarding the relationship between the critical wind speed of tree-fall and the properties of the tree can be found in Chapter 5. The collected information will be used to calculate the critical wind speed of trees (Chapter 5). Although they are not collected in the WERL damage survey, tree height, crown height, and diameter should also be collected if possible as they also contribute to the tree-fall risk to the wind. The critical wind speed of trees is then used in a vortex model to generate tree-fall patterns and estimate the near-surface wind speed (Chapter 7).

Tree

Species: White Pine
DBH: 12 inch (30 cm)
Failure mode: Uprooted
Fall direction: 31º NE

Figure 2.5. Example documentation of tree damage.

Unlike the conventional damage survey, not only the failed trees are surveyed, but also survived trees are surveyed in the WERL damage survey. Godfrey and Peterson (2017) propose a method that utilizes the proportion of failed and standing trees to estimate the EF Scale of the tornado, in which a modified Godfrey-Peterson method will be addressed in detail in Chapter 7. Multiple visits to the damage-site can be very beneficial, especially when collecting information on survived trees due to the inaccessibility of the damaged site immediately after the tornado. Assuming that the standing trees are the same as the trees that survived the tornado, the information on standing trees is also collected: the location, DBH, and species. Mapping of the failed and survived trees of the Naplate, IL tornado is shown in Figure 2.6. The mapping of tree survey exhibits an apparent damage pattern where more trees failed near the estimated tornado center and more trees survived further away.

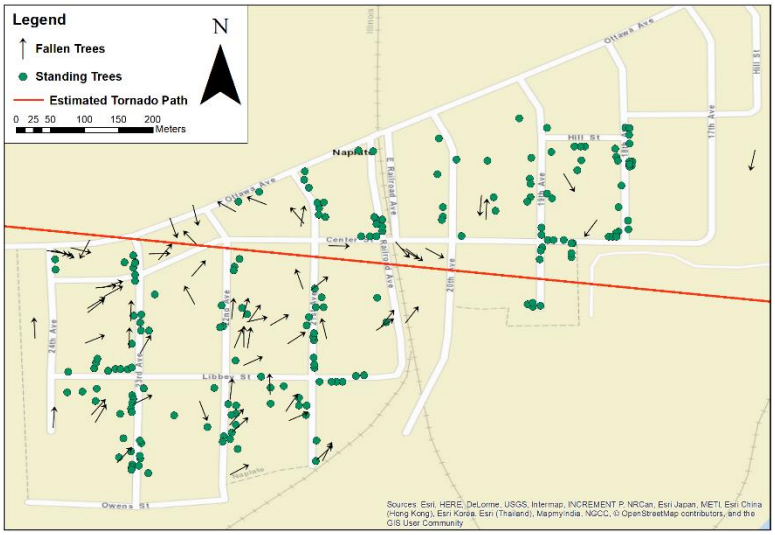

Figure 2.6. Map of fallen and standing trees in Naplate, IL on ArcGIS with estimated tornado path (red line). The fall direction of the fallen trees is shown in black arrow and the location of the standing trees in green circle.

2.3.1.3 Crops

Crop damages that resemble the tree-fall patterns from tornadoes were recognized by the WERL. The WERL realized the need for more damage indicators especially in a rural area and conducted damage surveys in crop fields in an attempt to apply tree-fall analysis on crop damage. In the ground-based crop damage survey, the fall direction of the crops in several transects perpendicular to the tornado center is documented using a GPS unit camera. Figure 2.7 shows the fall directions of soybean of the Sidney, IL tornado at five different transects on ArcGIS, illustrating patterns similar to tree-fall patterns where the fall directions converge to a line. An interesting discovery in this damage survey is the formation of convergent and divergent patterns of soybeans. A convergent pattern (black arrows) was identified on the northside, and a divergent pattern (blue arrows) on the south side of the tornado center in Figure 2.7. An up-close photograph of the convergent pattern with a diameter of approximately 2 m is shown in Figure 2.8. These

small-scale patterns, which may have been invisible from the air, also demonstrate the importance of a ground-based survey. The analysis of near-surface wind field on soybean field and further discussion of convergent and divergent pattern of the Sidney, IL tornado will be discussed in Chapter 6. Detailed information on aerial photos and orthomosaics will be discussed in section 2.3.3.

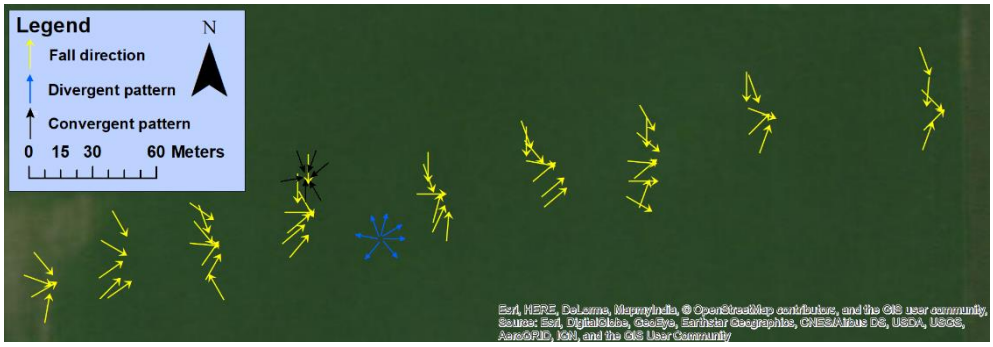

Figure 2.7. Soybean fall pattern documented at multiple transects on ArcGIS. The arrows indicate the fall direction of soybeans with divergent pattern (blue) and convergent pattern (black).

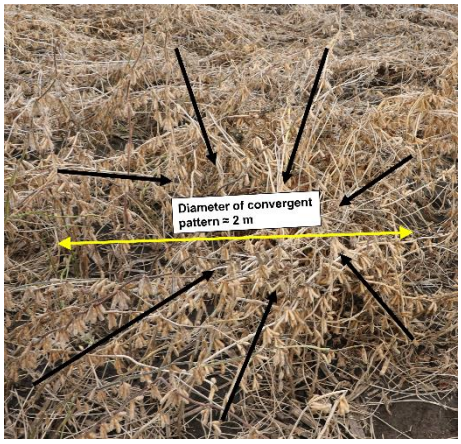

Figure 2.8. Convergent pattern found in soybean damage in Sidney tornado, IL.

2.3.1.4 Traffic signs

Similar to trees and crops, traffic signs fail in tornadoes in the direction of wind-blown and can be used to estimate the characteristics of the tornado. In addition to the failed signs, the non-failed traffic signs of the Naplate, IL tornado were also documented as the non-failed signs can be used to estimate the upper bound near-surface wind speed (Boughton et al., 2012). The location of all traffic signs and the direction of fall for the failed signs were documented using GPS unit cameras. The location and fall direction of the failed signs are shown in blue arrow and the location of the non-failed signs is shown in gray circle in Figure 2.9. Detailed dimensions of a total of 38 traffic signs were also documented (e.g., height above the ground and dimensions of the signages, thickness, and other dimensions of the sign-posts). An example image of a failed traffic sign and its dimensions are shown in Figure 2.10. Conveniently, the metal posts of all the traffic signs surveyed in the village of Naplate were identical galvanized U-channel steel. Using the dimensions of the traffic signs, the projected area of the traffic signs and the bending moment capacity of the steel posts can be calculated, which are used to estimate the critical failure wind speed of the traffic signs (Chapter 5). The critical wind speed of these traffics signs then can be used to compare the estimated wind field from other methods or to extract the Rankine vortex (RV) parameters and generate an independent near-surface wind field (Chapter 7).

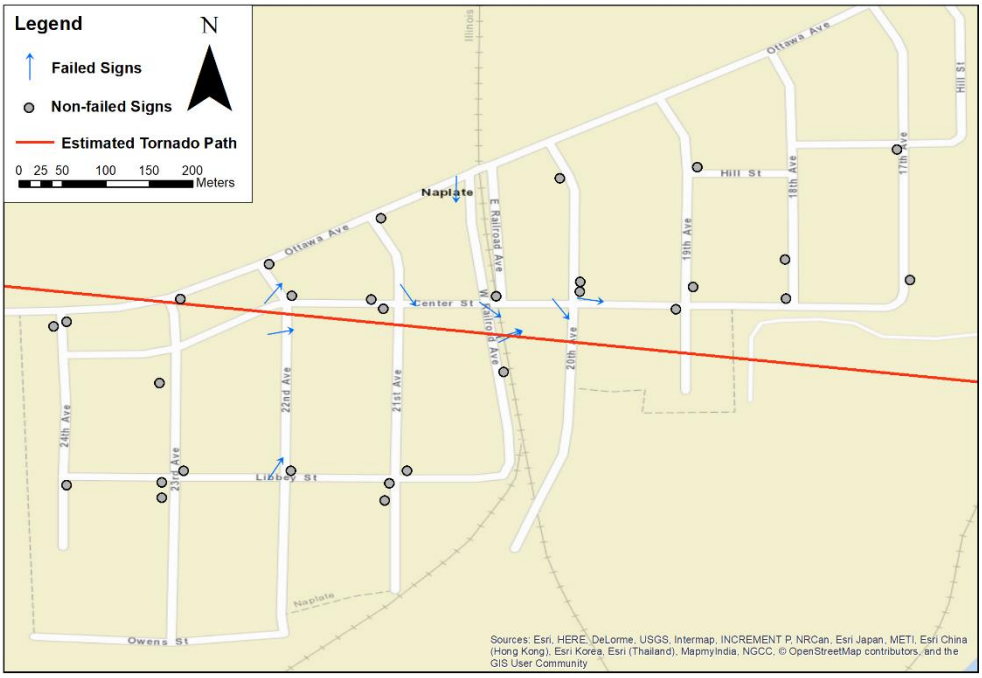

Figure 2.9. Map of failed and non-failed traffics signs in Naplate, IL on ArcGIS with estimated tornado path (red line). The fall direction of the failed signs is shown in blue arrow and the location of the non-failed signs in gray circle.

Traffic Sign

Sign type: Stop (30”×30”) / Speed limit (18”×24”)
Height: 2.4 m (8 ft)
Steel type: U-channel
Fall direction: 174º S

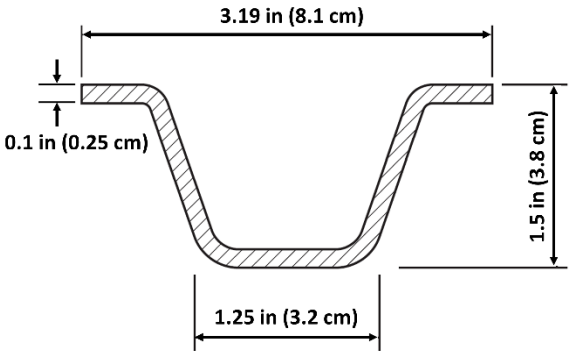

Figure 2.10. Example documentation of a sign damage.

2.3.2 Social Media Images

As social media has become an increasingly important venue for information, it has become a critical medium for disseminating information during natural disasters. More recently, researchers have identified social media as a new source of first-hand information during and after these events. Social media is one of the fasted media to obtain post-disaster information; images extracted from social media, such as Twitter and Facebook, are often used for crisis mapping, analysis of public responses, and debris tracking (Middleton et al., 2013; Knox et al., 2013; Ukkusuri et al., 2014). Images or videos from social media, often taken immediately after the damage occurs, can be a valuable tool in damage surveys, helping researchers identify survey locations and preserving perishable data that may be obscured as cleanup and repairs begin. With the increase in popularity of consumer unmanned aerial vehicles (UAVs or drones), previously scarce low-elevation overhead video and images are commonly made available on social media. Data from these sources can fill in the gaps of other methods or can be used as another independent method to improve the estimates of tornado wind fields.

A total of 109 images related to the Naplate, IL tornado immediately after the tornado were extracted manually from Twitter and YouTube. The extracted images were images of residential buildings and the others were images of low-rise buildings (EF Scale DI 17), metal building systems (DI 21), and a warehouse building (DI 23) (McDonald and Mehta, 2006). Most of the images were taken using UAVs. The UAV footage from social media has some advantages over the still images taken during the damage survey: some structures could be viewed at angles that are not visible from the ground, revealing or clarifying damage patterns. For example, Figure 2.11 shows a snapshot image of a structure taken from UAV footage immediately after the Naplate, IL tornado (Figure 2.11(a)), and the photograph taken during the damage survey (Figure 2.11(b)).

The roof of the structure was covered with a tarp of the first survey, and thus the structure was initially rated as a DOD 4 due to the inward collapse of the garage door but was re-rated as a DOD 6 after discovering from the social media image that a large section of the roof structure was removed.

(a) social media image (b) damage survey image

Figure 2.11. Images of the same damaged residential building (a) retrieved from social media, and (b) taken by the WERL during damage survey. (Image by ABC 7 Chicago and authors, respectively).

Primarily, the social media images validated the initial damage survey assessment of residential buildings. However, some DOD ratings for the residential buildings were revised based on the additional information revealed by images obtained through social media. The UAV footage was exceptionally useful for estimating the damage state of the buildings that were inaccessible during the damage survey. Ground access for some damaged industrial buildings was restricted for safety and security concerns. Five damaged buildings were evaluated primarily from the UAV footage: four allocated within the grounds of the Pilkinton glass factory, two service buildings (DI 21) at the LaSalle County Highway Department, and one at the LaSalle County Nursing Home (DI 17). Of the two buildings at the glass factory, the metal roof panels had been removed on one, and the other was partially collapsed with significant structural damage. DOD 4 (DI 23) was assigned

to the former building and DOD 7 (DI 21) to the latter building. The two LaSalle County service buildings had roof damages with purlins buckled and were rated as DOD 5 (DI 21). A single low-rise building at the LaSalle County Nursing Home also had significant roof damages and was rated as DOD 3 (DI 17) (McDonald and Mehta, 2006). A comprehensive damage survey of the Naplate, IL tornado including all the damage indicators (DI 2, DI 17, DI 21, DI 23, trees, and traffics signs) is shown in Figure 2.12. A detailed analysis of wind speed estimation and comparison of different independent methods suited for each damage indicator will be discussed in Chapter 7.

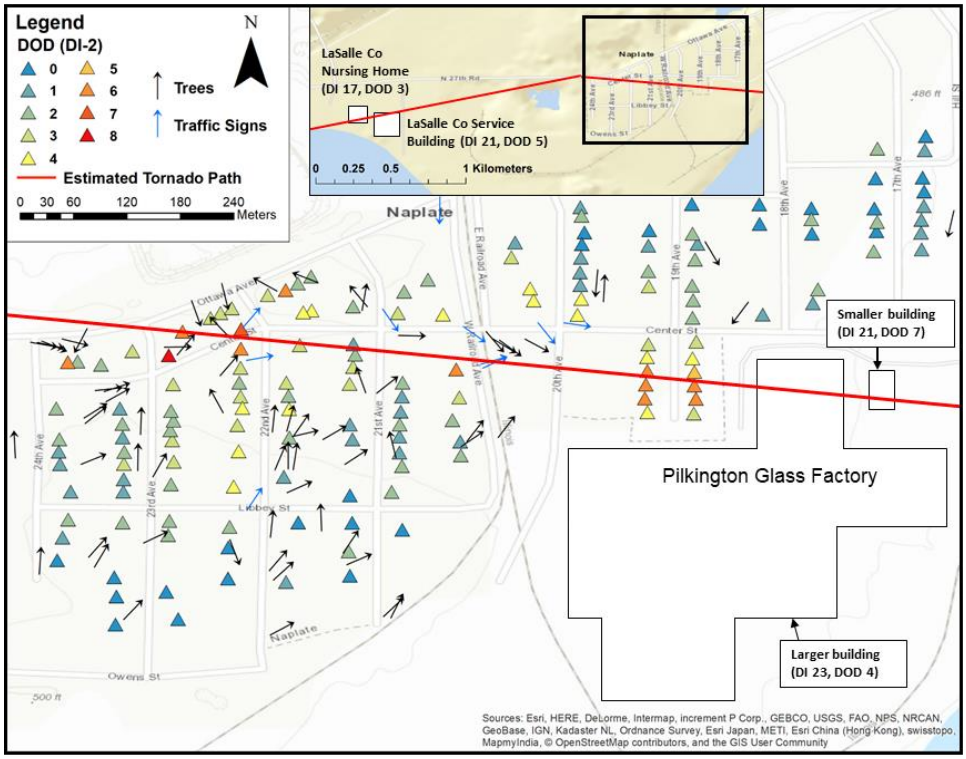

Figure 2.12. Summary of the Naplate, IL tornado damage survey along with the location of LaSalle Co nursing home and service building. The residential buildings with their DOD rating are shown in triangles. Tree damage and traffic sign damage with direction are indicated with black and blue arrows, respectively. The estimated tornado centerline is shown with a red line.

2.3.3 Aerial Survey

Documentation of damages is an essential part of the near-surface wind speed estimation of a tornado; the geographic coordinates and fall direction (if tree or crops) of damage indicators must be obtained. However, tornadoes often inflict damage to a large area, damaging thousands of residential buildings (Burgess et al., 2014; Kuligowski et al., 2014; Roueche and Prevatt, 2013) and knocking down thousands to millions of trees and crops (Fujita, 1989; Karstens et al., 2013; Godfrey and Peterson, 2017) and it may be infeasible to survey the entire damaged area. For tornadoes that damage large areas, aerial photographs are often taken and used to examine the extent of the damage and visualize the overall damage pattern. The georeferenced aerial imageries of these damage sites are obtained by flying aircrafts or Unmanned Aerial Vehicles (UAV) and used to access the damage. On July 18, 2018, a large volume of corns was damaged with marks of a tornado in Bondurant, IA; the damage survey was conducted by the WERL. For the Bondurant, IA tornado, a UAV was used to document the corn-fall patterns (Figure 2.13) as the damaged area was significantly large and thus not feasible to cover the entire area on the ground. However, the properties of corns, such as the spacing from one another, growth stage, diameter, and height, were still examined and documented on the ground. This information with the result from experimental testing will also be used later in Chapter 5 to calculate the critical wind speed of corns, which will serve as one of the input parameters in the tree-fall analysis application on cornfields.

For larger-scale tornadoes, aircrafts are suggested whereas UAVs are more suitable for smaller-scale as there is a trade-off between the resolution and capturing the extent of the damage. UAVs are particularly useful in visualizing the damage path, damage width, and the damage pattern of crops because they can fly much closer to the ground and provide much higher resolution. Once a series of georeferenced aerial photographs are obtained from aircrafts or UAVs,

the georeferenced images are then “stitched” together into a composite image, creating an orthomosaic map. Orthomosaics are geometrically corrected images using 3D point clouds, points containing the X, Y, Z position, and the color information, which can be generated using commercial software such as, OpenDroneMap, Agisoft, DroneMapper, etc. Figure 2.13(a) and Figure 2.14(a) show parts of the orthomosaic of the Bondurant, IA tornado taken by a UAV and that of the Joplin, MO tornado taken by an aircraft. In addition to UAVs, LiDARs can also be a great supplement in post-storm damage assessments as they can provide visuals of inaccessible places and preserve the damage information in great detail. These remote sensing techniques are frequently used in forensic investigations and are already in use for post-storm damage surveys (Radhika et al., 2015; Womble et al., 2017; Womble et al., 2018)

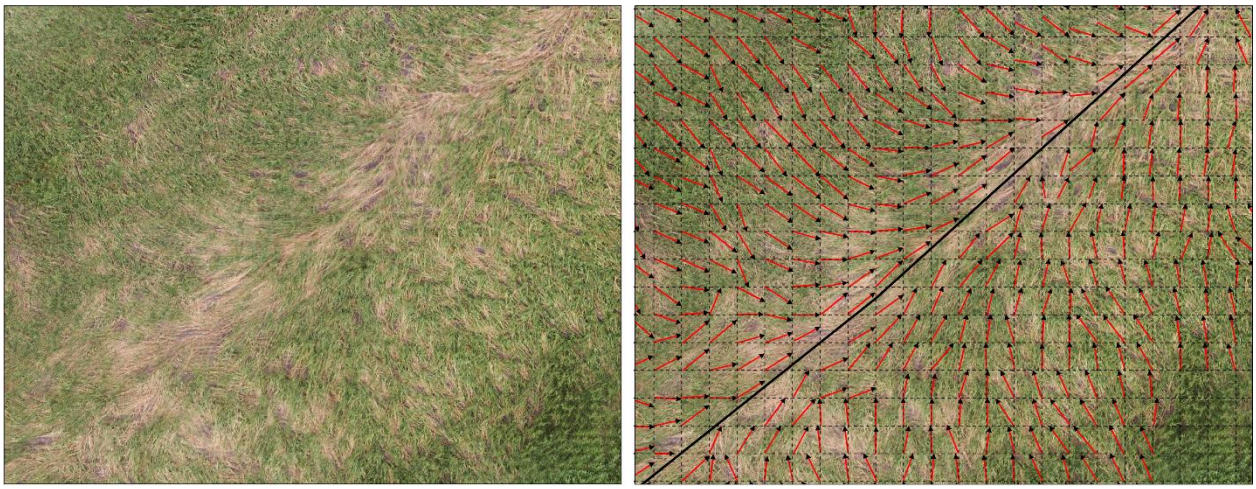

(a) orthomosaic (b) annotated corn-fall

Figure 2.13. Corn-damage documentation of Bondurant, IA tornado: (a) orthomosaic of corn damage and (b) the corn-fall pattern annotated.

(a) orthomosaic (b) annotated tree-falls and damaged buildings

Figure 2.14. Digital conversion of (a) residential building and (b) tree damage of Joplin, MO tornado on ArcGIS.

Once orthomosaics are created, images of damage indicators then can be converted into informative digital data and documented on a GIS. The damaged buildings are converted to polygons (geolocation and damage state) as shown in Figure 2.14(b). The fallen trees (Figure 2.14(b)) and crops (Figure 2.13(b)) were converted to digital vectors (geolocation and direction). Figure 2.14 shows the digital conversion of damaged residential buildings into damage-based color-coded polygons and the digital conversion of tree damage images into vectors (yellow arrows) of the Joplin, MO tornado. The building footprint polygons, usually publically available on the online GIS database or USGS, are colored based on the severity of the residential buildings: in this example, 1) green is light damage, 2) yellow is medium damage, 3) orange is heavy to totaled damage, and 4) red is demolished. The tree-fall vectors are drawn from the root of the tree into the direction of the tree fallen. In the National Institute of Standards and Technology (NIST) report, the damage state of approximately 7,500 damaged residential buildings and the fall direction of approximately 5,000 trees were determined on the Joplin, MO tornado (Kuligowski et al., 2014). Additional 2,000 trees were identified by the WERL researchers. In the same way, the corn damage pattern can be manually documented as shown in Figure 2.13(b). Instead of tagging

individual corn, the orthomosaic is divided into small grid boxes and the direction of a group of fallen corn stalk is annotated in each box.

Once all damage indicators are annotated on the GIS map, the damage pattern and damage width of the entire damage site can now be visualized. Figure 2.15 shows the aerial photograph and annotation of the damaged buildings and trees of the Joplin, MO tornado. The tree damage also exhibits a pattern where the trees have fallen in the opposite direction of the translation of the tornado (the tornado translated from west to east) and converge near the center of the tornado. These damage patterns of the tornado are later analyzed and used to estimate the near-surface wind speed of real-case tornadoes (Chapter 7).

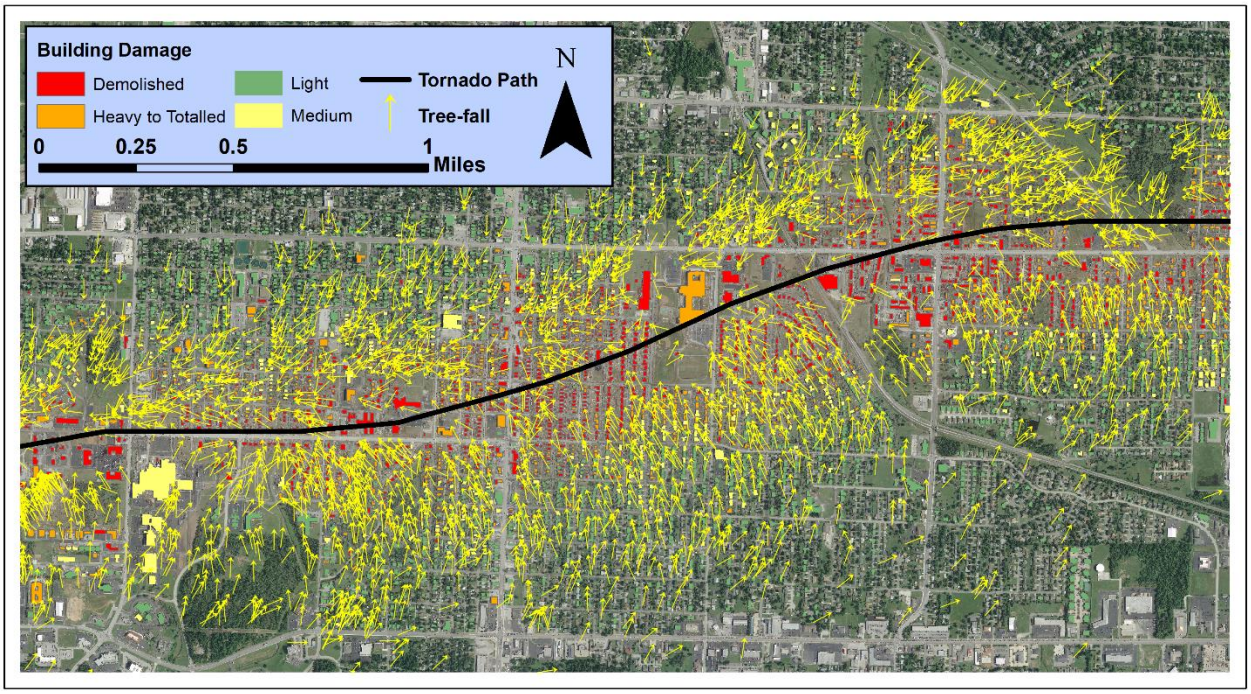

Figure 2.15. Tree-fall (yellow arrow) and building damage (colored polygon) pattern of Joplin, MO tornado.

2.4 Summary

Chapter 2 presents the detailed process of data collection necessary for estimating the near-surface wind speed of a tornado. The data collection can be largely divided into two parts: 1) ground-based damage survey and 2) aerial survey. The ground-based damage survey can provide detailed information about the damage indicators that are unobtainable from air. The information, such as construction quality, diameter and type of trees and, and the dimension of signs, is valuable information that can be used to help estimate the more accurate near-surface wind speed of the tornado. Aerial photographs are also beneficial for visualizing the damage pattern of larger-scale tornadoes and crop damage.

The data collection mostly includes documenting the damage of residential buildings, trees, crops, and signs. To assess the damage, the Damage of Degrees (DOD) of residential buildings and the fall direction of cantilever-like DIs are documented in this study. Images and videos obtained from social media can also be used as supplementary data. The damage pattern of the DIs exhibits a distinct pattern that can be used to analyze the tornado characteristics. A summary table of all the damage surveys conducted and aerial photographs collected is shown in Table 2.3. The table includes all the tornadoes discussed in this study.

Table 2.3. EF scale rating with associated wind speed ranges.

City/State or Province	Date/Year	EF rating by NWS	Data collection type	Damage indicators
Tuscaloosa, AL	27 April, 2011	EF-4	Aerial photograph	Tree, residential building
Joplin, MO	22 May, 2011	EF-5	Aerial photograph	Tree, buildings
Sidney, IL	9 September, 2016	EF-2	Ground-based survey	Crop (soybean)
Albany, GA	22 January, 2017	EF-3	Ground-based survey	Tree, residential building
Naplate, IL	28 February, 2017	EF-3	Ground-based survey	Tree, residential building, sign, etc.
Jacksonville, AL	19 March, 2018	EF-3	Aerial photograph	Tree, residential building
Bondurant, IA	19 July, 2018	EF-2	Aerial photograph	Crop (corn)
Alonsa, MB	3 August, 2018	EF-4*	Aerial photograph	Tree
Cookeville, TN	3 March, 2020	EF-4	Ground-based survey and aerial photograph	Tree, residential building

*Rated by Environmental Canada

CHAPTER 3: AUTOMATED TREE-FALL PATTERN IDENTIFICATION

3.1 Introduction

For tornadoes that damage large areas, aerial photographs are often taken and used to examine the extent of the damage and visualize the overall tree-fall pattern. In the past, high-resolution aerial photographs and Geographic Information System (GIS) software have been the primary tools to document the tree-fall patterns (Karstens et al., 2013; Lombardo et al., 2015). A non-exhaustive total of 10,300 trees and 94,500 trees were identified on the Joplin, MO and Tuscaloosa-Birmingham, AL tornado, respectively, in Karstens et al. (2013). Furthermore, a total of 130,000 downed trees have been "tagged" for the Great Smoky Mountains National Park, TN, and Chattahoochee National Forest, GA tornadoes (Godfrey and Peterson, 2017). Tediously, the geographic coordinates and fall direction of each individual tree image have been identified and converted to digital vectors manually in the past. The tree "tagging" process requires an excessive amount of manpower and time, and thus an automated process is essential to increase the efficiency of the near-surface wind field estimation process. With the recent development of advanced image processing techniques and remote sensing technology, many studies identifying tree stems and classifying different species in the forest from aerial photographs have been established (Dralle and Rudemo, 1996; Key et al., 2001; Mallinis et al., 2008; Sugumaran et al., 2003). More recently, other methods using image processing and remote sensing have been extended and applied to automatically detect damage and debris after severe windstorms. Chehata et al. (2014) apply the image segmentation technique to extract the difference in the parameters of the multispectral pre- and post-storm images and detect the damaged areas. Radhika et al. (2012) identify the path of tornado-borne debris using texture-wavelet analysis. Radhika et al. (2015) and Womble et al.

(2007) detect building damages after windstorms in the satellite images by applying feature extraction technique such as edge detections and classification using Artificial Neural Network (ANN) and using the RGB distribution difference and correlation of pre-and post-storm images, respectively. These techniques are also applied to the tree damage assessment in hurricanes, where Barnes et al. (2007) adopt an image-driven data mining approach to detect tree damages and Szantoi et al. (2012) utilize the RGB color filter and image recognition tools, such as edge detection and line detection technique, to identify downed trees and debris. The various proposed image processing tools, such as the RGB color filter and line detection technique, are also used in this study to identify trees from aerial photographs. Although the preceding studies provide great tools and insight in detecting trees, no studies determining the fall direction of downed trees automatically have been established in the past. In this chapter, a semi-automated tree-fall pattern detection method using an RGB filter and line detection technique and its accuracy on the Alonsa, MB tornado will be discussed.

3.2 Methodology

The semi-automated tree-fall pattern identification process broadly consists of four parts: 1) separation of the stems and leaves using RGB color filter, 2) Object detection and noise object filter, 3) Line detection using Hough transformation, and 4) Tree-fall direction determination based on relative position vector. A flow chart of the entire identification process including the MATLAB functions used in the analysis is shown in Figure 3.1. The detailed process of each part will be discussed in the corresponding section. For the processing tool, the MATLAB 2017a Image Processing Toolbox (MathWorks, 2019) was used. Note that the image processing algorithm is highly dependent on the resolution of the image and it is recommended to use an image with at

least 20-cm resolution. A sample of the same images with different resolutions was tested; the accuracy of fall direction dropped significantly for images lower than 20-cm resolution as the shape and integrity of the trees in the image started to be compromised.

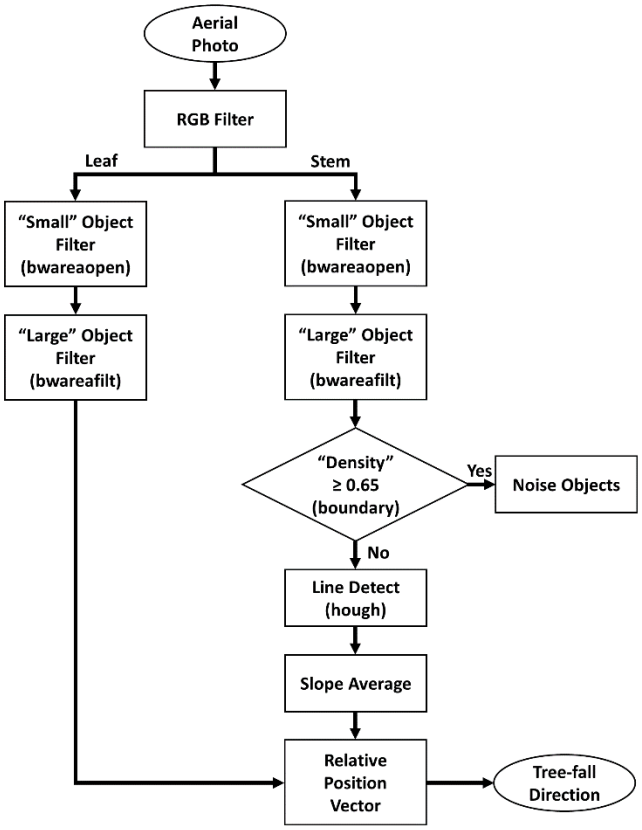

Figure 3.1. Flow chart of the automated tree-fall direction identification process from aerial photo to the tree-fall direction.

3.2.1 Separation of Stems and Leaves Using RGB Color Filter

In image processing, image filtering changes the range (i.e. the pixel values) of an image and alters the colors of the image. An RGB-based color filter, commonly used in image processing practice to extract specific colors from an image, is applied to extract pixels associated with trees in the aerial photographs. Using the color difference in the image, an RGB color filter can be

utilized to even separate the stem (including the branches) and leaf pixels. Though, the RGB color image can be alternatively represented and processed in other color spaces, such as HSI (Hue, Saturation, Intensity), HSV (Hue, Saturation, Value), YIQ (Luminance, In-phase, Quadrature), etc. (Chien and Tseng, 2011). In this study, the RGB-based color filter is used because the aerial imageries were acquisitioned in the RGB color model. According to Chien and Tseng (2011), distortions may occur during the transformation from RGB to HSI color space, which may cause several undesirable phenomena. In the RGB filter process, the image is first converted to digital numbers (DNs), in which each pixel consists of three channels: red, green, blue. DN is defined by a number between 0 to 255 that represents the "intensity" of light where 0 represents black (no light) and 255 represents white (very bright light). To extract specific pixels, any pixels in which DNs fall within the predetermined ranges of DN for all three channels are selected, and the selected pixels are converted to binary numbers where 1 is presented as white (activated) and 0 is represented as black (non-activated), creating a black-and-white binary image (Szantoi et al., 2012). In general, the DN ranges can be selected by looking at the DNs of a specific pixel and the overall DN distribution. For example, the DNs of a "red" pixel in the left figure in Figure 3.2 (original image), are 203, 23, and 25 for R-, G-, and B-channel, respectively. From the DNs of the "red" pixel, an upper bound and lower bound of DN that contains most of the "red" pixels can be decided for each channel. To extract the pen from the original image, an RGB color filter is applied with DN ranges of 160-220, 0-40, and 0-40 for R-, G-, and B-channel, respectively, and the selected pixels are converted to a binary image.

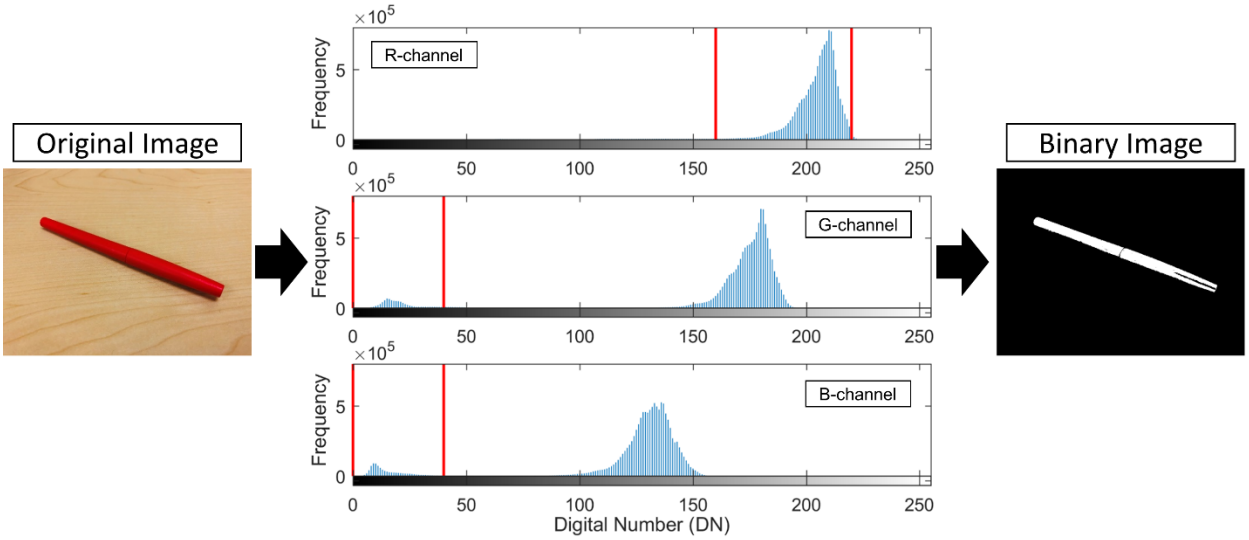

Figure 3.2. RGB color filter illustration, where the histogram of the DN of all the pixels in the original image is shown and the pixels that represent the red pen are selected (red lines in the histogram) and converted to a binary image.

After the RGB color filter is applied, an additional filter that removes "small objects" and background noise using a simple algorithm used for detecting objects in a binary image is applied to the image to eliminate noise. Pixels are considered part of the same object if their edges or corners touch (i.e. two adjacent pixels are both activated along the horizontal, vertical, or diagonal direction). The specific process of applying an RGB filter to trees and separating the stem and leaf pixels will be discussed in the application section (section 3.3.2).

3.2.2 Object Detection and Noise Objects Filter

One major disadvantage of the RGB color filter is that any pixels that have a similar color as the target object (e.g. trees in this study) would be selected though they are not part of the target object. Thus, additional filters are required to remove any non-target objects that bypass the noise filter described in section 3.2.1. In this filter, the size and distinguished shape of the trees are used to decide whether the object detected should be considered a tree or a non-tree object. The trees

have a finite size, in other words; a finite number of pixels in the aerial photographs. Utilizing the object detection algorithm, a simple filtering approach of setting a threshold for a maximum number of pixels in the detected objects can be used to filter out any large non-target objects. Such large objects include roads, large parts of earth, greenhouses, and roofs of commercial buildings that have similar colors as the trees.

Although the above filtering method is effective for objects that are much larger than trees, it cannot filter out smaller objects. Using the difference in the shape between trees or a group of trees and objects, another threshold filter can be applied to filter out smaller non-tree objects, such as objects include roofs of residential houses and vehicles. In general, these smaller non-tree objects have a relatively monotone color and thus show a very "concentrated" area in a binary image, whereas trees or a group of trees are less dense as shown in Figure 3.3(b) and (e): the ratio of activated pixels (shown in yellow) to the non-activated pixels (black) within the red boundary of trees in Figure 3.3(b) is less than the ratio of the roof in Figure 3.3(e). Using this concaved-shape characteristic of tree stems due to the presence of branches, the noise objects can be distinguished from trees. For all the objects detected, the boundary of the objects can be determined using an α-shape. In computational geometry, an α-shape is often used to define and capture the "shape" of a given set of points in a plane, where "shape" is defined as the complements of all closed discs (i.e., discs with radii of $-1/\alpha$) that contain all the points (Edelsbrunner et al., 1983; Edelsbrunner and Mücke, 1994). Figure 3.3.B and E show examples of the α-shape boundary (red line) and activated pixels (yellow) of objects detected from Figure 3.3(a) and (d), respectively. Depending on the alpha value, or a shrink factor (S) as defined in MATLAB, the boundary of the object can be tightened or loosened, where $S = 0$ corresponds to the smallest convex set of the points and $S = 1$ corresponds to the tightest single-region boundary around the points. An example

of how the boundary tightens as the shrink factor increases is shown in Figure 3.3(c) and (f). Once the α-shape is defined and the algorithm returns the vertices of the objects, the vertices are used to calculate the area of the boundary of objects, and the "density" of the activated pixels within the boundary can be determined. The "density" (D) is expressed as the ratio of the number of activated pixels to the area of the boundary; that is, for an object with D = 1.0, every pixel within the α-shape boundary of the object is activated. Due to their shape characteristics, the trees have many "holes" or "empty spaces", resulting a relatively low value of "density" (D = 0.11 for S = 0; and D = 0.49 for S = 1.0, shown in Figure. 3.3(c)), whereas the noise objects such as roofs have a relatively "concentrated" area with high density (D = 0.66 for S = 0; and D = 0.98 for S = 1.0, shown in Figure 3.3(f)). As illustrated in Figure 3.3(c) and (f), the boundary of the object is loose for low shrink factor and tight for high shrink factor, in which the difference between the "density" of the group of trees and the roof is greatest when the shrink factor is defined as 0.5. Thus, a "density" threshold can now be introduced removing non-tree objects. Note that the "density" threshold would depend on the value of the shrink factor (S). If a higher S was used, the threshold would also need to be higher as the boundary of the trees would be tighter and subsequently increase the "density". Thus, the threshold value should change accordingly if a different shrink factor is used. Using a shrink factor that maximizes the difference in the "density" between the trees and other objects is recommended but not necessary.

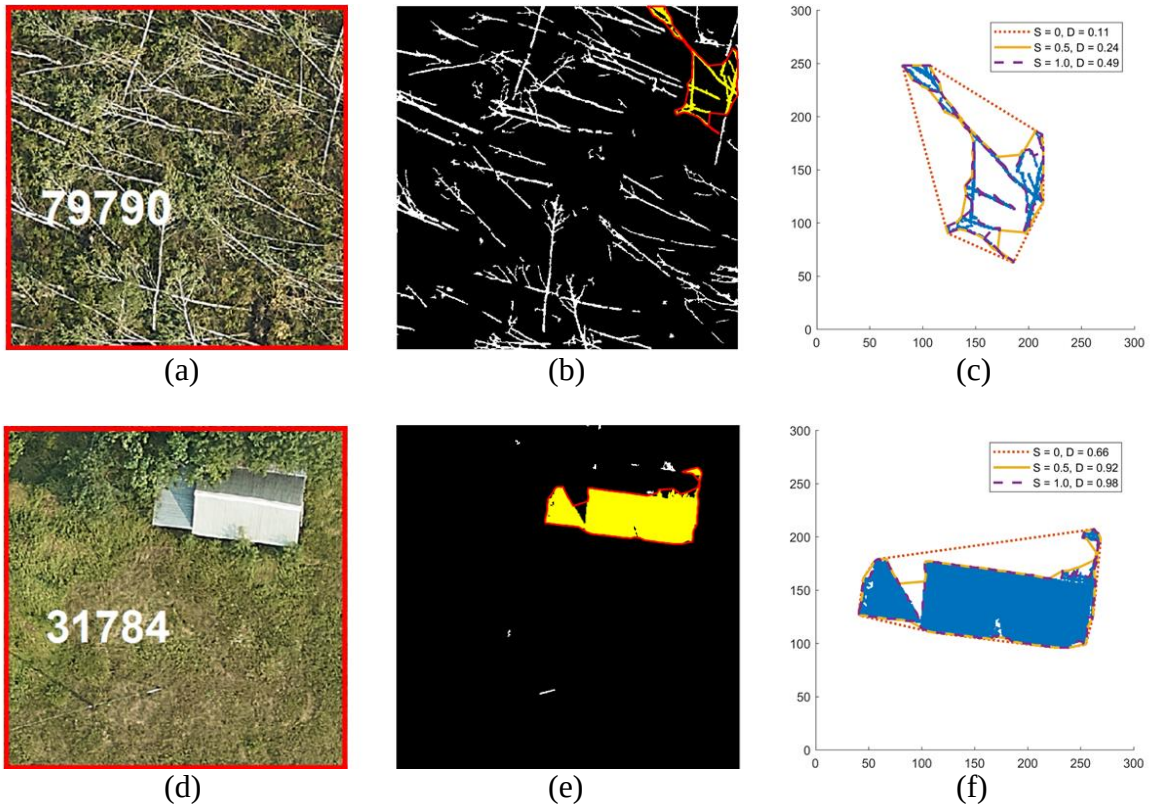

Figure 3.3. Examples of α-shape boundaries with different shrink factor of detected objects and trees: (a) original image with trees, (b) object detected (yellow) and α-shape boundary of a group of trees (red), (c) α-shape boundary of trees with $S = 0$ (red dotted line), $S = 0.5$ (yellow solid-line), $S = 1.0$ (purple dashed-line), (d) original image with a roof, (e) object detected (yellow) and the α-shape boundary of roof (red), (f) α-shape boundary of roof with different shrink factors.

3.2.3 Line Detection Using Hough Transformation

Once the noise objects are filtered out, the down trees are identified in the binary image by detecting lines using the Hough transformation. The binary images are divided into smaller grid boxes and the Hough Transformation is applied to determine the slope of the downed trees. Hough transformation, a technique widely used in image processing and computer vision that extracts features, such as lines and circles (Ballard, 1981), is applied to the stem pixels to detect lines in the binary image and determine the slope of the tree stems. Because of its automatic nature, the Hough transformation has broad applications, including biomedical image segmentation, pattern

recognition, machine learning, autonomous car, etc. (Cheng et al., 1989; Fu and Mui, 1981; Rosten et al., 2010; Urmson et al., 2008). Other edge techniques, such as Canny filter, Sobel filter, and wavelet-based transform, can also be a great tool to extract lines (Aydin et al., 1996; Canny, 1986; Sobel, 1978; Torre and Poggio, 1986; Zhang et al., 2009). However, the Hough transformation was used in this study to extract the lines of trees as the Hough transformation can directly provide the geometric information of the detected feature, specifically the slope of the line in this study, whereas other edge detection techniques can only detect the outlines of an image and further complicated analysis or algorithm is required to automatically extract the geometric information. To enhance the line detection process using Hough transformation, two morphological operations are performed beforehand: 1) one that bridges a gap between unconnected pixels in a binary image by changing the 0-valued pixels to 1 if their neighbor pixels are nonzero and not connected (Figure. 3.4(a)), and 2) another that fills a hole that changes the 0-valued pixels to 1 if the 0-valued pixels are surrounded by 1-valued pixels (Figure 3.4(b)). Performing these two operations fills any gaps or holes within the stems made from the color filtering and subsequently increases the chance of detecting lines when the Hough transformation is applied. This process is repeated until the image no longer changes.

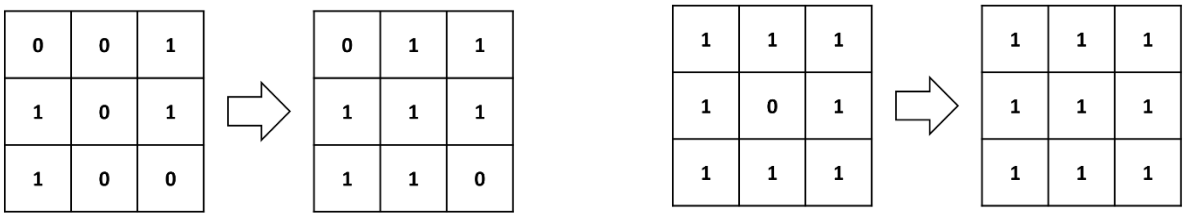

(a) bridge operation (b) fill operation

Figure 3.4. Illustration of pixel morphological operations: (a) bridge operation that bridges a gap between unconnected pixels and (b) fill operation that fills a hole surrounded by activated pixels.

Once the morphological operations are performed, the Hough transformation can now be applied to detect lines. In the Hough transformation, a straight line can be defined as the following equation:

$$\rho = xcos(\theta) + ysin(\theta) \tag{3.1}$$

where θ is the angle (from -90° to 90°, and counter-clockwise is positive) of its normal and ρ is the distance from the origin (Duda and Hart, 1972) as shown in Figure 3.5(a). An example line with θ = 45° and $\rho = 2\sqrt{2}$ in Figure 3.5(a) consists of an infinite number of points (x_1,y_1; x_2,y_2; x_1,y_3;…), in which all the straight lines that pass through each point can be represented in a θ-ρ plane as shown in Figure 3.5(b). In other words, every line in the *x*-*y* plane can be represented as a unique point in the θ-ρ plane. The point in Figure 3.5(b) that the three curves intersect results the line that includes all three points in the *x*-*y* plane. Using this analogy, a binary image, which can be regarded as a group of points in the *x*-*y* plane, can also be transformed to points in θ-ρ plane, and the points with many overlaps, or local maxima, are identified as lines in the image. In the application of identifying the tree-fall pattern, a high maximum number of local maxima, or peaks, should be decided to ensure capturing a wide range of θ and ρ, i.e., tree-fall directions. Furthermore, a minimum line length and a minimum distance between lines can be optionally added in the MATLAB function, which is recommended since the trees have a finite height and spacing with each other. After the Hough transformation is applied, the median of the angles (θ) of lines in the grid box is determined assuming that the trees within the same grid box fall in the relatively same direction. The median slope of tree stems (θ_{med}) is determined rather than the slop of individual tree stem because identifying and differentiating the stems and branches of one tree

from the other is difficult. Differentiating the leaf and stem pixels of one tree from the others is even more difficult which is necessary for identifying the individual tree-fall direction of the downed tree. Furthermore, some trees may fall downwind depending on the strength of the trees, which may produce outliers within the grid box. As the average value can be sensitive to outliers, the median value is used to represent the prevailing wind direction, which produced a better result than the average value.

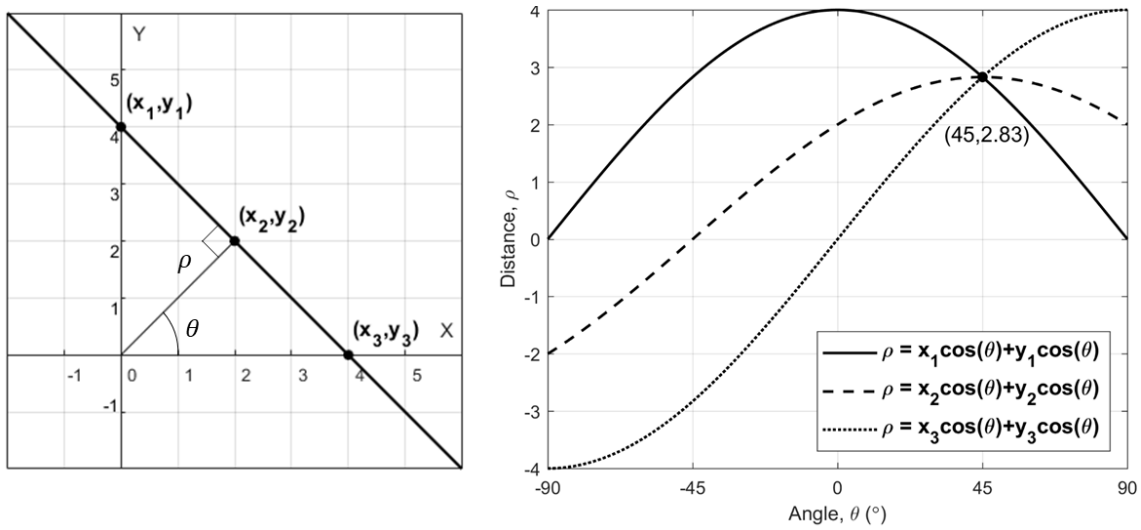

(a) (b)

Figure 3.5. Illustration of Hough transformation: (a) points (x_1, y_1), (x_2, y_2), (x_3, y_3) on a line in x-y plane with angle (θ) and distance from origin (ρ), and (b) curves in θ-ρ plane that pass through (x_1, y_1), (x_2, y_2), (x_3, y_3) points. The intersection of all three curves represents the line in the x-y plane.

3.2.4 Tree-fall Direction Determination Based on Relative Position Vector

Even after obtaining the median angle, the question of which direction the trees have fallen remains unsolved; e.g. whether the trees have fallen towards either side of the median slope of the trees. The median tree-fall direction ($\bar{v}_{med}$) is then determined, using the relative position of the leaves from the stems. The relative position vector of each leaf pixel with respect to each stem

pixel within a certain distance (r_{thresh}) can be determined, and the average relative position vector ($\bar{w}_{avg}$) is calculated as shown in Eq. (3.3).

$$r = \sqrt{(x_j - x_i)^2 + (y_j - y_i)^2} \tag{3.2}$$

$$\bar{w}_{avg} = \left(\frac{\sum_{i=1}^{N} \sum_{j=1}^{M} (x_j - x_i)}{N + M}, \frac{\sum_{i=1}^{N} \sum_{j=1}^{M} (y_j - y_i)}{N + M} \right) \text{ for } r \leq r_{thresh} \tag{3.3}$$

where x_i, y_i and x_j, y_j represent the x and y-coordinate of all the stem and leaf pixels, respectively, and N and M are the total number of pixels for each of them. Initially, the approximate size of the tree branches can be used for r_{thresh}. However, a more detailed analysis can be done to increase the accuracy of $\bar{w}_{avg}$, in which an example is shown in section 3.3. Once the $\bar{w}_{avg}$ is obtained, the median tree-fall direction ($\bar{v}_{med}$) is decided by taking the minimum difference between the $\bar{w}_{avg}$ and either end direction of the θ_{med} $\left((90 + \theta_{med}) \text{ or } -(90 - \theta_{med})\right)$. The differences ($d_1$, d_2) are calculated using the inverse cosine of the dot product of the two vectors as shown in the following:

$$d_1 = \cos^{-1}\left(\frac{\bar{w}_{avg} \cdot \left[\cos\left(-(90 - \theta_{med})\right), \sin\left(-(90 - \theta_{med})\right)\right]}{\left|\bar{w}_{avg}\right| \cdot \left|\cos\left(-(90 - \theta_{med})\right), \sin\left(-(90 - \theta_{med})\right)\right|} \right) \tag{3.4}$$

$$d_2 = \cos^{-1}\left(\frac{\bar{w}_{avg} \cdot \left[\cos\left((90 + \theta_{med})\right), \sin\left((90 + \theta_{med})\right)\right]}{\left|\bar{w}_{avg}\right| \cdot \left|\cos\left((90 + \theta_{med})\right), \sin\left((90 + \theta_{med})\right)\right|} \right) \tag{3.5}$$

Thus, the $\bar{v}_{med}$ is decided as $(90 + \theta_{med})$ if d_2 is smaller than d_1, and $-(90 - \theta_{med})$ if vice versa. An example illustration of tree-fall direction determination is shown later in section 3.3. The

median fall direction is calculated instead of the individual tree-fall direction because identifying and differentiating the leaf and stem pixels of one tree from the others is extremely difficult as mentioned before. In addition, although the value may be different from the median value and the average tree-fall direction is used to define the tree-fall pattern and estimate the near-surface wind speed in tree-fall analysis, both measurements represent the prevailing wind direction.

3.3 Application

3.3.1 General Information and Aerial Imagery of Alonsa, MB Tornado

On the 3 August 2018, a tornado occurred and traveled from the forest in the southwest of Alonsa into Lake Manitoba with a path length of 12.5 km and a maximum width of 800 m. The georeferenced aerial photographs of the post-damage of Alonsa, MB tornado (EF 4) were taken ten days after the tornado by the Northern Tornadoes Project (Sills et al., 2020). Over the forest west of Alonsa, MB, a plane flew approximately 300 m (1000 ft) above the entire length of the tornado track, producing a total of 26 orthomosaics with a combined length of 13,000 m (42,650 ft) and width of 8,000 m (26,245 ft), and a pixel resolution of 5-cm (about 2-in).

3.3.2 Application to Alonsa, MB Tornado

The semi-automated tree-fall pattern identification technique is applied to the Alonsa, MB tornado, a heavily forested area in the west of Alonsa, MB where the tornado traveled and damaged a countless number of trees. The general framework described in section 3.2 is applied to the Alonsa, MB tornado with specific input parameters and the result is shown in this section. For illustration purpose, a part of the Alonsa, MB aerial photo is chosen and used as an example throughout the section. The photo and its location with respect to the entire tornado track are shown

in Figure 3.6. The image is divided into 500×500-pixel (25×25-m) grid boxes with the corresponding number.

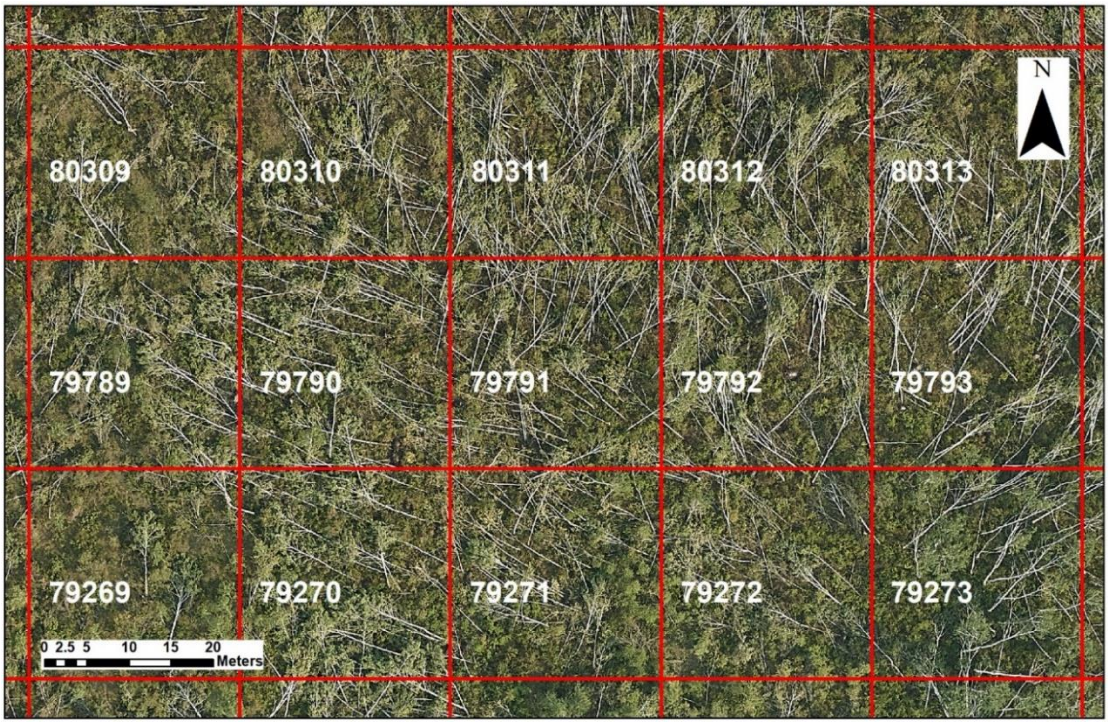

(a)

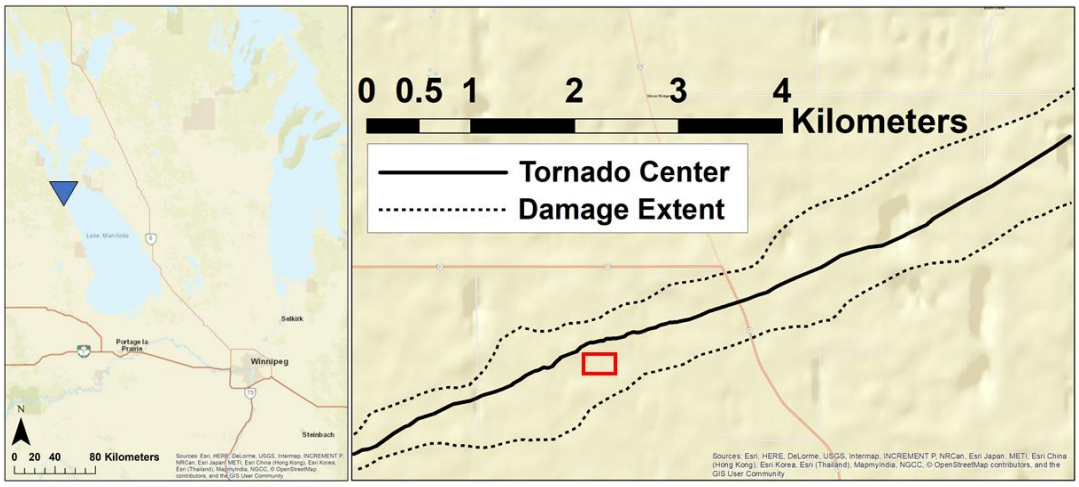

(b)

Figure 3.6. The location of the example image with respect to the entire tornado track: (a) example tree-fall image of the post-damage Alonsa, MB tornado, and (b) tornado occurred location in Manitoba and estimated tornado center and damage extent.

First, the tree stems and leaves in Figure 3.6(a) are separated using an RGB color filter. DN ranges of 85-255 (both leaves and stems) and 145-255 (stems), respectively, for all three channels are selected. The binary images of IM-79790 are shown with both leaves and stems (Figure 3.7(a)) and with just the stems (Figure 3.7(b)) after applying the RGB color filter. For the noise filter, any objects detected with the number of pixels less than 50 are considered as noise and removed from the image (Figure 3.7(c) and (d)). Finally, the binary image with the stems alone (Figure 3.7(d)) is subtracted from the image of the leaves and stems together (Figure 3.7(c)), resulting in an image with just the leaves (Figure 3.7(e)). Therefore, the ranges of DN for stems and for leaves become 145-255 and 85-145, respectively, for all three channels. To avoid any overlaps in classifying pixels, the ranges are selected such that there are no overlaps. Figure 3.7(f) shows the final image of extracting and separating the leaves (red) and stems (blue) from IM-79790. Note that the range of DN and noise filter pixel size of 50 are determined manually based on trial and error and a different range may result in a better outcome. A general guideline for noise filter pixel size is to keep increasing the pixel size until a noticeable amount of stem or leaf pixel is removed. Significant removal of stem-leaf pixels will affect the tree-fall direction calculation. Regarding the DN range selection process, although more advanced filtering processes, such as vector median filtering and Euclidean distance transformation, may improve the accuracy over a range of colors (Astola et al., 1990; Barni et al., 2000), the manually determined color range has proven its effectiveness in this study, and thus no such advanced color filtering process was applied.

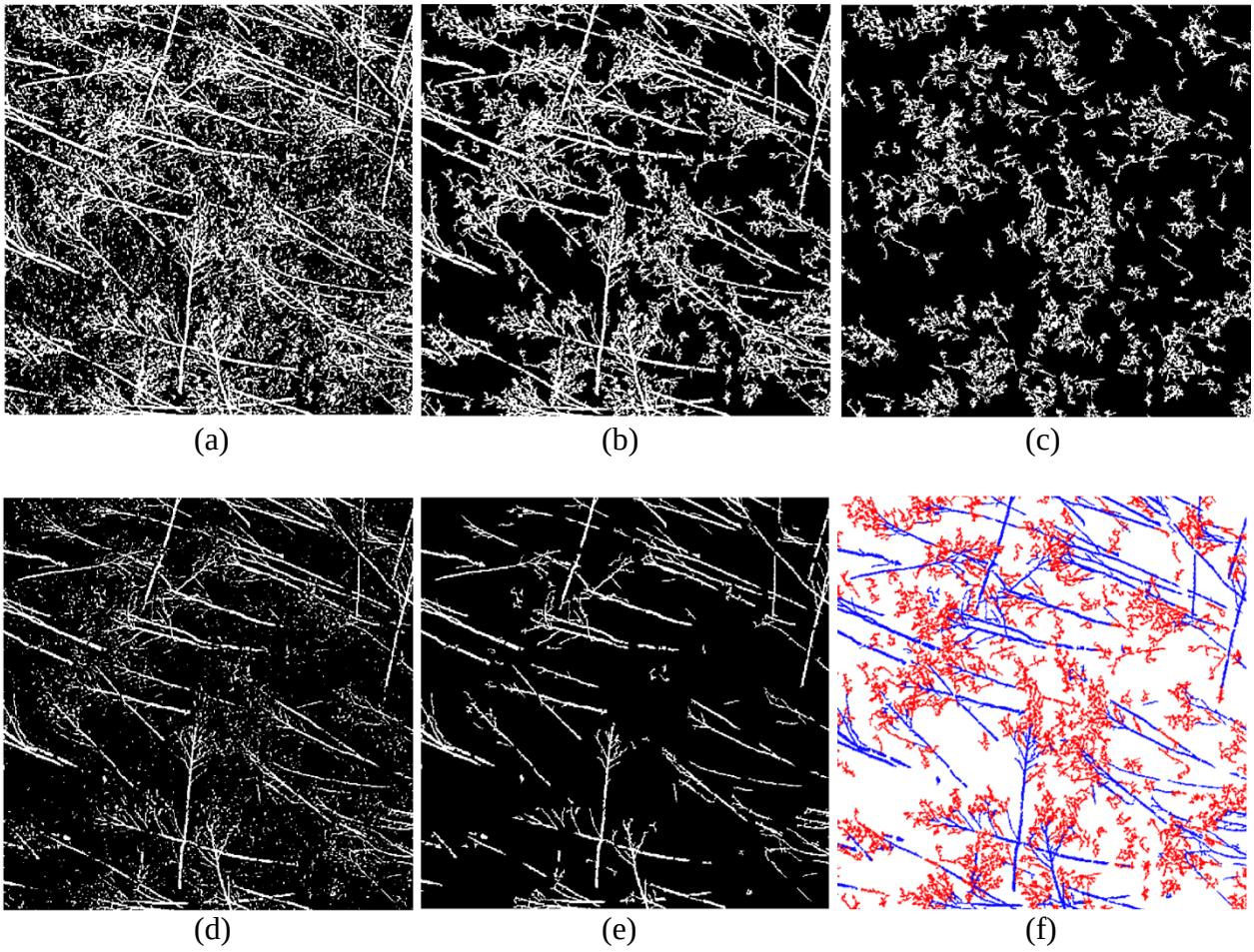

Figure 3.7. Illustration of tree detection using RGB filter and separating leaf and stem pixels of IM-79790: (a) tree binary image after RGB filter (DN: 85-255), (b) stem binary image after RGB (DN: 145-255), (c) tree binary image after noise filter, (d) stem binary image after noise filter, (e) leaf binary image after subtracting (d) from (c), (f) final image after RGB, noise filter where red and blue denotes the leaves and stems, respectively.

After the RGB color filter, non-tree large objects are removed from the binary image of Alonsa, MB tornado. Based on a random sampling of 7,890 objects that are detected as trees, the maximum pixel size of these trees is 11,772. Thus, a threshold of 12,500 pixels is established, removing any object that consists of more than 12,500 pixels from the binary image. Then, the "density" filter was applied with a shrink factor of 0.5. For the Alonsa, MB tornado, the "density" of a total sample of 115 detected trees has a mean value of 0.383 and a standard deviation of 0.081,

in which the distribution of the "density" of trees is shown in Figure 3.8. Based on the distribution of the "density" of the detected trees, the filter threshold is set as D = 0.65, the mean value plus three standard deviations. In other words, any object detected with "density" greater than 0.65 is removed from the binary image. Once the large objects are removed, the binary images are divided into smaller images (500×500-pixel): a total of 166,400 grid boxes, each having corresponding image numbers from 000000 to 166399 (e.g. Figure 3.6(a)). The grid box size of 500×500-pixel (25 m^2) is decided as 2.5 times the height of the trees (approximately 10 m) so that the size is small enough that the assumption of trees falling in the relatively same direction is not violated but large enough that a sufficient number of trees are present within the grid box. A minimum of three trees within each grid box should be used to generate a relevant median value.

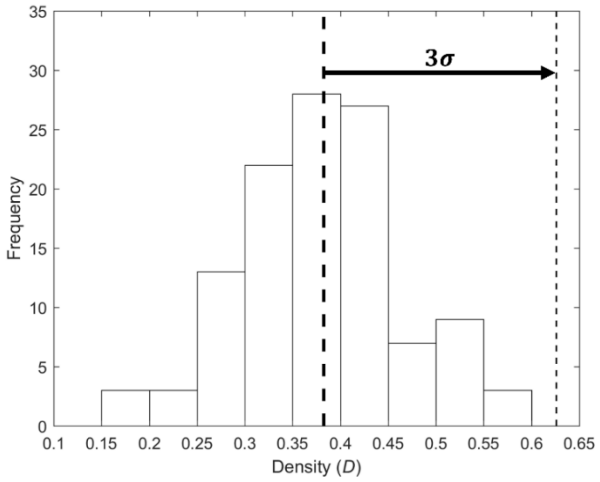

Figure 3.8. Distribution of "density" (D) of 115 detected trees. The thick dashed line represents the mean D and the thin dashed line represents the value of three standard deviations above the mean.

In the application of Hough transformation to the Alonsa, MB aerial photo, the maximum number of peaks (number of local maxima) is set to 700 based on the analysis similar to Figure 3.8 using the number of peaks. For randomly chosen 192 grid boxes, the mean number of peaks is

217.2 with a standard deviation of 140.7, setting the maximum number of peaks to mean plus three standard deviations. Furthermore, thresholds of a minimum length of 20 pixels and a minimum distance of 2 pixels between lines are applied. With a 5-cm resolution aerial photo, it is assumed that the trees would have a minimum length of 20 pixels (1 m) and a minimum of 2 pixels (0.01 m) distance from each other. Figure 3.9(a) shows the result of applying the Hough transformation to the stem binary image of IM-79790 (Figure 3.7(d)). The green lines represent all the lines detected with a minimum length of 20 pixels. After the Hough transformation is applied, the median of all the angles of the line in the grid box is determined. The median slope (θ_{med}) from the Hough Transformation is 51.2° ((2) in Figure 3.9(b)), which means the tree-fall direction becomes either in the northeast direction (128.8° in meteorological coordinate, Figure 3.9(b)-(2)) or southwest direction (308.8° in meteorological coordinate, Figure 3.9(b)-(3)). Using the leaf and stem pixels and applying Eq. 3.3, the $\bar{w}_{avg}$ is calculated as 149.7° for IM-79790 (Figure 3.9(b)-(4)).

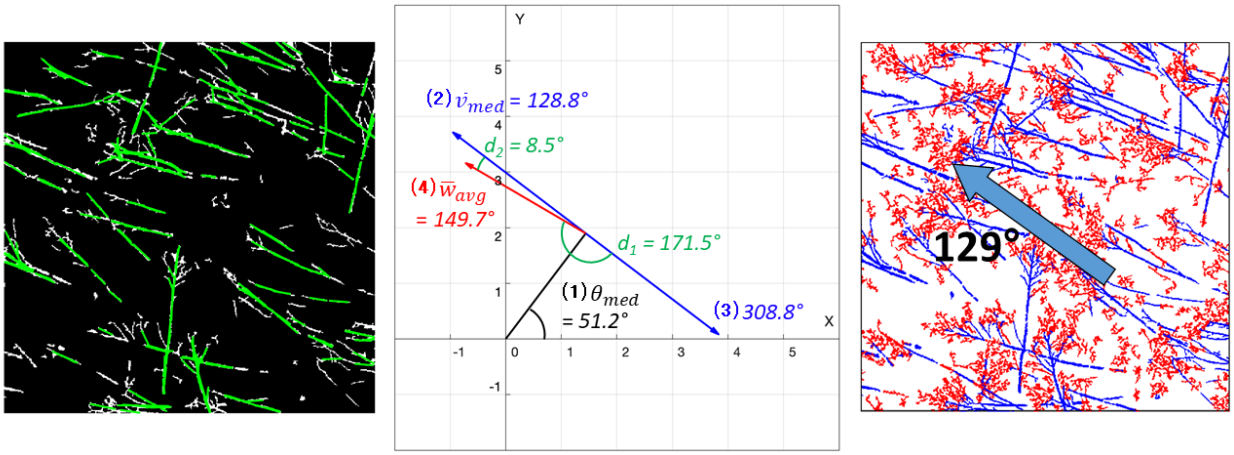

(a) (b) (c)

Figure 3.9. (a) lines detected from binary image of trees after applying Hough transformation, (b) illustration of the median slope, the average tree-fall direction, the relative position vector, and d_1 and d_2 of the binary image, and (c) annotated averaged tree-fall directions of IM-79790 determined from d_1 and d_2.

Lastly, the relative position vector of leaf pixel (red in Figure 3.9(c)) with respect to each stem pixel (blue in Figure 3.9(c)) within the distance (r_{thresh}) of 20 pixels (1.0 m) is determined. The r_{thresh} of 20 pixels is decided based on 50 randomly selected grid boxes. The "true" tree-fall directions within each grid box are pre-determined manually ("tagged" manually and then averaged), and the difference in the angle between the "true" tree-fall direction and the $\overline{w}_{avg}$ is calculated for all 50 samples. The mean and standard deviation of the difference between the two and the percentage error for different distances are summarized in Table 3.1. The error is defined as the percentage of how many $\overline{w}_{avg}$'s calculated are correctly estimated out of the 50 samples. Based on the mean, standard deviation, and error, the r_{thresh} of 20 pixels is decided to be used. Using the r_{thresh} = 20 pixels, the d_1 and d_2 (θ_{med} = 51.2, $\overline{w}_{avg}$ = 149.7°) becomes 171.5° and 8.5°, respectively, from Eq. 3.4 and 3.5 (Figure 3.9(b)). Choosing the smallest of two, $\bar{v}_{med}$ results to be 141.2° (128.8° in meteorological coordinate). Figure. 3.9(b) shows the final annotated tree-fall direction for IM-79790 and Figure 3.10 shows the final annotated tree-fall directions of each grid box of Figure 3.6(a).

Table 3.1. The difference between the average relative position vector ($\overline{w}_{avg}$) and the "true" tree-fall average direction and the error using different distance (r).

Distance (Pixel)	Mean Difference (°)	SD Difference (°)	Error (%)
5	39.62	34.32	10
10	36.62	28.25	6
15	32.03	28.02	4
20	32.90	26.98	2
25	31.82	31.54	4
30	32.90	26.29	4
35	39.40	33.72	10
40	41.65	36.80	10
45	47.15	40.58	14
50	51.48	43.83	12

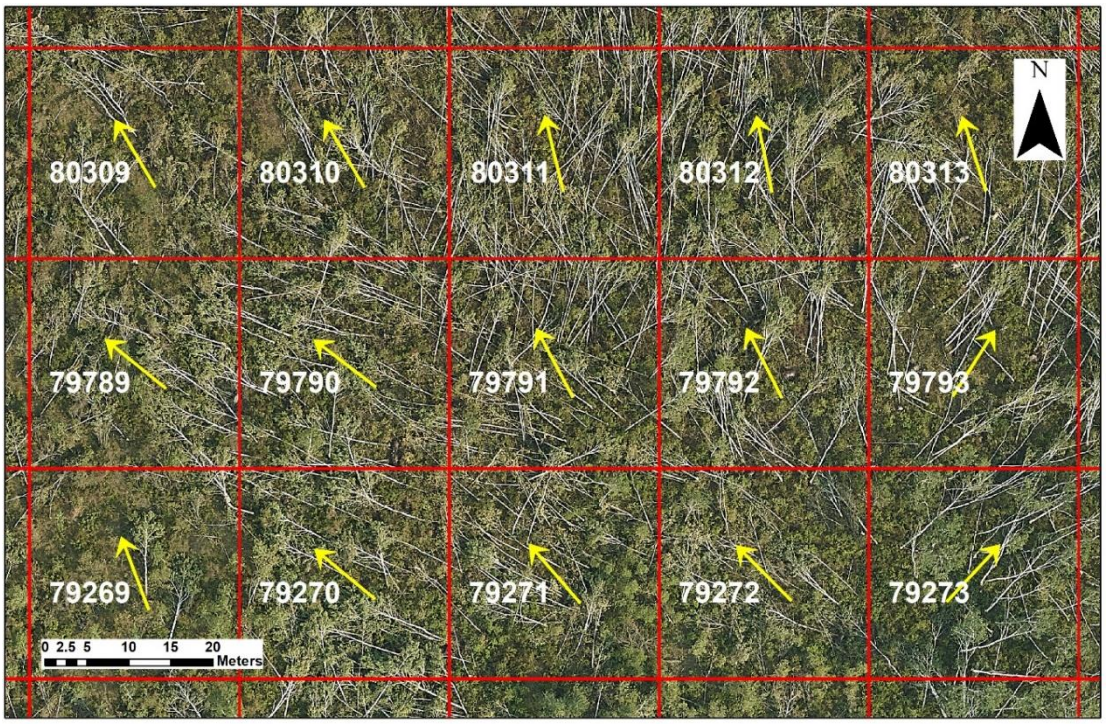

Figure 3.10. Tree-fall directions annotated for each grid box of Figure 3.6(a) using the proposed semi-automated tree-fall identification method.

In order to reduce the computational cost, a sample of 30,000 leaf pixels and 15,000 stem pixels are randomly selected for any grid box that contains more than 30,000 leaf pixels or 15,000 stem pixels instead of processing all the pixels. In other words, M and N become 30,000 and/or 15,000, respectively, in Eq. 3.3. Note that the sample pixel number is decided based on computational memory (16 GB). Depending on the availability of the computational memory of the user, the user may choose a different sample number, though the user should note that the result may change significantly if the sample number is too low. The result between using the 30,000/15,000 randomly selected pixels and using all the pixels for the 50 samples shows an average of 0.5-degree difference. The ratio between the two is kept as two because the number of pixels of the leaf was approximately double that of the stem in general for all sub-images.

The proposed method is applied to the entire tornado track. Figure 3.11 shows two transects of the tree-fall pattern identified (yellow arrows) using the semi-automated method and the estimated tornado centerline (black line). The tornado centerline is estimated based on the most intense damage based on the aerial photographs (Lombardo et al., 2015). The detected tree-fall patterns of the two transects exhibit patterns similar to the general tree-fall patterns (red arrows) (Chapter 4). More detailed analysis of estimating the near-surface wind speed of the Alonsa, MB tornado using tree-fall analysis is discussed in Chapter 7.

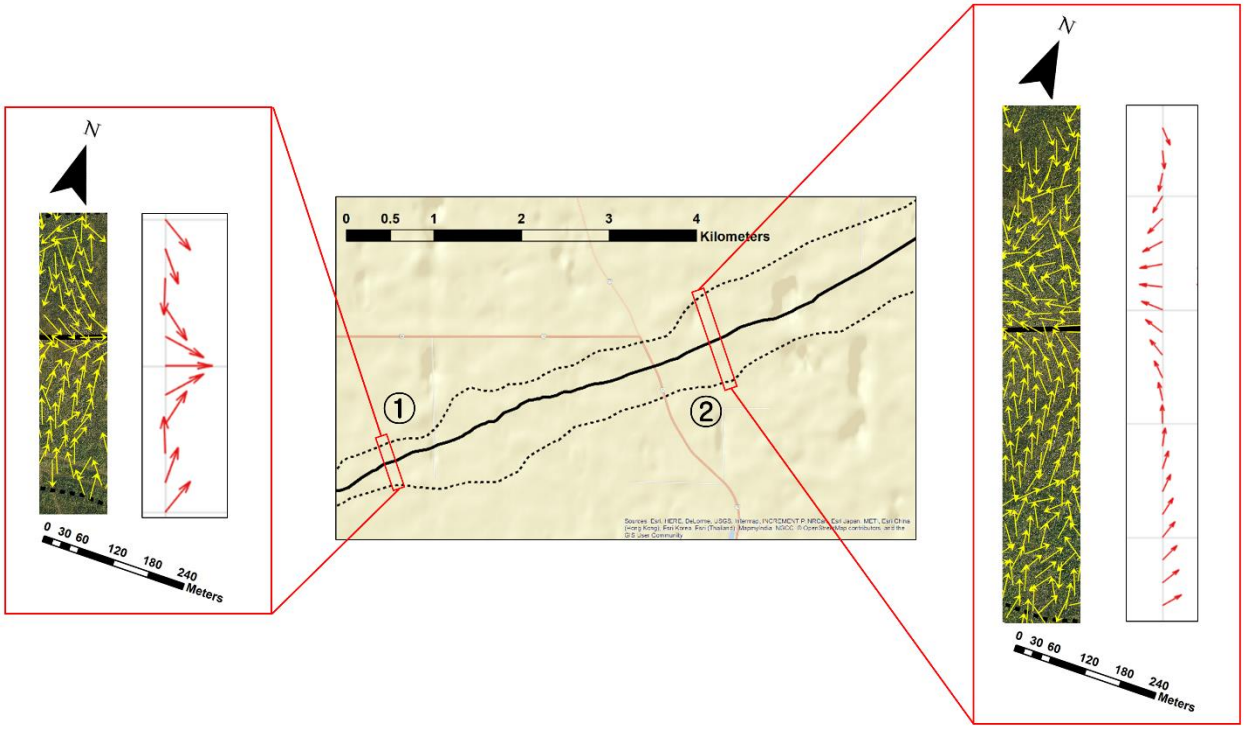

Figure 3.11. Observed (yellow arrows) tree-fall pattern identified from the semi-automated method and simulated general (red arrows) tree-fall pattern of two transects from Alonsa, MB tornado. Red boxes indicate the location of each transect with respect to the tornado track. The observed pattern figures are rotated with respect to the tornado translational direction.

3.4 Error Assessment

Error assessments are performed to ensure the accuracy of identifying trees and determining the median tree-fall direction. For error assessment, four orthomosaics are randomly chosen, and a total of 14,923 trees are manually "tagged" in ArcGIS, meaning the tree image receives an electronic label with its tree-fall direction and geographic coordinates, and used to evaluate the accuracy of the automated tree-fall identification method. Two types of errors are defined and assessed: 1) tree-fall identification error and 2) tree-fall direction error. The tree-fall identification error is evaluated based on the percentage error of false positives and true negatives. Then, the median tree-fall directions using the automated method and using the conventional manual tree-fall "tagging" method are compared to evaluate the tree-fall direction error.

3.4.1 Tree-fall Identification Error

For the four orthomosaics chosen, a total of 3,271 grid boxes are used to determine the tree-fall identification error. Each grid box is evaluated into four categories: 1) true positive (correct labeling: downed trees detected when there are), 2) false negative (incorrect labeling: no downed trees detected where there are), 3) false positive (incorrect labeling: downed trees detected when there are none), and 4) true negative (correct labeling: no downed trees detected when there are none), in which the error of each grid box was determined one-by-one manually. Table 3.2 shows a conventional contingency table of the tree-fall identification method. Some verification metrics, commonly used in forecasting, are used to evaluate the quality of the identification method (NOAA, 2020b). Using the values in Table 3.2, the equation and value of each metric are summarized in Table 3.3. The Probability of Detection (POD) and the Critical Success Index (CSI) are 0.946 and 0.852, respectively, with a False Alarm Ratio (FAR) of 0.104. The overall accuracy (Gold et al., 2020) of the method is 0.953. The overall accuracy represents the effectiveness of correctly identifying both positives and negatives. The method shows a promising result in identifying the trees.

Table 3.2. Contingency table of tree-fall identification.

Trees Detected	**Trees Observed**	
	Yes	**No**
Yes	889 (True Positives)	103 (False Positives)
No	51 (False Negatives)	2,228 (True Negatives)

Table 3.3. Equation and value of verification metric on tree-fall identification error.

Metric	Equation	Value
POD	TP / (TP + FN)	0.946
FAR	FP / (TP + FP)	0.104
CSI	TP / (TP + TN+FP)	0.852
Accuracy	(TP+FN) / (TP + TN+FP+FN)	0.953

3.4.2 Tree-fall Direction Error

The tree-fall direction error is calculated by comparing the automated method with the conventional method, using the 14,923 manually "tagged" trees that amounted to a total of 1,032 grid boxes. All the manually "tagged" downed trees within the same grid box are grouped together and their median fall direction is determined. Then, the median tree-fall directions of the automated method and the conventional method of the 1,032 grid boxes are compared by calculating the difference in the tree-fall direction for each grid box. Figure 3.12 shows the histogram of the differences for all 1,032 grid boxes, in which 39% of them have a difference of less than 10 degrees and about 73% of them have a difference of less than 45 degrees. A difference of 160 degrees or greater has a relatively large proportion (12%) as shown in the distribution. However, this result is encouraging and implies that the automated method is able to estimate the median slope of the tree-falls (θ_{med}) adequately, but the estimation in the median tree-fall direction ($\bar{v}_{med}$) is inadequate for those particular grid boxes as the error in average relative position vector ($\overline{w}_{avg}$) is large. Improving the estimation of leaves location with respect to the stems, perhaps separating leaves from one tree to another though may be challenging, may increase the accuracy of tree-fall direction significantly. Furthermore, although the error may seem large, the overall tree-fall pattern obtained using the semi-automated method exhibited a compatibly similar pattern to the general

tree-fall pattern (Chapter 4). Hence, such error may not affect the near-surface wind field estimation considerably. If necessary, an additional algorithm can be developed that flags the grid boxes with a tree-fall that is significantly different from the neighboring grid boxes. The tree-fall direction in the grid box can be inspected and changed the direction manually if in fact labeled incorrectly.

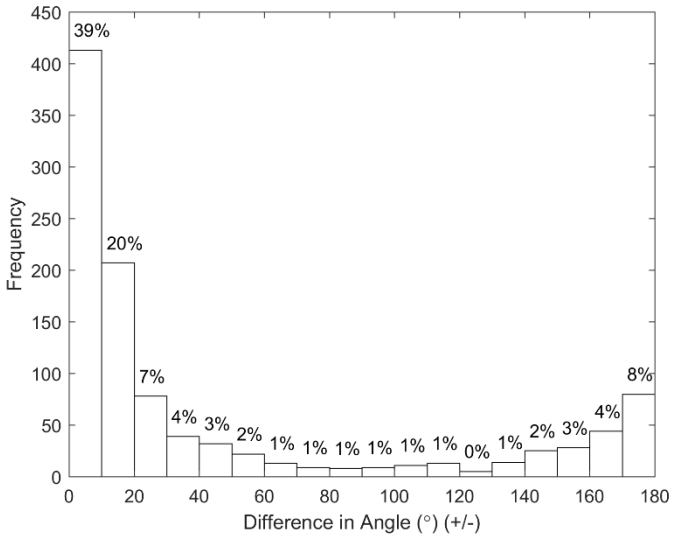

Figure 3.12. Histogram of difference in tree-fall direction between the manual "tagging" method and the automated method.

3.4.3 Limitations

The semi-automated method developed in this study has a few limitations. In the tree-fall identification process, the method often works inadequately when the number of downed trees in a grid box was small. Some large pieces of earth that have a similar color to the tree stems were not filtered out from the "density" threshold. Additionally, near the edge of the tornado damage path, some foliated trees, which were not downed but only the leaves were blown off, were detected as downed trees. In the tree-fall direction determination process, the error between the

semi-automated and the manual "tagging" method was large when the tree-fall directions were not consistent, which violates the assumption of the trees within the same grid box falling in the relatively same direction. Furthermore, the median tree-fall direction ($\bar{v}_{med}$) was incorrectly estimated when the number of leaf pixels detected was high. With a high number of leaf pixels, there is a large overlap of leaves among trees, which often results in a miscalculation in the relative position vector. Furthermore, the automated method may not be able to capture small-scale phenomena (e.g. sub-vortices) within the tornado because the method can only determine the prevailing wind direction within the grid box.

In addition, although the proposed method may have shown a comparable result, the method was developed based on the tornado post-damage aerial photographs in Alonsa, MB, which is a heavily forested area with fairly uniform species of trees. Thus, some input parameters used in this study may have to be adjusted for other post-damage imageries. For tornadoes occurred in urban areas or areas with a diverse species of trees, the proposed method may not perform adequately due to excessive noise objects, and thus additional and more complex filters may be required to obtain compatible results. For different tree types, the stem and leaf would have a different color so the DN range must be adjusted accordingly. Particularly, for evergreen trees, such as pine trees, that have a large crown area, the stems may not be entirely visible in the image which would require an alternative way to detect the slope of the tree. An edge detection technique may be a better approach for obtaining the tree-fall slope. For the edge detection technique, the minimum resolution of the image may be lower as it seems to reserve the shape of the trees even in a lower resolution image. Although the proposed method was effective for the Alonsa, MB tornado, image processing may not be the most practical solution for broader applications. In deep learning, a convolutional neural network (CNN) is widely used to analyze visual imageries and

extract patterns. Potentially, CNN with a sufficient number of trained images of downed trees could be an alternative and a more generalized method for automatically detecting tree-fall patterns. Sills et al. (2020) have used deep learning technique for detecting downed trees and has shown preliminary result with potential for improvement.

3.5 Summary

This chapter introduces a semi-automated method of identifying tree-fall patterns from an aerial photograph using image processing techniques. The method specifically extracts the central tendency of the fall direction and location of a group of trees. The general framework is first developed and then applied to a specific case, the Alonsa, MB tornado. The general framework is described as following:

1) The downed trees are detected using an RGB color filter and defining different ranges of digital number (DN) enables separating the stem and leaf pixels.
2) The object detection tool is used to remove any noise and objects other than trees. The "density" of the detected objects is defined using the number of activated pixels within the boundary of the objects to filter out additional noises.
3) The Hough transformation is applied to identify lines in the stems, in which the median tree-fall direction is determined based on the relative position of the leaf pixels to the stem pixels and the median slope of the lines obtained from the Hough transformation.

The above identification method is applied to the Alonsa, MB tornado with specific input parameter values, and the tree-fall directions are identified. The error is assessed by a manual

process and comparing the result to the manual “tagging” method. Following are the findings from the error assessment:

- The proposed method demonstrated a great result in identifying downed trees in each grid box.
- The error assessment in the tree-fall direction shows less accurate but still comparable results in determining the tree-fall direction, where 59% of the estimated trees had a difference less than 20 degrees and 74% had a difference less than 45 degrees.
- The directional error was high for grid boxes with a high number of leaf pixels. With a high number of leaf pixels, there is a large overlap of leaves among trees, which often results in a miscalculation in the relative position vector. Due to the incorrect estimation of the relative position vector, a relatively high percentage of fall-direction had a difference greater than 160-degree.
- Although the proposed method may require additional work and improvement, it is still able to capture the pattern that can be used in the tree-fall analysis, and it demonstrates a great capability in the automation of tree damage assessment, which can be very beneficial in near-surface wind field estimation of tornadoes in heavily forested areas.

CHAPTER 4: TREE-FALL ANALYSIS INTRODUCTION

4.1 General History and Development of Tree-fall Analysis

Johannes Letzmann, who was a pioneer of tornado research and influenced by Alfred Wegener, attempted to construct a composite wind field of a translating vortex by superposing the rotational and translational velocities. Consequently, Letzmann determined the tornadic wind field and created hand-drawn hypothetical forest damage patterns (Peterson, 1992), which became the foundation of the tornado wind field modeling using tree-fall patterns and influenced many modern tornado researchers in reconstructing tornadic wind fields. For example, combining a tree resistance to wind model by Peltola et al. (1999) and a tornado wind field model, Holland et al. (2006) adopted Letzmann's model and generated analytical tree-fall patterns that could be used to assess the storm characteristics. More recently, other researchers have compared the analytical patterns to the actual observed patterns and estimated the near-surface wind field of various tornadoes (Bech et al., 2009; Beck and Dotzek, 2010; Karstens et al., 2013; Lombardo et al., 2015). Other methods of estimating the near-surface wind field using tree damage, but independent of the tornado vortex model, have also been developed. Godfrey and Peterson (2017) estimated the probability of trees blown down at different wind speeds based on the wind resistance model by Peltola and Kellomäki (1993) and determined the EF-scale of forest damage. Another vortex independent method developed by the Northern Tornado Project (NTP) and called the ‘forest box method’ uses a ‘population-based’ approach that assigns an EF scale using the percentage of snapped and/or uprooted trees along the tornado damage path (Sills et al., 2020).

Tree-fall analysis is exceptionally useful in estimating the near-surface wind speed of a tornado in heavily forested regions where the number of structures is very limited (Godfrey and

Peterson, 2017). The tree damage from tornadoes in these regions can range from thousands to millions (Bech et al., 2009; Beck and Dotzek, 2010; Blanchard, 2013; Fujita, 1989; Godfrey and Peterson, 2017; Hall and Brewer, 1959), often displaying the full extent of the tornado damage. Moreover, tree-fall analysis using an idealized vortex model can recreate the near-surface wind field with the time history of wind speed and direction (Lombardo et al., 2015) as opposed to structural damage where only the maximum wind speed can be estimated. Besides, using the idealized vortex model, the near-surface wind field can be determined by the damage pattern with or without the knowledge of the critical wind speed of tree-fall (Beck and Dotzek, 2010; Karstens et al., 2013; Lombardo et al., 2015). Despite the advantages, the tree-fall analysis also has some limitations. First, the presence of trees is critical, and too little damaged trees may not able to provide an estimation. The 20 May 2013 Moore, OK EF-5 rated tornado was a case where a consistent tree-fall pattern was lacking due to a relatively small sample of trees (Burgess et al., 2014). A full damage pattern or at least a transect showing the full extent of the tree damage is needed (Beck and Dotzek, 2010; Karstens et al., 2013; Lombardo et al., 2015). Secondly, the estimated wind field uses an analytical vortex model, which is an approximation derived from idealized conditions (Gillmeier et al., 2018; Rankine, 1882), whereas radar observations show that the wind field of tornadoes is much more complicated in reality (Doviak and Zrnić, 1993; Refan et al., 2017; Wurman, 2002; Wurman and Gill, 2000; Wurman et al., 2014). Moreover, tree-fall patterns are occasionally influenced by external factors, such as Rear Flank Downdraft (RFD) wind or underlying topography, which is not accounted for in the current tree-fall analysis methods (Karstens et al., 2013; Godfrey and Peterson, 2017). To enhance these limitations, the idealized vortex models and topographic effects are examined in Chapter 6.

A consistent modification and fine-tuning of tree-fall analysis over the past decades by other researchers has proven a large demand for tree-fall analysis due to various reasons discussed in Chapter 1. The author also recognized great potential in tree-fall analysis and a wide range of applications: tree-fall analysis is not limited to trees but is also applicable to other cantilever-like damage indicators (e.g., crops, signs). Recognizing the potential, the tree-fall analysis is further improved by determining the critical wind speed of other damage indicators (Chapter 5). In this chapter, the general process of tree-fall analysis using a vortex model is presented. A modification of the output comparison method and substituting averaged critical wind speed of tree with fragility functions are also presented. Moreover, generic tree-fall patterns and interaction plots, which can be used to estimate initial input parameters, are produced in this chapter. Although tree-fall analysis can be modified using the critical wind speed of other damage indicators as mentioned before, the critical wind speed (V_c) will be referred to the critical wind speed of trees in this chapter for the purpose of presenting the process of tree-fall analysis.

To summarize the entire process of tree-fall analysis with corresponding chapters, a schematic drawing of the tree-fall analysis process is shown in Figure. 4.1. The tornado damage pattern is first obtained through ground surveys and aerial photos (Chapter 2 and 3). The observed tree-fall pattern is compared to the generic tree-fall patterns produced and 'classified' in this chapter, in which the generic tree-fall patterns can be used to estimate initial input parameters. Based on the ground survey information gathered, the critical wind speed of the damage indicators is obtained (Chapter 5). An idealized vortex model is used to simulate a tornado and tree-fall pattern (Chapter 6). The observed pattern is then compared to the simulated patterns and the input parameters are iterated until the outputs of both observed and simulated patterns 'match'. Finally,

the near-surface wind field is reproduced with the "best-matched" parameters (Chapter 7). A detailed explanation of each step is discussed in the following subsections and other chapters.

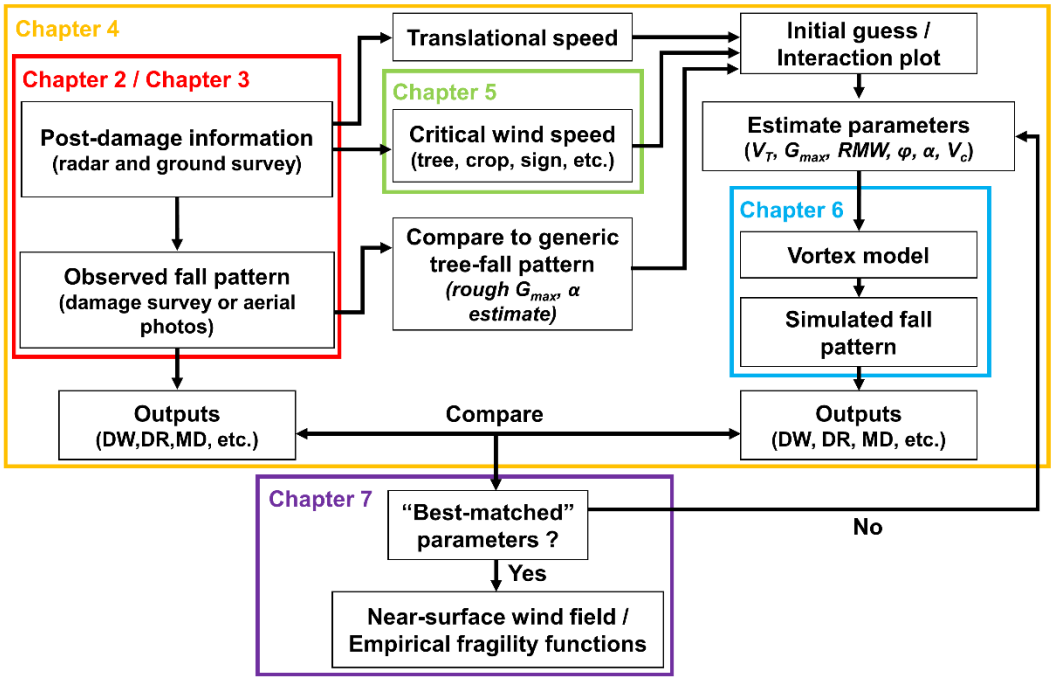

Figure 4.1. General process of tree-fall analysis.

4.2 Methodology

4.2.1 Rankine Vortex Model and Tree-fall Analysis Inputs

4.2.1.1 Rankine vortex wind profile

In the tree-fall analysis, an idealized vortex model is used to simulate the numerical tornado wind field and tree-fall patterns. Although there are several different idealized vortex models (discussed in detail in Chapter 6) and any idealized vortex models can be used, a Rankine vortex (RV) model (Rankine, 1882), which is a simple vortex model that is widely used to describe the wind distribution of tornadoes and hurricanes, is generally used in the tree-fall analysis (Bech et al., 2009; Beck and Dotzek, 2010; Karstens et al., 2013; Lombardo et al., 2015). The horizontal

wind speed distribution of an RV model has two regions: 1) a core region where the rotational wind velocity increases until the radius of maximum wind speed (*RMW*) and 2) an outer region with exponential decay of velocity beyond *RMW*, as shown in Figure. 4.2. In the equation, the rotational wind speed (V_{rot}) at different radii (r) is described as following:

$$V_{rot}(r) = V_{max}\left(\frac{r}{RMW}\right)^{\varphi} \quad \text{for } r \leq RMW$$

$$V_{rot}(r) = V_{max}\left(\frac{RMW}{r}\right)^{\varphi} \quad \text{for } r > RMW \tag{4.1}$$

where φ is the decay exponent and V_{max} is the maximum speed at *RMW*. Typically, φ = 1.0 has been used in Letzmann's work and other studies (Beck and Dotzek, 2010). However, recent studies suggest that the decay exponent ranges between 0.5 and 0.8 based on Doppler radar data of tornadoes (Bluestein, 2007; Kosiba and Wurman, 2010, Wurman and Alexander, 2005). Thus, typically, a range of 0.5 to 1.0 is used for the input value during the simulation. An example of a normalized RV model with different exponent values is shown in Figure. 4.2. Thus, the tree-fall analysis requires three parameters from the Rankine vortex model: V_{max}, *RMW*, and φ. Although the RV model is commonly used to approximate the tornado wind field, one should note that the model produces an idealized wind field. Near-surface tornadic wind fields are often asymmetric due to surface interaction and instability (Refan et al., 2017; Refan and Hangan, 2018). Thus, further improvement in the near-surface wind fields is accommodated in Chapter 6.

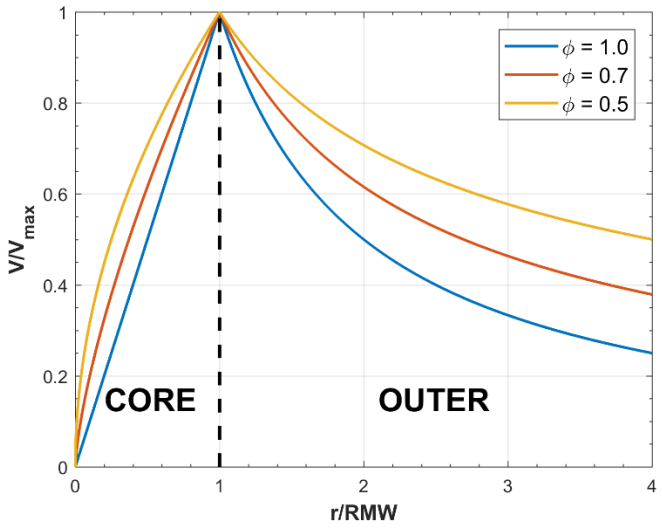

Figure 4.2. Rotational wind speed profiles at different exponent decay normalized by the maximum velocity and the radius of maximum wind speed.

4.2.1.2 Tornado wind field and wind components

Although mobile Doppler radar measurements suggest a stronger tangential component than the radial component even on the lowest elevations (Wurman and Alexander, 2005), it is noteworthy that the radial and vertical velocities measured by the Doppler radar observations are inadequately resolved near the surface (Karstens et al., 2013; Refan et al., 2017) and a significant radial component is often observed in tree-fall patterns (Karstens et al., 2013; Lombardo et al., 2015). Hence, the rotational wind speed (V_{rot}) of tornado near-surface is decomposed into two components: the radial component (V_r) and tangential component (V_θ), as shown in Figure 4.3. The magnitudes of V_r and V_θ are determined by alpha (α), which is the angle between V_{rot} and V_r, and are defined by following:

$$V_r = V_{rot}\cos(\alpha)$$
$$V_\theta = V_{rot}\sin(\alpha) \quad (4.2)$$

The V_{rot} can be described as purely radial and tangential at α = 0° and α = 90°, respectively. Although it is weak, an outflow is occasionally present in a tornado (Kosiba and Wurman, 2010; Refan et al., 2017) and represented by α greater than 90°. Thus, the amount of inflow in the tornado is determined by the α parameter. As the V_{rot} is derived from the Rankine vortex model, by definition (Eq. 4.2), the magnitude of both V_r and V_θ follows the wind profile of the RV model (Potvin et al., 2009). Figure 4.3 illustrates the wind direction of each grid point at different α parameters. The black circle represents the tornado center.

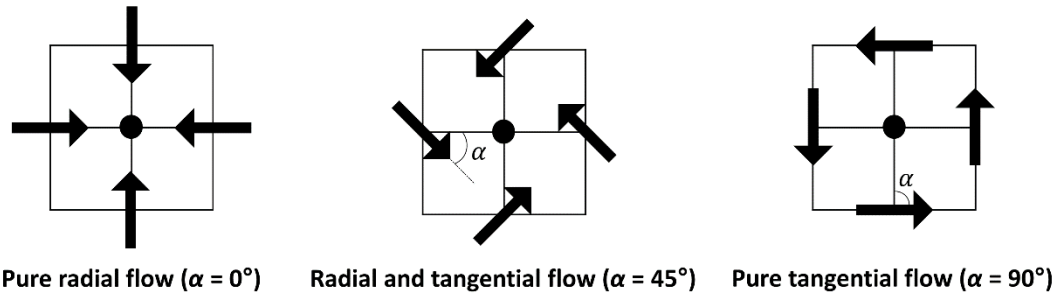

Figure 4.3. Wind direction at each grid point at different α values.

Adding the translation speed of the tornado (V_T) to the V_{rot} yields the resultant wind speed ($\hat{V}$) in the wind field at any radius. Figure 4.4 illustrates the wind components and the resultant wind speed at a specific radius. Typically, constant translational speed is assumed in the analysis for simplicity and the storm motion of the parent convective storm obtained from radar or ground observation is used as a proxy for the translational speed of the tornado (Beck and Dotzek, 2010; Lombardo et al., 2015). However, if available, one may use a time-varying translational speed. Karstens et al. (2013) estimated and used the translational speed of two tornadoes (Joplin, MO,

and Tuscaloosa-Birmingham, AL tornado) at different times based on the tornado vortex signature (TVS) positions.

The V_{max} and V_T of the tornado parameters can be combined into a new informative parameter: G_{max}, which is the ratio between V_{max} and V_T:

$$G_{max} = \frac{V_{max}}{V_T} \tag{4.3}$$

G_{max} value represents the magnitude of the rotational velocity in the tornado compared to the translational velocity, which has a great effect on the tree-fall pattern (section 4.3.1). The maximum resultant wind speed ($\hat{V}$) can be derived from G_{max} and V_T. For a point where $r = RMW$ and the V_T vector is aligned with the V_{max}, the magnitude of two vectors can be summed to determine $\hat{V}$:

$$\hat{V} = V_{max} + V_T = G_{max} \cdot V_T + V_T = V_T(G_{max} + 1) \tag{4.4}$$

The maximum wind speed of the simulated tornado can be quickly calculated with Eq. 4.4. An example simulated wind field of a translating tornado with one set of RV parameters (V_T = 13.4 m/s (30 mph), G_{max} = 4.5, RMW = 482 m (0.3 miles), α = 45°, φ = 0.55) is shown in Figure 4.4. Note that the translation direction of the tornado is left to right and that wind speed below 65 mph (below EF-0) is not colored. The point of maximum overall wind speed ($\hat{V}$) is also shown.

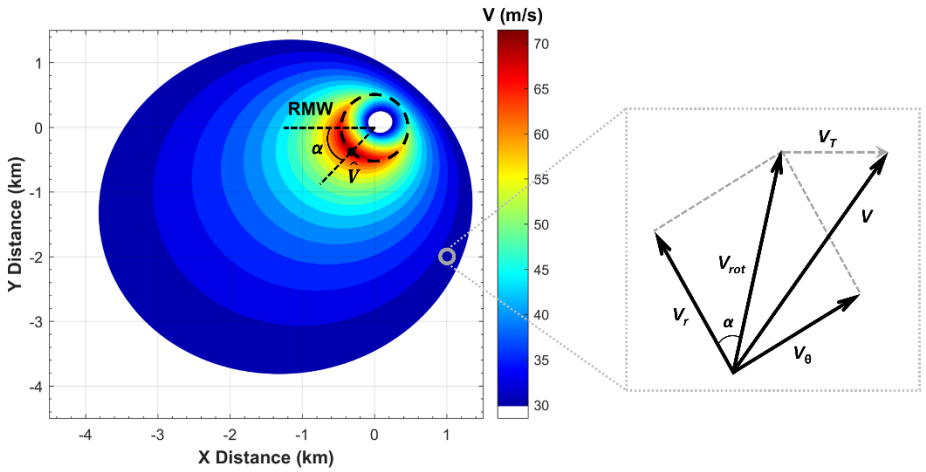

Figure 4.4. A translating tornado vortex on a grid (left); and wind components (V_r, V_θ, and V_T) and the resultant wind speed (V) at a specific point (right).

4.2.1.3 Critical wind speed of tree-fall parameter

Another parameter used in the tree-fall analysis is the critical wind speed of tree-fall (V_c), which is the wind speed at which the tree falls. Depending on the damage indicator (cantilever type: tree, crop, sign) used in the "tree-fall" analysis, the critical wind speed of the damage indicator shall be used. By introducing the critical wind speed value, a "hypothetical" tree-fall at each grid point can be generated. It is assumed that the tree falls in the direction of wind blowing at the instant when V (Figure 4.4) exceeds the V_c as the tornado vortex translates over the domain. The V_c can be determined using tree properties obtained in ground surveys as mentioned in the mechanistic tree risk model by Peltola and Kellomäki (1993) and Peltola et al. (1999). In addition to trees, the V_c of various crops has been modeled and tested in agricultural fields (Berry et al., 2003; Sterling et al., 2003; Baker et al., 2014), which can enable the application of tree-fall analysis in agricultural areas. The theoretical and experimental analysis of obtaining the V_c of trees, crops, and signs will be discussed in detail in Chapter 5. Typically, a single average value of V_c is used in the analysis, suggested by Beck and Dotzek (2010), due to the uncertainties and variability of

the tree characteristics; a sample of failed trees is collected and their average V_c is calculated (Chapter 5). However, in case the tree property information is unobtainable and the V_c value is unknown, the V_c can be treated as a random variable.

4.2.2 Model Outputs and Comparisons

4.2.2.1 Tree-fall pattern outputs

As shown in Figure 4.1, the simulated tree-fall pattern must be compared to the observed pattern in the tree-fall analysis. In order to make an accurate comparison, numerically defined outputs of the tree-fall pattern are necessary. Example outputs are damage width (*DW*), damage ratio (*DR*), and mean direction (*MD*); an illustration of these outputs is shown in Figure 4.5. Note that the tree-fall pattern of Figure 4.5 is produced by the translating tornado vortex in Figure 4.4 with V_c = 38 m/s (85 mph) with a grid spacing of 0.1 km and an average spacing of 0.3 km is used for the *MD*. The *DW* is the total width of the tree damage, and *DR* is the ratio of the *DW* on either side of the confluence line (*CL*) in a given transect:

$$DR = \frac{DW_2}{DW_1} \tag{4.5}$$

where DW_2 and DW_1 are the *DW* on the north and south side of the *CL*, respectively (Figure 4.5). The confluence line is defined as the estimated location where the tree-fall pattern converges to a line parallel to the tornado translating motion. However, the tree-fall pattern may not always converge, causing the *DR* to be indeterminate and thus may not be the most appropriate output to use in some cases. As the *DR* may be undefined in some cases, an additional output, *MD*, is

introduced. *MD* is the average tree-fall angle within certain spacing or bin, which can be used for tree-fall patterns without a confluence line.

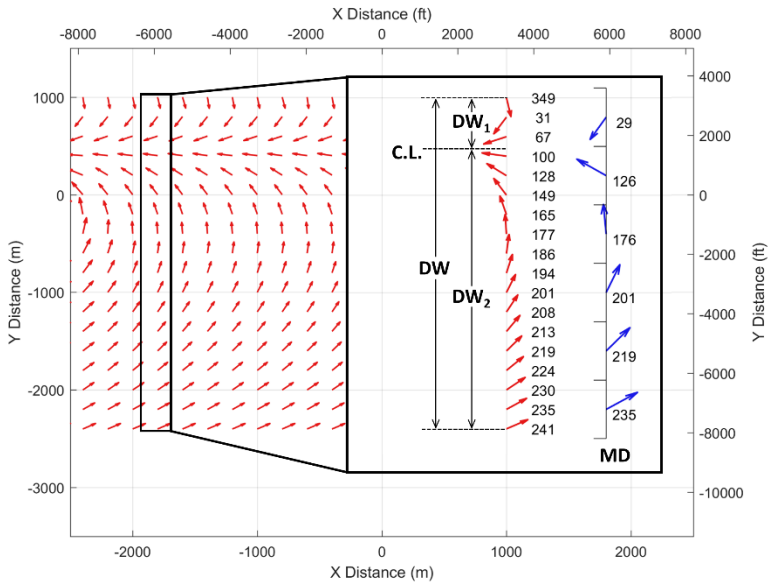

Figure 4.5. Tree-fall pattern produced by the translating tornado vortex in Figure 4.4 with V_c = 38 m/s (85 mph); Illustration of output *DW*, *DR*, and *MD*.

4.2.2.2 Comparison of outputs

The outputs of the observed pattern also need to be defined to compare with the simulated pattern. The outputs of the observed pattern are determined the same way the outputs of the simulated pattern are determined. In a transect, the *DW* is determined by the extent of the tree damage, and the *DR* is determined by the location of where the tree converges and Eq. 4.5. Note that the outputs of the observed tree-fall pattern must be defined in a transect perpendicular to the translational direction of the tornado so that the comparison between the simulation and observation is consistent. An example of the observation outputs (*DW*, *DR*, and *MD*), using the tree-fall pattern of the Joplin, MO tornado, is shown in Figure 4.6. To estimate the average angle of tree-fall, a minimum of three trees within each bin in the transects shall be used to generate an

average value at the central point of the bin for both the observed and simulated tree-fall. To satisfy the minimum requirement for the average fall direction, a bin size of 500×500 m was used for the example in Figure 4.6.

Once the outputs of the observed and simulated pattern are determined, the "best-matched" combination of parameters can be ascertained by comparing the outputs (*DW*, *DR*, and *MD*) of the two patterns. As opposed to scalar outputs (*DW*, *DR*), *MD* is a directional output and thus the cosine of the angle between the simulated and observed direction vector (i.e. unit vector) can be used for comparison. The cosine of the difference in angle is computed as shown in Eq. 4.6.

$$cos(\beta) = \frac{\overline{v_o} \cdot \overline{v_s}}{|\overline{v_o}| \cdot |\overline{v_s}|} = \overline{v_o} \cdot \overline{v_s} \tag{4.6}$$

Beta (β) denotes the angle between ($\overline{v}_o$) and ($\overline{v}_s$). Index *o* and *s* represent the observed and simulated, respectively. Since ($\overline{v}_o$) and ($\overline{v}_s$) are both unit vectors as they only represent the direction, the denominator in the fraction is one and the final product of cos(β) becomes a simple dot product of two vectors. The dot product is one if the vectors are parallel with each other and zero if they are perpendicular to each other.

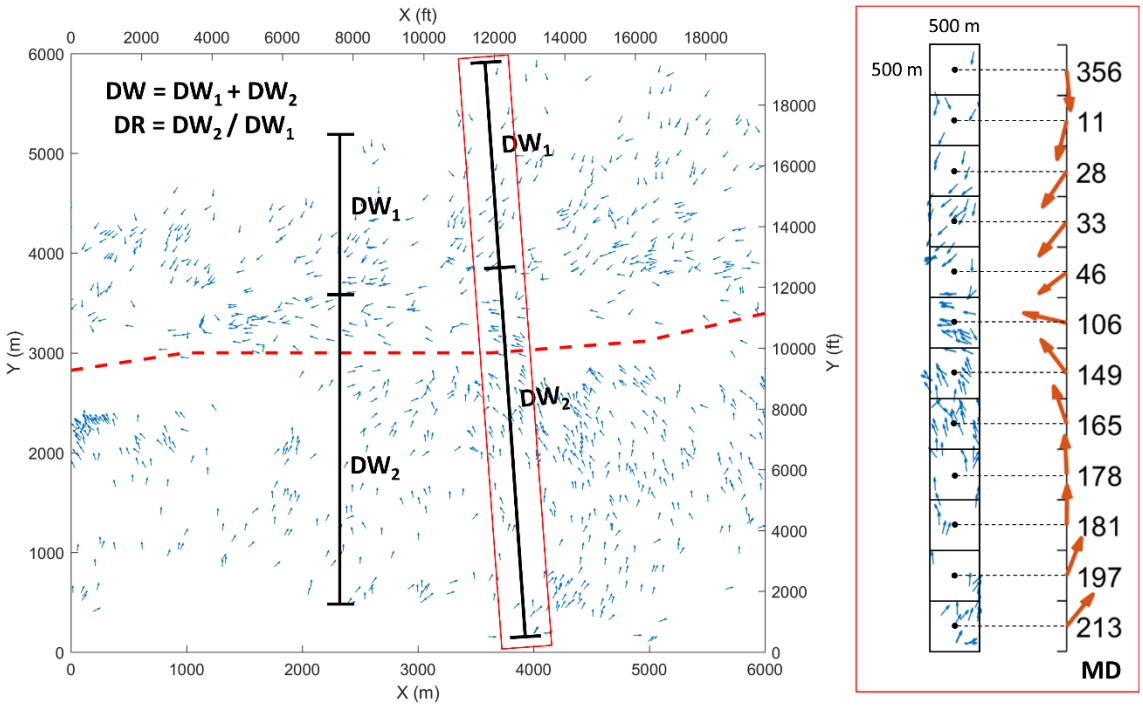

Figure 4.6. Illustration of the observation outputs using transects of tree-fall pattern of tree-fall Joplin, MO tornado.

In general, multiple transects perpendicular to the tornado track at different locations are selected. For the comparison, a root-mean-square error (E_{rms}) can be used to quantify the difference between the observed and the simulated pattern:

$$E_{rms} = \sqrt{\sum \left(\left(1 - \frac{DW_{i,s}}{DW_{i,o}}\right)^2 + \left(1 - \frac{DR_{i,s}}{DR_{i,o}}\right)^2 + \Sigma(\cos(\beta_{i,j}) - 1)^2 \right)} \qquad (4.7)$$

where i represents the index of the transect and j represents the index of each bin in the transect. The DW and DR are normalized by the observed outputs. Using the E_{rms} value, the "best-matched" parameters, input parameters that best describes the observed tornado, then can be determined.

In the initial process of parameter determination, an approximate range of the parameters is first estimated based on the overall tree-fall pattern (section 4.3.1) and interaction plots (section 4.3.2). The initial range of estimated parameters is then prescribed into the vortex model that generates different tree-fall patterns with different outputs. With Eq. 4.7, the error between the observed pattern and many different simulated patterns is calculated. This process is iterated until the parameter combination with the lowest E_{rms} value is determined. Finally, the wind field that "best" represents the actual tornado wind field can be generated using the "best-matched" parameters. Real-life applications of the tree-fall analysis are discussed later in Chapter 7.

There are other methods of comparing the observed and simulated patterns in other studies. Bech et al. (2009) and Beck and Dotzek (2010) compared the overall tree-fall pattern from the tornado to the simulated pattern. Although this method may be valid, one should take caution as different combinations of parameters can produce similar patterns. A more detailed comparison method was developed by Karstens et al. (2013), normalizing the averaged tree-fall directions by subtracting the estimated tornado translation direction. The mean cross-section of the normalized direction plots for observed and simulated was then compared.

4.3 Tree-fall Patterns and Outputs

4.3.1 Generic Tree-fall Patterns and Outputs

4.3.1.1 Tree-fall patterns using average V_c

Different combinations of the RV and V_c inputs can produce different tree-fall patterns with different outputs, in which different distinctive patterns are investigated and "classified" in this section. Examples of tree-fall pattern simulated with parameters of a generic tornado (V_T = 13.4 m, RMW = 322, φ = 0.5, V_c = 38 m/s) and an assumed V_c, and their outputs are illustrated in this

section. Figure 4.7 shows that the generic tree-fall pattern changes significantly with G_{max} and alpha (α). In case of a "high G_{max}" (generally 4.0-6.0), the rotational speed of the tornado is much greater than its translation speed and thus the trees are more likely to fall inward, towards the center of the vortex and the opposite direction of translation. Typically, these "backward-falling" tree-fall patterns (relatively high G_{max}) are found in the aftermath of tornadoes corresponding to EF 4 or greater). On the other hand, a "low G_{max}" (generally 1.0-3.0) suggests a relatively higher translational speed and/or weaker rotational wind speed. Thus, "forward-falling" trees are produced where the trees are more likely to fall in the direction of translation for the same V_c. These types of tree-fall patterns are commonly found in tornadoes corresponding to EF 3 or less. Examples of tree-fall patterns with two different G_{max} values are shown in Figure 4.7(a) and 4.7(b). As the G_{max} increases from 3.0 (Figure 4.7(a)) to 4.5 (Figure 4.7(b)) with a constant $\alpha = 0°$, an apparent change of tree-fall pattern and an increase in damage width (*DW*) are noticed. If the V_T is unchanged, Eq. 4.4 implies that an increase in G_{max} results in an increase V_{max}, therefore causing more trees to fall. On the other hand, the damage ratio (*DR*) is unaffected by the change in G_{max} (Figure. 4.7(a)-(b)). With the confluence line located along the center of the tornado for both G_{max} = 3.0 and G_{max} = 4.5, the *DR* becomes 1.0 for both cases, as the *DW* on the south and north side of the confluence line are the same. It is important to note that the general range of "low G_{max}" and "high G_{max}" and the tree-fall pattern that they produce may vary because the tree-fall patterns (backward or forward falling patterns) are highly dependent on V_T and V_c. For example, the tree-fall patterns may still show a "forward falling" pattern even with a "high G_{max}" if the V_T is small. However, a "typical" tree-fall pattern is produced using V_T and V_c estimated from Joplin, MO tornado as a reference (Karstens et al., 2013; Lombardo et al., 2015).

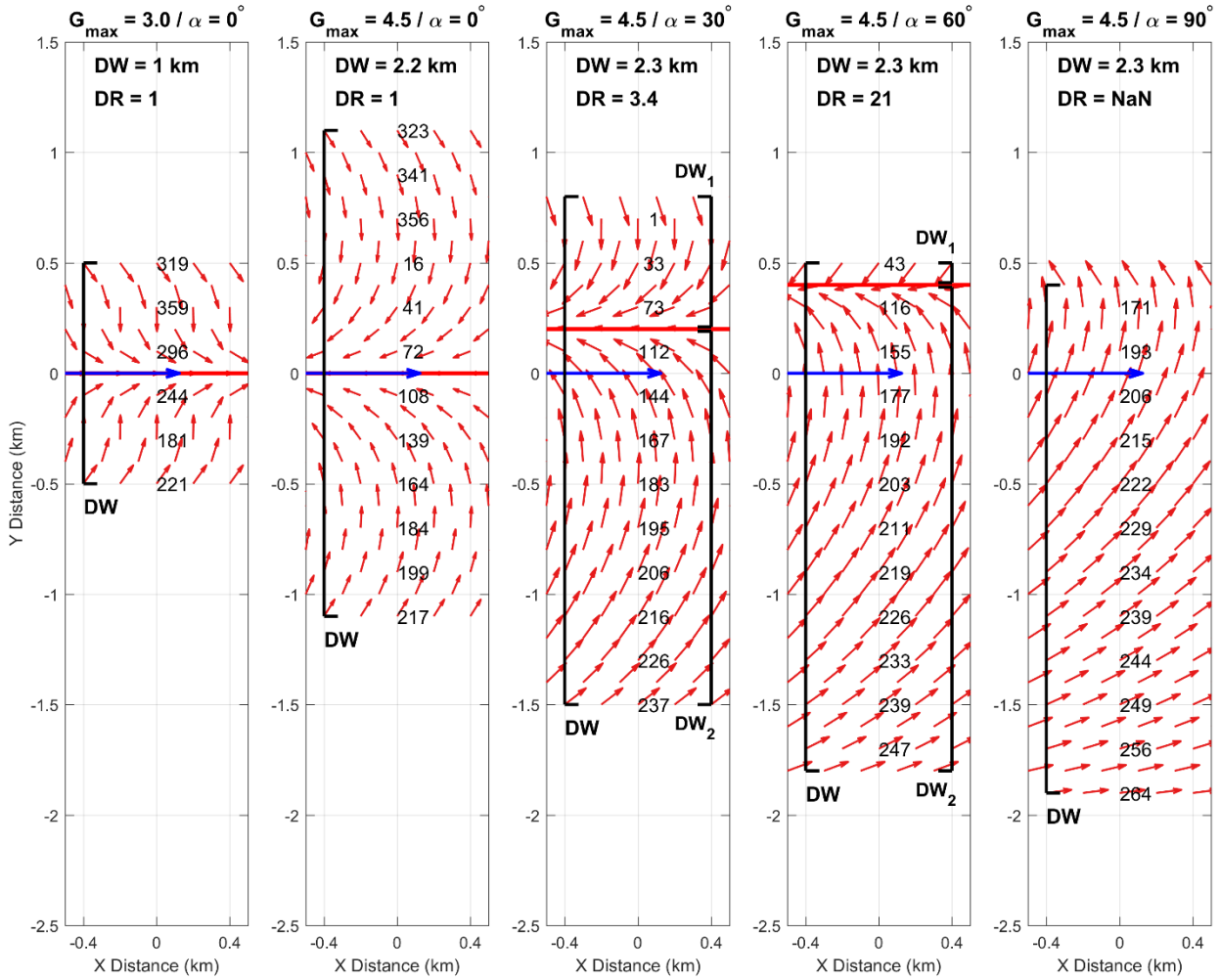

Figure 4.7. Examples of tree-fall patterns with different G_{max} (a-b) and α (b-e).

The alpha (α) parameter also contributes significantly to the tree-fall pattern. As α increases from 0° to 90°, the simulated vortex flow changes from a pure radial flow to a pure tangential flow. Unlike G_{max} parameter, α has a great effect on the *DR* due to the change in the vortex flow and little effect on the *DW*. It is evident that the *DR* increases significantly from 1.0 to 21 (Figure 4.7(b)-(d)) whereas the *DW* hardly changes. As α increases, the tangential flow increases and the confluence line starts to shift north of the tornado center, causing the *DR* to increase drastically. Eventually, the confluence line for α = 90° becomes undefined and the *DR* is no longer applicable

(Figure 4.7(e)). Note that the *DR* is highly sensitive to the grid spacing. Using a fine grid spacing (at least *DW* to grid spacing ratio of 5:1) is suggested as a more accurate *DR* will result though a prolonged computational time is expected. A grid spacing of 0.1 km was used for Figure 4.7. Note that the tornado vortex is moving from left to right (blue arrow) and the parameters not shown in the title are kept constant. The confluence line is indicated in red line and the fall directions are labeled at $x = 0$ where 0 is due the true south and increases clockwise. A more detailed analysis of outputs tendency is discussed in section 4.3.2. Chen and Lombardo (2019) also provides an analytical solution of tree-fall patterns and great examples demonstrating how tree-fall patterns change with input parameters.

In Fujita (1993), various corn damage patterns: “comma-shaped”, “swirling”, “Eye-shaped” patterns, are introduced to illustrate the characteristics of tornadoes and downbursts using crop damage. It is perceived that some of these crop patterns that Fujita emphasizes in his study resemble the tree-fall pattern, which can also be produced numerically and used to describe the characteristics of tornadoes. Figure 4.8 shows examples of tree-fall patterns generated at the beginning of the tornado simulation. Represented by a black arrow, Figure 4.8(a) resembles the “comma-shaped”, and Figure 4.8(b) resembles the “swirling” pattern of crop damage in Fujita 1993. Alpha (α) = 45º and $\alpha = 90°$ were used for the “comma-shaped” pattern and the “swirling” pattern, respectively. All the other parameters used for the simulation are the same as in Figure 4.4 and Figure 4.7. These patterns may also be used to estimate tornadoes in the early stage and may have some application in tornadogenesis although further detailed investigation is necessary.

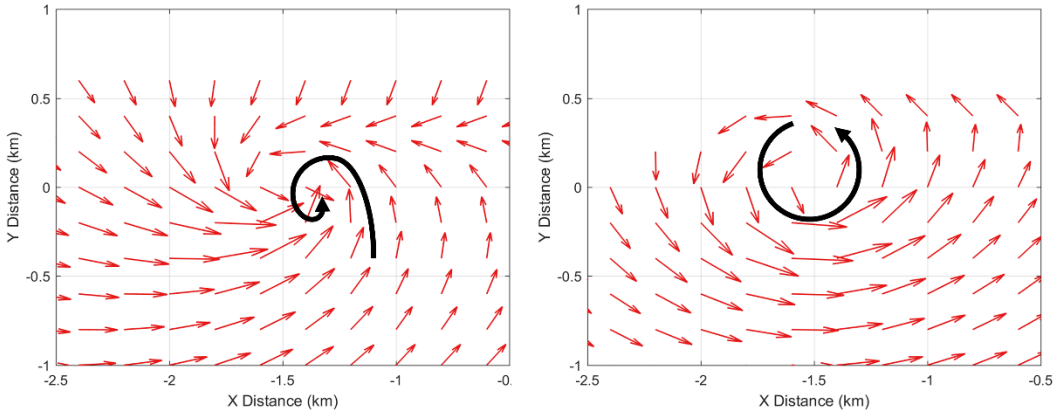

(a) "comma-shape" / α = 45° (b) "swirling" / α = 90°

Figure 4.8. Examples of the simulated fall pattern in the beginning of the tornado that resembles (a) "comma-shape" and (b) "swirling" pattern.

4.3.1.2 Tree-fall patterns using fragility function

Empirical or analytical tree fragility curves can be also used in a replacement of a single V_c value, in which tree fragility function is a probability function of tree failure at a given wind speed. The fragility function can quantify the vulnerability of trees and may also be used in tree-fall analysis to produce a more realistic tree-fall pattern. It can be useful in a situation where the damaged tree information is unavailable and thus the critical wind speed of tree-fall is unobtainable. Figure 4.9 shows an empirical tree fragility curve developed using empirical data: wind field estimated from the tree-fall patterns (Lombardo et al. 2015) and the tree damage (both failed/non-failed) of 22 May 2011 Joplin, MO tornado.

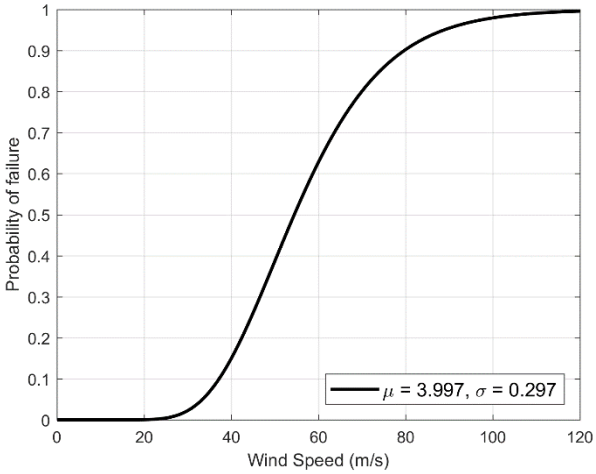

Figure 4.9. Empirical tree fragility curve of the Joplin, MO tornado and the parameters of lognormal cumulative distribution function.

To simulate a tree-fall pattern using an empirical tree fragility, the probability of failure is assigned based on the maximum wind speed the grid point experiences and the fragility function, and the tree-fall (fail/not fail) in each grid point is decided using a binomial distribution and the probability of failure. For example, if the maximum velocity at a grid point is 80 m/s, the probability of failure of the "hypothetical" tree at the grid point is 90 percent. A further detailed process of building empirical tree fragility curves is presented in Chapter 7. Figure 4.10 shows the comparison between the tree-fall pattern using the single V_c and using the tree-fragility. A tornado is simulated with the following parameters: V_T = 13.4 (30 mph), G_{max} = 4.5, *RMW* = 322 m (0.2 miles), α = 20°, V_c = 38 m/s (80 mph), φ = 0.5. Figure 4.10(a) and 4.10(b) exhibit the generic tree-fall pattern and tree-fall pattern using the Joplin, MO tornado tree fragility, respectively. The damage width and pattern are consistent over the X distance for Figure 4.10(a) whereas the damage width and tree-fall pattern somewhat vary for Figure 4.10(b). Although there are some scattered tree-falls around the central tree-fall patterns in Figure 4.10(b), both patterns show roughly similar *DW* and converge near Y = 0.2 km. Although the tree-fall pattern simulated with the Joplin fragility

curve may display a more realistic tree-fall pattern and demonstrate great potentials, more fragility curves are necessary to make a generalization and to be incorporated in the tree-fall analysis.

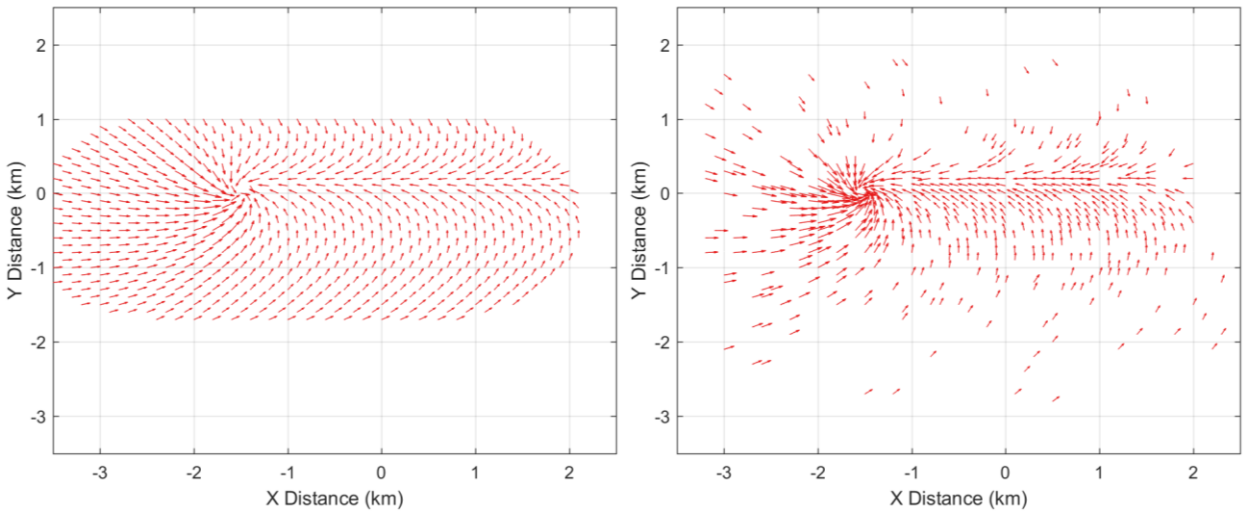

(a) generic tree-fall pattern (b) tree-fall pattern using fragility function

Figure 4.10. Tree-fall patterns of (a) generic tree-fall pattern and (b) Joplin, MO tree fragility.

4.3.2 Interaction between Parameters

Different combinations of input parameters interact with each other differently and therefore produce different outputs. The interaction effect between parameters is important in the iteration process; how the outputs change with parameters must be determined to reduce the error and eventually reach the "best-match" parameters. The relationships between different parameters and their interaction effects are shown in Figure. 4.11. The plots exhibit regression lines of the percentage change of the outputs (*DW, DR*) over the percentage change of different inputs. In Figure. 4.11(a), it is evident that the *DW* increases as G_{max} and V_T increase, but decreases as φ and V_c increase. As a result, a rapid increase in slope is noticed as G_{max} increases and V_c decreases. Intuitively, a lower V_c would result in an increase in *DW* since more trees would fall due to lower critical tree-fall wind speed. Figure 4.2 illustrates a slower wind speed decay for lower φ, resulting

in a wider *DW*. A higher G_{max} and V_T contributes to a higher maximum resultant wind speed ($\hat{V}$) (refer to Eq. 4.3), thus a simultaneous increase in both G_{max} and V_T increases the *DW* significantly. Although the *DW* interaction is rather intuitive, the *DR* interaction is much more complicated and less intuitive because the *DR* is very sensitive to the confluence line (*CL*), which may not always exist. Furthermore, the position of the *CL* is dependent on the tree-fall pattern and the size of the *DW* on the south and north side (referred to as DW_1 and DW_2 in Figure. 4.7), which are also dependent on the total *DW*. The interaction plots of the *DR* with different G_{max}, α, and V_c are shown in Figure 4.11(a). One apparent notice is that the *DR* increases significantly as α increases (as also shown in Figure 4.7). For a low α (top row of Figure 4.11(b), the slopes are rather flat, indicating that G_{max}, *RMW*, and V_c do not contribute significantly, but the interaction effects take place and the other parameters begin to contribute to the change in *DR* more as α increases. The *DR* shows great sensitivity to the change in *RMW* for a high G_{max} and α and a low V_c (blue line in bottom right figure of Figure. 4.11(b) displaying almost a 120 % increase (large negative slope), but shows very little sensitivity for other combinations. The direction of the relationship between the *DR* and *RMW* also changes from positive to negative as the G_{max} increases from decrease of -33.3 % increase of 33.3 % for α = 50 % increase and V_c = 0 % increase (red line in bottom row of Figure 4.11(b), and changes from negative to positive as the G_{max} increases from decrease of -33.3 % increase of 33.3 % for α = 50 % increase and V_c = 17 % increase (yellow line in bottom row of Figure 4.11(b). This demonstrates the complexity and the interaction of parameters. Thus, the interaction plots are beneficial for the initial estimate or adjustment of parameters, but shall not be used to estimate the exact outputs of the tree-fall patterns. The outputs of the tree-fall shall be calculated from the actual pattern. Note that these trends are valid only within the range of the parameter change and thus estimation outside of the parameter range should not be extrapolated.

Also, note that the reference parameters to percentage change are: (1) V_T = 13.4 m/s (30 mph), G_{max} = 4.5, φ = 0.8, V_c = 26.8 m/s (60 mph) (Figure 4.11(a)); and (2) G_{max} = 4.5, V_c = 26.8 m/s (60 mph), α = 30°, *RMW* = 563 m (0.35 miles) (Figure 4.11(b)). The following parameters are fixed for each plot: (1) α = 15°, *RMW* = 482 m (0.3 miles) (Figure 4.11(a)); and (2) φ = 0.8, V_T = 13.4 m/s (30 mph) (Figure 4.11(b)).The trend and exact values are also subject to change for different reference parameters, but the general trend should be similar. These interaction plots can be useful for general interpretation of the RV and other parameters.

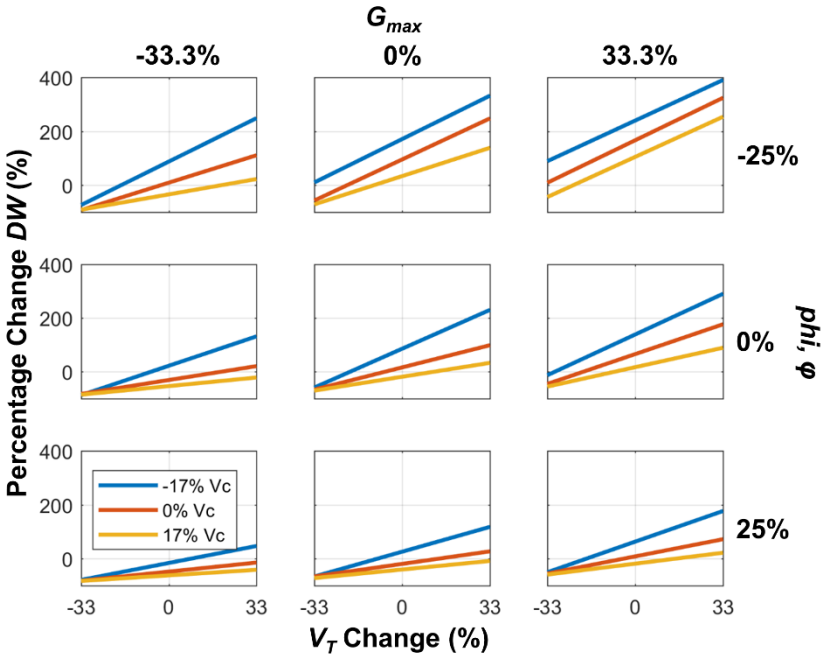

(a) percentage chagne in *DW*

Figure 4.11. Interaction plots of (a) *DW* and (b) *DR*.

Figure 4.11. (continued)

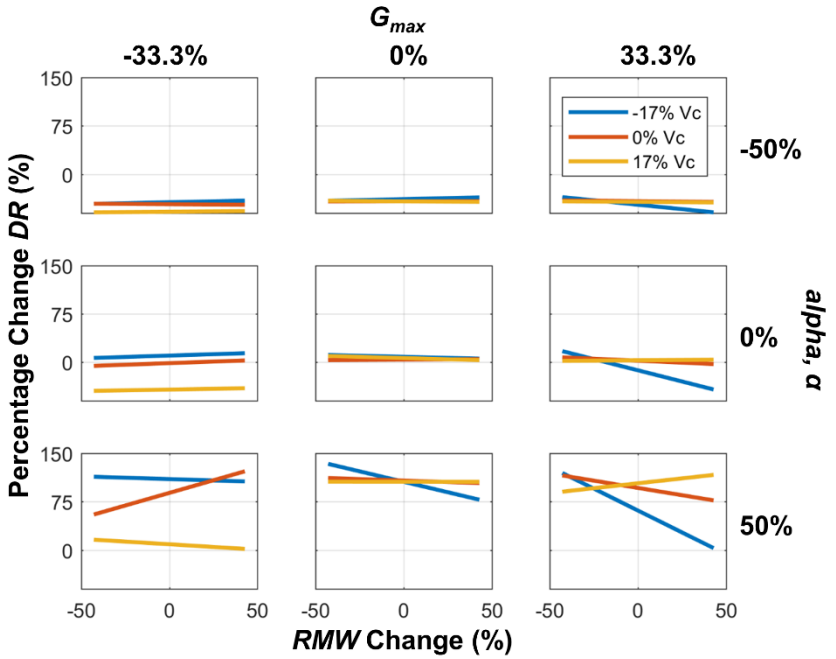

(b) percentage chagne in *DR*

4.4 Summary

This chapter introduces the tree-fall analysis, which utilizes the patterns of fallen trees during a tornado event and characterizes the patterns. The method simulates a translating Rankine vortex (RV) with its associated parameters and generates a tree-fall pattern with a critical wind speed of tree-fall (V_c) value. Many different tree-fall patterns can be generated using different combinations of input parameters. The important parameters typically used in the tree-fall analysis are summarized in Table 4.1. The simulated patterns are then used to match the observed tree-fall pattern of an actual tornado. The patterns are numerically defined (outputs), and the outputs of the simulated pattern are compared to the observed pattern. The process is iterated until the RMS error reaches the minimum value and the "best-matched" parameters can be determined. Using the

estimated parameters, the near-surface wind field map of the tornado can be reconstructed and used as an independent method of wind speed estimation from structural damage.

Table 4.1. Summary of general input parameters used in the tree-fall analysis.

Parameter	**Description**	**Key points**
V_T	Tornado translational speed	Obtain typically from storm vector of the parent storm; strong positive correlation with *DW*
G_{max}	Ratio between V_{max} and V_T	Positive correlation with EF rating in general; significant effect on tree-fall pattern and strong positive correlation with *DW*
RMW	Radius of maximum wind speed	Determine location of strongest wind; positive correlation with *DW*
φ	Wind profile decay exponent	Ranges between 0.5 to 1.0 based on radar observation; positive correlation with *DW*
α	Angle between V_{rot} and V_r	Determine the amount of inflow in the tornado; significant effect on tree-fall pattern and strong positive correlation with *DR*
V_c	Critical wind speed of tree-fall	Can be replaced with critical wind speed of other damage indicators (crop, sign); negative correlation with *DW*

CHAPTER 5: TREE/CROP/SIGN MODULE

5.1 Introduction

Tree damage is also included in the EF Scale as damage indicators 27 and 28 for softwood and hardwood trees. However, the EF scale guidance on wind speed estimation based on trees, both TH and TS, has several flaws. According to Peterson (2003), the ratio of uprooted trees to snapped trees increases with an increase in wind speed, but the EF scale guidance shows the opposite (Edwards et al., 2013). The EF scale also fails to take the tree property, such as the trunk diameter and species, into account (Edwards et al., 2013), which certainly has an effect on the critical wind speed that the tree fails (Peterson, 2003). Even though the EF Scale for trees (DI 27, 28) exists and may allow estimating the wind speed of the tornado to some extent, single tree damage cannot provide wind speeds of an intense tornado (EF 4 or 5 tornado) due to the limitation of tree resistance because the maximum wind speed of the EF-scale of trees is 74.6 m/s (167 mph). Thus, a more detailed analysis of estimating the critical wind speed of tree-fall is necessary.

In this chapter, not only the critical wind speeds (V_c) of tree-fall but also crop-fall and sign-fall are investigated using a load-resistance framework, which is shown in Figure 5.1. The wind loading is calculated based on the wind speed, the projected area, and the aerodynamic and dynamic properties. The resistance, which is highly dependent on the size, the material properties, and the geometry, is obtained either analytically or experimentally. If the loading is greater than the resistance, a failure occurs. In fact, this framework presented is applicable to any cantilever-like damage indicators and used to estimate the bounds of a near-surface tornadic wind speed, potentially very useful in forensic engineering. In addition, tree-fall analysis using a single average

V_c can also be an independent V_c estimation method, which will be discussed in more detail in Chapter 7.

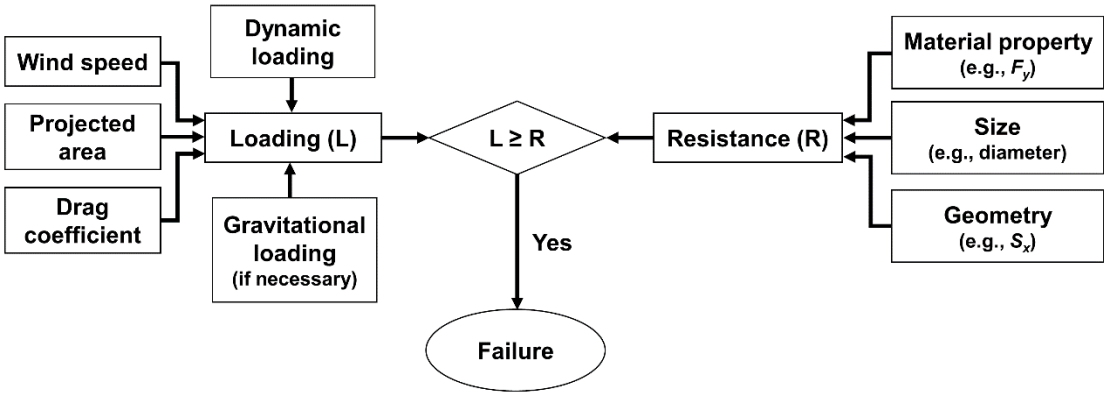

Figure 5.1. General framework of load-resistance model of a cantilever-like damage indicator.

5.2 Critical Wind Speed of Tree-fall

5.2.1 Introduction on Critical Wind Speed of Tree-fall

Although the intensity of the majority of the tornadoes is estimated based on structural damage, tree damage is used in some cases (Peterson, 2003). In forested areas where no buildings are present, often tree damage is the only damage indicator and becomes exceptionally important. However, the current EF Scale method on estimating the wind speed based on tree damage (DI-27, 28) has many shortcomings: it does not account for the tree properties, such as the diameter, height, and species of the tree. Nonetheless, many studies have shown that the properties of trees highly affect the stability and damage of trees (Peterson, 2003; Peterson, 2007; Cannon et al., 2015; Cucchi et al., 2004). Moreover, the current EF scale can only estimate wind speed up to 75 m/s (167 mph) as mentioned in Chapter 2. Edwards et al. (2013) suggest that the variations in the

tree should be accounted for in the EF scale and a better understanding of tree failure in wind is necessary.

As mentioned in Chapter 4, the V_c of tree-fall is an essential parameter in tree-fall analysis. Tree-fall analysis, which uses aggregate information on tree damage, can overcome the EF scale limitation and estimate wind speeds of tornadoes associated with the EF 4 and 5 range. With the tree information collected in damage surveys or from aerial photos, a more accurate V_c of tree-fall can be estimated and used to improve near-surface estimates of tornado wind speed.

5.2.2 Literature Review

5.2.2.1 HWIND model

An analytical solution of V_c of tree-fall is based on the mechanistic tree stability model by Peltola and Kellomäki (1993) and Peltola et al. (1999). Many studies have used the Peltola model, known as commonly known as the HWIND model, as the base for determining the V_c of tree-fall (Beck and Dotzek, 2010; Godfrey and Peterson, 2017; Holland et al., 2006). The two major forces in the HWIND model are the wind and gravity force (Figure 5.2), which causes the overturning moment. The mean horizontal wind profile ($\bar{U}$) is determined by the Logarithmic Law boundary layer, which is expressed as follows:

$$\bar{U}(z) = \frac{u_*}{k} \log\left(\frac{z - z_h}{z_o}\right) \tag{5.1}$$

where z is the height, u_* is the friction velocity, k is the von Karman's constant, which is around 0.4, z_h is the zero-plane displacement, and z_o is the roughness length. Alternatively, a simpler mean wind speed profile, the Power Law, can also be used. The Power Law is written as:

$$\overline{U}(z) = \overline{U}_{10}\left(\frac{z}{10}\right)^{\alpha} \tag{5.2}$$

where $\overline{U}_{10}$ is the mean wind speed at 10-m height, and α is the power-law exponent. Note that the power-law exponent, α, is different from the α in Chapter 4. Figure 5.3 shows the vertical profile of the horizontal wind using the Logarithmic Law with z_o = 0.5 m, used for very rough terrain (e.g., mature regular forest), and the Power Law with α = 0.25 for Exposure B (ASCE, 2016). Both profiles match very well; the Power Law is commonly used for engineering purposes (Holmes, 2015). Note that the horizontal wind velocity from both the Logarithmic Law and the Power Law is a mean wind speed ($\overline{U}$). However, trees normally fail at an extreme value (gust wind) and thus the mean wind speed needs to be adjusted for the extreme wind loading (Peltola et al., 1999). The Power Law mean wind speed profile can be adjusted using a 3-s gust-speed power-law exponent: $\hat{\alpha}$ = 1/7 for Exposure B (ASCE, 2016). The gust wind speed profile shows a "flatter" profile than the other profiles as shown in Figure 5.3. Since the vertical profile of the horizontal wind of a tornado still remains elusive and very little is known especially near the ground, the gust wind speed ($\widehat{U}$) profile is assumed for a tornado. Using the gust wind speed profile, the wind-induced force (F_1) at different height then can be calculated:

$$F_1(z) = \frac{1}{2} \cdot C_d \cdot \rho \cdot A(z) \cdot \widehat{U}(z)^2 \tag{5.3}$$

where C_d is the drag coefficient, ρ is the air density, and A is the projected frontal area of the tree. In addition to the wind-induced force, a force due to gravity acts on the tree (Figure 5.2). The gravitational force (F_2) is obtained simply by the green mass and gravitational constant:

$$F_2(z) = M(z) \cdot \mathrm{g} \tag{5.4}$$

where *M* is the green mass of the stem and crown and *g* is the gravitational constant. The HWIND model divides the tree into a 1-m segment and obtains the 1-m increment forces.

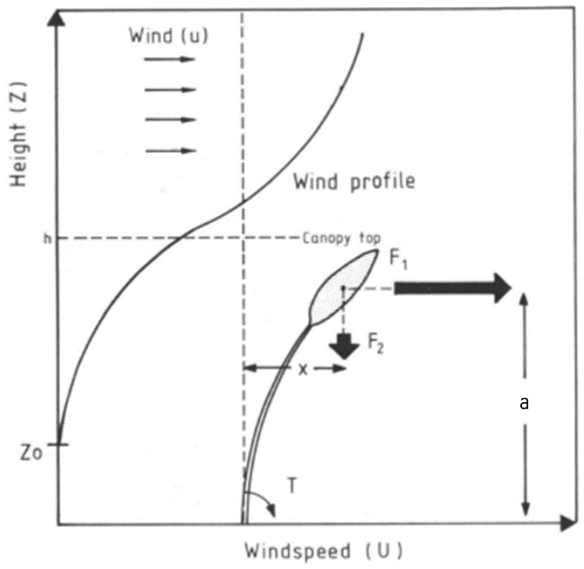

Figure 5.2. Illustration of the forces (wind, gravity) exerted on a tree that causes overturning moment (Peltola and Kellomäki, 1993).

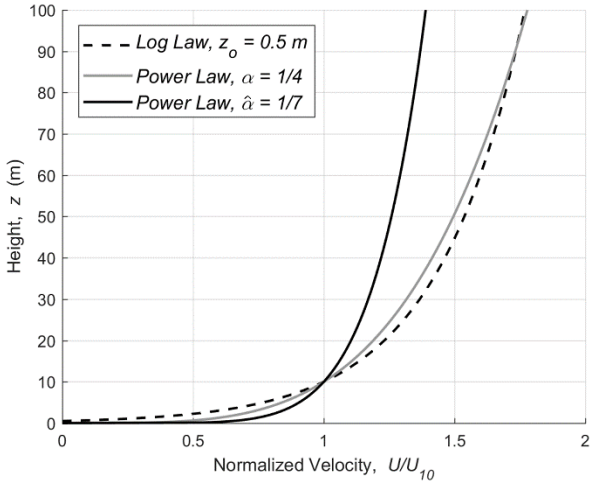

Figure 5.3. Comparison of the mean wind speed profile using Logarithmic Law for very rough terrain and Power Law for Exposure B.

The total overturning moment at the base of the stem is then obtained by summing the moments caused by the 1-m segment gravitational force and the horizontal deflection (x), and 1-m segment wind-induced force and the height of the tree. Thus, the total overturning moment equation can be written as:

$$T(z) = F_1(z) \cdot z + F_2(z) \cdot x \tag{5.5}$$

$$T_{total} = (F_1(z) \cdot z + F_2(z) \cdot x) \tag{5.6}$$

where the $T(z)$ is the 1-m segment overturning moment, and T_{total} is the total overturning moment exerted on the base of the tree. Pennala (1980) assumes the bending of the stem is directly proportional and inversely proportional to the wind force and the stem's stiffness, respectively, and expresses the horizontal deflection as:

$$x(z) = \frac{F_1 \cdot a^2 \cdot h \cdot \left(3 - \frac{a}{h} - \frac{3l(z)}{h}\right)}{6EI} \qquad for\ z \geq a$$

$$x(z) = \frac{F_1 \cdot a^3 \cdot \left(2 - \frac{3(l(z) - b)}{a} + \frac{(l(z) - b)^3}{a^3}\right)}{6EI} \qquad for\ z < a \tag{5.7}$$

where x is the horizontal deflection from wind at each height (z), a is the distance from ground level to the crown center, h is the height of the tree, $l(z)$ is the distance from the tree top, E is the elastic modulus, I is the area moment of inertia of the stem, and b is the distance between the crown center and the top of the tree.

Typically, tree failures are categorized into two: 1) uprooting and 2) stem breakage. Uprooting is highly dependent on the weight and strength of the soil. The supporting moment of the total root-soil plate anchorage (RS_{sup}) is defined as:

$$RS_{sup} = \frac{\mathrm{g} \cdot Mass \cdot RS_{mean}}{A_{rsw}} \tag{5.8}$$

where *Mass* is the fresh mass of the root-soil plate, RS_{mean} is the mean depth of the root-soil plate volume, and A_{rsw} is the proportion (%) of the root-soil weight of the total belowground anchorage by Coutts (1986). If the total overturning moment (*T*) exerted on the tree exceeds the RS_{sup}, an uprooted tree failure would occur. The stem breakage failure is highly correlated to the diameter at breast height (DBH) of the tree. In other words, the larger trees would have larger resistance to stem breakage. The maximum overturning moment that a tree can stand without the stem breaking ($STEM_{res}$) is expressed as:

$$STEM_{res} = \frac{\pi}{32} MOR \cdot DBH^3 \tag{5.9}$$

where MOR is the modulus of rupture. A tree is assumed to break at the stem if the total overturning moment (*T*) exceeds the $STEM_{res}$.

From Eq. 5.3 and 5.4, the exerting overturning moment is expected to increase as the tree size increases due to an increase in projected frontal area (*A*) and mass (*M*). However, the RS_{sup} is more depended on the root-soil weight (Eq. 5.8) as opposed to the size of the tree. Though, the weight of the root-soil would increase as the DBH increases because larger trees would have larger and deeper root systems. On the other hand, the $STEM_{res}$ increases exponentially (Eq. 5.9) as the

tree size increases. Naturally, it can be speculated that an uprooting failure is more likely to occur than stem breakage for larger trees, which is often observed in the field.

5.2.2.2 Winch tests

Oftentimes, it is difficult to obtain accurate resistance parameters (e.g., *Mass*, A_{rsw}, *MOR*) during a damage survey. The critical overturning moment (M_{crit}) of trees can be used instead within the windthrow risk models (Nicoll et al., 2006), in which the resistance overturning moment of trees is obtained by performing a winch test. Winch test measures the force to take down trees with a load cell and calculates the M_{crit} of the trees. Many studies often conduct winch tests to simulate the action of wind and investigate the effects of tree properties (e.g., species, size) on the M_{crit} of trees (Nicoll et al., 2006; Cannon et al., 2015; Cucchi et al., 2004; Moore, 2000; Peltola et al., 2000; Peterson and Claassen, 2013; Ruel, 2000). Peltola et al. (2000) measured the M_{crit} of trees to obtain the *MOR*. Cucchi et al. (2004) performed a winch test on Maritime pines (softwood) to determine if the overturning moment differs within a stand (trees inside the stand and edge trees near the border exposed to prevailing winds) and for different soil condition (wet soil and dry soil). The result suggested that the M_{crit} of the trees on the edge of the stand (edge trees) is stronger than that of the trees within the stand (inner trees) possibly due to the larger root system developed for edge trees. The M_{crit} of trees on dry soil was greater than that of trees on wet soil, with a ratio of snapped to uprooted trees of 1:1.3 and 1:7.3 for the trees on dry soil and wet soil, respectively. Moreover, Peterson and Claassen (2013) performed a winch test on western cottonwoods and valley oaks (hardwood) and suggested that the M_{crit} is not significantly influenced by the moisture, density, or texture of the soil. Cannon et al. (2015) performed a winch test on loblolly pines, or *Pinus*, (softwood), tulip poplars, or *Liriodendron*, (hardwood), and other hardwood trees. They

discovered that the M_{crit} was significantly influenced by tree size and failure mode (uproot, stem breakage), but the M_{crit} did not differ between species. Figure 5.4 shows the pooled regression of the M_{crit} vs. stem mass of all species. Though, studies of tree damage surveys after catastrophic wind events have shown greater damage to coniferous (softwood) than deciduous (hardwood) trees (Foster, 1988; Peterson, 2007). Cannon et al. (2015) suggested that wind force acts differently on different species, and the differences in the projected frontal area and drag coefficient (discussed in section 5.2.2.3) that influence the wind-induced force are the factors that cause the difference in damage.

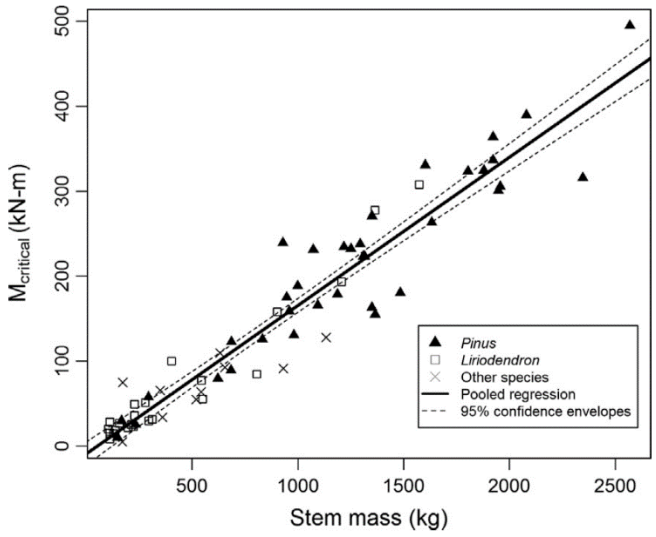

Figure 5.4. Regression line and confidence bounds of critical turning moment (N-m) vs. stem mass (kg) for all species pooled (Cannon et al., 2015).

In this study, the regression analyses from Cucchi et al. (2004) and Cannon et al. (2015) are used to obtain the M_{crit} of trees instead of the analytical M_{crit} from the HWIND model due to the following reasons: 1) difficulty of obtaining tree and soil properties in the damage site needed for calculating the M_{crit}, 2) simplicity, 3) generalization of the M_{crit} among tree species. Although

Cannon et al. (2015) and Peterson and Claassen (2013) suggest that the stem mass predicts the M_{crit} better than other regressors, such as DBH^3, $DBH^2 \times h$, and tree mass, it is often very difficult to measure the stem mass in the field without cutting and weighing the tree. The linear regression of the M_{crit} vs. $DBH^2 \times h$ (Figure 5.5) is used to calculate the V_c of tree-fall because it was not feasible to measure the stem mass during the damage survey. The regression line for edge trees on wet soil, which mostly uprooted, from Cucchi et al. (2004) and the uprooting regression line from Cannon et al. (2015) produced a comparable result, supporting the statement from Cannon et al. (2015) that the M_{crit} is less influenced by species. The difference between the two lines is that the regression line from Cannon et al. (2015) passes the origin assuming that a tree with a zero DBH would have a zero M_{crit}, whereas the regression line from Cucchi et al. (2004) does not.

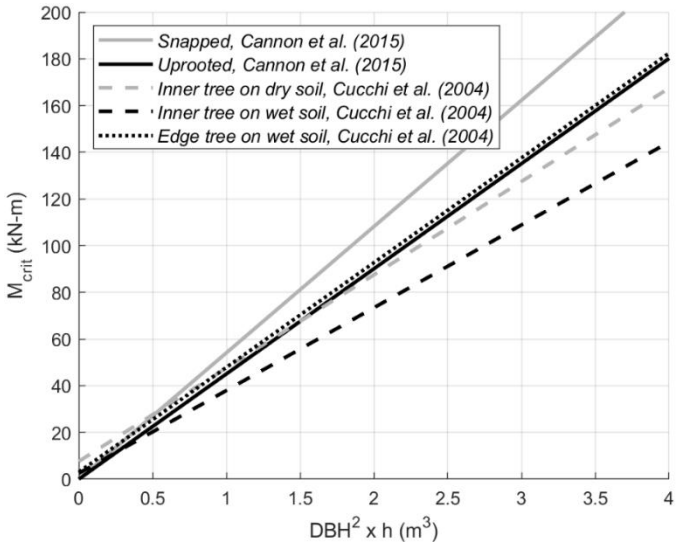

Figure 5.5. Linear regressions of M_{crit} vs. $DBH^2 \times h$ of trees on various conditions.

5.2.2.3 Drag coefficient

Drag coefficient is one of the essential parameters in finding the V_c of tree-fall (discussed in more detail in section 5.2.3). It is a non-dimensional number that quantifies the drag of an object

and is highly dependent on the geometry of the object (Holmes, 2015). While other parameters such as DBH, height, and projected frontal area, can be collected or measured during the survey both from ground and aerial, the drag coefficient is obtained from testing by measuring the force acting on the tree. The drag coefficient is defined as the following equation:

$$C_d = \frac{2D}{\rho U^2 A} \tag{5.10}$$

where D is the drag force measured. It is noteworthy that the drag coefficient equation (Eq. 5.10) can be used to estimate, not only for trees but also the C_d of any object. In a wind tunnel, the horizontal drag force can be directly measured with a force balance, and the projected frontal area is determined photographically (Mayhead, 1973). In Mayhead (1973), a variety of commercial coniferous trees were tested and found a difference in the drag coefficient among species possibly due to the flexibility (or stiffness) of the tree, amount of foliage, and the variations in the morphology. Rudnicki et al. (2004) tested three morphologically different coniferous trees and investigated the drag coefficient and the amount of frontal area reduction with increasing wind speed. Vollsinger et al. (2005) investigated the drag coefficient and the frontal reduction of deciduous trees. They discovered that the drag coefficients of deciduous trees were significantly less than those of common conifers due to flexible branches and reconfiguration of leaves in high wind speed, and thus using drag coefficients for conifers in replacement of drag coefficients for hardwoods would lead to significant overestimation of drag. Cao et al. (2012) examined the effects of porosity, view angle, and turbulence intensity on drag and found out that the crown porosity had much effect whereas the view angle and turbulence intensity did not. Drag coefficient can also be estimated using field measurement. Kane and Smiley (2006) measured the drag of juvenile Red

maple trees by placing the trees on the back of a moving truck and estimated the drag coefficient. Koizumi et al. (2010) and Koizumi et al. (2016) estimated the drag coefficient using a strain gauge on a high wind day although the number of sample trees was very small. Table 5.1 summarizes the result of drag coefficients on various coniferous and deciduous trees collected from various works of literature. Note that many of the drag coefficients listed in Table 5.1 are extrapolated values.

Based on the literature review of drag coefficient of different species of trees, it can be concluded that the drag coefficient varies with species due to the variation in stiffness, foliage, and morphology. The drag coefficient of all the species cannot be possibly estimated and reviewed in this section. Though, replacing the drag coefficient of the same type (coniferous or deciduous) and species with similar morphology and amount of foliage listed in Table 5.1 may be a good substitute for all other species, and is used in the calculation of V_c of tree-fall.

Table 5.1. Summary of drag coefficients of various coniferous and deciduous trees

Type (coniferous/deciduous)	**Species**	C_d	**Velocity (m/s)**	**Reference**
Coniferous (softwood)	Grand fir	0.36*	30.5	Mayhead (1973)
	Corsican pine	0.32*	30.5	Mayhead (1973)
	Douglas fir	0.22*	30.5	Mayhead (1973)
	Western redcedar	0.22	20.0	Rudnicki et al. (2004)
	Norway spruce	0.35*	30.5	Mayhead (1973)
		0.59*	30.0	Koizumi et al. (2016)
	Sitka spruce	0.35*	30.5	Mayhead (1973)
		0.40*	26.0	Mayhead et al. (1975)
	Scots pine	0.29*	30.5	Mayhead (1973)
		0.35*	26.0	Mayhead et al. (1975)
	Western hemlock	0.14*	30.5	Mayhead (1973)
		0.47	20.0	Rudnicki et al. (2004)
	Lodgepole pine	0.20*	30.5	Mayhead (1973)
		0.34*	26.0	Mayhead et al. (1975)
		0.47	20.0	Rudnicki et al. (2004)
Deciduous (hardwood)	Poplar	0.10*	30.0	Koizumi et al. (2010)
	White birch	0.14*	30.0	Koizumi et al. (2016)
	Paper birch	0.15	20.0	Vollsinger et al. (2005)
	Black cottonwood	0.17	20.0	Vollsinger et al. (2005)
	Red alder	0.22	20.0	Vollsinger et al. (2005)
	Bigleaf maple	0.26	20.0	Vollsinger et al. (2005)
	Trembling aspen	0.28	20.0	Vollsinger et al. (2005)
	Red maple	0.59	20.0	Kane and Smiley (2006)

*Drag coefficient extrapolated to the specific velocity

5.2.3 Projected Frontal Area

Directly obtaining the projected frontal area of a tree (A) from a ground-based damage survey is very challenging, thus it should be estimated indirectly. The projected frontal area equals the sum of the stem frontal area and crown frontal area. While measuring the DBH of trees is relatively easy in a ground-based damage survey, obtaining the measurement of height, crown height, and crown width (or crown diameter) is often difficult due to inaccessibility in a damage site. These other dimensions can be predicted from the past studies which have predicted dimensions of different trees, such as height and crown height, based on the DBH and the growth rate of the tree (Bechtold, 2003; Curtis, 1967; Dawkins, 1963; Feldpausch et al., 2011; Hemery et al., 2005; Hökkä, 1997; Mamoun et al. 2012; Mamoun et al. 2013; Nowak, 1990; Peper et al., 2001). The crown frontal area can be calculated assuming a triangular shape where the crown height is the height of the triangle and crown width is the base of the triangle (Rudnicki et al., 2004). Thus, the crown frontal area (A_{crw}) can be written as Eq. 5.11.

$$A_{crw} = \frac{h_{crw} \cdot D_{crwn}}{2} \tag{5.11}$$

where h_{crw} is the crown height and D_{crw} is the crown diameter. The stem frontal area is the total area of the stem from the ground up to the crown, but the stem of the tree tapers off with height, forming a trapezoidal shape. Taper linear equations of 34 different tree species across the Southern United States were developed by Larsen (2017). The diameter (d) at any height (z) of the tree is expressed in a linear equation:

$$d(z) = DBH + p_b(z - bh) \tag{5.12}$$

where p_b is the taper rate, which can be found in Larsen (2017), and bh is the breast height (1.4 m or 4.5 feet). Using the area of a trapezoid, the stem frontal area (A_{stem}) becomes:

$$A_{stem} = (h - h_{crw}) \cdot \left(DBH - p_b bh + p_b(h - h_{crw})\right) \tag{5.13}$$

By adding the crown frontal area and the stem frontal area, the total frontal can be written as Eq. 5.14.

$$A = A_{crw} + A_{stem} = \frac{h_{crw} \cdot D_{crw}}{2} + (h - h_{crown}) \cdot \left(DBH - p_b bh + p_b(h - h_{crw})\right) \tag{5.14}$$

However, there are a lot of assumptions and uncertainties are involved in this process of estimating the total frontal area, especially if the h, h_{crw}, and D_{crw} are estimated based on the DBH alone. Moreover, Kane and Smiley (2006) discovered that assuming a triangular frontal shape overestimated the drag coefficient of red maple by 14 %.

A more accurate way of obtaining the frontal area is through an aerial survey if available. By using photogrammetry and image processing tools, the frontal area of trees in aerial photographs can be estimated by multiplying the pixel count with pixel size. The number of pixels of the frontal area can be extracted as the same image processing technique used in Chapter 3. A demonstration is shown with a sample tree from the Alonsa, MB tornado aerial photograph. The sample image of the tree is cropped from the aerial photograph (Figure 5.6(a)). The RGB color filter is applied to the sample tree (Figure 5.6(b)) and then the noise filter is applied (Figure 5.6(c)). Even though the background noise is removed using a noise filter, some earth noise still needs to

be removed. Using the object detection function, the binary image (Figure 5.6(c)) can be separated into different objects and just the tree pixels can be selected (yellow pixels in Figure 5.6(d)). Refer to Chapter 3 for the detailed procedure and algorithm of extracting tree pixels. The crown and stem are differentiated at bottom of the branches (Figure 5.6(e)). The number of pixels then can be counted for DBH, h, h_{crw}, A_{stem}, A_{crw}, which can be converted to actual heights and areas. With the resolution being 5-cm, the DBH, h, h_{crwn}, A_{stem}, and A_{crw} are equaled to 25 cm (5 pix × 5 cm/pix), 8.6 m (172 pix × 5 cm/pix), 4.3 m (86 pix × 5 cm/pix), 1.16 m^2 (463 pix × 25 cm^2/pix), and 7.14 m^2 (2856 pix × 25 cm^2/pix), respectively. Thus, the total frontal area of the sample tree becomes 8.3 m^2. Note that all of the dimensions extracted using image processing are dependent on the number of pixels, which is highly sensitive to the digital number (DN) range, so a careful selection of DN range is necessary (refer to Chapter 3).

Figure 5.6. Tree dimensions extraction process from an aerial photograph.

5.2.4 Sensitivity Analysis

As shown in section 5.2.2.1, the analytical solution of V_c of tree-fall is very complicated and contains lots of parameters, and thus lots of uncertainties are present. In order to find out which

parameters affect the V_c of tree-fall more and focus the attention on the more "important" parameters, a sensitivity analysis is performed. For the sensitivity analysis, the Power Law is used to generate a wind profile instead of the Logarithmic Law. The area moment of inertia of the stem (I) is calculated as $\pi/64 \times \text{DBH}^3$ (Peltola and Kellomäki, 1993) and the linear regression of uprooted trees from Cannon et al. (2015) was used to obtain the M_{crit} instead of using Eq. 5.8 for RS_{sup} for the reasons stated in section 5.2.2.2. The sensitivity analysis produced very little difference using the linear regression of snapped trees. Figure 5.7 shows the result of sensitivity analysis of the HWIND model with the following reference values: C_d = 0.3, α = 0.143, W = 4.5 N, DBH = 64 cm, h = 20 m, A = 177 m^2, h_{crw} = 16 m, and E = 7.86 GPa, where W is the weight of the tree.

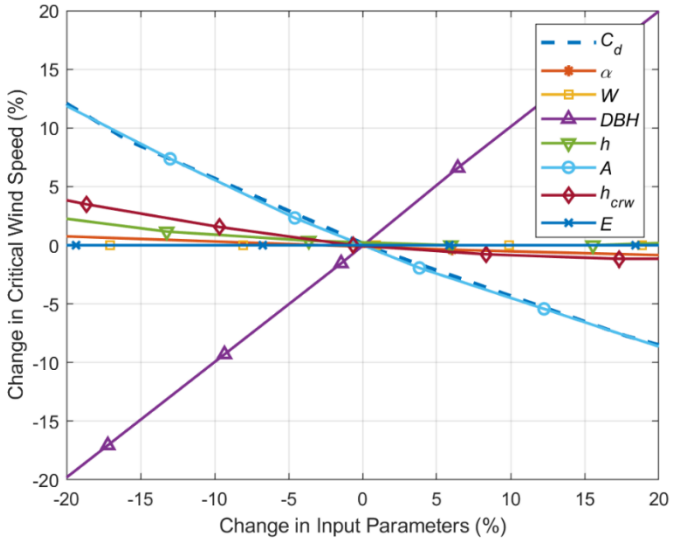

Figure 5.7. Sensitivity analysis of the HWIND model.

Sensitivity analysis shows V_c is strongly influenced by the drag coefficient (C_d), the projected frontal area (A), and the DBH. The A and C_d exhibit a negative correlation with V_c. Larger trees would have more surface area for the wind to act on and a larger drag coefficient would produce greater wind-induced force, subsequently decreasing the V_c. The sensitivity analysis

implies that DBH is the most sensitive to V_c. Thus, an accurate measurement of DBH is suggested in damage surveys. The DBH shows a strong positive correlation with V_c since the M_{crit} is proportional to the square of DBH. On the other hand, elastic modulus (E), weight (W), power-law exponent (α), and the crown height (h_{crw}) are much less sensitive than the other parameters.

5.2.5 Critical Wind Speed of Tree-fall Estimation

5.2.5.1 Application on Naplate, IL tornado ground-based survey

The critical wind speed of tree-fall in the village of Naplate, IL is determined using the HWIND model and the tree information collected during the damage survey (Chapter 2). Although the HWIND requires more tree property information, such as h, h_{crw}, and A, such property information was unobtainable due to the clean-up and repair process in the damage site; only the DBH and species of the failed tree were documented. Despite the large uncertainty in the estimate, therefore, other unobtained properties were estimated using the DBH relationship studies mentioned in 5.1.3.

For the failed trees, all of them failed by uprooting except a few that had broken branches, and most of them were Elm and White pine trees. Because the Naplate, IL tornado occurred in February, the deciduous trees were defoliated. Another visit to the village of Naplate, IL took place in June and most trees that survived the tornado were identifiable as a Maple tree; out of the 186 surveyed trees, 110 trees (59 %) were Maple trees. Based on the species similarities, a C_d of 0.20 (Lodgepole pine) is used for the White pine trees and 0.22 (Red alder) is used for Elm trees. For all the other trees, a C_d of 0.26 (Bigleaf maple) is used assuming that the unidentifiable trees were Maple trees. Although the Red maple tree C_d (0.59) is also included in Table 5.1, a more conservative C_d is used. The M_{crit} is estimated using the regression lines from Cucchi et al. (2004)

and Cannon et al. (2015). The linear regression of edge trees on wet soil is used for Cucchi et al. (2004) because the trees in the village of Naplate, IL were sparsely scattered, and thus a stronger root system is assumed to be developed. Moreover, all of the damaged trees were failed by uprooting, which matches the observation described in Cucchi et al. (2004). The uprooted regression line is used for Cannon et al. (2015). Note that the two regression lines show a very comparable result, except that the regression line from Cucchi et al. (2004) does not pass the origin (Figure 5.5).

Figure 5.8 shows the V_c vs. DBH using M_{crit} regression lines from Cucchi et al. (2004) shown in red symbols and Cannon et al. (2015) shown in black symbols. For the same DBH, the White pine tree has the highest V_c most likely due to the largest drag coefficient. Using the M_{crit} regression line from Cucchi et al. (2004) and Cannon et al. (2015) showed very little difference for trees with larger DBH (> 40 cm), but a significant difference for trees with smaller DBH (< 20 cm). For trees using the Cucchi et al. (2004) regression with DBH under 20 cm, the V_c decreases exponentially as DBH increases. This behavior is often observed in the field where smaller juvenile trees (small DBH) survive a tornado than larger older trees likely due to smaller projected frontal areas. Perhaps using a M_{crit} regression line that does not cross the origin is a more appropriate measurement. The mean and standard deviation of V_c using M_{crit} value from Cucchi et al. (2004) are 35 m/s (78 mph) and 7.2 m/s (16 mph), respectively. Overall, the V_c displays a consistent pattern where the V_c increases with DBH rather consistently because the other parameters (e.g., h, h_{crw}, A, M_{crit}) were estimated based on regression lines of DBH. The estimation does not show a realistic behavior and may not be feasible. As mentioned previously, the variation in tree property and dimension is considerably large, which is not reflected in Figure 5.8. Thus, a more accurate estimation, or a direct measurement, of tree dimensions (other than just DBH) is highly

recommended during damage surveys. Note that the all points shown in Figure 5.8 are fallen trees in Naplate, IL, and the shape of points represents different estimation methods.

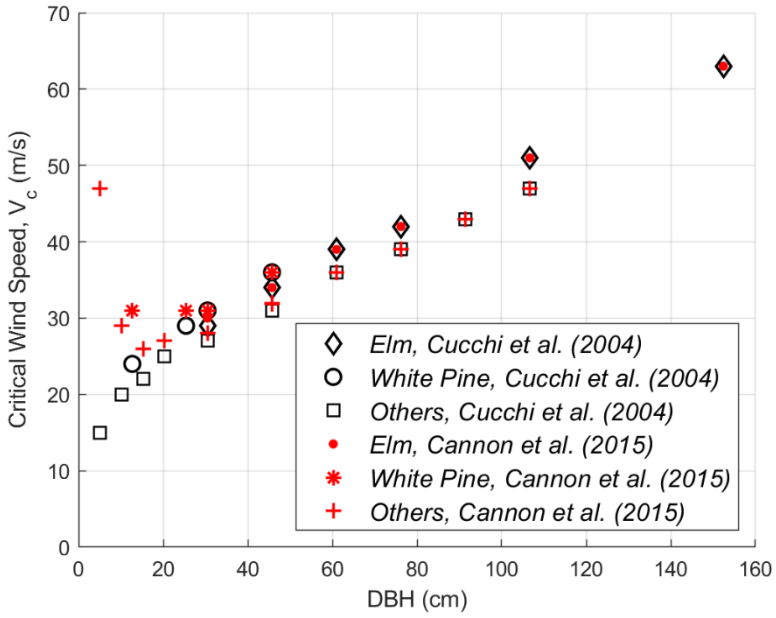

Figure 5.8. Critical wind speed of tree-fall of the Naplate, IL tornado.

5.2.5.2 Application on Alonsa, MB tornado aerial survey

The critical wind speed of tree-fall of the Alonsa, MB tornado is also determined using the HWIND model and the tree information extracted from the aerial photographs. The aerial photographs of tree damage show that the majority of the trees failed in stem breakage. According to the Manitoba forest observatory, most of the trees were Trembling Aspen, Balsam Poplar, and other hardwood species. Thus, a drag coefficient of 0.28 (Trembling Aspen) is used in the calculation of Alonsa, MB tornado V_c. A total of 41 trees are sampled, in which out of 41 samples, four of them failed by uprooting and the rest failed by stem breakage. It is important to note that a complete-random sampling was infeasible and only isolated trees were selectively chosen because it is very challenging to separate a single tree among overlapping fallen trees. The h, h_{crw}, A, and

DBH of the sampled trees are estimated using the image processing technique (section 5.2.3), and the M_{crit} value is estimated using Cannon et al. (2015). The estimated V_c vs. DBH is shown in Figure 5.9 with a mean and standard deviation of 47.5 m/s (106 mph) and 12.5 m/s (28 mph), respectively. A much higher V_c (about 30 mph greater mean V_c) is estimated for the Alonsa, MB tornado compared to the V_c for Naplate, IL tornado. However, a higher V_c is perhaps expected for the Alonsa, MB tornado because most trees in the Alonsa, MB tornado (Trembling Aspen and Balsam Poplar) were tall and slender trees, which have less projected frontal area (Wang et al., 1998), and also failed by stem breakage. Alternatively, an error may have occurred due to selective sampling of isolated trees. According to Cucchi et al. (2004), the M_{crit} of edge trees of the forest is much greater than that of inner trees because the roots grow deeper into the ground developing a stronger anchoring system. Another possible source of error is the estimation of the projected frontal area. An incorrect selection of DN range and removal of noise pixels may significantly underestimate the area, which is inversely correlated with the V_c. An independent method of estimating the V_c by treating the V_c as a random variable in tree-fall analysis can be used to compare the V_c estimation using HWIND method (Chapter 7).

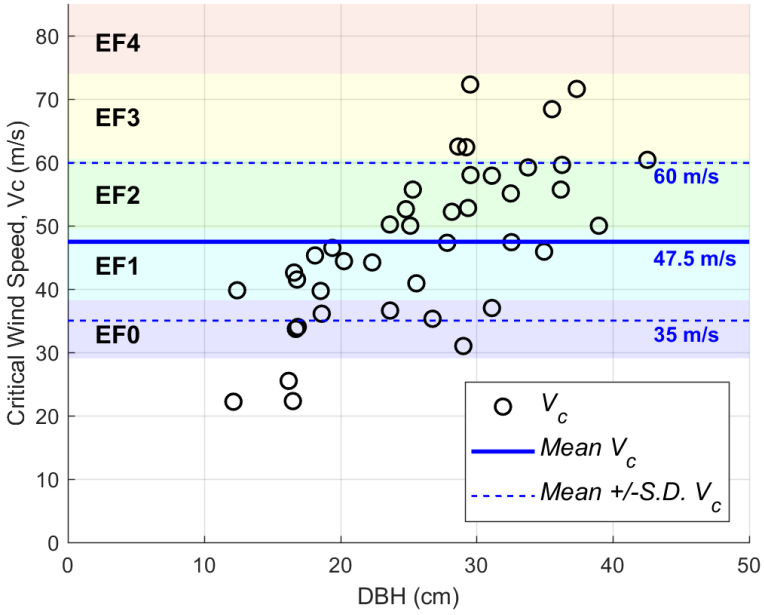

Figure 5.9. Critical wind speed of tree-fall of the Alonsa, MB tornado.

5.3 Critical Wind Speed of Corn-fall

5.3.1 Introduction on Critical Wind Speed of Corn-fall

In addition to trees, crops are also susceptible to wind damage. For the past decades, a significant loss of crop damage from thunderstorms and tornadoes occurred in the United States: an average of 70 million dollars annual loss (NOAA, 2018). Due to wind lodging of crops from the wind hazards, the crop yield reduces considerably (Berry and Spink, 2012; Carter and Hudelson, 1988; Cleugh et al., 1998). The majority of the tornadoes in the United States damage agricultural areas, in which a large portion of the cropland is used to grow corn (USDA, 2020). In fact, corn damage from tornado has been frequently observed in the past (Eshelman and Standford, 1977; Fujita 1993; Forbes and Wakimoto, 1983; Guyer and Moritz, 2003; Meng and Yao, 2014). However, the wind speed estimation of these tornadoes poses a challenge due to the lack of structures in these regions (Guyer and Moritz, 2003), and the corn damage, oftentimes, is the only damage observed in the field. With the lodging wind speed of crop or the V_c of crop-fall, the near-

surface wind speed estimation of tornadoes in cropland can be done using tree-fall analysis. Yet, very little is known about the lodging wind speed of crop and more studies is surely needed. Although certainly there are other crop damages caused by tornadoes, only the lodging wind speed of corn will be examined in this section due to the availability of data in this study.

To properly investigate the corn damage by tornadoes, an estimation of lodging wind speed of corn, in which lodging is defined as the permanent deformation of the stem from its original vertical position in consequence of insufficient strength in flexure leading to buckling (Gardiner et al., 2016), is needed. In the past years, there have been a few studies of the development of mechanical lodging models of wheat and cereal (Berry et al., 2003; Berry et al., 2004) and experimental investigation of model parameters of wheat (Sterling et al., 2003). More recently, a generalized crop lodging model has been developed where the model can be applied to a wide range of crops (Baker et al., 2014). The V_c of corn-fall is obtained through the analytical model and the result from experimental tests.

5.3.2 Experimental Tests on Corn

Although a few analytical models of crop lodging have been developed, not many experimental works have been conducted on corn. To estimate the bending moment capacity of corn stalks at the base, a series of 3-point bending moment tests on corn at different stages was carried out. Bending moment capacity is generally considered the most appropriate strength measurement in stalk lodging (Robertson et al., 2017), in which a 3-point bending moment test is often used to measure the bending moment capacity on corn (Al-Zube et al., 2018; Robertson et al., 2014, Robertson et al., 2017). All of the past studies measured the bending moment capacity of the corn at the harvest stage. Though, it has been reported that tornadoes occur across all months

and seasons (NOAA, 2020c), and thus damage can occur all around the year. An experimental test of measuring the bending moment capacity of corn at different growth stages was conducted to understand the bending moment capacity relationship with the growth stage and the size of the corn.

A sample of corn was collected from a local cornfield grown by the Department of Crop Science at the University of Illinois Urbana-Champaign. A total of 10 sets of tests with 12-20 samples each time were conducted from mid-July to early November. Following the guidelines of the past studies on measuring the bending moment capacity on corn, the bending moment capacity of corn from growth stage V9 to R6 was measured. In general, corn starts to be susceptible to wind damage at stage V8 (Thelen, 2017), in which the canopy height reaches about 0.6 m (24 in). Refer to Ransom and Endres (2020) for a detailed description of different corn growth stages. The force-displacement curve of the sample corn was recorded at 10 Hz, in which the force was measured with a 2,2240-N (500-lb) load cell at a 50 mm/min loading rate. The nominal bending moment for each corn was calculated from the nominal force with a moment arm of 23 cm (9 in). The loading point was generally 18 to 23 cm (7-9 in) above the base, and displacement is defined as positive moving downward. Figure 5.10 shows the experimental setup of the 3-point bending moment test on a corn stalk.

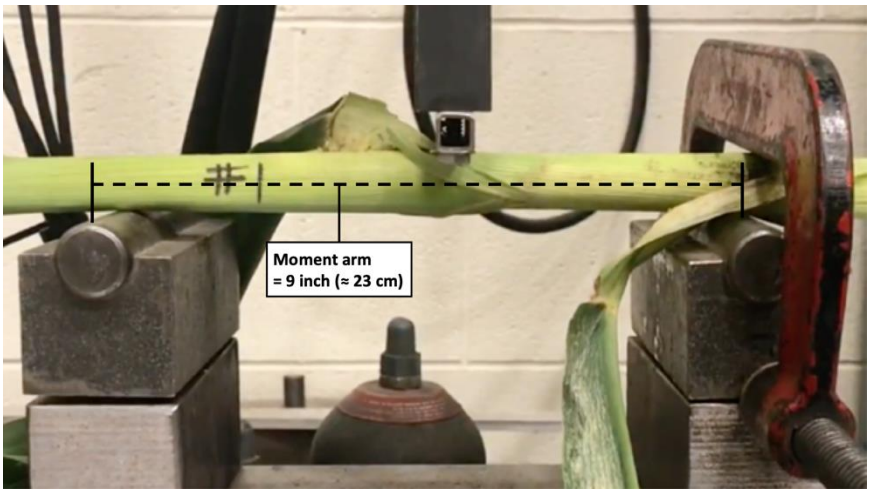

Figure 5.10. Experimental setup of a 3-point bending moment test on a corn stalk.

With the maximum force measured (P_{max}), the critical bending moment (M_{crit}) can be calculated using the following equation:

$$M_{crit} = \frac{P_{max} L}{4} \tag{5.15}$$

where L is the span length (or the moment arm) (AISC, 2017). According to Robertson et al. (2015) and Robertson et al. (2017), the loading position (on the node or internode) and orientation (perpendicular to the major or minor axis) have significant effects on the bending moment capacity. Although the loading position and orientation were recorded in the experiment, the M_{crit} was not differentiated by these factors to include a variety of failure modes and all the M_{crit} values were included in the analysis of the V_c of corn-fall. However, differentiating them may help understand the failure mechanism of corn and may be worthy of future study. Figure 5.11 shows examples of the force-displacement curve of a corn stalk. The force-displacement curve showed two general behaviors: 1) a sudden drop in the force after the force reaches P_{max} (Figure 5.11(a)),

in which this type of failure is defined snapping, 2) a gradual decrease of force after the point of P_{max} (Figure 5.11(b)), in which this type of failure is defined as creasing. Note that the scale is different for the two figures. A possible reason for different failure modes is the randomly distributed local imperfections in material or geometry (Robertson et al., 2015).

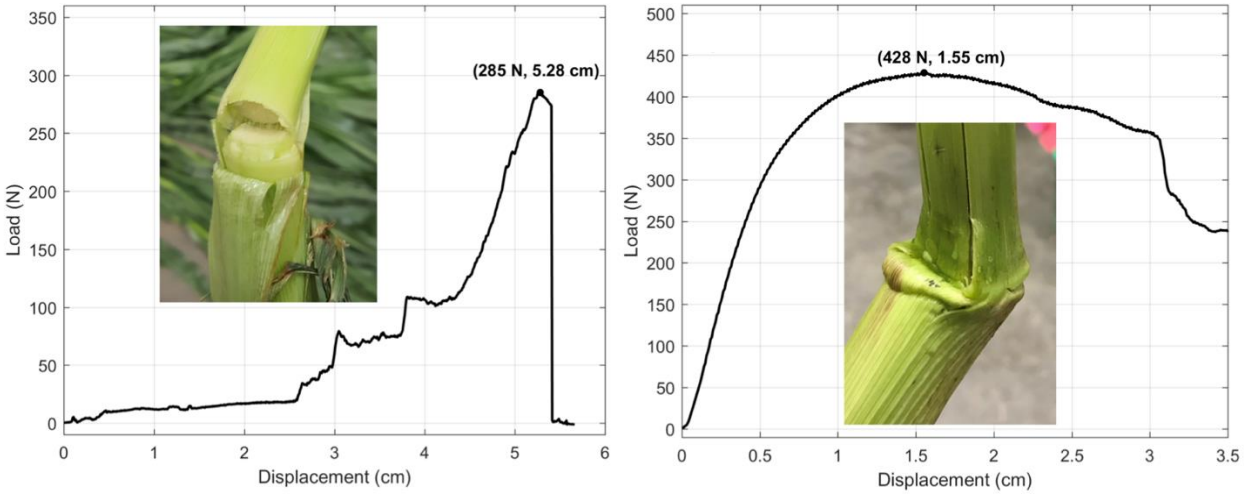

(a) snapping (b) creasing

Figure 5.11. Force-displacement curves and image of corn (a) snapping and (b) creasing.

The corn was grouped by the growth stage of the corn that was collected on each test day. A box plot of the recorded bending moment capacity (M_{crit}) for a different group of growth stage is shown in Figure 5.12, where the median value is the red central mark, the 25th and 75th percentiles are the edges of the blue box, the most extreme data points without the outliers are on the whisker, and the outliers (red "+") extend outside of +/–2.7 standard deviations from the mean value assuming a normal distribution. The mean diameters (blue circle) of each test sample are also shown in Figure 5.12. The bending moment capacity showed a wide variation where the bending strength was as low as 5 N-m and as high as 53 N-m for some growth stages. The box plot of the bending moment at the growth stage of R3-4 and R4-5 showed similar values with the

result from Robertson et al. (2014). The maximum M_{crit} occurred at the growth stage of R3-4, but the highest median value occurred at the growth stage of R4-5. In general, the M_{crit} increased in the early stage as the diameter increased until growth stage R4-5, and then decreased again as the diameter decreased. The bending moment capacity of a crop is a function of radius cubed (Baker et al., 2014). Although the relationship was not examined in this study, the stalk diameter is theorized to have a significant positive correlation with M_{crit}.

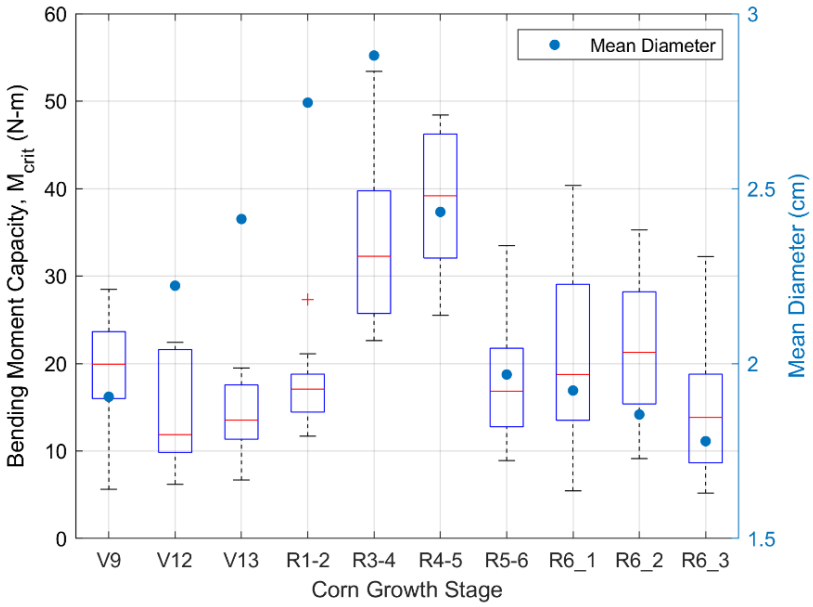

Figure 5.12. Box plot of bending moment capacity of corn overlaid with the mean diameter at various growth stages.

5.3.3 Critical Wind Speed of Corn-fall Estimation

Using the bending moment strength and corn dimensions obtained from the 3-point bending moment test, the critical lodging wind speed of corn is calculated with different crop lodging models. Berry et al. (2003) and Baker et al. (2014) models are adopted to back-calculate the critical lodging wind speed of corn using the bending moment capacity directly measured

instead of the analytical bending moment value. Although the analytical bending moment capacity can be obtained from the generalized crop lodging model (Baker et al., 2014), the analytical bending strength still requires an estimate of stem yield stress and stem wall thickness, which are still unknown for most crops. With a proper and careful experimental procedure, a more accurate and realistic value of the bending moment capacity may be obtained. The V_c of a generalized crop is defined as (Baker et al., 2014):

$$\alpha = \left(\frac{\mu g X^2}{npEI}\right)^{0.5} \tag{5.16}$$

$$\overline{U} = \left(\frac{\omega_n^2\left(\frac{X}{g}\right) n\left(\frac{\sigma\pi a^3}{4}\right)\left(1-\left(\frac{a-t}{a}\right)^4\right)}{\left(1+\omega_n^2\left(\frac{X}{g}\right)\right)(0.5\rho A_{CF}X)\left(\cos\left(\frac{\alpha x}{l}\right)-\cot(\alpha)\sin\left(\frac{\alpha x}{l}\right)\right)\left(1+6.86I_u\left(1+0.366\left(\frac{\pi}{4\theta}\right)\right)^{0.5}\right)}\right)^{0.5} \tag{5.17}$$

where μ is the mass of the unit area, g is the gravitational constant, X is the height of the center of mass, n is the number of stems per plant, p is the number of plants per unit area. E is the Young's modulus of the stem, I is the second moment of area of the stem, ω_n is the radial natural frequency, X is the height of the center of mass, σ is the stem yield stress, a is the stem radius, t is the stem wall thickness, A_{CF} is the plant drag area, x is the distance up the stem from the ground, l is the length of the stem, I_u is the turbulence intensity, θ is the damping ratio. Detailed derivation can be found in Baker et al. (2014). Using the bending moment capacity measured from the 3-point bending test, Eq. 5.17 can be replaced with:

$$\bar{U} = \left(\frac{\omega_n^2 \left(\frac{X}{g}\right) M_{crit}}{\left(1 + \omega_n^2 \left(\frac{X}{g}\right)\right)(0.5\rho A_{CF} X)\left(\cos\left(\frac{\alpha x}{l}\right) - \cot(\alpha)\sin\left(\frac{\alpha x}{l}\right)\right)\left(1 + 6.86 I_u \left(1 + 0.366\left(\frac{\pi}{4\theta}\right)\right)^{0.5}\right)} \right)^{0.5} \quad (5.18)$$

Although the entire derivation is not shown, Eq. 5.18 still follows the load-resistance framework presented in Figure 5.1. It is important to note that the $\bar{U}$ is defined as an hourly mean wind speed, but the wind that causes the crop to lodge is the gust, not the mean wind (Joseph et al., 2020). Thus, an hourly wind speed to effective gust conversion is necessary; the conversion factor can be found from Berry et al. (2003):

$$\frac{V_g}{\bar{U}} = 1 + 0.42 I_u \times \ln\left(\frac{3600}{\tau}\right) \quad (5.19)$$

where V_g is the gust speed and τ is the effective loading period. A suitable averaging time (effective loading period) should be considered due to the fluctuation in wind loading, which is defined as 4.5×height/mean velocity and taken as 0.3 seconds for crops suggested by Baker (1995). Joseph et al. (2020) further examined the dynamic and aerodynamic parameters for corn, oats, and oilseed rape and estimated the crop lodging speed with the Baker et al. (2014) model. Most of the dynamic and aerodynamic parameters of corn were taken from Joseph et al. (2020): ω_n = 0.7 Hz × 2π, θ = 0.11, I_u = 0.59. All the other parameters were measured directly from the sample except that the A_{CF} was measured directly. The frontal area was calculated by multiplying the diameter and the height of the corn stalk and then adding the total leaf area. The total leaf area is estimated from the product of an average leaf area of corn, 268 cm^2 (McKee, 1964), and the number of leaves on each corn stalk. The A_{CF} is then obtained by multiplying the mean drag coefficient of corn for the entire

canopy of C_d = 0.17 from Wilson et al., (1982). Figure 5.13 shows the result of the V_c of corn-falls at different growth stages at the corn height of 2.5 m. The V_c of growth stage V9 exhibits relatively high wind speed compared to the rest due to small height and project frontal area. However, it is suspected because younger corn has a smaller projected area and height. From field observations, root lodgings where the roots are pulled out of the ground have been observed more frequently for younger, more flexible corn (Thelen, 2017). Although the result showed a comparable result with Joseph et al. (2020), a full-scale validation is essential for future work.

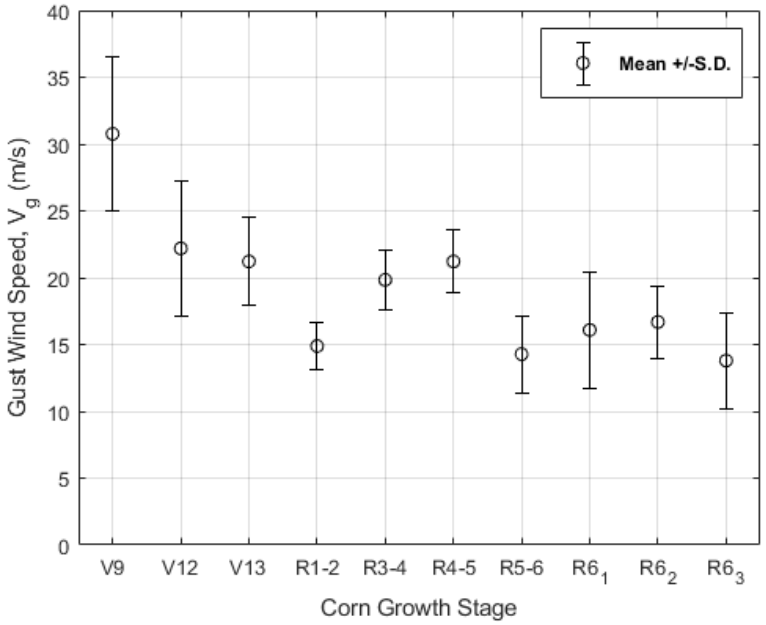

Figure 5.13. Critical gust wind speed range of corn at different growth stages.

5.4 Critical Wind Speed of Sign-fall

5.4.1 Introduction on Critical Wind Speed of Sign-fall

The tornado wind speed at a specific location can also be estimated using forensic analysis, a method where structural capacity is evaluated to calculate the wind load and wind speed required for the observed failure. Forensic analysis can be applied to building failures, as described in

Coulbourne and Miller (2012) which investigates the performance and failure of school buildings after the 2011 Joplin, MO tornado in detail. Boughton et al. (2012) applied forensic analysis to failed and non-failed road signs at different locations to estimate the peak gust of the Yasi tropical cyclone.

In general, traffic signs are engineered, following standardized guidance (IDOT 2016). The material properties and dimensions are relatively well-known compared to trees. In the Tropical Cyclone Yasi report, both failed and non-failed road signs are used to estimate the peak gust of a cyclone (Boughton et al., 2012), where the failed traffic signs were used to estimate the lower bound wind speed and the non-failed signs for the upper bound wind speed, using the bending moment capacity. The same method can be applied to estimate the wind speed bounds of a tornado. The failure wind speed of the traffic signs is calculated using the bending moment capacity of the steel post and the area of the signage, assuming the failure mode is yielding at the base of the steel post. The V_c of these traffics signs then can be used to extract the Rankine vortex (RV) parameters and generate an independent near-surface wind field (Chapter 7). However, the number of traffic signs found in the damage survey is usually much less than the number of trees, and a ground-based damage survey is usually necessary (Boughton et al. 2012; Rhee and Lombardo 2018) because traffic signs are hard to identify from aerial photos of large-scale tornadoes. In the case of a large-scale tornado, the aerial photograph is often acquired by flying aircraft and forced to trade off the resolution for a larger area.

5.4.2 Experimental Tests on Traffic Sign

The bending moment capacity of the steel posts can be estimated in two different ways: measuring the bending moment capacity of sample steel posts and an analytical solution of the

bending moment capacity. In general, two types of U-channel steel posts are used for traffic signs, specified by the Illinois Department Of Transportation (IDOT) (IDOT, 2016). Samples of steel posts were given by the La Salle County Highway Department and tested at the Newmark Civil Engineering Laboratory at the University of Illinois Urbana-Champaign to measure the bending moment capacity from a three-point bending moment test. Figure 5.14 shows the experimental setup of the 3-point bending moment test on a steel post. The maximum force (P_{max}) that caused Type B steel post to bend was 14.6 kN as shown in the force-displacement curve (Figure 5.15). The maximum bending moment capacity (M_{max}) can be calculated using Eq. 5.15. With a span length of 800-mm (32-inch), the bending moment capacity was calculated to be 2,960 N-m.

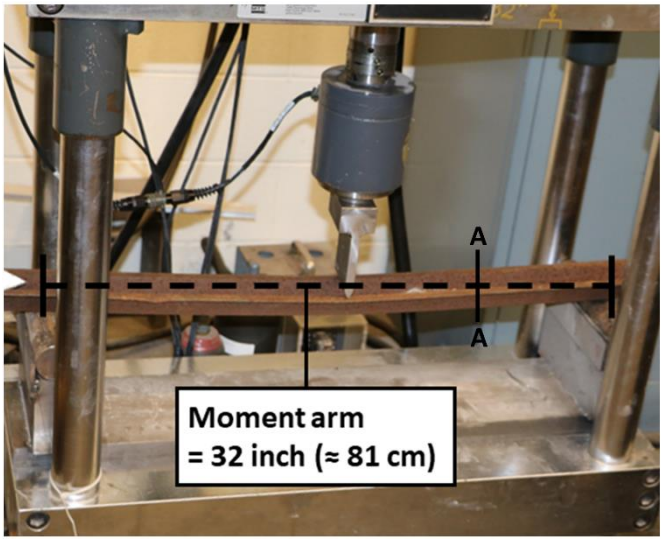

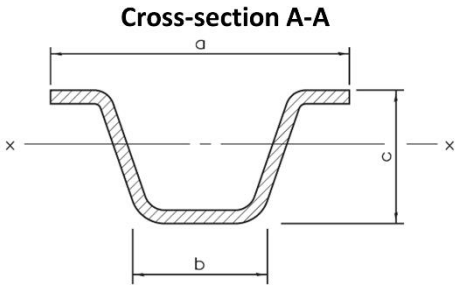

Steel Properties

Steel Type	a, in (mm)	b, in (mm)	c, in (mm)	Sx-x, in^3 (mm^3)	lbs/ft (kg/m)
Type A	3.0625 (78)	1.25 (32)	1.438 (37)	0.223 (3.654)	2.00 (2.98)
Type B	**3.1875 (81)**	**1.25 (32)**	**1.50 (38)**	**0.341 (5.588)**	**3.00 (4.46)**

Figure 5.14. Experimental setup of the 3-point bending moment test and dimensions and properties of Type B steel post.

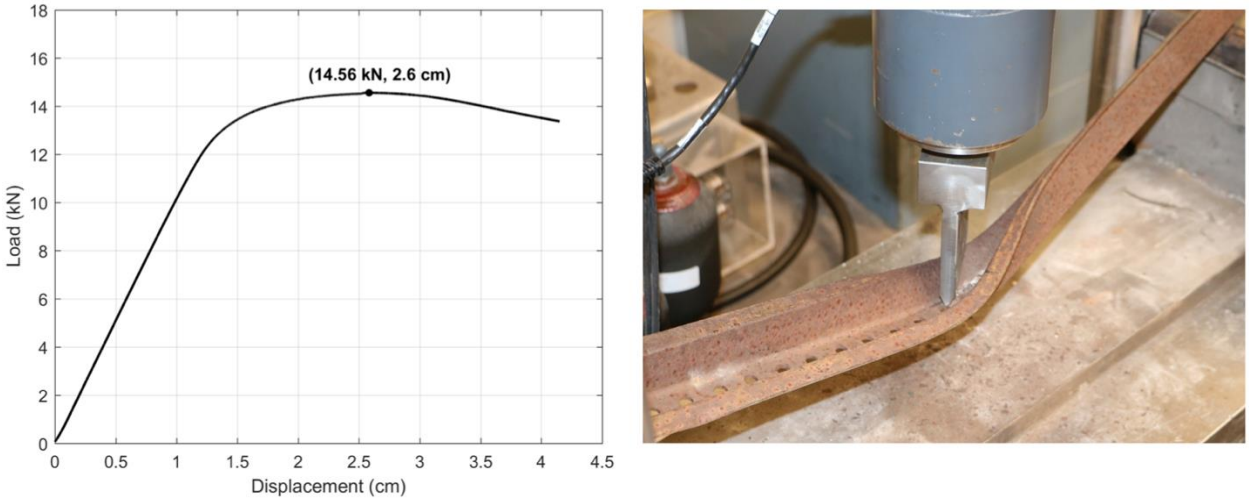

(a) force-displacement diagram (b) failure mode of U-channel

Figure 5.15. Three-point bending moment result of Type B steel post: (a) force-displacement curve and (b) image of failure mode.

Although Boughton et al. (2012) assume that a plastic hinge is formed at the base and uses the plastic moment capacity of the steel post, the bent images of U-channel steel post (Figure 2.11 and Figure 5.15(b)) suggest that U-channel steel post failed in Lateral Torsional Buckling (LTB) and the steel post did not reach the full plastic state (AISC, 2017). The difference in failure mode is caused by the difference in the cross-section of the sign poles. A simpler and faster approach to obtain the bending moment capacity is through an analytical solution. The analytical solution for the yield bending moment (M_y) and plastic bending moment (M_z) is calculated as follows:

$$M_y = F_y \cdot S_x \tag{5.20}$$

$$M_z = F_y \cdot Z_x \tag{5.21}$$

where F_y is the yield strength of the steel, S_x is the elastic section modulus, Z_x is is the plastic section modulus of the steel post (AISC, 2017). The M_z may be used if the steel posts forms a fully

plastic hinge for any type of steel. Although the above equations may be used for simplicity, more detailed equations for various unbraced lengths (L_b) and bending coefficients (C_b) can be used and found in AISC (2017), but additional material properties must be known. With the yield strength (F_y) of 410 MPa (60 ksi) (Steel Gr 60) and section modulus (S_x) of 5.6 mm^3 for Type B (IDOT, 2016), the bending moment capacity of 2,310 N-m was obtained. As expected, the yield bending moment from the analytical solution is less than the M_{max} estimated from the experimental result. One should note that the failure limit state depends on the geometry and may be different for different types of metal posts. Although the plastic bending moment was not used for the U-channels because they did not reach a full-plastic state, one can use Eq. 5.20 or Eq. 5.21 to estimate the bending moment capacity of a sign post if a plastic hinge is formed (Boughton et al., 2012). The analytical solution allows rapid estimation of bending moment capacity given the material properties are known. The estimated maximum bending moment capacity (M_{max}) is used later in this section to estimate the critical wind speed of traffic signs. The maximum bending moment capacity was assumed to be the same for all the traffic signs with Type B steel post.

5.4.3 Critical Wind Speed of Sign-fall Estimation

Once the bending moment capacity of the traffic sign-post is obtained, the V_c of the traffic signs can be determined. The V_c at different locations then can be used to estimate the near-surface wind field of Naplate, IL tornado. The V_c is calculated from the net wind force exerted on the traffic sign and the wind-induced moment applied at the base of the sign (Boughton et al., 2012). The peak net wind load (F_n) and moment (M_w) exerted on the traffic sign-post including any number of signs is obtained by the following Eqns:

$$F_{n,i} = \frac{1}{2}\rho {V_c}^2 C_{F,n} A_i \tag{5.22}$$

$$M_w = \sum \left(F_{n,i} \cdot l_i\right) = \sum \left[\left(\frac{1}{2}\rho {V_c}^2 C_{F,n} A_i\right) \cdot l_i\right] \tag{5.23}$$

where ρ is the air density, V_c is the critical wind speed (3-s gust velocity at the centroid), $C_{F,n}$ is the net drag coefficient (ASCE, 2016), A_i is the area of each plate on a traffic sign, and l_i is the distance from the base of the steel post to the centroid of each plate. The $C_{F,n}$ of rectangular signboard varies with the aspect ratio, clearance ratio, and wind direction (Cook, 1990; ESDU, 1989; Letchford, 2001). Notably, Letchford (2001) found that the $C_{F,n}$ is almost constant for wind directions within ±45° normal to the sign plate. Note that a 3-s gust speed is assumed for the V_c in Boughton et al. (2012). Thus, unlike the V_c of tree and crop, a mean wind speed conversion is not required. Considering the traffic sign fails when the wind-induced moment exerted exceeds the bending moment capacity ($M_w \geq M_{max}$), the V_c of the traffic sign becomes:

$$V_c \geq \sqrt{\frac{M_{max}}{\sum \left[\left(\frac{1}{2}\rho C_{F,n} A_i\right) \cdot l_i\right]}} \tag{5.24}$$

Note that the M_{max} can be replaced with the analytical solution, M_y or M_z, depending on the availability and the failure limit state of the sign pole.

In the Naplate, IL tornado, a total of 37 traffic signs were surveyed and their V_c was estimated. Out of the 37 surveyed traffic signs, a total of 9 signs had failed, and 28 signs had survived. Figure 5.16 shows the map of the surveyed traffic signs of Naplate, IL tornado with their estimated V_c. From the surveyed map, a rough idea of the near-surface wind field of Naplate, IL

can be estimated. The maximum wind speed of the tornado, which occurs near the tornado center, can be estimated. The traffic signs with V_c estimated greater than 55 m/s (123 mph) and 50 m (164 ft) or less away from the estimated tornado center are labeled (lower bound in a red box and upper bound in a blue box) in Figure 5.16. Assuming that the wind direction is within ±45° normal to the sign plate, the maximum lower bound V_c is 47 m/s (106 mph) and the maximum upper bound V_c is 64 m/s (142 mph), which are approximately 35 m (115 ft) away north and 40 m (130 ft) away south from the estimated tornado center, respectively. Hence, from the bounds of the V_c of the traffics signs, it can be speculated the maximum near-surface wind speed of Naplate, IL tornado was greater than 47 m/s (106 mph) but less than 64 m/s (142 mph). The time-varying $C_{F,n}$ due to directionality and estimation of the entire tornado wind field using the V_c of all traffic signs will be discussed in Chapter 7.

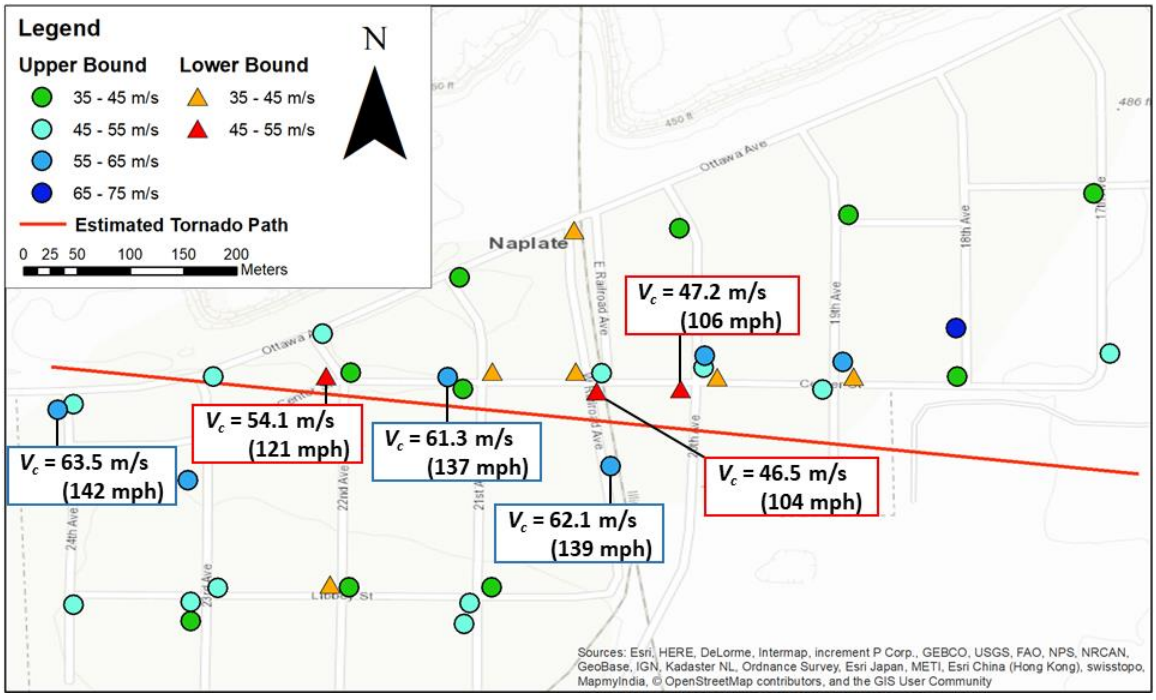

Figure 5.16. Map of the critical wind speed of traffics signs of Naplate, IL.

5.5 Summary

This chapter summarizes the process of estimating the critical wind speed of three different damage indicators: trees, corn, and traffic signs. The estimation of V_c can be used individually to estimate the tornado intensity, or as an input parameter in the tree-fall analysis. The following points are the summary of the V_c estimation for different damage indicators:

- For estimating the V_c of trees, the HWIND model was used and modified such that the vertical profile of horizontal wind represents a gust profile instead of a mean profile. Also, the M_{crit} of the tree was directly obtained from Cucchi et al. (2004) and Cannon et al. (2015) using $\text{DBH}^2 \times h$. The V_c estimation of tree-fall in the village of Naplate, IL showed that the linear regression line of the M_{crit} that does not pass the origin showed a more realistic behavior.
- Input parameters for the HWIND, such as the height, crown height, and projected frontal area, can be estimated using the DBH relationship or using image processing technique (discussed in Chapter 3) if the aerial photographs are available. Estimation using the DBH relationship did not reflect the behavior of variation in the trees whereas the estimation using the image processing technique did chapter variational behavior. However, the image processing technique may have overestimated the V_c of tree-fall in the forest of Alonsa, MB.
- A sample of commercial hybrid corn at different growth stages was collected and a 3-point bending moment test is performed to measure the M_{crit} of corn.
- The V_c of corn-fall at different growth stages is estimated using a generalized crop lodging model from Baker et al. (2014) and the direct measurement of bending moment capacity.

The hourly mean wind speed from the generalized crop lodging model is then converted to a 3-s gust wind speed by multiplying a gust factor.

- To estimate the V_c of traffic signs, the Boughton et al. (2012) method is adopted. Instead of the plastic moment, the yield moment is assumed and used since the traffic sign posts (U-channel) in Naplate, IL were presumed to fail in LTB.

CHAPTER 6: WIND FIELD MODULE

6.1 Introduction

A wind field model is an essential part of the tree-fall analysis. In Chapter 4, the modified Rankine vortex model is used to simulate the wind field of a tornado. However, there are other idealized vortex models that are often used to represent a tornado wind field. The question of whether one performs better than the other still remains in question. In this chapter, the different characteristics of vortex models are first reviewed. Their compatibility is examined by comparing the models to radar observations and the feasibility in tree-fall analysis by generating tree-fall patterns using each model. Tree-fall analysis is not limited to idealized vortex models but can also incorporate other models. Other tree-fall patterns are generated and examined using other wind field models (asymmetric vortex model and downburst models). The second part of Chapter 6 investigates the effect of topography on wind fields and on the tree-fall pattern. The tornado dynamic response to topography and the ESDU topographic speedup factor is added to the modified Rankine vortex model and the tree-fall pattern is compared to the tree-fall pattern generated from the wind fields of a Large Eddy Simulation (LES).

6.2 Wind Field Models

6.2.1 Idealized Vortex Models

In fluid dynamics, a vortex is defined as a region of air or fluid revolving around an axis, in which the flow field of the fluid can be acquired by solving the Navier-Stokes-Equations (NSE) (Ting and Klein, 1991). A tornado is defined as a violently rotating, narrow column of air (Davies-Jones et al., 2001) and has a similar flow structure as a vortex. Although the structure of a tornado

is much more complex, the wind field of a tornado is simplified and often described by a vortex flow. The velocity equations of a vortex are derived from the NSE and imposing ideal conditions, in which the vortex is called an idealized vortex (Gillmeier et al., 2018).

Many studies on physical testing (Church et al., 1979; Church et al., 2004; Haan et al., 2008; Natarajan and Hangan, 2012; Gillmeier et al., 2018; Refan et al., 2018) and numerical simulation (Bodine et al., 2016; Ishihara et al., 2011; Lewellen and Lewellen, 2007; Lewellen et al., 2000, Nolan, 2012; Noland et al., 2017) of a tornado-like vortex have shown that the structure of the vortex varies with swirl ratio (S). The definition of swirl ratio varies, but generally swirl ratio is a function of the ratio between tangential and radial velocity (Baker and Sterling, 2017; Natarajan and Hangan, 2012; Kuai et al., 2008). For weak swirl ratios, a one-cell vortex (Figure 6.1(a)) is formed where an intense inward flow ascends while rotating about a vertical axis. As the swirl ratio increases, a downdraft develops along the rotating axis and a vortex breakdown (Figure 6.1(b)) occurs aloft. The vertical position of the vortex breakdown moves downward as the swirl ratio increases and the breakdown bubble touches the ground, forming a two-cell vortex (Figure 6.1(c)). For very high swirl ratios, the vortex can split and form a multi-vortex structure (Figure 6.1(d)). These vortex structures have also been observed in tornadoes by Doppler radar instruments (Agree et al., 1975; Refan et al., 2017; Wurman, 2002; Wurman et al., 2014).

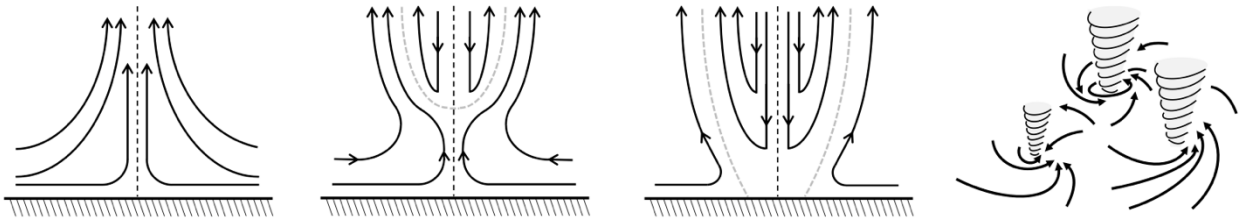

(a) one-cell vortex (b) vortex breakdown (c) two-cell vortex (d) multi-vortex

Figure 6.1. Change in vortex structure as swirl ratio increases (adopted from Davies-Jones, 1982).

In general, Rankine (Rankine, 1882), Burgers-Rott (Burgers, 1948; Rott, 1958), and Sullivan (Sullivan, 1959) vortex models are the most commonly used idealized vortex models to describe the wind field of a tornado (Gillmeier et al., 2018). Because of the simplicity, the Rankine vortex (RV) model, sometimes referred to as the Rankine-combined vortex model, is the most commonly used vortex model in tree-fall analysis (Bech et al., 2009; Beck and Dotzek, 2010; Holland et al., 2006; Karstens et al., 2013; Lombardo et al., 2015). The Rankine vortex model used in each study is modified and may be slightly different from one another. In this dissertation, the RV model is modified by varying the decay exponent and assuming that the radial component follows the same velocity profile as the tangential component as mentioned in Chapter 4. Refer to Eq. 4.1 in Chapter 4 for the radial and tangential velocity fields of the modified RV model used in this chapter. More recently, Baker and Sterling (2017) developed a complete three-dimensional vortex model. All the idealized vortex models assume a steady-state, incompressible flow and neglect the gravitational force, but differs in the assumption of viscosity.

6.2.1.1 Burgers-Rott vortex model

Another idealized vortex model that fits the tangential velocity profile of one-cell tornadoes is the Burgers-Rott model (Wood and Brown, 2011). Some Doppler radar observations have shown that the viscous one-celled Burgers–Rott vortex (BRV) model fits the tangential velocity profile of one-celled tornadoes better than the Rankine vortex model (Bluestein, 2007; Tanamachi et al., 2007; Kosiba and Wurman, 2010). The BRV model assumes a viscid flow and the following degrees of freedom: 1) the tangential velocity (V_θ) is only dependent on the radial distance (r), 2) the vertical velocity (V_z) is solely and linearly dependent on the vertical distance (z), and 3) the

radial velocity (V_r) is solely and linearly dependent r as a result of assumption 1 and 2 (Gillmeier et al., 2018). The NSE reduces to the following expressions (Wood and Brown, 2011):

$$\bar{V}_\theta(\bar{r}) = \frac{1.4}{\bar{r}}(1 - \exp(-1.2564\bar{r}^2)) \tag{6.1}$$

$$\bar{V}_r(\bar{r}) = -\bar{a}\bar{r} \tag{6.2}$$

$$\bar{V}_z(\bar{z}) = 2\bar{a}\bar{z} \tag{6.3}$$

$$\bar{a} = \frac{2\nu}{V_{\theta,max}RMW} \tag{6.4}$$

where $\bar{V}_r$ is the V_r normalized by the $V_{\theta,max}$, $\bar{V}_z$ is the vertical velocity normalized by the $V_{\theta,max}$, and $\bar{z}$ is the vertical distance normalized by the *RMW*, and ν is the kinematic viscosity of air.

6.2.1.2 Sullivan vortex model

Sullivan (1959) obtained the exact solutions of the NSE of a steady, viscous two-cell vortex (Wood and Brown, 2011), in which the air flows downward in an inner cell close to the axis and rises in the surrounding outer cell (Davies-Jones and Wood, 2006). The Sullivan vortex (SV) model follows the same assumption as the BRV assumption except that the SV model assumes that the V_z is dependent on both the r and the z (linearly), and the V_r is only dependent on the r. The velocity equations of the SV model can be expressed as (Gillmeier et al., 2018):

$$\bar{V}_\theta(\bar{r}) = \frac{1}{\bar{r}}\frac{H(x)}{H(\infty)} \quad \text{where } x = \bar{r}^2 \tag{6.5}$$

$$H(x) = \int_0^x \exp(-x' + 3\int_0^{x'} \frac{1}{x''}(1 - \exp(-x''))dx'')dx' \tag{6.6}$$

$$\bar{V}_r(\bar{r}) = -\bar{a}\bar{r} + \frac{2bv}{\bar{r}}(1 - \exp(-\bar{r}^2)) \tag{6.7}$$

$$\bar{V}_z(\bar{r}, \bar{z}) = 2\bar{a}\bar{z}(1 - b\exp(-\bar{r}^2)) \tag{6.8}$$

where *b* is the shape factor that enables solutions for two-celled vortex structures. Wood and White (2011) developed a new parametric model to depict a realistic-looking tangential wind profile of tornadoes and dust devils; the tangential velocity equation is simplified to:

$$\bar{V}_\theta(\bar{r}) = \bar{r}^{2.4}[0.3 + 0.7(\bar{r}^{7.89})]^{-0.435} \tag{6.9}$$

Wood and Brown (2011) further modified the SV model and developed a modified SV model that represents a two-cell vortex structure with a broader downdraft region:

$$\bar{V}_\theta(\bar{r}) = \bar{r}^{10}[0.091 + 0.909(\bar{r}^{22})]^{-0.5} \tag{6.10}$$

This velocity profile, which will be referred to as the modified SV model, has been shown to fit the tangential velocity profile of a dust devil measured by a mobile Doppler radar in Bluestein et al. (2004).

6.2.1.3 Baker vortex model

In addition to the three vortex models, a three-dimensional vortex model has been recently developed by Baker and Sterling (2017), which is referred to as the Baker vortex model (Gillmeier et al., 2018). The Baker vortex (BV) model provides a more generalized form that can produce velocity fields of both a one-cell and two-cell vortex. The BV model assumes an inviscid flow

with all the velocity being a function of both $\bar{r}$ and $\bar{z}$ and a boundary condition where the radial velocity starts at zero at ($\bar{r}$ = 0, $\bar{z}$ = 0), reaches a maximum value at ($\bar{r}$ = 1, $\bar{z}$ = 1), and then falls back to zero at ($\bar{r}$ = 0, $\bar{z}$ = ∞). This gives the BV model an advantage over BRV and SV model in that the radial component exhibits a more realistic behavior. The velocity equations of the generalized BV model can be expressed in the form of:

$$\bar{V}_\theta(\bar{r},\bar{z}) = \frac{K\bar{r}^{\gamma-1}[\ln(1+\bar{z}^{\beta+1})]^{\gamma/(\alpha+1)}}{(1+\bar{r}^{\alpha+1})^{\gamma/(\alpha+1)}} \tag{6.11}$$

$$\bar{V}_r(\bar{r},\bar{z}) = -\frac{(1+\alpha)(1+\beta)\bar{r}^{\alpha}\bar{z}^{\beta}}{\alpha^{\alpha/(1+\alpha)}\beta^{\beta/(1+\beta)}(1+\bar{r}^{\alpha+1})(1+\bar{z}^{\beta+1})} \tag{6.12}$$

$$\bar{V}_z(\bar{r},\bar{z}) = \frac{\delta(1+\alpha)^2\bar{r}^{\alpha-1}\ln(1+\bar{z}^{\beta+1})}{\alpha^{\alpha/(1+\alpha)}\beta^{\beta/(1+\beta)}(1+\bar{r}^{\alpha+1})^2} \tag{6.13}$$

$$S = K\frac{\gamma^{(\gamma-1)/(\alpha+1)}[\ln(2)]^{\gamma/(\alpha+1)}}{\gamma^{\gamma/(\alpha+1)}} \tag{6.14}$$

where K is a constant related to the swirl ratio; δ is the ratio between the vertical and horizontal length scales ($\delta = z_m/r_m$); α, β, and γ are parameters that allow for different shapes of the velocity profile. For the BV model, a realistic assumption of the radial velocity is first assumed, and then the tangential and vertical velocity distributions are derived through the momentum equations and continuity equation, respectively. Thus, unlike other vortex models, the velocities are normalized by the maximum radial velocity ($\bar{V}_\theta = V_\theta/V_{r,max}$; $\bar{V}_r = V_r/V_{r,max}$; $\bar{V}_z = V_z/V_{r,max}$) and the distances are where the $V_{r,max}$ ($V_r(r_m, z_m) = V_{r,max}$) occurs ($\bar{r} = r/r_m$; $\bar{z} = z/z_m$). In the BV model, the swirl ratio (S) is defined as the ratio between the maximum tangential velocity and the maximum radial velocity ($S = V_{\theta,max}/V_{r,max}$), and γ is defined as $\bar{r}^2 = \gamma - 1$ at $V_{\theta,max}$; $\gamma < 1$ would be physically unrealistic. The V_θ of the BV model also exhibits an unrealistic behavior where the velocity

increases to infinity for $\bar{z} = \infty$. It is assumed to be realistic for heights relatively close to the ground where surface roughness affects the magnitude of the velocity. In the BV model, a two-cell vortex is simulated by adding velocity fields of a downdraft with no swirl. The downdraft is assumed a downwards vertical velocity and an outward radial velocity near the vortex core. Because the downdraft is assumed to have no swirl, the tangential velocity is assumed zero. The radial ($\bar{V}_{r,d}$) and vertical velocity ($\bar{V}_{z,d}$) equations for the downdraft are written as:

$$\bar{V}_{r,d}(\bar{r},\bar{z}) = \frac{4\tilde{r}\tilde{z}}{(1+\tilde{r}^2)(1+\tilde{z}^2)} \tag{6.15}$$

$$\bar{V}_{z,d}(\bar{r},\bar{z}) = \frac{-4\delta \ln(1+\tilde{z}^2)}{(1+\tilde{r}^2)^2} \tag{6.16}$$

where $\tilde{r} = 1/\varepsilon_r \bar{r}$ and $\tilde{z} = 1/\varepsilon_z \bar{z}$ with scaling factors, ε_r and ε_z, for $\bar{r}$ and $\bar{z}$, respectively. By adding the downdraft velocity profiles (Eq. 6.15-16) to the vortex velocity profiles (Eq. 6.11-13), the velocity profile of a two-cell vortex can be obtained. Figure 6.2. represents the normalized velocity profiles of a two-cell vortex at $\bar{z}$ = 1 with a downdraft within the core (α = 4, β = 1, γ = 2, S = 1, δ = 1, ε_r = 0.3, ε_z = 1). The velocity profiles of Figure 6.2(c) exhibit a similar structure as Figure 6.1(c). Note that the velocity equations are non-linear, and the superposition of the downdraft flows onto the vortex profiles violates the consistency of the NSE. However, the result of adding the two shows a reasonable representation of a two-cell vortex structure, which has some merit for engineering purposes. Despite many studies that attempted to solve the NSE, there has not been a model that can represent the velocity profiles of a multi-vortex structure.

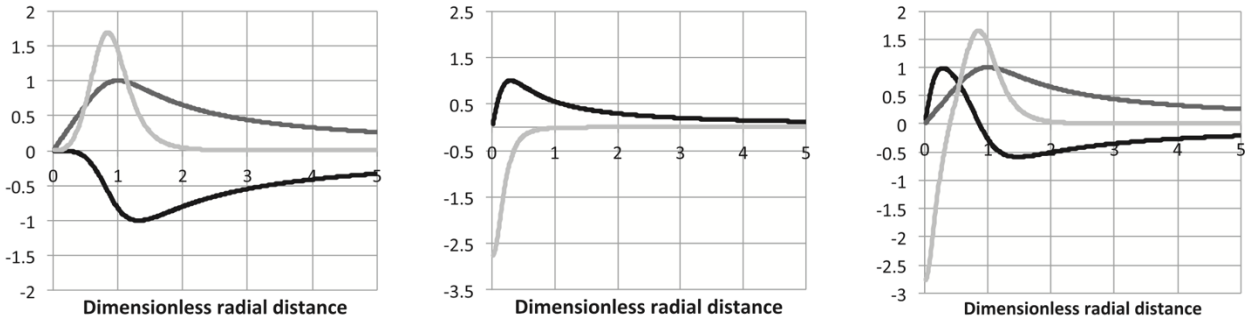

a) one-cell vortex b) downdraft c) two-cell vortex (sum of (a) and (b))

Figure 6.2. Velocity profiles of a one-cell vortex (a), downdraft (b), and two-cell vortex (c) derived from the BV model (Baker and Sterling, 2017)

6.2.1.4 Tangential velocity profile comparison

Unlike the radial and vertical velocity, the tangential velocity profile shows a more realistic shape for all vortex models mentioned before. In this section, the tangential velocity profiles of the idealized vortex are compared. Figure 6.3 shows a comparison of the normalized V_θ of the modified RV, BRV, SV, and modified SV model. The modified RV model has an advantage over others where the shape of the profile can be varied with decay exponent (phi) but has a discontinuity at $\bar{r} = 1$ whereas the other models show a smoother curve. The V_θ profile of the BRV model and the RV model with $\varphi = 0.5$ has a wider profile than the rest, meaning that the wind speed at the same radius is higher and could cause wider damage. The V_θ profile of SV and modified SV model resembles the profile of a two-cell vortex structure (Figure 6.1(c)) where the velocity becomes zero or close to zero near $\bar{r} = 0$ because the outward radial velocity of the downdraft pushes the tangential velocity further away from the center. The modified SV model has a very flat region within the core with a very sharp gradient of velocity change.

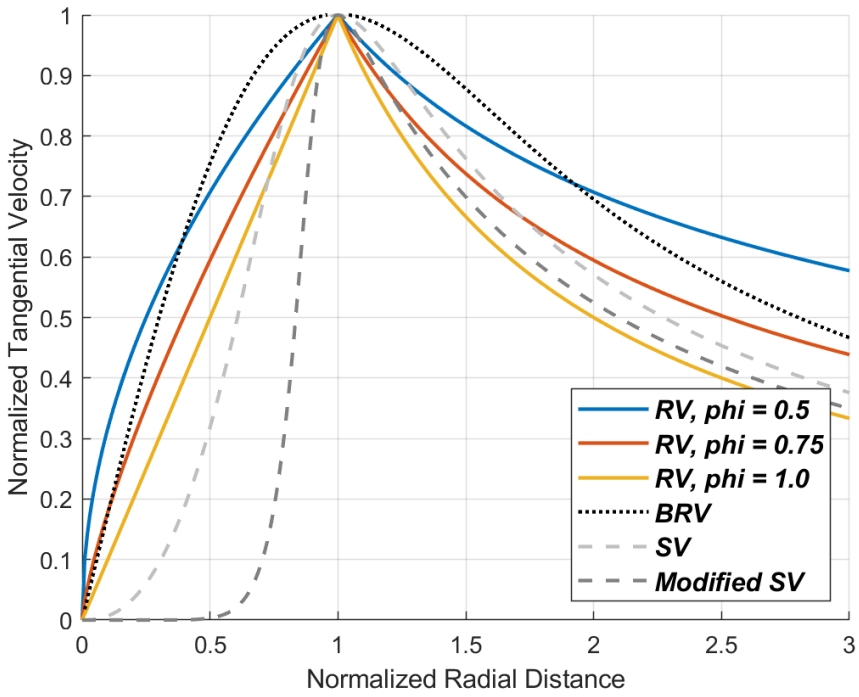

Figure 6.3. Comparison of the tangential velocity profiles of different idealized vortex models.

With three different shape parameters (α, β, and γ), the BV model can produce a variety of different V_θ profiles. Figure 6.4 shows the normalized V_θ of the BV model at $\bar{z} = 1$ with different α and γ parameters. A swirl ratio (S) and β parameter of one is assumed, although the β value does not affect the result because $\bar{z} = 1$. As suggested before, a γ value of at least two is used. The effect of α and γ parameter on the shape of the V_θ profile is shown in Figure 6.4(a). A V_θ profile of a one-cell vortex is produced with a γ value of two, and the V_θ profile starts to resemble the profile of a two-cell vortex as γ increases. The α parameter affects the rate of velocity change; the velocity increases inside the core and decreases outside the core more abruptly as α increases. The BV model holds a great versatility such that it can produce a V_θ profile very similar to other models as shown in Figure 6.4(b) where the BV model is fitted to the BRV, SV, and modified SV model.

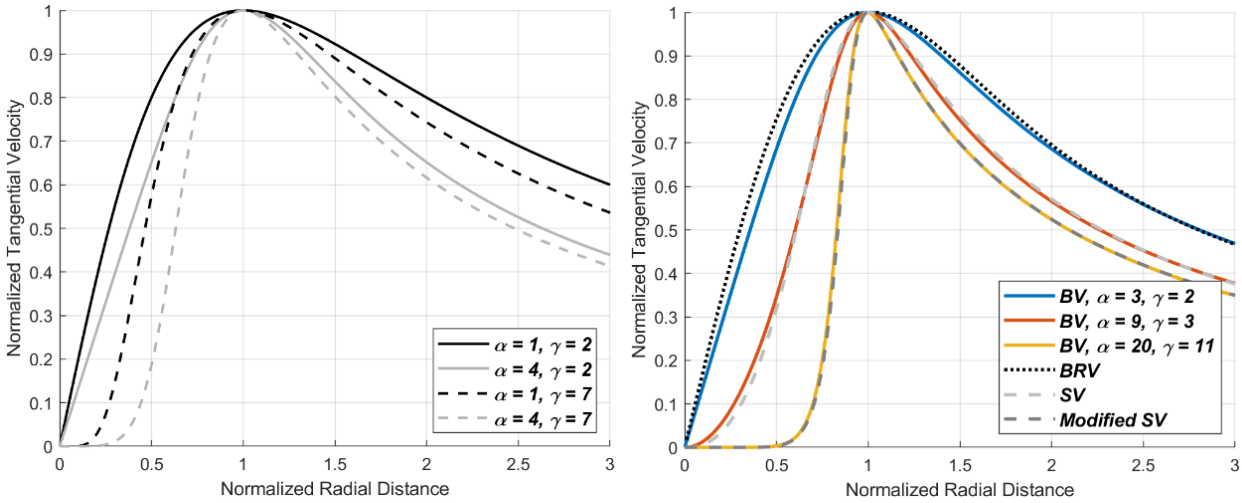

a) BV model with different shape parameters b) BV model fitted to other models

Figure 6.4. Different shapes of tangential velocity profile of BV model and comparison to other vortex models.

6.3 Vortex Model Radar Comparison and Tree-fall Patterns

6.3.1 Full-scale Radar Comparison

While Gillmeier et al. (2018) provides a great review of idealized vortex models, a full-scale validation is necessary to examine the sustainability of the model. Full-scale 3-D wind field measurements of multiple tornadoes were collected using DOWs (Doppler on Wheels) and compiled in Refan et al. (2017), which can be used to verify or calibrate the idealized vortex models. A total of 9 volumes (volumetric samples from radar) of azimuthally averaged wind field are compiled from five different tornadoes: two volumes from Spencer, SD 1998 (F4), one from Stockton, KS 2005 (F1), one from Clairemont, TX 2005 (F0), two from Happy, TX 2007 (EF0), and three from the Goshen County, WY 2009 (EF2) tornado. Since most engineers are interested in the near-surface wind field, the radar data is examined at the lowest elevation above ground level (40-50 m). The radar data below this elevation is unavailable because the wind field close to

the ground is difficult to obtain with radar instruments as mentioned in Chapter 1. Table 6.1 summarizes the nine volumes of the tornado wind field data set from Refan et al. (2017).

Table 6.1. Summary of the tornado radar data set.

Name of Tornado, Volume # (Abbreviation)	$V_{\theta,max}$[a] **(m/s)**	z_{min}[b] **(m)**	r_{max}[c] **(m)**	z_{max}[c] **(m)**	**Vortex Structure**
Clairemont, V1 (Clr v1)	36.3	40	96	200	Vortex breakdown
Happy, V1 (Hp v1)	39.0	50	160	50	Single-celled
Happy, V2 (Hp v2)	37.9	50	160	250	Touch-down
Goshen Co, V1 (GC v1)	42.2	47	150	47	Two-celled
Goshen Co, V2 (GC v2)	42.0	40	150	160	Vortex breakdown
Goshen Co, V3 (GC v3)	42.9	41	100	41	Two-celled
Spencer, V1 (Sp v1)	60.2	51	192	51	Two-celled
Spencer, V2 (Sp v2)	64.1	51	208	51	Two-celled
Stockton, V1 (Stc v1)	50.7	43	220	43	Single-celled

[a] $V_{\theta,max}$ is the maximum tangential velocity in the entire volume.
[b] z_{min} is the lowest height available.
[c] r_{max} and z_{max} are the radial distance and elevation at where $V_{\theta,max}$ occurs.

To examine the validity of the idealized vortex model, the radar measured wind speed of each component from Refan et al. (2017) are fitted and compared to the idealized vortex models: 1) modified RV model (RV), 2) BRV model, 3) SV model (SV_1), 4) modified SV model (SV_2), 5) BV model (BV_{rad}), and 6) modified BV model (BV_{tan}). Due to the effect of centrifuging of debris and hydrometeors at low-level, the Ground-Based Velocity Track Display (GBVTD) method, which is a method used to extract the 3D flow field of a tornado from Doppler radars (Lee et al., 1999), introduces a mathematical bias in the radial and vertical velocity (Nolan, 2013). As stated

in section 6.2.1.3, the BV model is formulated around the radial velocity and the tangential velocity and distance are normalized by the $V_{r,max,}$ and the radius at which the $V_{r,max}$ occurs. Because of the mathematical bias in the radial velocity, the fitted BV model produced significant errors in some cases. Thus, the BV models normalized by $V_{\theta,max,}$ and the radius at which the $V_{\theta,max}$ occurs (BV_{tan}) are also produced as suggested by Baker and Sterling (2018). In Baker and Sterling (2018), the BV model is modified such that velocity components are formulated around and normalized by the tangential velocity and the RMW at which the $V_{\theta,max}$ occurs. Since the RV, BRV, SV_1, and SV_2 models are not a function of $\bar{z}$, the velocities and radii are normalized by $V_{\theta,max}$ and RMW at the lowest height. Furthermore, only the tangential wind components of the vortex models are compared just as Refan et al. (2017) because the least-squares fit did not converge or performed very poorly for the radial and vertical components perhaps due to the bias in the wind speed estimate. To test the goodness of fit, the root-mean-square error (RMSE) is determined for each fit. The RMSE measures the differences between the observed value and the value predicted by the model (Eq. 6.17).

$$RMSE = \sqrt{\frac{\sum\left(V_{i,radar} - V_{i,fit}\right)^2}{N}} \tag{6.17}$$

where $V_{i,radar}$ is the wind speed value estimated by the radar at different radii, $V_{i,fit}$ is the wind speed value estimated by model fit at the corresponding radius, and N is the total number of radar observations at the lowest elevation. A lower RMSE value represents a better fit.

Figure 6.5 shows the tangential wind speed of the nine volumes at the lowest height and the vortex models fitted to the radar data, using a nonlinear least-squares fit method (Coleman and

Yi, 1994; Coleman and Yi, 1996). Table 6.2 summarizes the RMSE values between the tangential wind speeds of each radar sets to the fitted vortex models. Among the six vortex models, the BV_{tan} model produced the "best" fit (lowest RMSE) for all nine volumes of radar sets. Having multiple shape factors that allow different profile shapes may be the most appropriate way to handle engineering models and better for providing realistic azimuthally averaged wind fields. For the same reason, the BV_{rad} model also produced comparable fits in some cases as shown in Figure 6.5(a), (b), (d), (e), and (g). However, the least-squares fit was much worse in the other cases because the $V_{r,max}$ occurred at a much higher height and/or outer radius. For example, the (r_m, z_m) occurred at (960 m, 900 m) and (784 m, 280 m) for Hp v2 and Sp v2, respectively. This large error may have been caused by an error in the radial velocity due to the centrifuging effect. The fits of the RV and BRV models were better than the SV models but worse than the BV models. Comparing the two models, the RV model performed slightly "better": five of the RV fits had lower RMSE than the BRV model. The figures suggest that the RV model is more flexible in terms of the shape of the wind profile, but the BRV model fits better in terms of the continuity and curvature of the wind profile. Although the vortex structure of GC v1, GC v3, Sp v1, and Sp v2 displays a two-celled vortex structure, both SV_1 and SV_2 models show relatively poor fits for all nine volumes. However, one should note that the least-squares fit is estimated at least 40 m above ground level and the core size could be much broader at lower heights as shown in Figure 6.1(c), in which the SV models may produce a much better fit. Table 6.3 shows the estimated parameters for each idealized vortex model using the least-squares fit. Note that there are no parameters to be fitted for BRV and SV models.

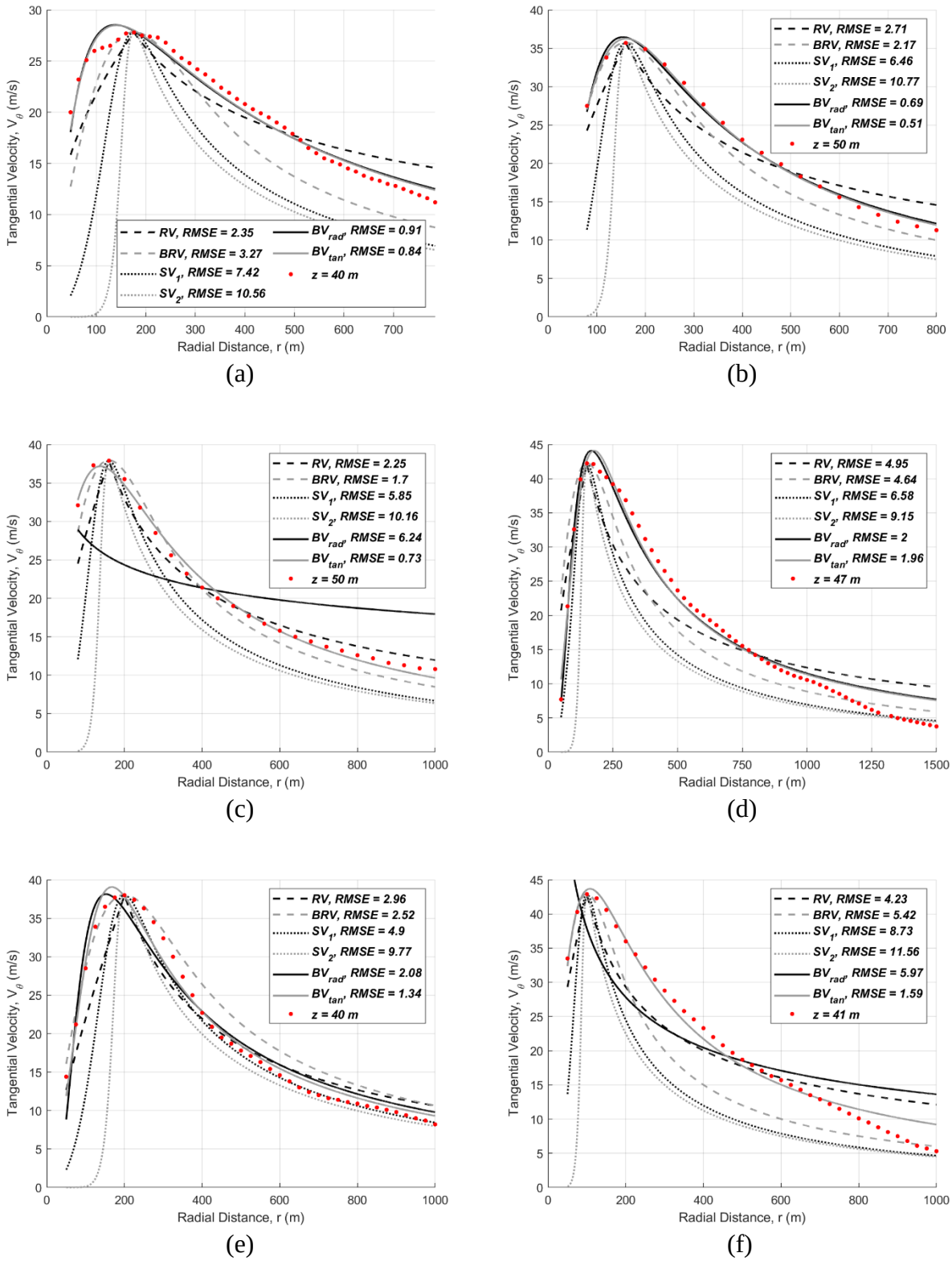

Figure 6.5. Tangential wind speed profile of radar data sets and fitted models: (a) Clr v1, (b) Hp v1, (c) Hp v2, (d) GC v1, (e) GC v2, (f) GC v3, (g) Sp v1, (h) Sp v2, and (i) Stc v1.

Figure 6.5. (continued)

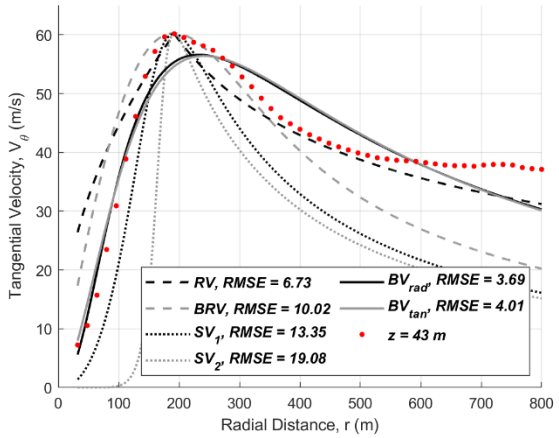

(g)

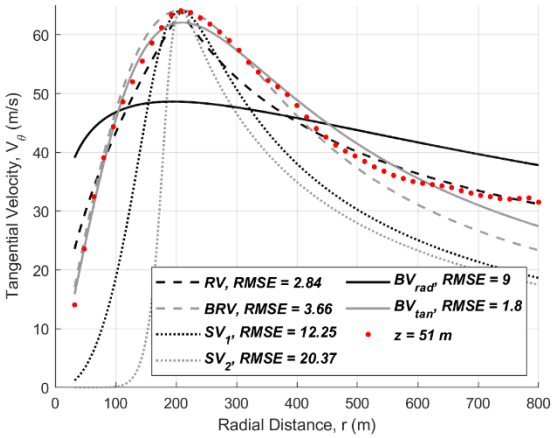

(h)

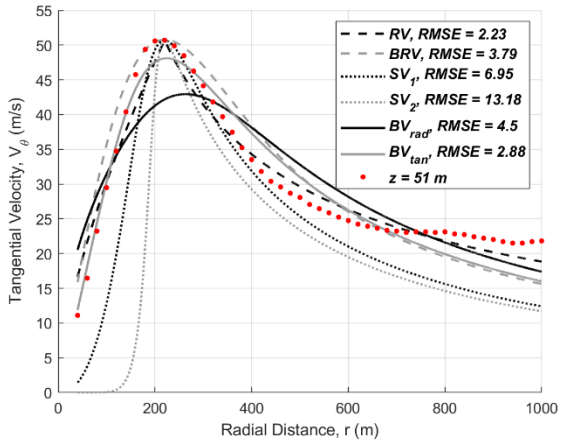

(i)

Table 6.2. RMSE between radar measured tangential wind speed and fitted vortex models.

	Clr v1	**Hp v1**	**Hp v2**	**GC v1**	**GC v2**	**GC v3**	**Sp v1**	**Sp v2**	**Stc v1**
RV	2.35	2.71	2.25	4.95	2.96	4.23	6.73	2.84	2.23
BRV	3.27	2.17	1.70	4.64	2.52	5.42	10.0	3.66	3.79
SV_1	7.42	6.46	5.85	6.58	4.90	8.73	13.4	12.3	6.95
SV_2	10.6	10.77	10.2	9.15	9.77	11.6	19.1	20.4	13.2
BV_{rad}	0.91	0.69	6.24	2.00	2.08	5.97	3.69	9.00	4.50
BV_{tan}	0.84	0.51	0.73	1.96	1.34	1.59	4.01	1.8	2.88

Table 6.3. Estimated idealized vortex model parameters using least-squares fit.

	RV	**BV_{rad}**				**BV_{tan}**			
	φ	K	γ	α	β	K	γ	α	β
Clr v1	0.43	0	3.27	0.07	-17.0	3.48	2.59	0.21	-1.31
Hp v1	0.56	18.4	2.73	1.19	3.00	3.04	2.01	1.73	-0.56
Hp v2	0.63	0.04	1.62	-1.00	-1.64	2.10	1.71	1.34	3.00
GC v1	0.65	0.12	4.53	1.47	-16.7	2.43	2.77	2.34	3.00
GC v2	0.79	42.8	5.39	1.08	3.00	3.10	2.49	2.62	-0.35
GC v3	0.55	1.33	1.11	-1.00	-2.03	3.24	2.16	0.97	3.00
Sp v1	0.46	26.2	3.23	0.67	3.00	3.64	2.56	0.95	3.00
Sp v2	0.53	2.47	1.24	0.01	-2.92	2.27	2.02	1.52	3.00
Stc v1	0.65	4.25	1.47	2.84	3.00	1.79	2.06	2.43	3.00

6.3.2 Tree-fall Patterns of Idealized Vortex Models

In Chapter 4, the modified RV model is used to produce tree-fall patterns and estimate the near-surface wind field. One great advantage of tree-fall analysis is that different vortex models other than the RV model can be also used to generate tree-fall patterns that may be more realistic. In this section, the tree-fall pattern produced from other idealized vortex models is presented and compared. In order to compare the tree-fall patterns of other idealized vortex models to the Rankin vortex model in Chapter 4, the same parameters and $V_{\theta,max}$ used in Figure 4.4 and Figure 4.5 are used to simulate the tornado wind field and tree-fall patterns: V_T = 13.4 m/s (30 mph), $V_{\theta,max}$ = 42.5 m/s (95 mph), RMW = 482 m (0.3 miles), V_c = 38 m/s (85 mph). Note that the tornado "dropped" is at x = -1.6 km (-1 mile) and traversed until the center reaches x = 1.6 km (1 mile) for all simulations. In addition, it is important to increase the kinematic viscosities by very large orders of magnitude to ensure reasonable magnitudes of radial velocity (Davies-Jones and Kessler, 1974; Refan et al., 2017). If a realistic value of kinematic viscosity of air (~10^{-5} m^2/s at 20 °C) is used, the radial velocity component of the BV and SV models becomes negligibly small. Figure 6.6 presents the tree-fall patterns generated using the BRV and SV model with a viscosity of 650 m^2/s, a much larger viscosity to generate a meaningful amount of radial flow. In Figure 6.6, a tree-fall pattern on the backside of the tornado is observed for both Figure 6.6(a) and 6.6(b). With no boundary conditions imposed in Eq. 6.2 and Eq. 6.7, the magnitude of V_r increases infinitely with r for BRV and SV model, generating infinite tree-falls beyond certain radial distance. Note that the V_r profile of the SV model becomes the same as that of the BRV model if the shape factor (b) is zero. Moreover, the tree-fall patterns display a swirling pattern only on the south side of the tornado because the translational speed is added on the south side and subtracted on the north side.

For both cases, the V_r near the tornado center is too small (even with unreasonably large viscosity) that the tree-fall pattern is unaffected by V_r and dominated by the V_θ.

Figure 6.6 exhibits unrealistic tree-fall patterns, suggesting that the radial velocity profiles of the BRV and SV models are inadequate to be used in the tree-fall analysis. Regardless of the uncharacteristic tree-fall pattern, a decrease in Damage Width (*DW*) between the tree-fall patterns of BRV and SV model because the decay rate of V_θ profile of the SV is much greater than that of BRV model (Figure 6.3). The tree-fall pattern of the modified SV model is not shown because the pattern shows very little difference from the tree-fall pattern of the SV model; the trees fall in the outer region as the V_c is assumed as 38 m/s (85 mph) despite the significant difference of the V_θ profile in the core region.

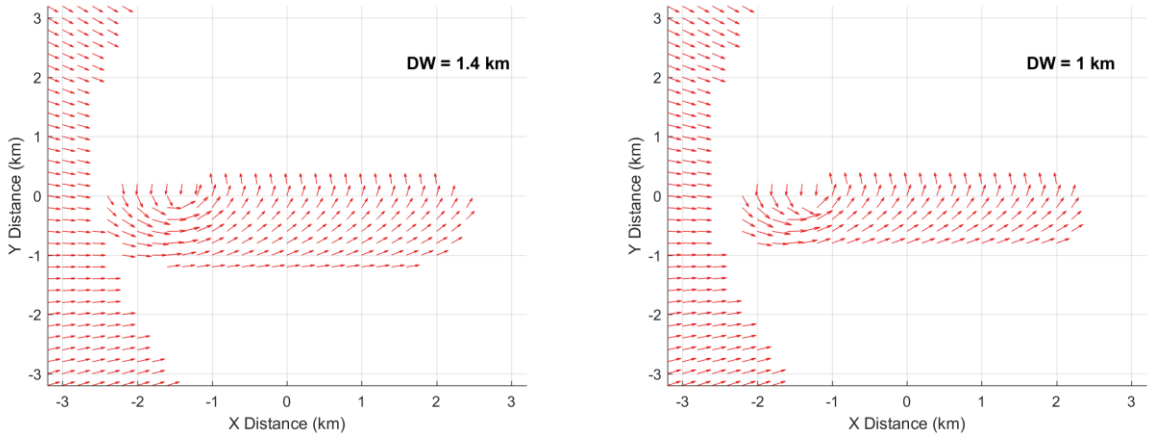

(a) BRV model (b) SV model, b = 1

Figure 6.6. Tree-fall patterns using (a) BRV model and (b) SV model.

The physically unrealistic boundary condition of the radial velocity of BRV and the SV models results in an unrealistic tree-fall pattern on the backside of the tornado, which would have caused damage in the entire domain if the tornado was simulated until further down in the *X*-

direction. Though it is possible to produce more realistic-looking tree-fall patterns, similar to the generic tree-fall pattern with α = 90° (Figure 4.7(e)), using the BRV and SV models if the near-surface tornado wind field is simulated with a very small *v*. However, it will result in a negligible amount of radial velocity whereas the tree-fall patterns observed in the field suggest that there is a significant radial inflow near the ground. An alternative way of producing realistic tree-fall patterns using the BRV and SV models is to use the tangential wind profile of the BRV and SV model for the radial wind profile, just as the modified RV model. Figure 6.7 shows the tree-fall patterns of RV, BRV, SV, and modified SV models assuming that the radial wind profile follows the tangential wind profile. The same input parameters of Figure 4.4 are used: V_T = 13.4 m/s (30 mph), G_{max} = 4.5, α = 45°, *RMW* = 482 m (0.3 miles), V_c = 38 m/s (85 mph), and φ = 0.55 (only for RV). Note that the tornado vortex is moving from left to right as indicated in blue arrow and the confluence line is indicated by the red line. The tree-fall patterns of BRV, SV, and modified SV model exhibit a similar overall pattern as the RV tree-fall pattern but *DW* and *DR* vary. The *DW* of SV and modified SV model is much smaller than that of RV and BRV model because of a narrower velocity profile (Figure 6.3). The wider the velocity profile is, the velocity that reaches the critical wind speed of tree-fall (V_c) extends further away from the tornado center, resulting in a wider *DW*. The *DR* of SV and modified SV model is much greater than that of the RV and BRV model. Despite the decrease in *DW* on both north and south sides of the confluence line, the *DR* is greatly affected by the decrease in the north side DW, resulting in a significant increase in *DR*. Although the *DW* and *DR* of the RV model differ greatly from other models in Figure 6.7, the modified RV model has a decay exponent (φ) that can be changed and produce similar outputs without changing the other parameters (e.g., V_T, G_{max}, *RMW*), demonstrating the advantage of a flexible model with shape factor (φ).

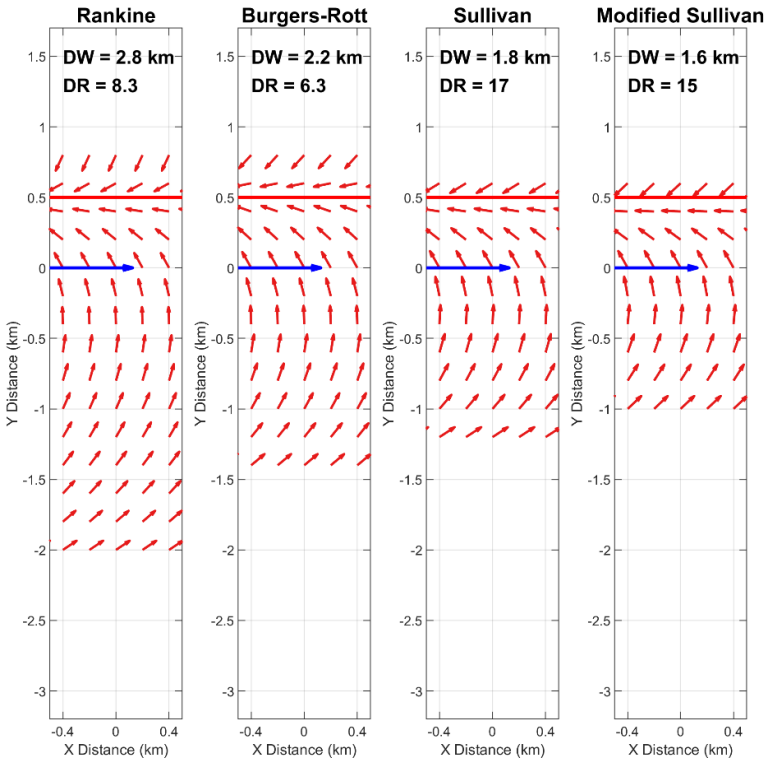

Figure 6.7. Comparison of tree-fall pattern of BRV, SV, and modified SV model to the RV model.

Figure 6.8 presents the tree-fall patterns generated using the BV model with different α and γ parameters, assuming $\bar{z} = 1$. To simplify the BV model, the radial component of the downdraft ($V_{r,d}$) was not considered. As the same boundary condition is assumed for the V_r profile of the BV model where $V_r = 0$ at $r = 0$ and $r = \infty$, the tree-fall patterns of the BV model show a more realistic and similar pattern to the tree-fall pattern in Figure 4.5 and no tree-falls was observed on the backside of the tornado. Multiple shape parameters of the BV model allow versatile wind profiles, which can produce more tree-fall patterns. As γ increases, the core size increases and the V_θ profile widens, increasing the *DW*. Note that Figure 6.4(a) is normalized by *RMW*, which occurs at different radii for different shape parameters. On the other hand, *DW* has a negative correlation with α and β. Although β has much less influence on *DW*; the *DW* decreases significantly as α increases but decreases only slightly as β increases. The *DR* relationship seems to be much more

complicated than the *DW*. As mentioned in Chapter 4, the input parameters interact with each other, complicating the output relationship. To understand the relationship between the outputs (*DW*, *DR*) and the input parameters of the BV model, detailed interaction analysis (see section 4.3.2) is necessary.

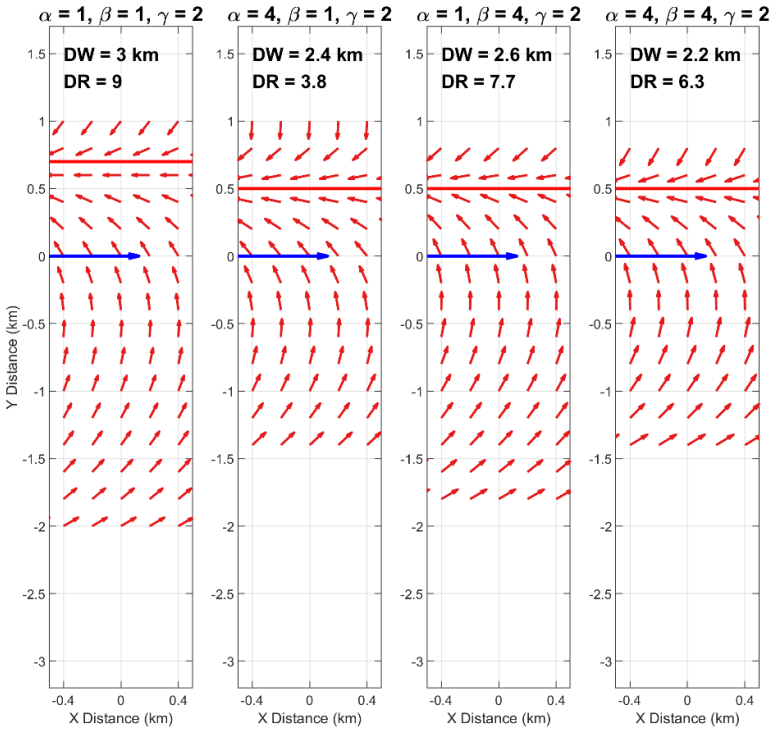

(a) $\gamma = 2$

Figure 6.8. Tree-fall patterns of BV model with different shape factors.

Figure 6.8. (continued)

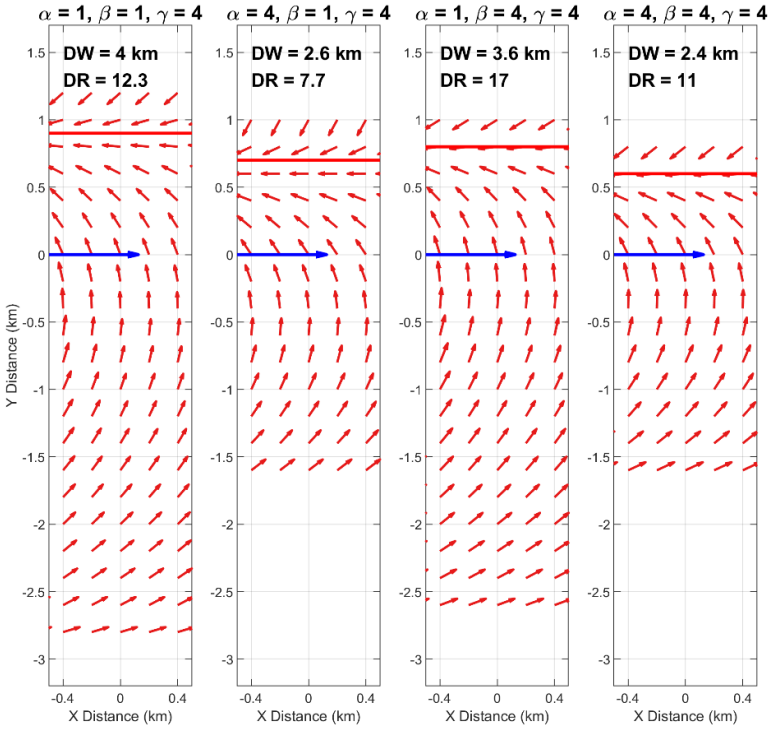

(b) $\gamma = 4$

6.4 Other Wind Field Models

6.4.1 Asymmetric Vortex Model

6.4.1.1 Asymmetric vortex wind field

In general, a stationary vortex model is assumed to be axisymmetric in tornado wind field modeling. However, studies have shown that some tornadoes exhibit a large asymmetry in the wind field even with the translation speed subtracted, possibly due to the additive effects of forward or rear flank downdraft (Doviak and Zrnić, 1993; Wurman and Gill, 2000) and surface interaction and instability (Refan et al., 2017; Refan and Hangan, 2018). The idealized vortex model can still be applied to such scenarios with some modifications to accommodate the external effects. One way to compensate to divide the idealized vortex model into quadrants and generate wind fields with different parameters at different quadrants. The divided quadrant parameters may

be able to generate a more realistic tree-fall pattern for some tornado cases. To illustrate the concept, an example of the divided wind fields using the RV model with different parameters is shown in Figure 6.9. Note that wind speed below 29 m/s (65 mph, EF 0) is not colored. The quadrant number is defined as follows: 1) Quadrant I (QI) is the northeast plane, 2) QII is the northwest plane, 3) QIII is the southwest plane, and 4) QIV is the northeast plane of the tornado center. The tornado wind field of Figure 6.9 is simulated with the same parameter used in Figure 4.3, except the φ is divided as $\varphi_{QI} = 0.6$, φ_{QII} and $\varphi_{QIV} = 0.55$, $\varphi_{QIII} = 0.5$. Such tornado may represent a possible scenario where the tornado is traversing over a region with different terrains on different sides of the tornado. However, further study is necessary to examine which parameter is affected by the external factor.

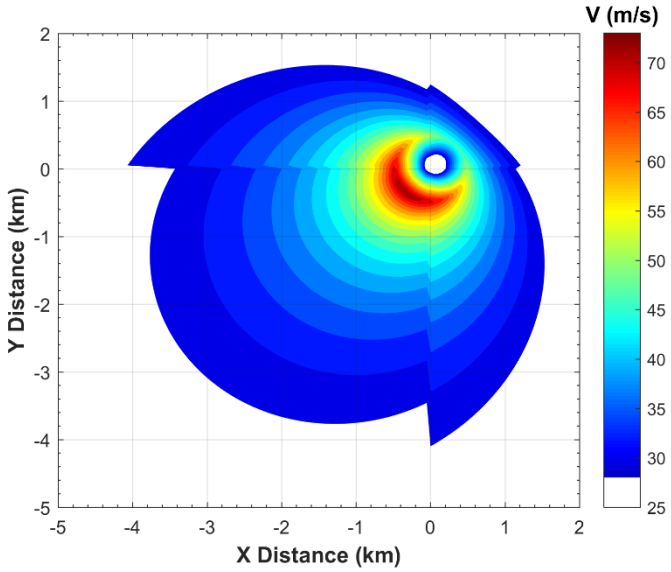

Figure 6.9. A translating tornado vortex with different RV parameters used in each quadrant.

In Chapter 2, convergent and divergent patterns of soybean are shown in Figure 2.7. It is speculated that these patterns possibly indicate the formation of multiple vortices. Moreover, many

studies have confirmed the existence of multiple vortices or small-scale vortices within a large vortex (Agee et al., 1975; Bluestein and Pazmany, 2000; Fujita, 1970; Pauley and Snow, 1988). Wurman (2002) was able to obtain radar images of a multi-vortex tornado using DOW and analyze them in more detail. Despite the existence of multi-vortex tornadoes, the wind field of a multi-vortex tornado remains elusive and no analytical model of a multi-vortex tornado has been developed as mentioned in section 6.2.1.3.

6.4.1.2 Asymmetric vortex tree-fall patterns

In this section, an example application and the tree-fall pattern of an asymmetric vortex model are presented. As mentioned in section 6.4.1.1, an asymmetric wind field is formed in some cases possibly because of the additive effect of rear flank downdraft (RFD) where the rear flank downdraft wraps around the backside of the tornado. This can be simulated using an asymmetric wind field and increasing the tangential wind speed on the southwest side (QIII) of the tornado. To replicate a RFD surge, an asymmetric tornado wind field is simulated in Figure 6.10 with V_T = 13.4 m/s (30 mph), G_{max} = 4.5, RMW = 482 m (0.3 miles), V_c = 38 m/s (85 mph), and varying α and φ. QIII is simulated with α_{QIII} = 45° and φ_{QIII} = 0.58, and the rest of the quadrants with α = 0° and φ = 0.6. On the south side of the simulated tree-fall pattern of Figure 6.10, tree-fall directions resulted from RFD surge pointing northwest (southwesterly wind) are observed. Only wind speed contour greater than 38 m/s (85 mph) is colored, and wind speed below the critical wind speed of tree-fall, V_c = 38 m/s (85 mph), is not colored. It is important to stress that the wind field division is a simple engineering fix, and strictly the discontinuity violates the NSE equations. Figure 6.11 shows a southeasterly wind direction on the very south side of the track from Alonsa, MB tornado, a possible RFD surge influenced tree-fall pattern, similar to the simulated pattern in Figure 6.10.

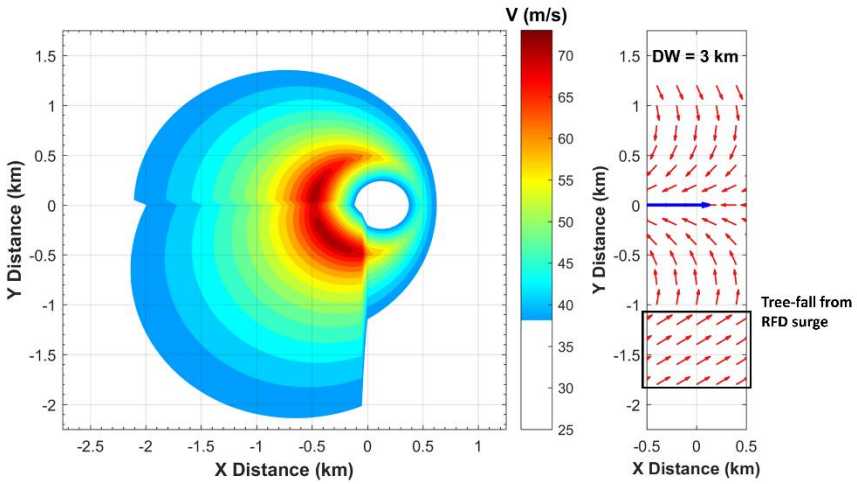

Figure 6.10. Asymmetric tornado wind field with RFD surge (α_{QIII} = 45°, φ_{QIII} = 0.58) and associated tree-fall pattern.

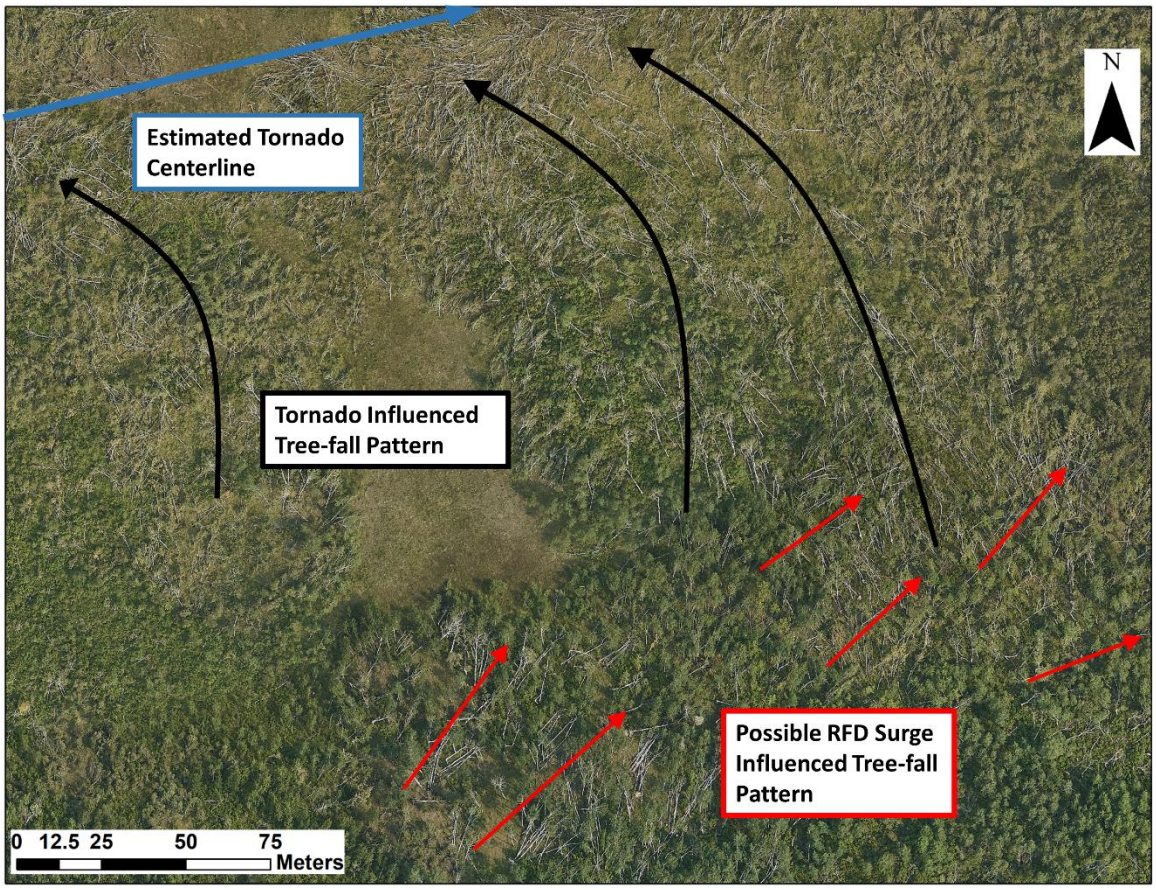

Figure 6.11. Possible RFD surge influenced tree-fall pattern from Alonsa, MB tornado. Blue arrow indicates the translation direction and estimated tornado center.

6.4.2 Other Windstorm Models

The tree-fall analysis can be applied to not only tornadoes but also to other windstorms with sufficient tree-fall as long as tree (or crop) damage is present. By substituting the tornado vortex model with other wind storm models, such as the downburst model (Holmes and Oliver, 2000) and the tropical cyclone model (Holland et al., 2010), the tree-fall pattern and near-surface wind field of other windstorms can be produced. With a sufficient number of damaged trees, the tree-fall analysis can be applied the same way, and the near-surface wind field of other windstorms can be estimated. Because hurricanes are simulated with vortex models, only downburst models will be addressed in this section.

6.4.2.1 Downburst wind field

A downburst is a strong ground-level wind system caused by a strong downdraft of air that burst outward radially on contact with the ground (Wilson and Wakimoto, 2001), often producing damaging winds. Fujita was first to discover and recognize the importance of a downburst event that another type of damaging other than tornadic or straight-line wind existed. Downburst event is highly divergent and associated with curved or straight winds (Fujita, 1981). As a result, many downburst events have been surveyed both on grounds and air, showing diverging damage patterns (Fujita, 1981; Fujita, 1989; Fujita, 1993), and also have been recorded on Doppler radar (Wilson and Wakimoto, 2001; Hjelmfelt, 1988). Later, Holmes and Oliver (2000) developed an empirical of a downburst calibrates with Hjelmfelt (1988) radar measurements. The radial profile of a downburst is also divided into two regions and can be expressed as:

$$V_r(r) = V_{r,max} \exp\left(-\frac{t}{T}\right)\left(\frac{r}{RMW}\right) \qquad \text{for } r \le RMW$$

$$V_r(r) = V_{r,max} \exp\left(-\frac{t}{T}\right) \exp\left(-\left(\frac{r - RWM}{R}\right)^2\right) \qquad \text{for } r \le RMW \qquad (6.18)$$

where t is the time variable, T is a time constant, and R is a radial length scale. The radar observations from Hjelmfelt (1988) suggest 50% of the RWM. The region of $r \le RMW$ is called the stagnation region where the radial velocity increases approximately linearly with r. In the outer region, the radial velocity decreases as shown in Figure 6.12.

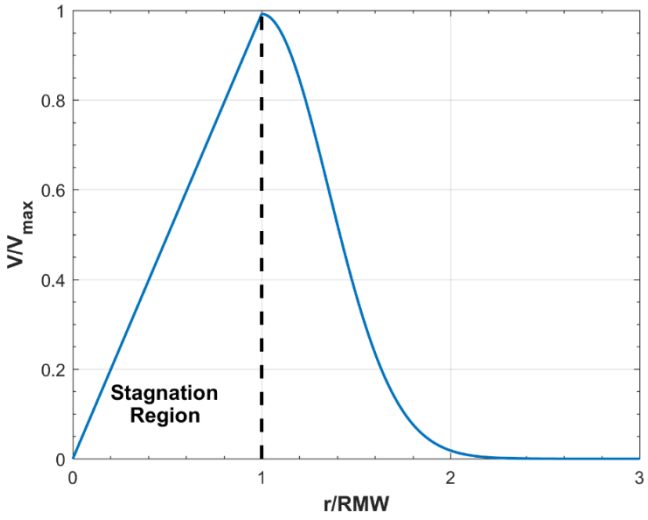

Figure 6.12. Radial wind speed profile of a downburst normalized by $V_{r,max}$ and RMW.

6.4.2.2 Downburst tree-fall patterns

Using the Holmes and Oliver model (HO model) presented in section 6.4.2.1, a downburst wind field and tree-fall pattern can be simulated. The velocity profile changes over time because of the time variable in the downburst model. Consequently, the downburst tree-fall pattern changes as the downburst traverses unlike the tree-fall pattern of a tornado even though constant parameters are assumed. Figure 6.13 shows the wind field of a translating downburst and the tree-fall patterns

generated with V_c = 38 m/s (85 mph). The downburst is simulated from -1.6 km (-1 mile) to 1.6 km (1 mile) with V_T = 13.4 m/s (30 mph), $G_{max,d}$ = 4.5, RMW = 482 m (0.3 miles), R = ½RMW, and T = 100 s where $G_{max,d}$ is defined as the ratio between the $V_{r,max}$ and the V_T. Because the damage width of the tree-fall pattern from a downburst is not consistent along the *x*-axis, the outputs must be defined differently from the tree-fall patterns of a tornado (Chapter 4). In Figure 6.13(b), outputs for a downburst are defined. DW_1 is defined as the greatest DW in the direction perpendicular to translation, DW_2 is defined as the DW in the direction of translation, and MD is the mean direction of tree-fall at DW_1. If the outputs of the observed tree-fall pattern of a downburst are determined, the output comparison method described in section 4.2.2.2 can be applied to estimate the parameters and the near-surface wind field of a real case downburst.

As shown in Figure 6.13(b), a tree-fall pattern diverging away from the center is observed. This diverging pattern is the primary feature of a downburst, which is commonly used to distinguish between a tornado and a downburst. Although a large-scale diverging pattern (not to be confused with a small-scale divergent pattern shown in Figure 2.7) can be produced from a tornado with $\alpha = 90°$ as illustrated in Figure 4.7(e), this pattern would require a tornado with a very small magnitude of radial component compared to the tangential component. Therefore, another difference between the tree-fall pattern of tornado and downburst is that the diverging pattern in tornadoes would have significant directional changes (or swirling pattern), whereas the diverging pattern in downbursts would have fewer directional changes (relatively straight-line wind) and be symmetric about the center. Yet, the tree-fall patterns from field observations show converging tree-fall patterns, suggesting that the radial component is significant. More observed tree-fall patterns from a tornado will be discussed in Chapter 7.

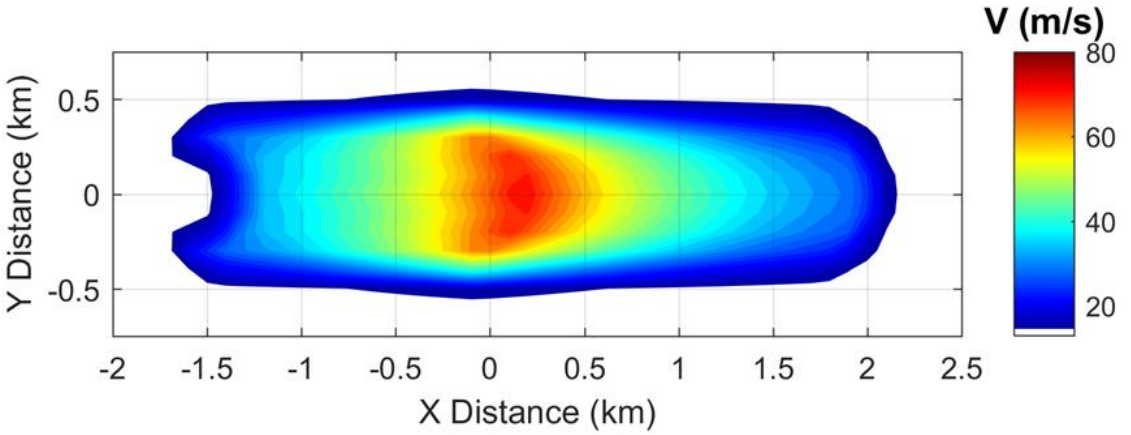

(a) wind field of a downburst

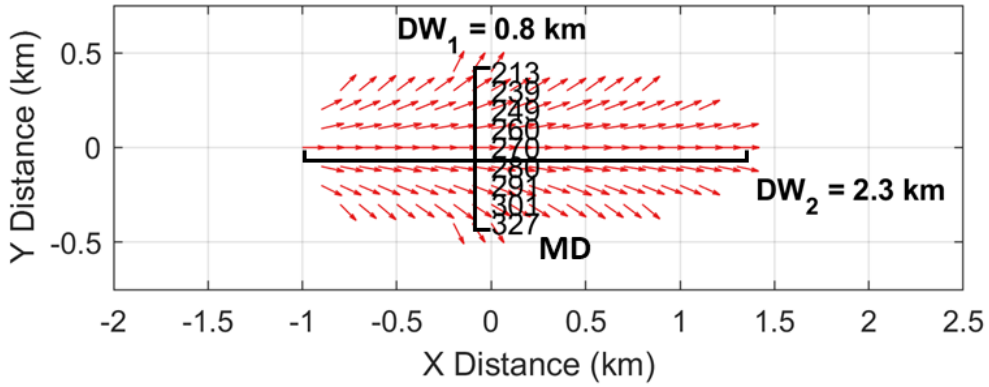

(b) tree-fall pattern of a downburst

Figure 6.13. Illustration of (a) a translating downburst wind field and (b) its associated tree-fall pattern.

6.5 Topographic Effects on Tornado Wind Field

Although most documented tornadoes occur in the Great Plains where the terrain is rather flat, a considerable number of tornadoes occur in mountainous regions in the southeast of the United States (Karstens, 2012). In fact, there have been many studies showing tornadoes occurring in mountainous regions with significant topography, which caused a large amount of tree damage (Bech et al., 2009; Beck and Dotzek, 2010; Cannon et al., 2016; Forbes 1998; Fujita, 1989; Karstens, 2012). In mountainous regions with complex terrain, the topography has a dramatic influence on the vortex structure and near-surface wind field of a tornado. The topography effect

is an especially complex phenomenon because the topography influences not only the dynamics of a tornado but also the localized wind flow. Because of the considerable change in the tornado dynamics and the local wind, the damage severity in regions of topography varies significantly more than on the flat surface. Despite the significant influence, not much is known regarding the effects of topography on tornadoes. In this section, how the topographic features of an idealized 3D hill affect the Rankine vortex parameters and the localized wind flow will be investigated in an attempt to incorporate the terrain effects in tree-fall analysis. The changes in RV parameters and the localized speed-up factors estimated using ESDU 91043 will be applied to a control simulation and generate tree-fall patterns. The tree-fall patterns will then be compared to the tree-fall pattern produced from the LES simulation.

6.5.1 Literature Review on Topographic Effects on Tornadoes

Nese and Forbes (1998)'s tornado risk model suggested that the ratio between the chance of a tornado striking a mountainous region and a non-mountainous region was much smaller than the ratio between the chance of an EF 2 tornado striking a mountainous region and a non-mountainous region. Based on the statistical evidence and over 40 damage surveys in mountainous regions, Forbes (1998) suggested that terrain mainly affects the structure of the tornado rather than the location of occurrence; the vortex diameter and the structure change as the tornado ascends and descends the hills. In Forbes (1998), four key points regarding the topographic effects on tornadoes are suggested based on field observations: 1) the damage swaths of tornadoes frequently contracts in width and intensify on downward slopes by vortex stretching, 2) a very intense swirl occurs at a spot on the downhill slope or at the base of the mountain, 3) the tornado intensity usually weakens on the uphill slope, and 4) often an intense tornado core re-emerges at the next

hilltop plateau. Cannon et al. (2016) investigated the change in the severity of forest damage caused by tornadoes in mountainous terrain and also showed evidence that tornado severity diminishes and strengthens as tornadoes travel upslope and downslope, respectively.

A few studies have been developed to understand the topographic effect using numerical and experimental simulation. Lewellen (2012)'s numerical study has become the foundational study of topographic effects on tornadoes. In his study, a large set of tornado-like vortices (over 250) were simulated using a high-resolution Large Eddy Simulation (LES) model over several different topographic features (e.g., ridges, valleys, hills) to investigate the changes in tornado path, structure, and intensity over different topographic conditions. His numerical simulations suggested that tornadoes are expected to weaken when ascending slopes and strengthen when descending slopes due to the topographic influence on corner flow swirl ratios, and also supported Forbes (1998)'s findings, particularly the tendency toward vortex reorganization on the uphill slope with an intense track appearing at the ridge top. In Nasir and Bitsuamlak (2018), a numerical tornado-vortex was traversed over 3D hills (steep and shallow hill) and the Fractional Speed-Up Ratio (FSUR), which is the ratio between the wind speed with and without the presence of the hill at a specific location, for each hill is calculated. The study shows a maximum FSUR as high as 2.5 for a steep hill. More recently, Satrio et al. (2020) conducted a more extensive numerical study using LES with a medium-swirl background vortex to investigate the effects of surface terrain in more detail. Their study found that the surface terrain resulted in an overall increase in 10-m horizontal winds and induced path deviations, vortex contraction/expansion, which were consistent with findings from Lewellen (2012). As the vortex crests the top of the hill, it acts to expand the near-surface vortex and contract as it descends. In Karstens (2012), an experimental tornado simulator was used to simulate a tornado-like vortex over an idealized 2D ridge and

escarpment. For both topographic models, a deviation of the vortex from the geometric centerline was observed by tracking the minimum surface pressure. Additionally, weakening of the vortex was observed near the crest of the two idealized models. On the other hand, an intensification occurred just before ascent and/or during and just after the descent. This finding was supported by the observations of tree-fall from the Little Sioux, IA Scout Ranch tornado over a 2-D ridge as shown in Figure 6.14. Figure 6.14 shows less severely damaged trees on the ridge crest line than those in the valleys on either side of the ridge. A clear gradient of tree damage along the tornado track also supports the finding of rapid vortex intensification while descending the ridge.

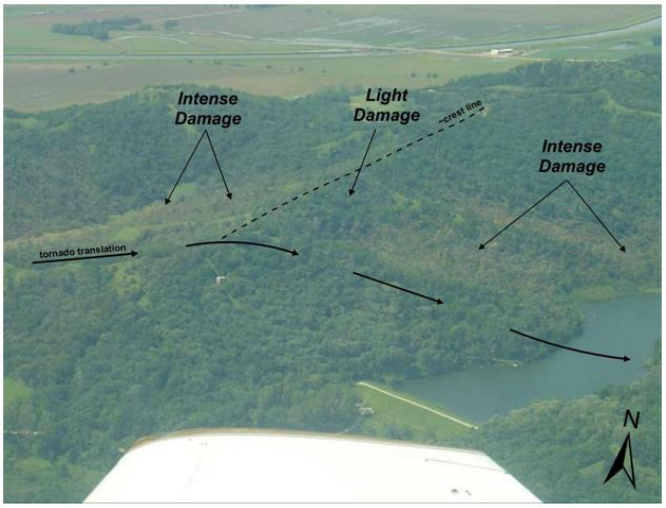

Figure 6.14. Oblique aerial image of the Little Sioux, IA Scout Ranch tornado over a 2-D ridge (Karstens, 2012)

6.5.2 ESDU Topographic Factor

As mentioned before, not only the vortex structure but the localized wind flow is also influenced by the topography. A general guideline on topographic effects on localized wind and the ABL topographic speed-up factor (K_L) can be found in ASCE 7-16. However, more detailed methods are presented for estimating the K_L for hills, embankments, escarpments, and valleys in

ESDU 91043: Mean wind speeds over hills and other topography, a manual developed by Engineering Science Data Unit (ESDU). The ESDU 91043 methods are derived from solving the NSE and calibrating against both full-scale and wind-tunnel measurements (ESDU, 1991). The methods can account for three-dimensional effects, wind inclination to the ridgeline, and effects of flow separation on steep topography. Moreover, irregular-shaped hills with bulges and depressions can be treated in this method.

In general, when the wind blows over a hill in an ABL condition, the wind decelerates near the foot of the hill before ascending and then accelerates as it moves over the hill. The magnitude of acceleration increases then decreases near the crest of the hill. The flow is again decelerated on the downwind side near the end of the hill, and then the wind eventually returns to the same conditions as for the undisturbed wind upstream of the hill. Figure 6.15 illustrates the general wind speed variation over a hill in a one-dimensional sense.

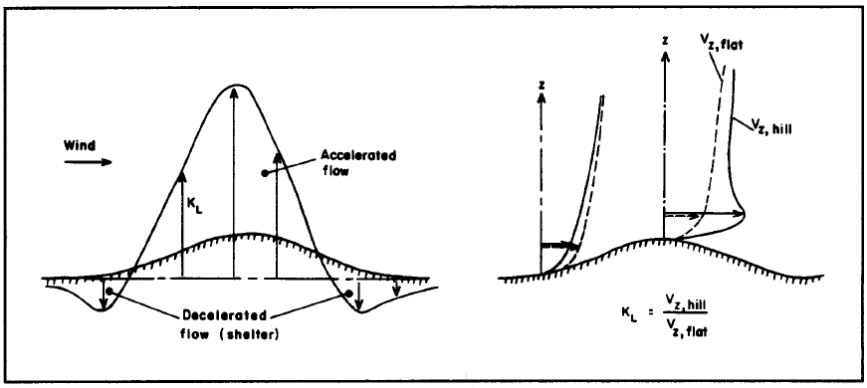

Figure 6.15. Illustration of wind speed variation near the ground over a hill (ESDU, 1991)

The ESDU 91043 uses the equivalent embankment method, which converts a hill into an "equivalent" embankment, and the K_L factor is defined as the following:

$$K_L = 1 + \Delta K_{L2d} f_{ar} + \Delta K_{L3d} \tag{6.19}$$

where ΔK_{L2d} is fractional K_L for two-dimensional topography, f_{ar} is the correction factor for effect on ΔK_{L2d} of three-dimensional topography, and ΔK_{L3d} is fractional K_L for three-dimensional topography. The three-dimensional effect is accounted as part of the flow over the central part of the hill is deflected around the sides, which requires a reduction in the speed-up factor over the central part of the hill span near the crest and an increase in the speed-up factor towards the sides. In section 6.5.3, the topographic factor on a tornado will be investigated by examining the LES simulations of a tornado over an idealized sinusoid 3D hill. The speed-up factor of the same 3D sinusoid hill (height of 50 m and length of 1000 m) used in the LES simulation is calculated in this section. Figure 6.16 shows the equivalent embankment of the 50-m hill and the one-dimensional K_L of the 50-m hill at 10 m Above Ground Level (AGL). The one-dimensional K_L profile in Figure 6.16(b) displays a similar pattern as the speed-up factor shown in Figure 6.15, where the flow decelerates on both sides near the base of the hill and accelerates as the wind ascends and descend the hill. Figure 6.17 shows the K_L of the 50-m hill in a two-dimensional plane along the X-direction. The detailed process of obtaining the K_L will not be discussed in this section as it is not the primary focus of this study, but it can be found in ESDU 91043.

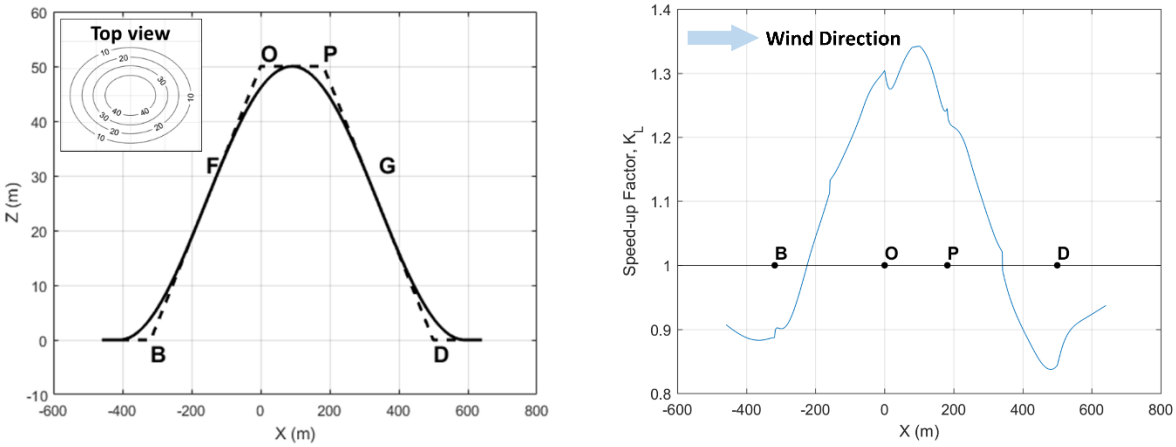

(a) equivalent embankment of 50-m hill (b) K_L of 50-m hill

Figure 6.16. Illustration of (a) equivalent embankment of 50-m hill and (b) one-dimensional K_L of the 50-m hill

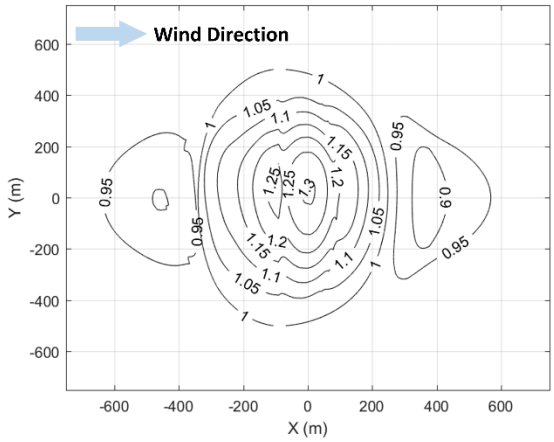

Figure 6.17. Two-dimensional K_L of the 50-m hill along the X-direction.

6.5.3 LES Simulation over Idealized Three-Dimensional Hill

One of the numerical simulations of Satrio et al. (2020) is used to examine the topographic effects on a tornado-like vortex over an idealized hill and incorporate topographic effects in the tree-fall analysis. Figure 6.18 shows the maximum 10 m AGL horizontal velocity of a tornado-like vortex with a translating speed of 10 m/s and the underlying topographic features (five

consecutive 3D sinusoid hills with a width of 1 km), where the black contour lines represent the elevation of the hills. The results show an increase in horizontal wind speed on the uphill and in the gap segment of 50-m hills and 100-m hills. In this section, the 50-m hill simulation is used to estimate the changes in RV parameters of the tornado-like vortex as the vortex translates over the hills, in which the changes in the RV parameters define the changes in the vortex structure (e.g., vortex compression, stretching). The tree-fall pattern generated using the RV model and using LES simulation is compared to evaluate the potential of applying tree-fall analysis over terrains. Note that the hills in the simulations are very idealized compared to the terrains in reality.

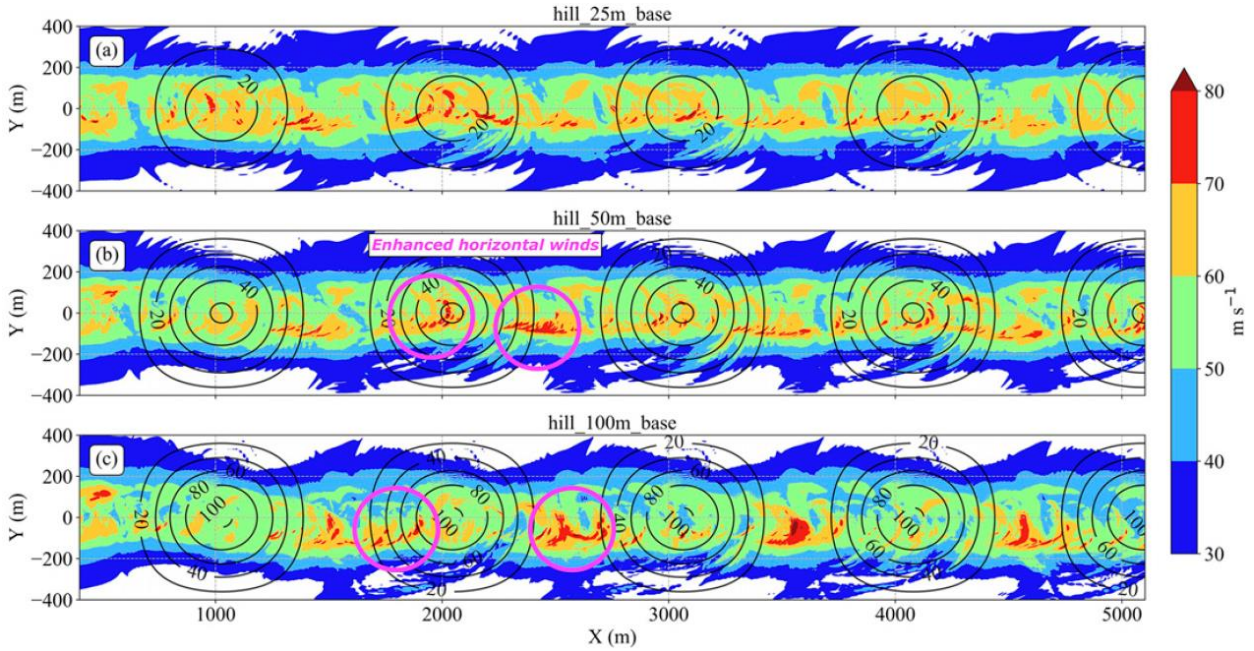

Figure 6.18. Maximum horizontal wind speed for (a) 25-m hill, (b) 50-m hill, and (c) 100-m hill (Satrio et al., 2020).

6.5.3.1 Change in tornado dynamics

Before examining the change in RV parameters of the LES simulation, the tornado center must be first estimated to accurately estimate the RV parameters. As observed in many other

studies (Karstens, 2012; Lewellen, 2012; Satrio et al., 2020), the path deviation of tornado center is a prevalent feature of a vortex as it traverses over terrain. The center of the vortex was estimated by tracking the location of minimum pressure (Karstens, 2012). However, in the case of the Satrio et al. (2020) simulation, the minimum surface pressure did not yield the vortex center due to the presence of sub-vortices pressure perturbation. Thus, instead, the geometric centroid of pressures below 15th percentile was used to estimate the vortex center. Figure 6.19 shows the estimated vortex center as the vortex traverses over 3D hills.

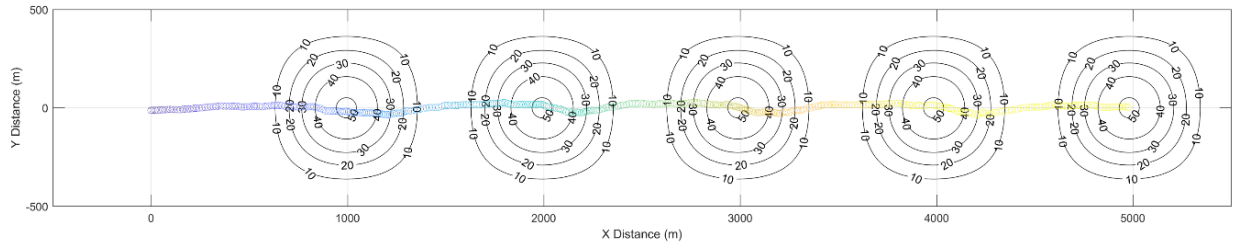

Figure 6.19. Estimated vortex center as the vortex traverses over idealized 3D hills.

Once the vortex center is estimated, the localized speed-up effect in the LES simulation must be removed in order to estimate the RV parameters. Thus, the wind field of the tornado-like vortex is first divided by the ESDU topographic speed-up factor, K_L, obtained from section 6.3.2. For each time step the vortex translates, each wind component (wind velocity in X and Y direction) of the 10 m AGL wind field at each grid point is divided by the corresponding directional K_L, in which the continuous K_L of five consecutive 50-m hills in (a) X-direction and (b) Y-direction is shown in Figure 6.20. Then, the RV parameters of each time step are estimated based on the azimuthal average of the horizontal wind speed. The V_{max} and RMW are estimated based on the maximum value of the azimuthally averaged horizontal wind speed and the radius at which the

V_{max} occurs. The decay exponent (φ) and α (angle between V_{rot} and V_{rad}) are estimated by curve-fitting the azimuthally averaged horizontal wind speed and averaging the angle between V_{rot} and V_{rad} of all grid points. Figure 6.21 illustrates an example estimation of φ and α of the tornado-like vortex at one time-step. Note that the K_L is wind is blowing in the same direction as indicated in 6.16 for each direction, and the K_L contour maps would be flipped horizontally and vertically for *X*-direction and *Y*-direction, respectively, if the wind blows from the opposite direction.

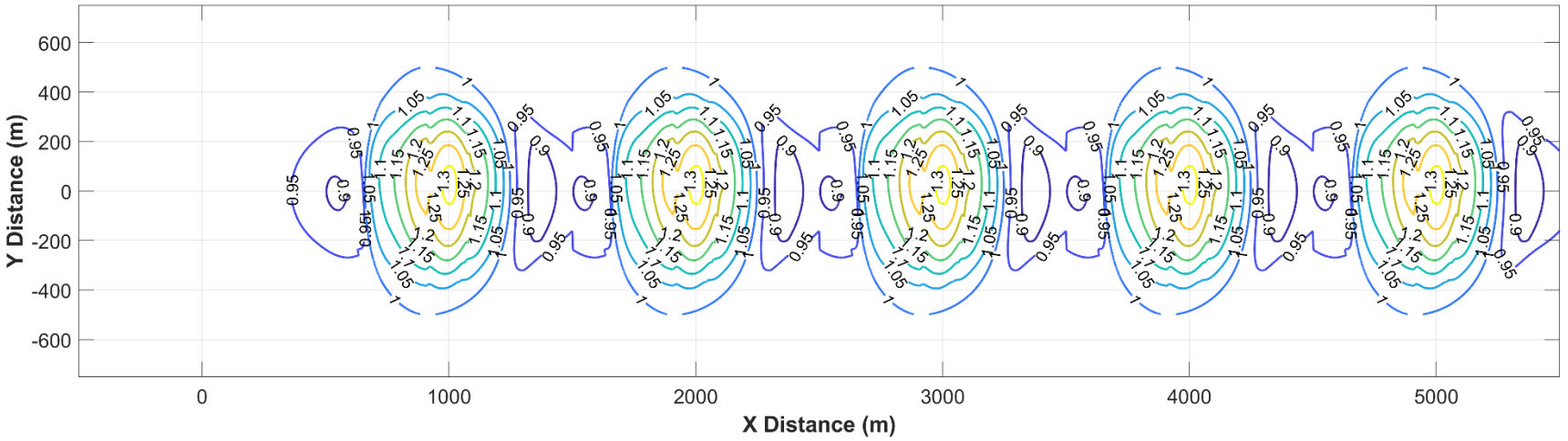

(a) *X*-direction

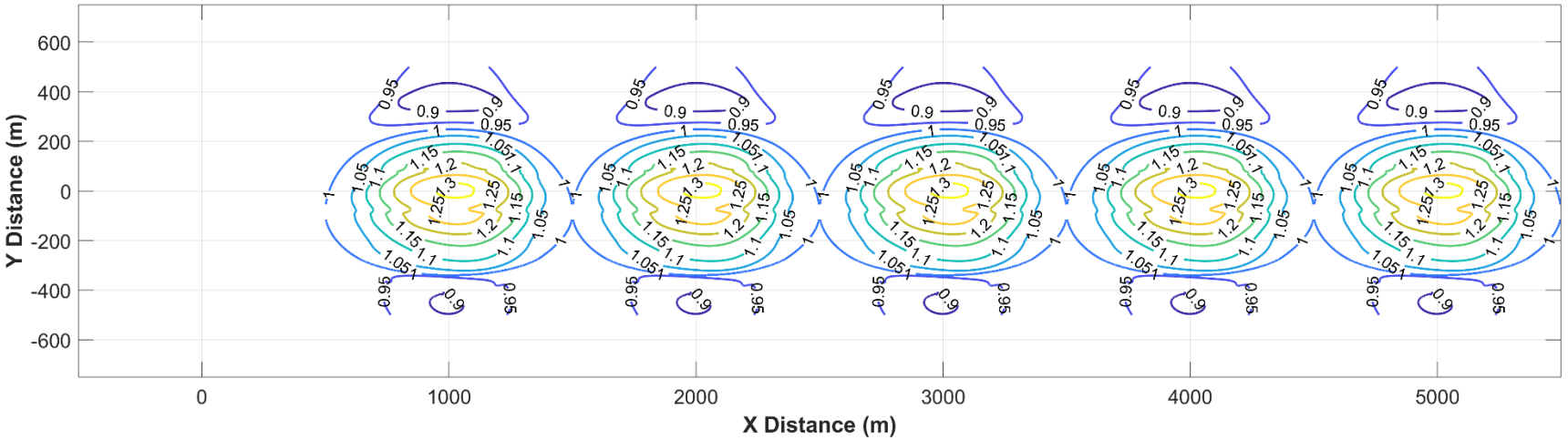

(b) *Y*-direction

Figure 6.20. Continuous K_L of five consecutive 50-m hills in (a) *X*-direction and (b) *Y*-direction.

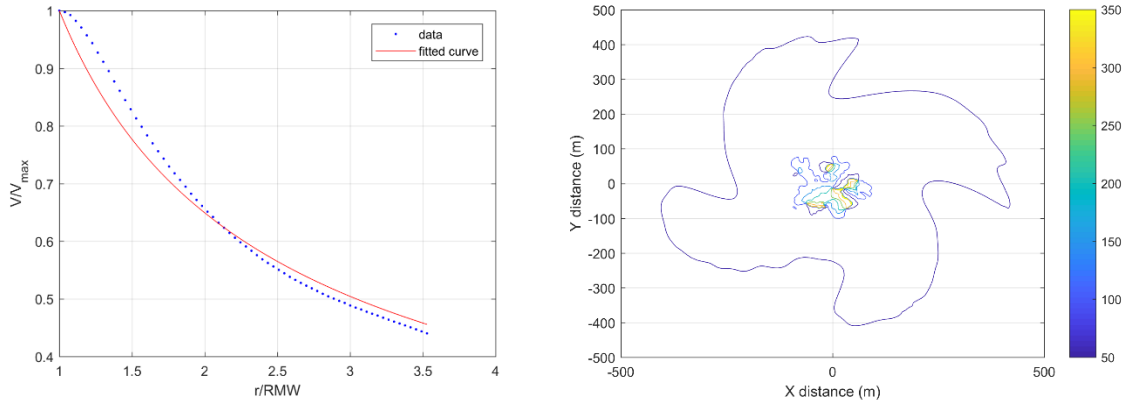

(a) horizontal wind speed fitted to RV model (b) estimated alpha contour

Figure 6.21. Illustration of (a) φ and (b) α estimation of LES simulated tornado-like vortex.

Figure 6.22 shows the estimated change in RV parameters of the LES simulation as the vortex translates over the 50-m hills, where the blue and green region indicate uphill and downhill regions, respectively, and the black dotted line indicates the crest of the hill. Dotted points are the individual estimated RV parameter at the estimated tornado center, and the smoothed curves are laid over. The change in RV parameters in Figure 6.22 suggests a change in the vortex structure. As the vortex climbs uphill, the vortex expansion can be observed by the increasing tendency of RMW and the decreasing tendency of φ. As a result of vortex expansion, the vortex weakens, indicated by the decreasing tendency of G_{max}, due to conservation of angular momentum. As the vortex moves downhill, the vortex is intensified with increasing G_{max} and contracts with decreasing RMW and increasing φ, narrowing the vortex. A more pronounced pattern is exhibited in the change of α where α is at the lowest (about 40°) when the vortex center is in the crest and reaches the highest (about 60°) when the vortex center is in the valley. This result is surprising because the valley flow would cause the more radial flow into the tornado, causing α to decrease. The possible source of error may have been caused from azimuthal average of α.

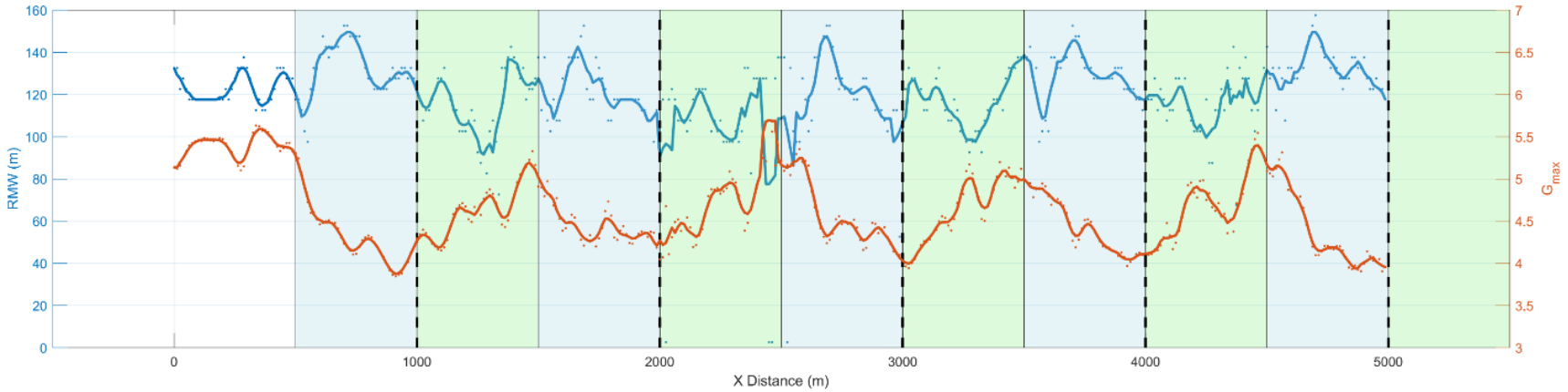

(a) G_{max} in red, *RMW* in blue

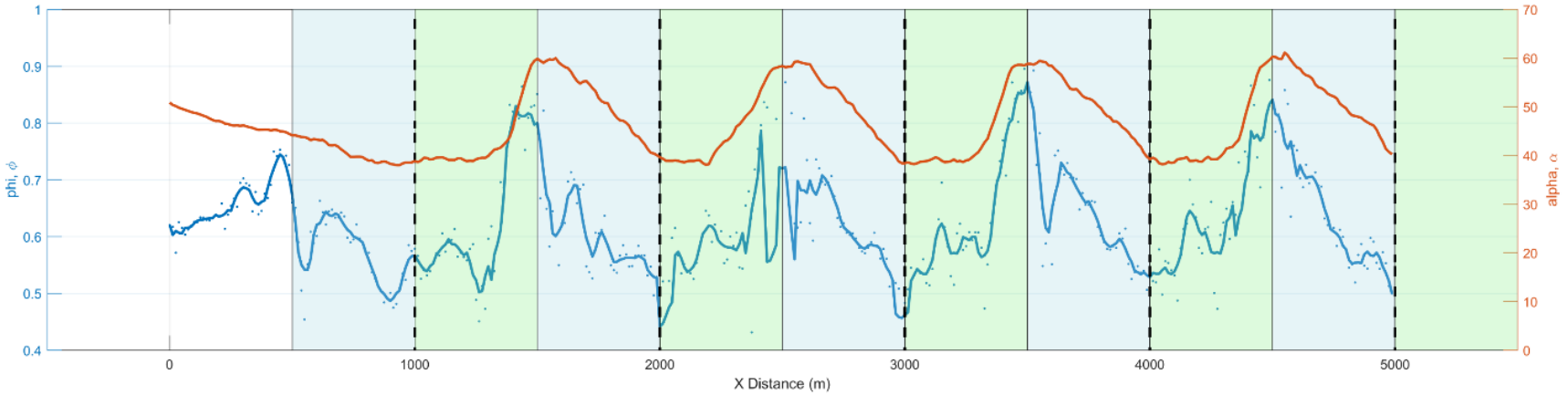

(b) α in red, φ in blue

Figure 6.22. Estimated RV parameters of the LES simulation translating over 50-m hills: (a) G_{max} and *RMW* and (b) α and φ.

6.5.3.2 Tree-fall pattern over idealized 3D hills

Using the RV parameters extracted from section 6.3.3.1 and the ESDU topographic speed-up factors, a near-surface (AGL 10 m) wind field of a tornado translating over consecutive 3D hills can now be simulated with an RV model, and the tree-fall pattern can be generated by setting a critical wind speed of tree-fall (V_c). Figure 6.23 displays (a) the tree-fall pattern from the LES simulation and (b) the tree-fall pattern using the RV model with V_c = 40 m/s. The two tree-fall patterns show moderately comparable agreement. Especially, when the vortex traverses over the first hill, a gradual decrease in the *DW* is observed on the uphill in both figures. Although the vortex is expanded, the *DW* (damage severity) is lessened because of the decrease in G_{max} (vortex weakening). Then, the *DW* starts to increase to near the crest of the hill. However, the *DW* decreases again for the RV simulation, whereas the *DW* continues to increase through the valley for the LES simulation. Other studies have shown that the most intense winds and severe damage tend to occur in between the hills or in the lowest valley (Cannon et al., 2016; Satrio et al., 2020), which is shown in Figure 6.23(a), but not in Figure 6.23(b). Another major discrepancy can be found in the location of the confluence line (*CL*) and thus in the *DR*. A south shift of *CL* and a reduction of *DR* are observed both uphill and in the valley for the LES simulation. However, they are only observed on the downhill side for the RV simulation. A possible reason for discrepancies between the two models is that the formation of sub-vortices in the valley, which are not represented in the RV model. LES simulations have shown formation of sub-vortices in the uphill due to relatively strong radial wind shears and in the valley due to vortex contraction (Satrio et al., 2020). Perhaps, the asymmetric RV model would have to be used in this case, avoiding azimuthal averaging. Due to the formation of sub-vortices, rapidly (but often temporally) increasing the horizontal wind, it is speculated that the *DW* is increased and the location of the *CL* and *DR* are

also largely affected, which is not captured in the tree-fall pattern of the RV model. As stated in section 6.5.1, the topographic effects on tornado is a very complex subject, and more study is necessary to accurately quantify the changes in the vortex structure and improve the localized speed-up factors. However, a moderately comparable tree-fall pattern between the LES simulation and the RV model has shown a great potential of incorporating topographic effects in the tree-fall analysis using the ESDU speed-up factor.

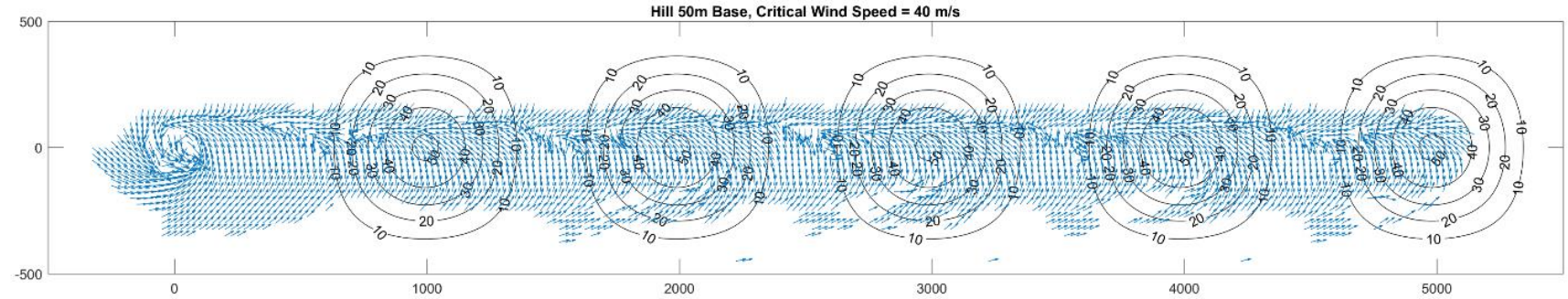

(a) LES simulation

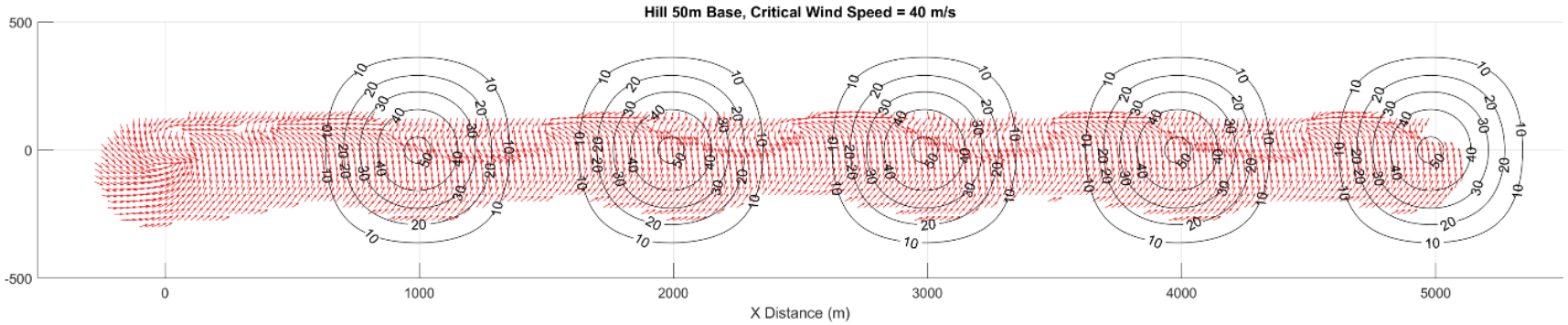

(b) RV model

Figure 6.23. Tree-fall pattern of (a) LES simulation and (b) RV model with V_c = 40 m/s.

6.6 Summary

In this chapter, different idealized vortex models that can be used in the tree-fall analysis are first reviewed and the tangential wind velocity profiles of the different vortex models are compared to the full-scale radar observations from Refan et al. (2017) to evaluate the goodness of fit of each model. The tree-fall patterns are also generated using different idealized vortex models and compared to the control tree-fall pattern (RV model). Topographic effects on tornado dynamics and localized wind flow and the application of topographic effects in tree-fall patterns are also investigated using ESDU speed-up factors and the LES simulation from Satrio et al. (2020). The following points are the important findings from this chapter:

- Due to multiple-shape factors, the wind profiles of the BV model best-fits the tangential velocity profile of the full-scale radar data although the tangential velocity should be normalized by the $V_{\theta,max}$ as suggested by Baker and Sterling (2018).
- The tangential velocity components of the SV and modified SV models did not match well with the full-scale radar data, even the two-celled structure vortex.
- The tree-fall pattern of the BRV and SV models produced unrealistic tree-fall patterns due to the unrealistic boundary condition, whereas the tree-fall pattern of the RV and BV models produced realistic tree-fall patterns. This implies that the boundary condition assumption of $V_r = 0$ at $r = 0$ and $r = \infty$ that Baker and Sterling (2017) imposes is valid at least near the ground where trees are present.
- The modified vortex model and other windstorm models can replicate tree-fall patterns caused by external factors, such as RFD surge and terrain effects, and other windstorms.

- The estimated RV parameters from the LES simulation over 3D sinusoid hills supported the findings of other numerical and experimental studies where the vortex expands in the uphill and contracts on the downhill.

CHAPTER 7: TREE-FALL ANALYSIS APPLICATION AND COMPARISON

7.1 Introduction

In this chapter, the tree-fall analysis is applied to estimate the near-surface wind field of five different tornado cases using the methodology described in previous chapters. The observed tree damage patterns acquired from Chapter 2 and Chapter 3 are compared to simulated tree-fall patterns using the methodology described in Chapter 4. The critical wind speed (V_c) values estimated from Chapter 5 are also used as input parameters of tree-fall analysis. Although other idealized vortex models are introduced in Chapter 6, the Rankine vortex (RV) model is used in this chapter because the number of variables in the Baker vortex model is too many, and the RV parameter has proven its effectiveness in Chapter 6. Not only tree damage is used to estimate the near-surface wind field, but tree-fall analysis is also applied to soybean and cornfields and compared to the EF scale rating rated by the NWS to examine the feasibility of tree-fall analysis on agricultural fields. In addition to tree-fall analysis, the Godfrey and Peterson (2017) method has been adopted and applied to the Naplate, IL tornado using both fallen and standing frees, and other methods are also used to estimate using damage indicators other than trees. Independent wind speed estimates of the Naplate, IL tornado using multiple methods are compiled and a comparison is made for cross-validation. Finally, empirical fragility curves of Joplin, MO and Naplate, IL tornado for residential buildings and trees are produced using the estimated near-surface wind field from the tree-fall analysis.

7.2 Near-surface Wind Field Estimation

7.2.1 Naplate, IL Tornado

7.2.1.1 Wind field estimation based on tree damage

The tree damage of the 28 February 2017 Naplate, IL tornado was collected during a ground-based damage survey (Chapter 2). Based on the tree-fall pattern from the damage survey, the tree-fall analysis (Chapter 4) was used to estimate the near-surface wind field of the Naplate, IL tornado, in which the damage survey map that shows fallen trees and standing trees is shown in Figure 2.6. Two different methods of utilizing tree damage are discussed in this section: 1) the tree-fall analysis method, and 2) the modified Godfrey and Peterson method. The two methods are different such that the tree-fall analysis uses the tree-fall direction of the fallen trees, whereas the modified Godfrey and Peterson method uses the proportion of fallen and standing trees.

For the tree-fall analysis, tree-fall directions and the tornado center must be identified as the tree-fall patterns are generated by simulating the near-surface wind field. The documented tree-fall directions and the estimated tornado center are shown in Figure 2.6. Refer to section 2.3.1.1 and section 2.3.1.2 for detailed tree damage survey and estimation of tornado center. From the tree-fall directions and the estimated tornado centerline, an approximate range of RV parameters (G_{max} and α) was first estimated. In Figure 2.6, a tree-fall pattern of the damaged trees (black arrow) that generally points toward the direction of the tornado translation (red arrow) can be observed. The tree damage pattern roughly resembles the tree-fall pattern in Figure. 4.7(a), and a low G_{max} (1.0-3.0) can be estimated based on this observation. Furthermore, the damage map shows an approximate confluence line slightly above the centerline and a *DW* on the northside approximately half of the *DW* on the southside, which translates to a *DR* of two. Based on Figure 4.7(b) and (c), it can be speculated that the α is less than 30° and greater than 0°. In the parameter

estimation process, a storm motion of 23 m/s (51 mph), estimated by the Storm Prediction Center (SPC, 2017), was used for the translational speed, and the *DW*, *DR*, and *MD* with an average bin of 100×100 m was used for the output comparison method. Through multiple iterations, the "best-matched" parameters that had the minimum E_{rms} (Eq. 4.7) were selected and the near-surface wind field with a maximum wind speed of 58 m/s (129 mph; EF-2) was recreated using the "best-matched" parameters as shown in contour in Figure 7.1. Note that the tree-fall analysis assumes wind speed at 10 m height with open terrain (Lombardo et al., 2015). The resulting "best-matched" parameters yielded less than a 4% difference in the *DW* and *DR*. The "best-matched" parameters estimated from the tree-fall analysis are listed in Table 7.1, and the normalized RV profile (grey line) using the estimated parameters is shown in Figure 7.5. For the Naplate, IL tree-fall analysis, the V_c was treated as a random variable and iterated until the minimum E_{rms} was reached. The minimum E_{rms} yielded a V_c of 34 m/s, which is very well compared to the mean V_c estimated using the HWIND model in section 5.2.5.1 of Chapter 5 (mean V_c of 35 m/s). The comparable result between two independent methods provides some level of validity for both methods.

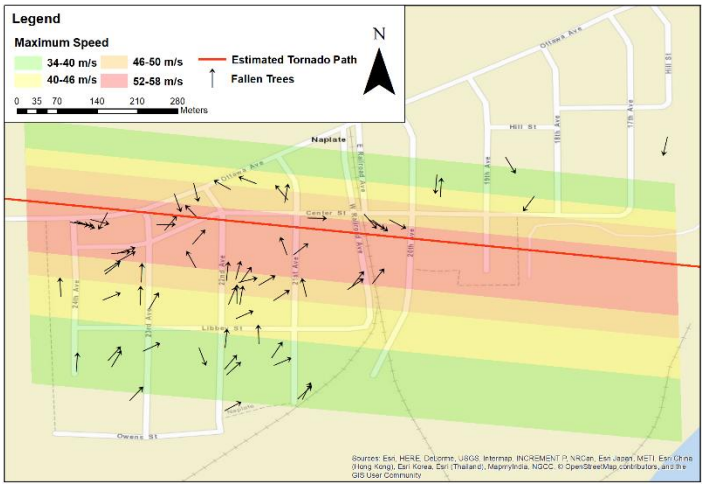

Figure 7.1. Tree-fall directions and near-surface wind field estimation of Naplate, IL using tree-fall analysis.

Adopted and modified from Godfrey and Peterson (2017), the near-surface wind field of the Naplate, IL tornado was estimated also using a "modified" Godfrey-Peterson method. In Godfrey and Peterson (2017), the damage site is divided into smaller grid boxes and assigns EF scale rating for each grid box based on the percentage of fallen trees using the probability of failure functions generated by the Peltola and Kellomäki (1993) tree stability model. The study areas used by Godfrey and Peterson (2017) are heavily forested: Great Smoky Mountains National Park (GSMNP) and Chattahoochee National Park (CNP) where the trees were densely populated, and sufficient numbers of trees were present within 100 × 100 m (330 × 330 ft) grid boxes. On the other hand, the village of Naplate is a residential area with the trees loosely spaced with a much smaller total number of trees. Hence, the Godfrey-Peterson method was modified using strips (i.e., long, narrow rectangles) parallel to the tornado instead of centerline boxes, assuming that the characteristics of the tornado remained constant for a path length of approximately 850 m (red line in Figure 7.2). Applying the strip method, a minimum number of five trees within strips was used and resulted in a spacing of 50 m strips. In other words, the width of the strips had to be 50 m to ensure at least five trees were contained within each strip. Figure 7.2 displays the damage survey map, showing the locations of the fallen trees (red circle) and the standing trees (green circle), overlaid with corresponding EF rating for each strip. The maximum standing to fallen tree percentage for 50 m strips was 50 %, which yields a possible maximum wind speed of 53 m/s (116 mph; low-end EF 2) (Figure 7.2) based on the tree fragility of tree-failure function by Godfrey and Peterson (2017). The Godfrey and Peterson (2017) method adopted the Peltola and Kellomäki (1993) model, which assumes wind speed at 10 m height and a roughness length of 0.20 m corresponding to a suburban terrain by Holmes (2015). Note that the probability function was built

based on the trees in GSMNP and CNP forest, in which the species may be very different from the trees in Naplate.

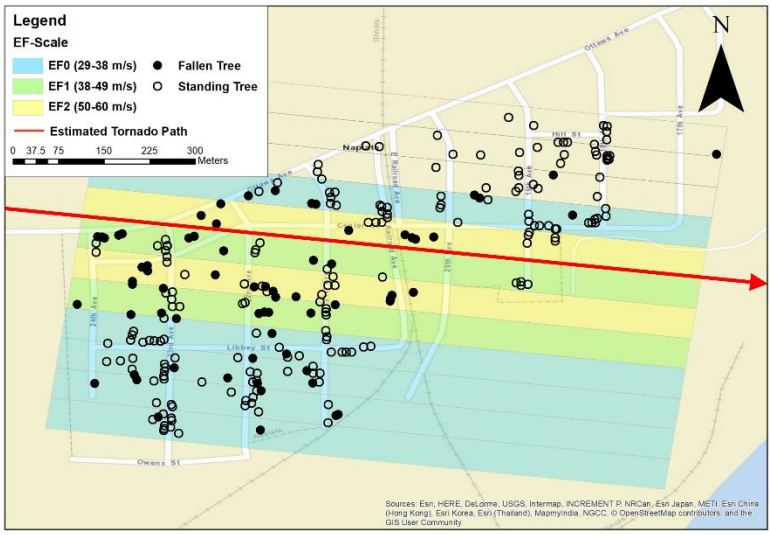

Figure 7.2. Documentation of fallen trees and standing trees and near-surface wind field estimation of Naplate, IL using the "modified" Godfrey-Peterson method.

7.2.1.2 Wind field estimation based on residential building damage

Among the 152 damaged DI 2 structures collected during the ground-based damage survey (Chapter 2), the two highest ratings were DOD 8 and DOD 7, and the maximum wind speed was estimated based on these two highest rating structures. Although the expected wind speed of DOD 8 and DOD 7 is 68 m/s (152 mph) and 59 m/s (132 mph), respectively (McDonald and Mehta, 2006), both structures had unreinforced masonry foundation walls (see Figure 2.4) and a lower wind speed was speculated than the expected wind speed. This example demonstrates and stresses the importance of careful and detailed field observation of construction quality and type during post-disaster damage surveys. Due to the poor construction quality of the structures, the lower bound wind speed was assigned to the two structures: 57 m/s (127 mph) for the DOD 8 rated

structure and 51 m/s (113 mph) for the DOD 7 rated structure. Assuming that the other DI 2 structures were in average condition, the expected wind speed of 55 m/s (122 mph) was assigned to all DOD 6 structures. Therefore, the maximum wind speed estimation based on the DI 2 structures was 57 m/s (127 mph) corresponding to an EF-2 rating tornado. It is important to note that the EF Scale method assumes "standardized" wind speed conditions (i.e., 10 m height, open terrain, 3-s gust) (Lombardo et al., 2015).

Estimating the tornado wind speed and the Rankine vortex parameters can be also done using a more detailed structural damage analysis. Notably, Roueche and Prevatt (2013) were also able to extract the parameters of an RV model using residential buildings (FR12). Instead of rating the tornado based on a single damaged structure, the Roueche and Prevatt (2013) method utilizes an aggregate of structures to estimate the tornado wind speed characteristics by grouping the damaged buildings into the corresponding EF Scale groups and fitting the parameters of the RV model to the EF-Scale-based wind speeds. For the Naplate tornado, the damaged residential buildings (DI 2) were grouped into DODs instead of the EF Scale to ensure more points to be fitted to the RV curve. Figure 7.3 depicts a box plot of the minimum (i.e., perpendicular) distance from the residential building to the tornado path (D) for each DOD group. The box plot assumes a normal distribution and shows the median (red center mark), the 25^{th} and 75^{th} percentiles (edges of the blue box), the most outer data points (whisker) inside of +/–2.7 standard deviations from the mean value, and outliers (red "+") that extends outside of +/–2.7 standard deviations. Because only one structure was rated for DOD 5, DOD 7, and DOD 8, the buildings rated DOD 5 through 8 were grouped into DOD 5-8. Then, the expected value of each DOD was fitted to the RV model with an RMW of 18 m estimated based on the mean value of the distance from the tornado path to DOD 5-8 damaged buildings. The translational speed of a tornado (V_T) is often hard to estimate.

Hence, the storm motion vector from radar observation is often used as a proxy for the translational speed of a tornado (Beck and Dotzek, 2010). The storm motion of the Naplate, IL tornado was estimated at 23 m/s (52 mph) by the Storm Prediction Center (SPC) (SPC, 2017) and was used as the tornado translational speed. An approximate V_T can also be estimated from the Tornado Vortex Signature (TVS) if the radar data is available (Karstens et al., 2013). Assuming the expected wind speed of DOD 5-8 (55 m/s or 122 mph) is the maximum wind speed (sum of maximum rotational wind speed and the translational speed), the maximum rotational wind speed would become 31 m/s (70 mph) and subtracting the V_T from the maximum wind speed, the maximum rotational wind speed (V_{max}) is estimated at 31 m/s (70 mph), which yields a G_{max} of 1.35. Then, the decay exponent (φ) was estimated by fitting the RV model to the points of the DOD group as shown in Figure 7.4. The estimated RV parameters from the residential buildings are shown in Table 7.1. Note that Figure 7.3 and Figure 7.4 are both shown in distance normalized by the estimated *RMW*.

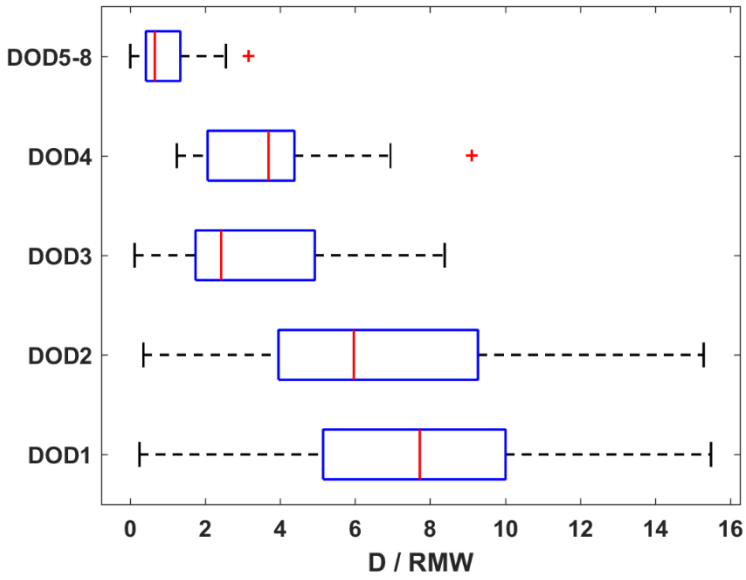

Figure 7.3. Boxplot of damaged residential buildings (DODs) for the Naplate, IL tornado.

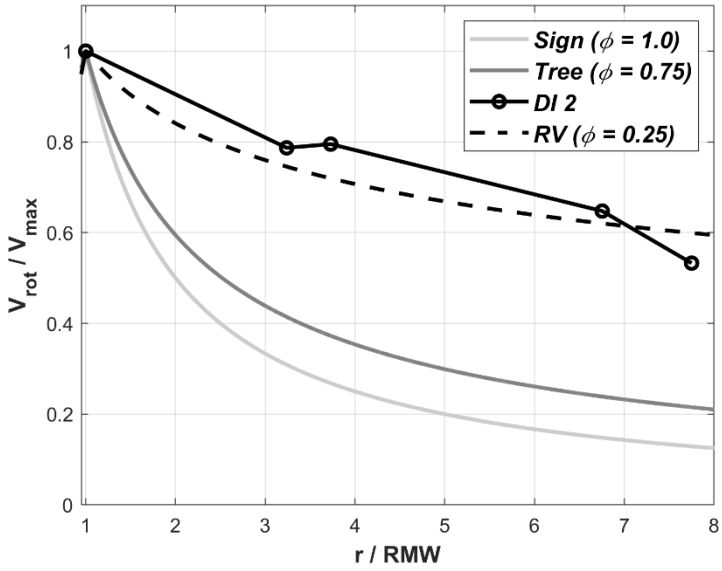

Figure 7.4. Decay exponent estimate of normalized RV model from residential buildings (DI 2), and comparison to other methods.

7.2.1.3 Wind field estimation based on sign damage

As mentioned in Chapter 5, the RV parameters and the near-surface wind field can also be estimated using the upper bound and lower bound critical wind speed traffic signs (V_c). Similar to how the wind speed indicators were used to calibrate and adjust the Holland wind field model (Holland, 1980) in Boughton et al. (2012), the critical wind speed velocity of failed and non-failed traffic signs were used to estimate the Rankine vortex parameters of the Naplate, IL tornado. Using the same iteration process of the tree-fall analysis, a series of tornadic wind fields with a translation speed of 23 m/s (52 mph) and different combinations of RV parameters, the failed traffic signs are simulated based on the critical wind speed obtained in Chapter 5. However, unlike the traditional tree-fall analysis, the wind direction must be considered in the V_c because the V_c of traffic signs is very sensitive to wind direction as opposed to trees and crops. Whether the wind is blowing normal to the flat-side of the sign plate or on the side, the wind load can vary significantly as the net drag coefficient ($C_{F,n}$) varies with wind direction (see section 5.4.3). Therefore, when simulating the

tornadic wind field, the $C_{F,n}$ becomes a function of direction and $C_{F,n}$ changes with the wind direction as the tornado traverses over: the net wind load (F_n) is zero when the angle between the sign plate and the wind direction is 0° (the wind direction and the sign plate is parallel) and, F_n is the greatest when the wind direction and sign plate are within +/- 45° perpendicular to each other. As the simulated tornado translates over time, the wind direction and the critical wind speed of each traffic sign are updated each time step; and if the wind speed at the location of the traffic sign exceeds the critical wind speed, the direction of the traffic sign fall is recorded. Then, the number of signs that failed, and the direction of the failed signs in the observation and simulation were compared and the error was calculated. Since the number of failed traffic signs is much smaller than the trees, the *DW* and *DR* are not a good measurement of simulation outputs. Thus, the error between the observation and the simulation is modified as follows:

$$E_N = \left(\frac{N_{obs} - N_{sim}}{N_{obs}}\right)^2 \tag{7.1}$$

$$E_\beta = \left(\frac{\sum\left(\cos\left(\beta_{j,obs}\right) - \cos\left(\beta_{j,sim}\right)\right)^2}{N_{obs}} + \frac{\sum\left(\sin\left(\beta_{j,obs}\right) - \sin\left(\beta_{j,sim}\right)\right)^2}{N_{obs}}\right) \tag{7.2}$$

$$E_{total} = \sqrt{E_N + E_\beta} \tag{7.3}$$

where N_{obs}, N_{sim}, β_{obs}, and β_{sim} indicate the number and the fall-direction of each failed sign in observation and simulation, respectively. E_N and E_β are the error in the number of failed signs and the error in the fall-direction between the observation and simulation, respectively. As the standard tree-fall analysis, the RV parameter combination that results in the minimum total error (E_{total}) is considered the best-match parameters, which are used to generate the near-surface wind field. The

maximum wind speed from the sign simulation was 58 m/s (130 mph). The wind speed was estimated at the centroid of the sign plate with an average height of 2.3 m and assuming suburban terrain. The critical wind speed is normally adjusted to the 10 m height and open terrain wind condition in Boughton et al. (2012). However, further adjustment was not carried out. The detailed estimated parameters are listed in Table 7.1, and the normalized RV profile using the estimated parameters is shown in Figure 7.4 and Figure 7.5 (light grey line).

7.2.1.4 Wind field estimation based on social media images

The social media images were also used to assess the damage of metal and low-rise buildings and estimate the near-surface wind speed of the Naplate, IL tornado. For the two metal LaSalle County service buildings (DI 21) that were given DOD 5 rating, an expected wind speed of 53 m/s (118 mph) was assigned and the expected wind speed of 45 m/s (101 mph) was assigned to the DOD 3 rated LaSalle County Nursing Home (DI 17). For the two Pilkington glass factory buildings (Figure 2.12), the expected wind speed is 46 m/s (103 mph) for the (upwind) structural steel industrial building (DI 23, DOD 4) and 64 m/s (143 mph) for the (downwind) metal building (DI 21, DOD 7). This estimated wind speed difference is surprising because (1) the two buildings are located only 30 m (100 ft) apart and (2) the upwind building with the lower wind speed estimate is more than double the size of the second building and located in a position which would likely shelter the second building from the maximum wind speeds (the translation direction). In addition, the condition and build quality of the downwind building is unknown while the upwind building was observed to be of very recent construction with no signs of corrosion. It seems most reasonable to estimate that the wind speed near this pair of buildings was of a magnitude that could explain both levels of damage, approximately 55 m/s (122 mph) — near the lower bound estimate of the

downwind DI 21 building and at the upper bound of the upwind structural steel building. As stated before, it is important to stress that structural damage is a function of many different factors. The difference in building height and internal pressure between the two buildings could have caused a large difference in wind speed estimation. However, the EF Scale method assumes wind speed at 10 m height and open terrain as mentioned before and does not account for these factors, which is one of the limitations of wind speed estimation based on structural damage. Moreover, an intense localized damage pattern may suggest debris impact, a multi-vortex tornado (Fujita, 1970), or changes in tornado characteristics due to the presence of obstacles (Satrio et al., 2020). The ongoing work of Satrio et al. (2020) discovered that the wind intensifies and forms a small vortex on the downwind side when a tornado-like vortex traverses over a large building, which may explain the large difference between the two Pilkington glass factory buildings.

7.2.1.5 Wind speed comparison between different methods

The estimated wind speed values from each method are compiled and compared in this section. Table 7.1 shows the RV parameters predicted from the residential buildings (DI 2) using Roueche and Prevatt (2013) method, the tree-fall analysis, and the traffic sign analysis; Figure 7.4 shows the normalized wind profile using the estimated RV parameter. Since the residential buildings cannot provide any wind directional information unless a debris analysis is performed, the α value cannot be determined. The G_{max} parameter resulted in the smallest difference because the three methods estimated a similar maximum wind speed value. However, the *RWM* and φ estimated from the residential buildings showed a large difference from the other two methods. The *RMW* estimated from the residential buildings was very low compared to the other methods. Since the distance from the tornado center (*D*) is normalized by the *RMW*, the *D*/*RMW*

consequently increases, causing the data points to spread out and the phi value to decrease significantly. It is believed that this may have resulted due to a small number of damaged structures and the narrow width of the storm compared to the size and spacing of the residential buildings. With a larger number of samples, the RV parameter estimation may have been more reasonable just as the Tuscaloosa, AL and Joplin, MO tornado in Roueche and Prevatt (2013). Alternatively, it may be erroneous to use and estimate the *RMW* by the minimum distance from the damaged structure to the tornado path in the Roueche-Prevatt method. Assuming a minimum distance to estimate the *RMW* implies that the maximum wind speed occurs perpendicularly south of the tornado center and equates to an alpha of 90°, which is significantly different from the alpha estimated by other methods. The estimated RV parameters for the tree-fall analysis and traffic sign analysis showed much better agreement with each other.

Table 7.1. "Best-matched" RV parameters of Naplate, IL tornado estimated from different methods.

RV Parameters	"Best-matched" value		
	Residential buildings	Tree-fall analysis	Traffic sign analysis
G_{max}	1.35	1.5	1.5
alpha (α)	-	27.5	16
RMW (m)	18	95	85
phi (φ)	0.25	0.75	1.0

The maximum wind speed estimated from each method is 57 m/s (127 mph), 58 m/s (129 mph), 52 m/s (116 mph), 58 m/s (130 mph), and 55 m/s (122 mph) for residential buildings, tree-

fall analysis, Godfrey-Peterson, traffic sign analysis, and the social media images (DI 17, DI 21, DI 23), respectively. The maximum wind speed estimated from all methods corresponds to the EF 2 category and shows good agreement. The estimated wind speeds with the corresponding method are summarized in Table 7.2. One should note that the wind speed estimation from sign analysis is made at the height of the centroid of sign plates (average of 2.3 m), much lower than the height estimated for all other methods (10 m). Assuming an Atmospheric Boundary Layer (ABL), the wind speed at 10 m would be much. However, the vertical wind profile of a tornado is not well understood and thus the wind speed at 10 m should not be hastily assumed. Furthermore, the maximum lower and upper bound of wind speed estimated from the traffic signs was 47 m/s (106 mph) and 64 m/s (142 mph) (see section 5.4.3). The maximum wind speed estimated from all other methods falls well within the bounds of wind speed estimated from traffic signs. Figure 7.5 shows the estimated wind speed profile using four different methods: DI 2 (square), tree-fall analysis (grey line), Godfrey-Peterson (rectangle), and traffics sign analysis (light grey line). All four wind speed profiles show a good agreement with an apparent pattern where the wind speed in the south side extends further out with a stronger wind speed than the north side of the tornado due to the additive effect of wind speeds ($V_{rot} + V_T$) on the south side and subtraction of wind speeds ($V_{rot} - V_T$) on the north side of the tornado. Specifically, alpha (α) values of 27.5 and 16 degrees were estimated from the tree-fall analysis and traffic sign analysis, respectively. A noticeable difference between the estimation from the residential buildings (DI 2) and the others is that the DI 2 wind speed profile is much narrower than the rest. The difference may have been caused by treating the signs and trees as point objects whereas buildings have a much greater areal extent. Perhaps, the difference emerged from the wide variation in the distance from the tornado especially for the lower DODs (Figure 7.3), which may be due to the complex factors affecting the damage state of

the structures, such as the subjective judgment of EF Scale, construction quality, aerodynamic effects, roof shape, etc. (Doswell, 2003; Edwards et al., 2013). In fact, numerous cases have been observed in the fields where a difference in the structural damage state was great between adjacent buildings.

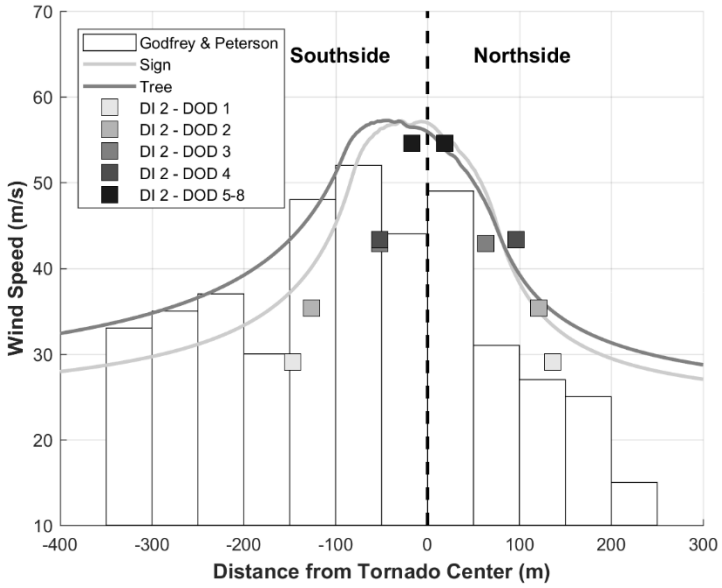

Figure 7.5. Comparison of the estimated wind speed profile of Naplate, IL tornado using different methods.

Table 7.2. Summary of maximum wind speed of Naplate, IL tornado estimated.

Damage Indicator	Method	Max. Wind Speed	Assumed Terrain Type	Height
DI 2	EF Scale	57 m/s (127 mph)	Open	10 m
DI 2	Roueche-Prevatt method	55 m/s (122 mph)	Open	10 m
Tree	Tree-fall analysis	58 m/s (129 mph)	Open	10 m
Tree	Godfrey-Peterson method	52 m/s (116 mph)	Suburban	10 m
Traffic Sign	Traffic sign analysis	58 m/s (130 mph)	Suburban	Avg. 2.3 m
DI 17, DI 21, DI 23	EF Scale (Social media)	55 m/s (122 mph)	Open	10 m

All five methods yielded a maximum wind speed lower than the peak wind speed of 69 m/s (155 mph) estimated by the National Weather Service (NWS) from the conventional damage survey (NWS, 2017). The peak wind speed of 69 m/s seems to be estimated based on the DOD 8 rating (total destruction of building) of metal building systems (DI 21), as opposed to DOD 7 rated by the WERL. This example demonstrates the difference in the subjective judgment of the EF scale method. The multiple wind speed estimates of the Naplate, IL tornado underscores the importance of a thorough comprehensive damage survey that documents different damage indicators and allows multiple independent estimates using different methods. The general agreement in the wind speed estimation using different approaches provides more confidence in the estimation and also supports the application of any subset of the methods depending on the circumstances and data availability

7.2.2 Sidney, IL Tornado Soybean Damage

On 9 September 2016 near Sidney, IL, an EF-2 rated tornado traversed over a large field of mature soybeans and corns (NWS, 2016), and intriguing crop damage patterns that resembled tree-fall patterns were noticed and a damage survey was conducted by the WERL. The soybean fall directions (red arrows) are shown in Figure 7.6, in which the detailed ground survey is addressed in section 2.3.1.3. An interesting discovery in this particular damage survey was the formation of convergent and divergent patterns of soybeans. More discussion on these patterns can be found in section 6.4.1.1. A tree-fall analysis was applied to the soybean field based on the soybean-fall direction collected during the ground-based survey. Low G_{max} (1.0-3.0) and α (0-20) were presumed initially as the larger scale soybean-fall pattern pointed toward the direction of the tornado translation and the damage on the south and north side of the confluence line was roughly

the same. The SPC recorded a storm motion of 15 m/s (34 mph) (SPC, 2016), which was used in the soybean-fall analysis. A random variable is assumed for the V_c of soybean because little is known about the V_c of soybean. If possible, the generalized crop lodging model can be used instead to calculate the soybean V_c (Baker et al., 2014). Only the *DW* and *DR* were used for output comparison, and the *MD* was not used due to the infeasibility of collecting a sufficient number of soybean fall directions in a ground-based survey. The tree-fall analysis on the Sidney, IL soybean field resulted in the "best-matched" parameters shown in Table 7.3. Figure 7.6 shows the simulated soybean-fall pattern (yellow arrow) and the resulting wind field (contour) with a maximum wind speed of 49 m/s (110 mph; EF 1), using the "best-matched" parameters. Considering the height of the soybeans (1.2 m on average) are much lower than the standard height for wind measurement (10 m), the maximum wind speed of the Sidney, IL tornado at 10 m may be greater than 49 m/s (110 mph).

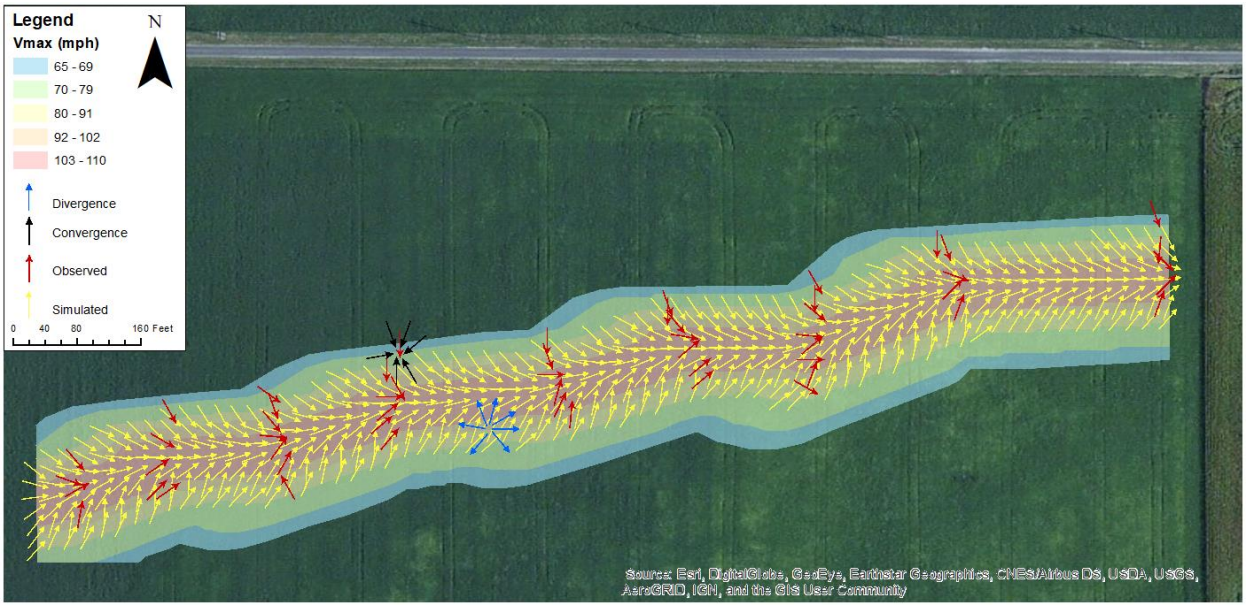

Figure 7.6. Observed soybean-fall pattern (red arrows) compared to simulated fall pattern (yellow arrows) and the near-surface wind field (contour) estimation of Sidney, IL tornado.

Table 7.3. “Best-matched” parameters of Sidney, IL tornado.

Parameters	“Best-matched” value
G_{max}	2.2
alpha (α)	5.0
RMW (m)	12.5
phi (φ)	0.65
V_c (m/s)	36

Because no structure was present in the vicinity, an EF 0 was rated in this particular location according to the NWS (NWS, 2016), whereas the maximum wind speed was estimated at 49 m/s (110 mph; EF 1) based on the crop-fall analysis. This supports the observation that EF-scale estimation is often underrated in agricultural areas and suggests that improvement of EF-scale or other means of wind speed estimation is essential. The patterns between the simulated and observed in Figure 7.6 show good agreement though the outputs (*DW* and *DR*) produced up to 40% difference for some transects. Possible discrepancies could have been inherited incorrect estimation of translation speed (V_T) and critical wind speed of soybean lodging (V_c). The mean storm motion predicted by the NWS was used as the translational speed in the simulation. However, possibly the averaged translational speed at the surveyed area was significantly different from the mean storm motion. Treating the translational speed as a random variable could be possibly improved the estimation (section 7.2.5.3). Moreover, the V_c of soybean is still unverified due to a lack of knowledge, in which the estimation from the tree-fall analysis could be unreliable. A V_c analysis of soybean should be considered using the generalized crop lodging model (Baker et al.,

2014). Despite the complexity, crop-fall analysis demonstrates a potential tornadic near-surface wind field estimation in agricultural areas.

7.2.3 Bondurant, IA Tornado Corn Damage

A tornado outbreak occurred on July 19, 2018, in central Iowa, in which one of the tornadoes (EF-2) touched down near Bondurant, IA, and damaged large fields of corn (NWS, 2018). Georeferenced orthomosaics were constructed using UAS based aerial 2D images collected following the event and the corn-fall directions were annotated (see section 2.3.3, Figure 2.13). Figure 7.7 presents the annotated corn-fall directions (yellow arrows) and the estimated tornado center (blue arrows), where the tornado center is estimated based on the most significant corn damage. The corn-fall pattern shown in Figure 7.13 resembles the generic tree-fall of Figure 4.7(a). The forward falling corn-fall pattern suggests a low G_{max} (1.0-3.0) and the confluence line being close to the estimated tornado center ($DR \approx 1$; Figure 7.8) suggests α close to zero.

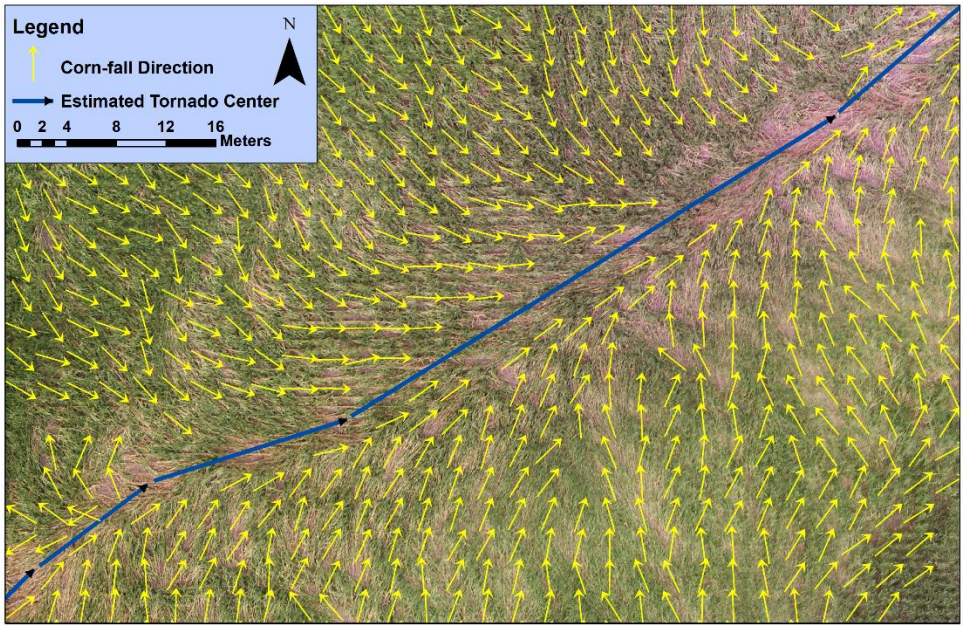

Figure 7.7. Observed corn-fall pattern and estimated tornado center of Bondurant, IA tornado.

Initially, a total of 12 transects were selected, and the corn-fall directions within the 12 transects were normalized based on the estimated tornado center. However, the corn-fall patterns showed fairly a consistent damage width and corn-fall directions throughout the track. With an average *DW* of 80 m, the difference between the minimum and maximum *DW* was less than 20 m. Thus, the corn-fall patterns of twelve transects were averaged into a single transect. Assuming that the tornado characteristic remained constant at the surveyed area, the averaged corn-fall direction in a single transect (shown in Figure 7.8(a) in blue arrows) was used to estimate the near-surface wind field of the Bondurant, IA tornado. The ground-based damage survey of the cornfield in Bondurant, IA showed that the growth stage of the corn was in between R4 and R6. Thus, a random variable between 12 m/s (lower bound) and 24 m/s (upper bound) of V_c was used as the input parameters, where 12 m/s (27 mph) is one standard deviation below the mean V_c of corn at R5-6 and 24 m/s (54 mph) is one standard deviation above the mean V_c of corn at R4-5 (see section 5.3.3, Figure 5.13). The mean storm motion of 13 m/s (29 mph) was used as a proxy of the translational speed of the tornado (SPC, 2018). Table 7.4 shows the result of the estimated "best-match" parameters of the Bondurant, IA tornado. The "best-match" parameters suggest that it was a very narrow tornado with very little rotation, or tangential velocity component, at least near the surface based on that *RMW* and α were estimated to be very small. Figure 7.8(a) shows the corn-fall pattern generated using the estimated RV parameters, which shows a good agreement with the observed pattern. However, the simulated corn-fall directions on both far south and north sides have a more westerly component compared to the observed pattern. This may imply that assuming a constant V_T on the entire domain is invalid and a modification may be necessary where the V_T decreases after a certain distance away from the tornado center. In other words, the V_T wind component would have a smaller V_T further away after a certain distance away from the tornado

center. Furthermore, a V_c of 24 m/s (54 mph) was estimated, which is the upper bound V_c of corn estimation for R4-5. This may also imply that the V_c of corn using the generalized crop lodging model (Baker et al., 2014) is underestimated, and a higher V_c may have been estimated from the corn-fall analysis if the bounds were greater. The corn-fall analysis yielded a maximum wind speed of 43 m/s (96 mph; EF1). Figure 7.8(b) shows the near-surface wind field of the Bondurant, IA tornado using the "best-match" parameters. For the same reason as the Sidey, IL tornado, the Bondurant, IA tornado was also rated an EF 0 at the damage location (NWS, 2018), which is lower than the 43 m/s (96 mph; EF 1) maximum wind speed estimated from the crop-fall analysis: another possible evidence of EF-scale method not being able to properly rate the tornado intensity due to lack of structures in rural areas.

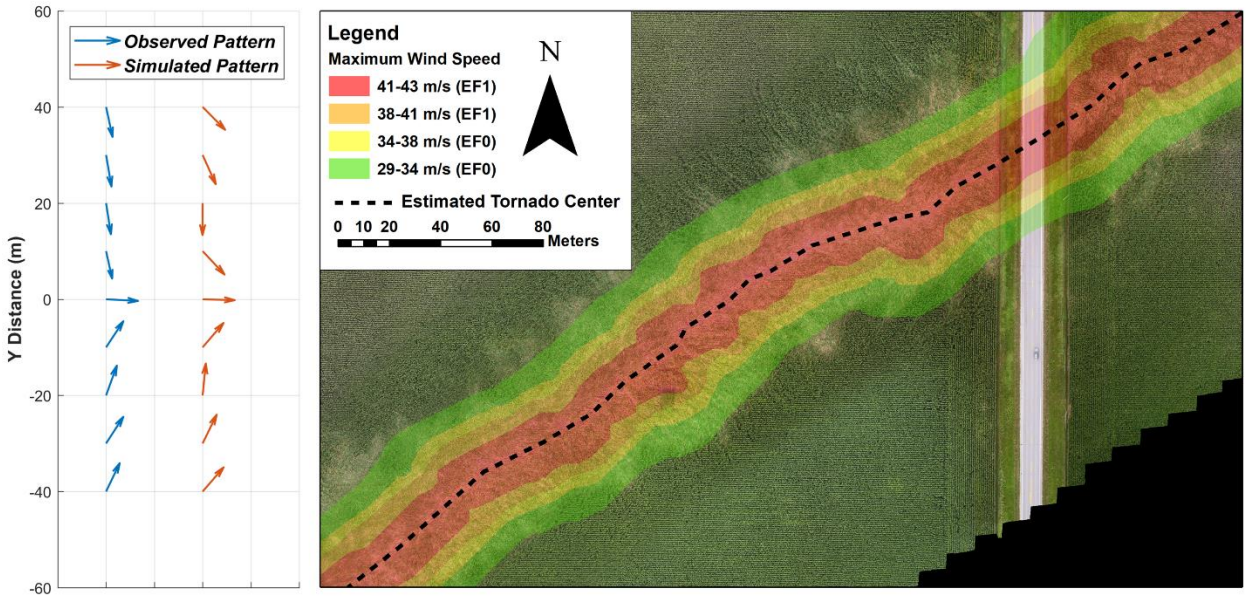

(a) corn-fall patterns (b) wind field contour

Figure 7.8. Comparison of (a) corn-fall patterns between observation and simulation and (b) near-surface wind field of Bondurant, IA tornado.

Table 7.4. “Best-matched” parameters of Bondurant, IA tornado.

Parameters	“Best-matched” value
G_{max}	2.3
alpha (α)	3.0
RMW (m)	20
phi (φ)	0.7
V_c (m/s)	24

7.2.4 Tuscaloosa, AL Tornado

The wind distribution within a tornado is very complex due to its continuously varying structure. The tornado wind field varies spatially and temporally and thus tornado wind field models should be able to capture these variations in wind components (Banik et al., 2007). These changes in wind components often result in a change in tree-fall pattern along the track, which suggests spatially and temporally varying RV parameters in the tree-fall analysis. For example, the 27 April 2011, Tuscaloosa-Birmingham, AL tornado translated through the city of Tuscaloosa (approximately 12 km) and caused severe structural and tree damage (NWS, 2011). A series of aerial photographs were acquired by the National Oceanic and Atmospheric Administration (NOAA) Remote Sensing Division, which are made available online by the Nation Geodetic Survey (NGS) (https://storms.ngs.noaa.gov/). The approximate ground sample distance (GSD) is 0.35 m per pixel. Approximately 6,000 fallen trees in the city of Tuscaloosa were converted to digital vector on ArcGIS. Along the tornado track in the city, a significant change in tree-fall patterns was noticed, indicating spatially varying RV parameters as the tornado translated from southwest to northeast. Figure 7.9 displays the digitally converted tree-fall direction and the

tornado track with the analyzed transects. The tree-fall directions normalized by the direction of the tornado track were determined and color-coded as the denoted range in the legend. An apparent increase in the *DW* and change in tree-fall direction can be noticed along the tornado track. Early in the track, the trees appear to fall more perpendicular to the tornado track. Most of the normalized tree-fall direction within the range of 0°-45° and 315°-360° (red) and 135°-225° (blue), suggesting a strong radial flow. However, as the tornado translates along the track, a more rotational pattern starts to form as more trees start to fall within the range of 225°-315° (black) near the center of the tornado track and 135°-225° (green) near the most south of the *DW*, indicating stronger tangential flow than earlier. Note that the normalized tree-fall direction is 0 due south with respect to the direction of the tornado track, increasing counter-clockwise. The increase in *DW* and *DR*, indicating growth of tornado size and increase in rotation (tangential flow), suggests that the tornado matured over time as it traversed. The tornado track can be divided into multiple sections or transects and analyzed individually. This can provide a detailed analysis of how the tornado characteristics and the near-surface wind field changed over time. The same tree-fall analysis method applied in the previous sections can be applied to determine them. A more detailed analysis of the near-surface wind field of a tornado with spatially and temporally changing RV parameters will be discussed in section 7.2.5.3. As shown on the top right corner of Figure 7.9, the tornado exited the city and entered a mountainous region with significant terrain, in which the near-surface wind field of the tornado is influenced by the topographic variation. The zoomed-in damage map displays a similar damage pattern examined in Chapter 5 where a number of trees that fell in the direction of the mountain ridges are noticed and more tree damage in the valley and less tree damage on the top of the hills are observed.

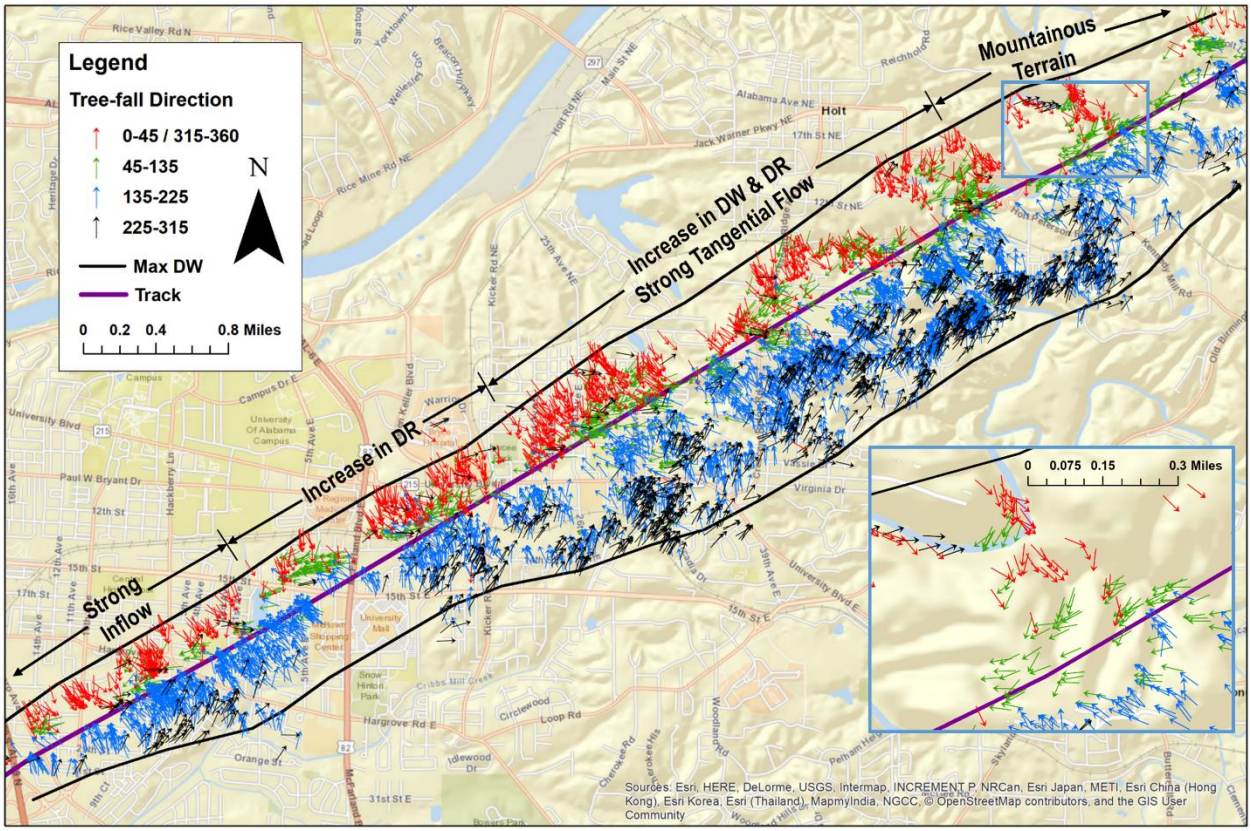

Figure 7.9. Tree-fall pattern and change in outputs of the Tuscaloosa, AL tornado.

7.2.5 Alonsa, MB Tornado

7.2.5.1 Initial parameter estimation

The tree-fall pattern obtained from the semi-automated tree-fall direction identification method (Chapter 3) is used to estimate the near-surface wind field of the Alonsa, MB tornado. A preliminary estimation was made based on Figure 3.11. Figure 3.11 shows two transects of the tree-fall pattern identified (yellow arrows) using the semi-automated method and the estimated tornado centerline (black line). The detected tree-fall patterns of the two transects exhibit patterns similar to the generic tree-fall pattern (see section 4.3.1.1; Figure 4.7). The tree-fall directions are oriented more towards the tornado translation for transect (1) similar to Figure 4.7(a), and in the opposite direction for transect (2) similar to Figure 4.7(c). The former pattern suggests a relatively

low rotational speed and thus a relatively low G_{max} parameter, and the latter pattern suggests a relatively high rotational speed with a greater G_{max} value. Based on the location of the confluence line and the *DR*, an estimation of alpha (α) of 0 to 5 degrees and 10 to 20 degrees can be made for transect (1) and transect (2), respectively, indicating significant radial inflow with little tangential flow and increasing tangential flow as the tornado matures. Also, in between transect (1) and transect (2), "transition" tree-fall patterns, a mix of forward-falling and backward-falling tree-falls, were observed. Judging from the tree-fall patterns, it can be speculated that the tornado grew and intensified as it translated north-east (Figure 7.10), similar to the Tuscaloosa, AL tornado.

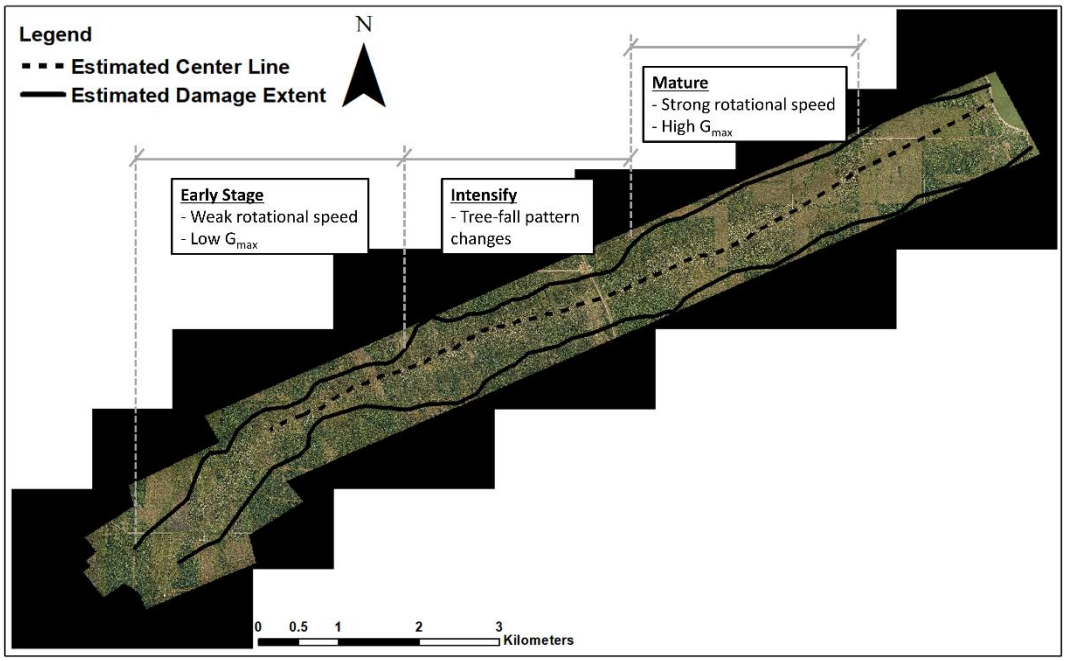

Figure 7.10. Orthomosaics of Alonsa, MB tornado and estimated center line and tree damage extent with tornado maturity stage annotated.

Before the iteration and parameter estimation process, non-tornadic tree-falls were removed and tree-fall directions with the large error were fixed manually. In the histogram of difference in tree-fall direction between the manual "tagging" method and the automated method

(Figure 3.12), 12% of the identified tree-falls had a difference in the tree-fall directions greater than 160º, which suggests that the median slope of the tree-falls was adequately estimated but the estimation in the median tree-fall direction was inadequate. As mentioned in section 3.4.2, an additional algorithm is applied which flags any grid box that has significantly large errors from the neighboring grid boxes. The tree-fall directions in these grid-boxes were inspected and the direction was changed 180º manually if the tree-fall direction is labeled incorrectly. Moreover, the automated tree-fall identification method cannot distinguish non-tornadic tree-falls from tornadic tree-falls, yet. Because the main interest lays in the near-surface tornadic wind field estimation, the non-tornadic tree-falls were subjectively identified and removed manually in order to avoid non-tornadic tree-falls to the estimation of the tornadic near-surface wind field. Refer to section 6.4 for application of tree-fall analysis and possibility of wind field estimation of non-tornadic events. Non-tornadic tree-falls that were removed include possible indications of microbursts and RFD surges, which were determined based on the tree-fall directions that show the flow characteristics of a downburst and an RFD. As shown in Figure 6.13(b), a downburst event produces a diverging tree-fall pattern due to straight-line flow characteristics (Fujita, 1981); any small-scale diverging patterns, which were observed especially on the far north side of the tornado track, were removed. Numerous westerly or southwesterly tree-falls were identified on the far south side, which could have been caused by the RFD surges (see Figure 6.10 and Figure 6.11). Converging tree-fall patterns, similar to the Sidney, IL tornado, were also identified on the far south side of the tornado and removed. It has been known that RFD can also induce airflow near the ground and enhance wind on the south side of the tornado track, which could produce temporarily enhanced sub-vortices. This phenomenon has been observed in the LES simulation

(Satrio et al., 2020). Moreover, as the non-tornadic tree-falls were being removed, false-positive tree-falls were also identified and removed together.

7.2.5.2 Wind field estimation using single V_T and V_c

Based on the preliminary results and Figure 7.10, the tree-fall patterns suggest a clear indication of the growth of tornado intensity, which affects the estimated RV parameters. The transect methods with multiple transects at different locations along the tornado track (see section 4.2.2.2) were applied to capture the change in the core size and intensity. In addition to the two transects in Figure 3.11, four more transects with different *DW* and tree-fall patterns were selected with a bin size of 50×200 m (height × width). A larger averaged width was used to reduce the variation of the tree-fall directions. Figure 7.11 shows the observed tree-fall patterns of the six transects normalized in the translational direction. The Y distance is the distance in the Y direction with respect to the estimated tornado center. As mentioned before, transect #1 shows a forward falling tree-fall pattern, transects #4-8 show a backward falling tree-fall pattern, and transect #2 shows a "transition" tree-fall pattern.

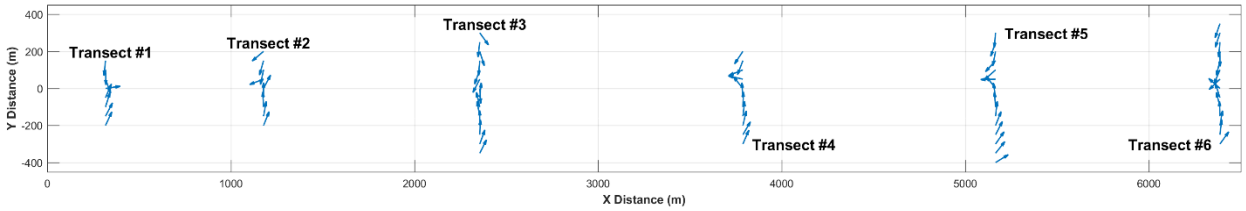

Figure 7.11. Observed tree-fall patterns of eight transects of the Alonsa, MB tornado.

With the initial G_{max} and α estimation from the preliminary result and the V_c estimation (47.5 m/s) using the HWIND model from Chapter 5 (see section 5.2.5.2), an independent RV

parameter estimation for each transect was made based on the minimum E_{rms}. For the first set of iterations, the V_T was treated as a random variable, which converged to a single value of 17 m/s (38 mph). Notably, the V_T estimation of 17 m/s (38 mph) complemented the mean storm motion vector, which is estimated at 18 m/s (40 mph) (COD, 2018). As a result, the second set of iterations was made using the converged single V_T value of 17 m/s (38 mph). The estimated RV parameters and the maximum wind speed for each transect using a fixed V_T and V_c are summarized in Table 7.5. The total maximum wind speed was 88 m/s (198 mph) occurred at transect #4, rating the Alonsa, MB tornado at a high-end EF 4 tornado. Figure 7.12 shows the change in RV parameters as the tornado travels, which suggests the evolution of the tornado. Each transect is represented in a circle. Based on Figure 7.12, a general increase in all parameters can be observed, suggesting a steady growth of tornado intensity and size as the tornado traversed over the forest of Alonsa, MB. As suggested by the preliminary results, an increase in alpha (α) is observed until the tornado intensity reached at the strongest (i.e., highest maximum wind speed) at transect #4 and then the estimated α decreases, indicating an increase and a decrease in the tangential velocity after transect #4. Overall, the "best-matched" parameters match the expectation of the preliminary result. Using the "best-matched" parameters, the near-surface wind field of the Alonsa, MB tornado is recreated as shown in Figure 7.13. The RV parameters were changed at the midpoint of each transect.

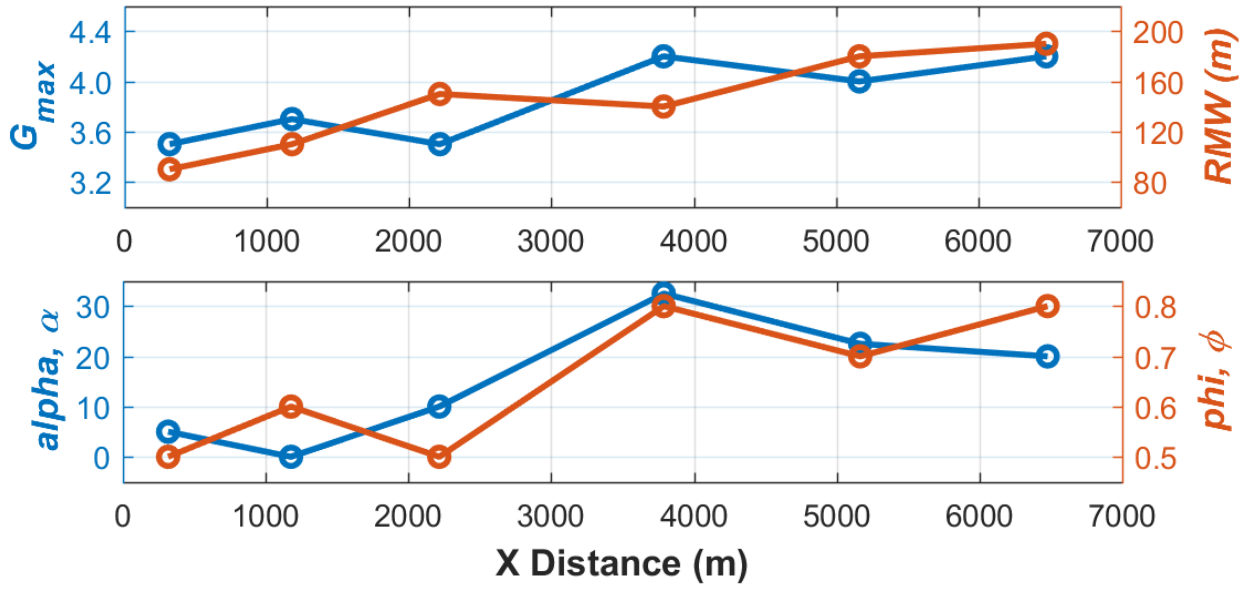

Figure 7.12. Change in "best-matched" RV parameter estimation of Alonsa, MB tornado.

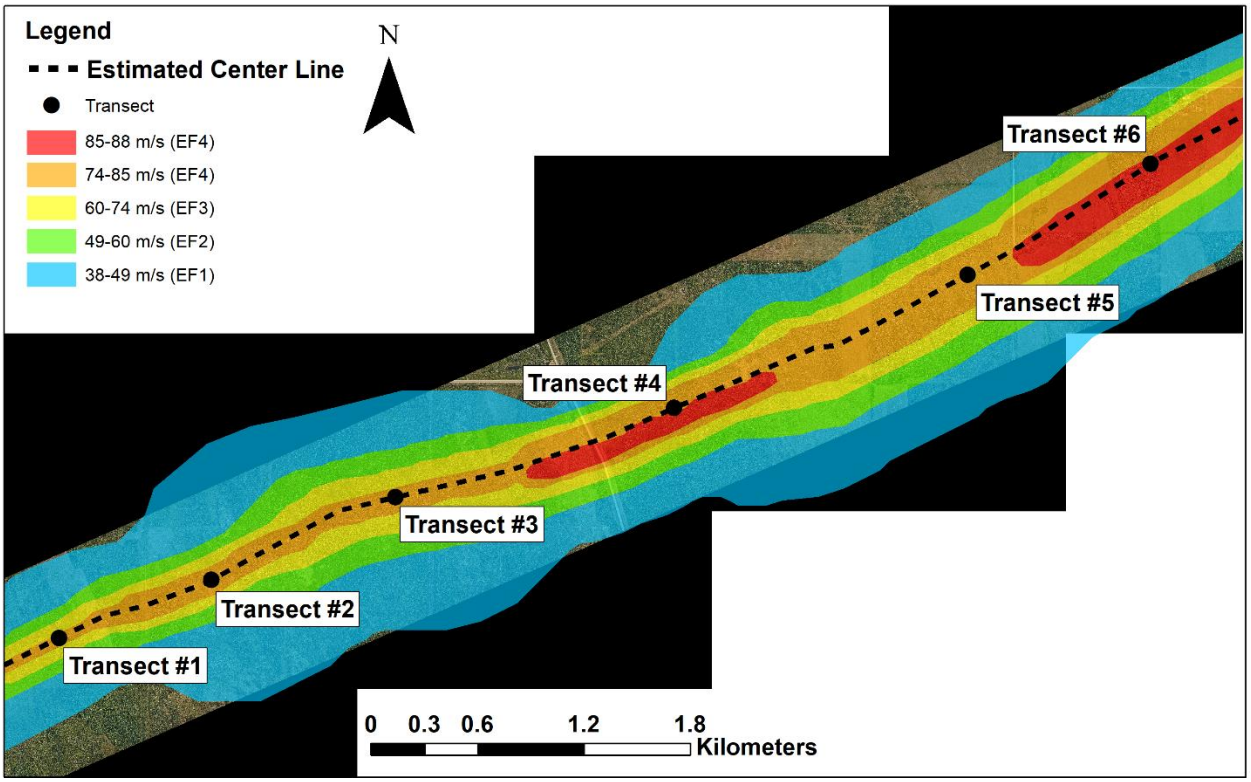

Figure 7.13. Estimated near-surface wind field of Alonsa, MB tornado.

Table 7.5. "Best-matched" RV parameters and the maximum wind speed of Alonsa, MB tornado at different transects with constant V_T (17 m/s) and V_c (47.5 m/s).

Transect #	G_{max}	α (°)	***RMW* (m)**	φ	***Max WS*** *
1	3.5	5	90	0.5	76.4 (171)
2	3.7	0	110	0.6	79.8 (179)
3	3.5	10	150	0.5	76.4 (171)
4	4.2	32.5	140	0.8	88.3 (198)
5	4.0	22.5	180	0.7	84.9 (190)
6	4.2	20	190	0.8	88.3 (198)

*Maximum wind speed at each transect in m/s (mph).

7.2.5.3 Wind field estimation using varying V_T and V_c

Instead of using a fixed V_c obtained using HWIND model, another set of parameter estimation was made treating the V_c as a random variable in order to verify the V_c estimation using the HWIND method and include more uncertainties. Since the V_T converged using a fixed V_c, the V_T was also treated as a random variable. Table 7.6 shows the "best-matched" RV parameters and the maximum wind speed of Alonsa, MB tornado with random variables V_T and V_c. The estimation shows an overall decrease in the maximum wind speed with a total maximum wind speed of 84.4 m/s (189 mph) but the general trend of the increase in parameters and the total maximum wind speed occurring transect #4 was comparable to the result of the parameter estimation with fixed V_T and V_c. The overall small decrease of V_T and V_c in the random variable method may suggest that the estimation of V_c using HWIND method was slightly overestimated. Despite the discrepancy in the magnitude, the trend of maximum wind speeds between the two methods shows a good agreement in Figure 7.14. Both methods rate the Alonsa, MB tornado at a high end of EF-4 category, which is what the tornado was rated by the NTP (Sills et al., 2020). The NTP conducted

a ground-based damage survey and discovered several homes destroyed with slab swept clean. Despite EF-5 rating damage states, the tornado was rated an EF-4 due to the construction quality. Furthermore, large trees were ripped off from the ground and traveled a far distance, and vehicles were lifted off from the ground (Sills et al., 2020). The tree-fall analysis and the NTP ground-based damage survey both suggest that the Alonsa, MB tornado was indeed a strong tornado.

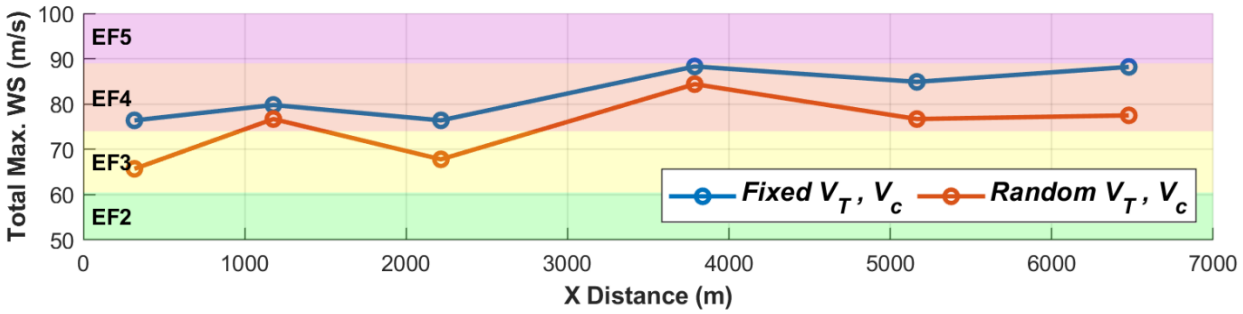

Figure 7.14. Total maximum wind speed comparison between constant V_T, V_c method and random variable V_T, V_c method.

Table 7.6. "Best-matched" RV parameters (percent change from Table 7.5) and the maximum wind speed of Alonsa, MB tornado at different transects with random variable V_T and V_c.

Transect #	V_T [a]	G_{max}	α [b]	RMW [c]	φ	V_c [a]	$Max\ WS$ [a]
1	15.6 (-8%)	3.2 (-9%)	10 (100%)	90 (-)	0.50 (-)	40.0 (-16%)	65.7 (-14%)
2	14.7 (-14%)	4.2 (+14%)	0 (-)	120 (+9%)	0.55 (-8%)	47.5 (-)	76.7 (-4%)
3	16.5 (-3%)	3.1 (-11%)	10 (-)	130 (-13%)	0.50 (-)	40.0 (-16%)	67.8 (-11%)
4	16.5 (-3%)	4.1 (-2%)	30 (-8%)	140 (-)	0.80 (-)	45.0 (-5%)	84.4 (-4%)
5	17.4 (+2%)	3.4 (-15%)	22.5 (-)	180 (-)	0.95 (36%)	37.5 (-21%)	76.7 (-10%)
6	15.2 (-11%)	4.1 (-2%)	20 (-)	180 (-11%)	0.9 (-11%)	37.5 (-21%)	77.5 (-12%)

[a] Maximum wind speed at each transect in m/s.
[b] alpha(α) in degree (°).
[c] Radius of maximum wind speed in m.

The tree-fall analysis selects the RV parameters based on the minimum E_{rms} and provides one independent estimate of the near-surface wind field. However, uncertainties still exist in the methodology (Roueche et al., 2018). Table 7.7 provides the uncertainty range of each RV parameter and the maximum wind speed at each transect. The uncertainty is quantified by calculating the mean (μ) and standard deviation (σ) of the set of parameters that produced E_{rms} within 10% of the minimum E_{rms}. These uncertainty ranges of parameters can be used to produce multiple near-surface wind fields and include epistemic uncertainties in building fragility functions (Roueche et al., 2018).

Table 7.7. Uncertainty range of RV parameters (within 10% of minimum E_{rms}) of Alonsa, MB tornado with random V_T and V_c at different transects.

Transect #	V_T (m/s)		G_{max}		α (°)		RMW (m)		φ		V_c		$Max\ WS^*$	
	μ	σ	μ	σ	μ	σ	μ	σ	μ	σ	μ	σ	μ	σ
1	15.5	2.52	3.30	0.20	7.83	2.99	92.0	4.06	0.52	0.03	40.8	6.13	66.7	10.0
2	14.1	2.23	3.95	0.45	1.86	2.20	132	12.0	0.75	0.15	41.5	5.16	69.2	8.17
3	15.9	2.81	3.05	0.07	6.88	2.00	121	7.86	0.5	0	37.1	6.53	64.5	11.4
4	15.1	2.48	4.28	0.43	30.1	1.55	134	15.0	0.88	0.09	39.0	5.91	79.8	14.5
5	16.1	2.63	4.06	0.53	20.9	1.21	150	22.0	0.92	0.07	35.2	5.94	81.7	15.7
6	15.8	2.03	4.47	0.40	17.4	2.49	135	13.1	0.80	0.14	38.6	5.20	82.5	11.3

*Maximum wind speed at each transect in m/s.

7.3 Tree-fall Analysis Application on Fragility Assessment

Fragility functions, which are probability functions of exceeding a certain limit state at a given wind speed, can provide quantitative insight into how a structure fails under different conditions. These fragility functions have been commonly developed analytically in the past (Amini and van de Lindt, 2014; Ellingwood et al., 2004; Lee and Rosowsky, 2005; Rosowsky and

Ellingwood, 2002). However, the recent tornado-based design paradigms propose a design based on limit states (Prevatt et al., 2012a; van de Lindt et al., 2013), in which a performance-based design (PBD) approach becomes necessary. Recently, an empirical approach of building fragility functions was adopted, using numerically reproduced wind fields (Nishijima et al., 2012; Roueche et al., 2017). One of the great advantages of tree-fall analysis is that it can reproduce the near-surface tornadic wind fields to be used in establishing empirical fragility functions, in which these empirically driven tornado fragility curves can be used to validate analytical fragility functions.

In this section, the maximum likelihood method from Roueche et al. (2017) is adopted. For each damage state, a binary damage state (0, 1) was assigned to each house with associated the maximum wind speed, and the lognormal best-fit parameters are determined. Then, the probabilities of structures meeting or exceeding a particular damage state at a given wind speed are determined. An illustration figure of lognormal fragility function and underlying empirical data from the Joplin, MO tornado is shown in Figure 7.15.

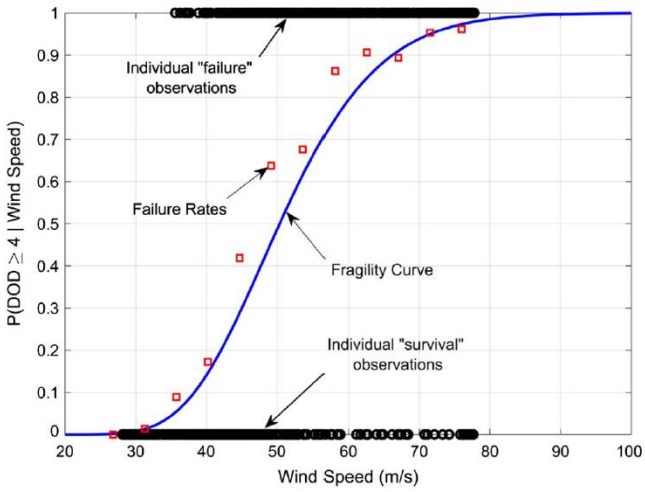

Figure 7.15. Illustration lognormal fragility fit and underlying empirical data from Joplin, MO tornado (Roueche et al., 2017).

7.3.1 Empirical Fragility Curves of Residential Buildings

Empirical fragility curves of the Naplate, IL tornado were developed using the maximum wind speed from the tree-fall analysis and the DODs of the residential houses collected from the survey. For each DOD, a binary damage state (0, 1) was assigned to each house with associated the maximum wind speed estimated from the tree-fall analysis (section 7.2.1.1). The best fit lognormal parameters were determined using the maximum likelihood functions and the probability functions of residential houses were built using the best-fit lognormal parameters. Figure 7.16 shows the fragility curves of residential buildings of Naplate, IL (blue lines) and Joplin, MO (red lines) tornado, in which the lognormal parameters of the Joplin, MO was taken from Roueche et al. (2017). Because of the relatively lower maximum wind speed of the EF 3 rated Naplate, IL tornado, the number of DOD 5 through 8 rated structures was enough to build meaningful fragility curves. Due to insufficient data for the higher DODs, only DOD 1 through DOD 4 were constructed. The curves show an evident increase in mean failure wind speed with higher DODs. Comparing the fragility curves of Naplate, IL to those of Joplin, MO tornado, DOD 1 and DOD 2 display very similar curves. Nonetheless, the curves for DOD 3 and DOD 4 show considerable differences; the probability of meeting or exceeding DOD 4 at a wind speed of 67 m/s (150 mph) is about 0.91 for the Joplin, MO tornado, whereas the probability is about 0.68 for the Naplate, IL tornado. The difference between the two regions may have been occurred because of regional differences between Naplate, IL, and Joplin, MO. The regional difference may include construction, common building type (e.g., wood, concrete masonry), and common roof type (e.g., gable, hip). However, it is believed that the large difference for DOD 3 and DOD 4 has resulted from the lack of number of damaged structures and the maximum wind speed of 58 m/s (129 mph) in Naplate, IL tornado; no data exist to fit the lognormal curve beyond the maximum wind speed.

A similar result is noticed in Roueche et al. (2018) where large differences are observed between different distributions for higher DODs as the fragility function is extrapolated beyond the observations. These fragility curves may be used to interpret and quantify the vulnerability of the residential houses to tornadoes and also used to validate analytical fragility functions. However, more empirical cases are certainly necessary to make a general interpretation and validation.

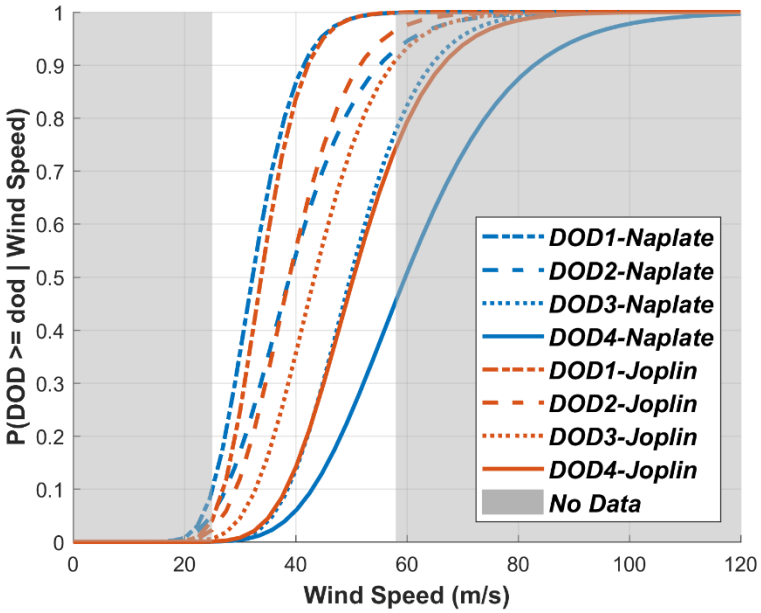

Figure 7.16. Comparison of empirical fragility curves of FR12 between Naplate, IL, and Joplin, MO tornado.

7.3.2 Empirical Fragility Curves of Trees

An empirical fragility model for trees can also be built using a similar process as the fragility curve of residential buildings. Empirical tree fragility curve can be obtained using the location of standing and fallen trees where a binary damage state (0, 1), zero for fallen trees and one for standing trees, is given to each tree with associated maximum wind speed retrieved from the tree-fall analysis, and the best-fit lognormal parameters are estimated using the maximum

likelihood functions. Using the near-surface wind field from tree-fall analysis (section 7.2.1.1) and the information from fallen trees and standing trees, empirical tree fragility curve for Naplate, IL, and Joplin, MO tornado are established. The probability functions of tree failures (down or up) under the tornado events with their best-fit parameters are shown and compared in Figure 7.17. The difference between the two curves may have been occurred also because of the regional difference, such as the type of trees and soil condition. However, the probability of failure for the Naplate, IL is considerably lower than that of the Joplin, MO tornado beyond 48 m/s. Due to the same limitation addressed in section 7.3.1, the difference is believed to have been resulted from the lack of number of trees (compared to number of trees in Joplin, MO) and the maximum wind speed of 58 m/s (129 mph) in Naplate, IL where no data exists to fit the lognormal curve beyond the maximum wind speed.

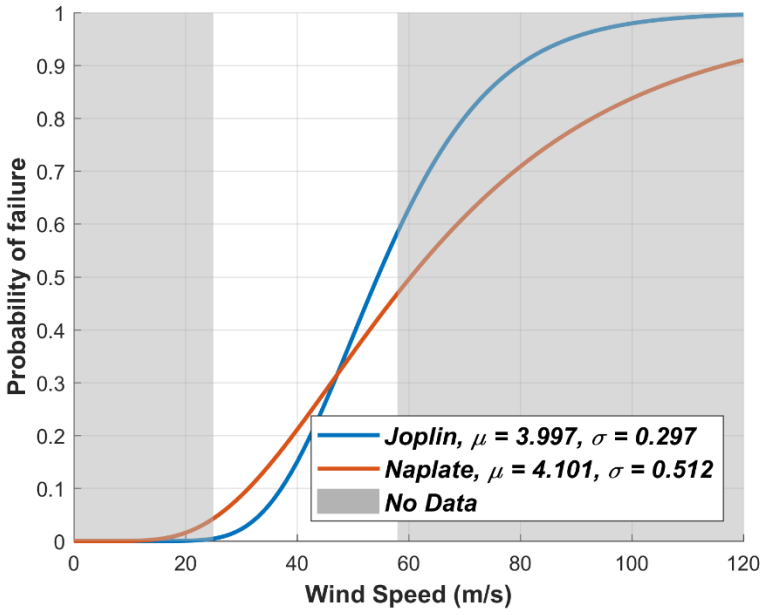

Figure. 7.17. Comparison of empirical tree fragility curves between Naplate, IL and Joplin, MO tornado.

More research on the empirical study is certainly needed for validation, and these fragility curves demonstrate great potential for validating the analytical tree-resistance models. Tree fragility curves can also be used as a V_c input parameter in the tree-fall analysis and produce more realistic looking tree-fall patterns as discussed in Chapter 4 (see section 4.3.1.2). Moreover, empirical fragility curves with more damage states (e.g., branch broken, uprooting, snapping) and with different species (e.g., coniferous and deciduous) can help improve tree damage indicator of the EF Scale method by understanding the damage behavior under tornadic wind.

7.4 Summary

The field observation data and methodology described in previous chapters are used to estimate the near-surface wind field of five different tornadoes: 1) Naplate, IL, 2) Sidney, IL, 3) Bondurant, IA, 4) Tuscaloosa, AL, and 5) Alonsa, MB tornado, and some results were used to validate the estimation from the tree-fall analysis. The observed damage patterns of these tornadoes are analyzed and compared to the simulation, in which the near-surface wind fields of these tornadoes were recreated, except the Tuscaloosa, AL tornado. Especially, the near-surface wind speed of Naplate, IL tornado was estimated using multiple different methods with different damage indicators, in which all methods showed a good agreement with each other. The empirical fragility curves of the Naplate, IL, and Joplin, MO tornado show the probability of failure for residential houses and trees under tornadic winds, which are important in performance-based design and validation for analytical fragility curves. The following conclusion can be made based on the near-surface wind field and fragility curve estimation:

- From the implication of Naplate, IL tornado analysis, it is recommended that detailed data collection on not only the damaged structures, trees, and signs but also the undamaged ones which can be used to help estimate the near-surface wind speed of a tornado is necessary.
- From the implication of Naplate, IL tornado analysis, aggregated damage information should be used to rate the tornado intensity instead of individual damage states as being done by conventional damage survey. Aggregated information improves individual estimates by providing valuable context and yields a more reliable result than any single damage indicator.
- The Naplate, IL tornado analysis showed that different approaches to wind speed estimation using different damage indicators still produced comparable results, providing more confidence in the estimation. The general agreement in wind speed estimation also supports the application of any subset of the methods depending on the circumstances and data availability.
- The near-surface wind field of Sidney, IL, and Bondurant, IA tornadoes were estimated using the tree-fall analysis, in which both estimates yielded an EF 1 category tornado as opposed to EF 0 rated by the NWS. Both cases are possible evidence of the EF scale method underrating the tornado intensity due to no structures present in the vicinity.
- The RV parameter estimation of Bondurant, IA tornado suggests that the V_c estimation using the generalized crop lodging model may underestimate the true V_c value of corn, and the corn-fall pattern of the Bondurant, IA tornado also suggests that assuming a constant translation speed over the entire simulation domain may be inaccurate.
- The tree-fall patterns of Tuscaloosa, AL, and Alonsa, MB tornado suggest a gradual increase in tornado intensity and size as the tornadoes traveled. In the early stage, more

forward falling trees can be observed, suggesting relatively small G_{max}, and less rotation (tangential component) is observed as the *DR* is close to one. Towards the end of the track, the *DW* and *DR* are increased, and tree-fall patterns show more backward falling trees, suggesting an increase in G_{max} with more tangential flow in the tornado. An increase in *RMW* is also noticed in Alonsa, MB tornado.

- Comparing the estimation result of V_T and V_c between the random variable method and the fixed variable method, there was a slight decrease in V_T and V_c for the random variable method, which may suggest a slight overestimation of V_c using the HWIND method.
- Empirical fragility curves of residential houses of Joplin, MO, and Naplate, IL tornado are built using the near-surface wind field estimated from tree-fall analysis and empirical data. The DOD 1 and DOD 2 fragility curves show little difference between the Joplin, MO and Naplate, IL tornado, but the difference is substantial for DOD 3 and DOD 4, which may have been caused due to lack of structures and the maximum wind speed capacity of the Naplate, IL tornado.
- Empirical fragility curves of trees are also built the same way as the residential building. A large difference is also noticed between the fragility curve of Joplin, MO, and Naplate, IL tornado most likely due to the same reason as the residential building.

CHAPTER 8: CONCLUSIONS AND FUTURE WORK

8.1 Conclusions

Tree-fall analysis has shown great potential in estimating the near-surface wind field of a tornado. To accurately estimate the near-surface wind field and broaden the application of tree-fall analysis using different damage indicators, five main objectives were outlined within the introduction of this dissertation. To this end, the research focused on the following objectives with concluding marks:

1) Documentation of tornado damage

   Total nine different damage surveys were conducted either or both on the ground and on air, collecting damage information of different damage indicators. Particularly, a semi-automatic tree-fall direction identification method using an image-processing technique was developed and the tree-fall pattern of Alonsa, MB tornado was obtained. The method showed a 95% accuracy of detecting downed trees and 74% of the downed trees showed less than 45 degrees difference in median fall direction from the traditional method (manually "tagging" trees).

2) Improve the existing method of estimating of near-surface wind field of tornadoes using tree-fall patterns

   Tree-fall analysis is a method of estimating the near-surface wind field of a tornado analyzing the tree-fall patterns, in which a Rankine vortex model is used to simulate a vortex and generate tree-fall patterns that resemble field observations. The tree-fall analysis is improved by further developing the comparison method and generalizing tree-fall patterns. Moreover, an alternative way of generating a more realistic tree-fall

pattern by using tree fragility functions is developed and interaction plots showing how different parameters interact with each other are presented.

3) Accurately estimate the critical wind speed of tree/crop/sign fall to be used in the tree-fall analysis

   There are many limitations in collecting data on a damage-site. The critical bending moment capacity, which is one of the important parameters to estimate the critical wind speed, is hard to obtain in the field. The HWIND model, a commonly used method of estimating the critical wind speed of trees, is modified such that only DBH and height of the trees are used to obtain the critical bending moment of trees. Moreover, the vertical wind profile is modified to a gust profile from a mean profile to produce a more realistic tornadic vertical profile. A series of bending moment tests were conducted on corns with different growth stages, and ranges of 3-s gust critical wind speed of corn at different growth stages estimated using a generalized crop lodging model are presented. The Boughton et al. (2012) method was used to estimate the critical wind speed of traffic signs of the Naplate, IL tornado, but the traffic signs of Naplate, IL were presumed to fail in lateral-torsional buckling (LTB), and not reaching fully plastic. Thus, the yield moment was used instead of the plastic moment.

4) Analyze different idealized vortex models to be used in the tree-fall analysis and the effects of topography

   The Sullivan vortex models did not match well with the full-scale radar measurements, while the modified Baker vortex model matched very well due to multiple shape factors allowing various shapes of wind profile. Burgers-Rott and Sullivan vortex models both produce an unrealistic tree-fall pattern because of the unrealistic boundary condition

whereas the Rankine and Baker vortex models do produce realistic tree-fall pattern, suggesting that the boundary condition assumption of $V_r = 0$ at $r = 0$ and $r = \infty$ may be valid at least near the ground where trees are present. The tree-fall patterns over idealized 3D sinusoid hills generated varying the RV parameters and using the ESDU K_L factor showed fairly reasonable agreement with the tree-fall pattern generated from the LES simulation. The general agreement between the two patterns demonstrates the potential of topographic effects in the tree-fall analysis. However, the discrepancy proves more research is required in regards to channeling flow and treating the formation of sub-vortices.

5) Apply tree-fall analysis to estimate near-surface wind field of different tornadoes, compare the estimated result to different methods, and evaluate the probability of structure and tree failure using empirical data

   A comprehensive damage survey of the Naplate, IL tornado allowed multiple different methods to be used in the estimation of the near-surface wind field. The comparable results increase the confidence level of the wind speed estimation and also support the application of any subset of the methods depending on the circumstances and data availability. The tree-fall analysis was used in agricultural fields damaged by tornadoes and produced a maximum wind speed of EF 1 rating. The result provided possible evidence of the EF scale method underestimating the tornado intensity in rural areas. The tree-fall patterns of Tuscaloosa, AL, and Alonsa, MB tornado, EF 4 rated tornadoes, show a general pattern where the tornado intensity, size, and tangential flow increase over time. Empirical fragility curves of residential buildings and trees were produced using the estimated near-surface wind field, which quantify the

vulnerability of residential houses and trees to tornadoes in the Midwest. Though, the results show that the number of empirical data is lacking especially in the damage states associated with high wind speed.

8.2 Recommendations and Future Work

Additional work that should be considered and areas that require improvement is to advance the method of estimating the near-surface wind field of a tornado using damage patterns are summarized as follows:

- Fully automated tree-fall identification method. Although the semi-automatic tree-fall identification method using image-processing technique showed great potential and reduced the labor-intensive data collection from aerial photographs, the method requires calibrating and adjusting parameters in application to other tornado cases, and thus more generalization process is needed. A machine learning technique may be a feasible alternative approach to fully automate the tree-fall identification process and apply it to many other post-damage aerial photographs.
- Automated near-surface wind field estimation package. In addition to the recent establishment of the Northern Tornado Project (NTP), a team aims to detect and document every tornado that occurs across Canada, the need to accurately and quickly estimating the near-surface wind field of a tornado is increasing. A software that automatically analyzes the tree-fall pattern and generates a near-surface wind field can be developed. Combining with the fully automated tree-fall identification method mention in the previous bullet, a full "package" of near-surface wind field estimation from a raw orthomasaic can be extremely beneficial to engineers and practitioners.

- Improvements in the estimation of critical wind speed. There has not been a significant improvement in the HWIND model, first developed in 1993, or development of any other models estimating the critical wind speed of trees ever since, possibly due to lack of full-scale measurements. No studies have been able to measure the drag coefficient of trees at the critical wind speed. As a result, a very rough drag coefficient is assumed in the HWIND model. It has been noticed that there are many different studies regarding determine the drag coefficient of different tree species. However, no studies have attempted to generalize the drag coefficients of trees, in which the key to generalizing is believed to be related to the morphology and the flexibility of the trees. Moreover, very little is known in regards to the critical wind speed of crops. Not only for corns, but further validation using full-scale data is also needed to improve the estimation of critical wind speed of crops and for the generalized crop lodging model to be applied to various crops.
- Development of multi-vortex wind field. One of the limitations of the existing wind field models and tree-fall analysis is that the wind field model cannot produce a multi-vortex structure despite the frequent observation of multi-vortex structures from radar and LES simulation. Thus, wind speed enhancement from sub-vortices cannot be replicated. Although it violates the NSE, super-positioning multiple vortex equations may be able to show the wind field of a multi-vortex structure.
- The topographic effects on tornado wind field. The topographic effects on tornado wind fields still remain elusive due to the complexity of airflow interaction with the terrain and the tornado dynamic change. More LES simulations on various topographic

features and case studies to validate the numerical studies are necessary to accurately estimate the near-surface wind field of a tornado in mountainous regions.

REFERENCES

Agee, E., Church, C., Morris, C., and Snow, J. (1975). Some synoptic aspects and dynamic features of vortices associated with the tornado outbreak of 3 April 1974. *Monthly Weather Review*, 103(4), 318-333.

AISC (2017). Steel construction manual. American Institute of Steel Construction, Chicago, IL.

Al-Zube, L., Sun, W., Robertson, D., and Cook, D. (2018). The elastic modulus for maize stems. *Plant Methods*, 14(1), 11.

Amini, M. O., and van de Lindt, J. W. (2014). Quantitative insight into rational tornado design wind speeds for residential wood-frame structures using fragility approach. *Journal of Structural Engineering*, 140(7), 04014033.

ASCE (2016). Minimum design loads for buildings and other structures. American Society of Civil Engineers 7-2016, Reston, VA.

Astola, J., Haavisto, P., and Neuvo, Y. (1990). Vector median filters. *Proceedings of the IEEE*, 78(4), 678-689.

Aydin, T., Yemez, Y., Anarim, E., and Sankur, B. (1996). Multidirectional and multiscale edge detection via M-band wavelet transform. *IEEE Transactions on Image Processing*, 5(9), 1370-1377.

Baker, C. J. (1995). The development of a theoretical model for the windthrow of plants. *Journal of Theoretical Biology*, 175(3), 355-372.

Baker, C. J., Sterling, M., and Berry, P. (2014). A generalised model of crop lodging. *Journal of Theoretical Biology*, 363, 1-12.

Baker, C. J., and Sterling, M. (2017). Modelling wind fields and debris flight in tornadoes. *Journal of Wind Engineering and Industrial Aerodynamics*, 168, 312-321.

Baker, C. J., and Sterling, M. (2018). Tornado vortex model developments. Unpublished manuscript.

Baker, C. J., Sterling, M., and Jesson, M. (2020). The lodging of crops by tornadoes. *Journal of Theoretical Biology*, 110309.

Ballard, D. H. (1981). Generalizing the Hough transform to detect arbitrary shapes. *Pattern recognition*, 13(2), 111-122.

Banik, S. S., Hong, H. P., and Kopp, G. A. (2007). Tornado hazard assessment for southern Ontario. *Canadian Journal of Civil Engineering*. 34 (7), 830-842.

Barnes, C. F., Fritz, H., and Yoo, J. (2007). Hurricane disaster assessments with image-driven data mining in high-resolution satellite imagery. *IEEE Transactions on Geoscience and Remote Sensing*, 45(6), 1631-1640.

Barni, M., Buti, F., Bartolini, F., and Cappellini, V. (2000). A quasi-Euclidean norm to speed up vector median filtering. *IEEE Transactions on Image Processin*g, 9(10), 1704-1709.

Bech, J., Gayà, M., Aran, M., Figuerola, F., Amaro, J., and Arús, J. (2009). Tornado damage analysis of a forest area using site survey observations, radar data and a simple analytical vortex model. *Atmospheric Research*, 93(1-3), 118-130.

Beck, V., and Dotzek, N. (2010). Reconstruction of near-surface tornado wind fields from forest damage. *Journal of Applied Meteorology and Climatology*, 49(7), 1517-1537.

Berry, P. M., Sterling, M., Baker, C. J., Spink, J., and Sparkes, D. L. (2003). A calibrated model of wheat lodging compared with field measurements. *Agricultural and Forest Meteorology*, 119(3-4), 167-180.

Berry, P. M., Sterling, M., Spink, J. H., Baker, C. J., Sylvester-Bradley, R., Mooney, S. J., Tams, A. R., and Ennos, A. R. (2004). Understanding and reducing lodging in cereals. *Advances in Agronomy*, 84(04), 215-269.

Berry, P. M., and Spink, J. (2012). Predicting yield losses caused by lodging in wheat. *Field Crops Research*, 137, 19-26.

Bechtold, W. A. (2003). Crown-diameter prediction models for 87 species of stand-grown trees in the eastern United States. *Southern Journal of Applied Forestry*, 27(4), 269-278.

Blanchard, D. O. (2013). A comparison of wind speed and forest damage associated with tornadoes in northern Arizona. *Weather and Forecasting*, 28(2), 408-417.

Bluestein, H. B. (2007). Mobile Doppler Radar observations of tornadoes. In *Proceedings of 4th European Conference on Severe Storms*, Trieste, Italy.

Bluestein, H. B., and Pazmany, A. L. (2000). Observations of tornadoes and other convective phenomena with a mobile, 3-mm wavelength, Doppler radar: The spring 1999 field experiment. *Bulletin of the American Meteorological Society*, 81(12), 2939-2952.

Bluestein, H. B., Thiem, K. J., Snyder, J. C., and Houser, J. B. (2019). Tornadogenesis and early tornado evolution in the El Reno, Oklahoma, supercell on 31 May 2013. *Monthly Weather Review*, 147(6), 2045-2066.

Bluestein, H. B., Weiss, C. C., and Pazmany, A. L. (2004). Doppler radar observations of dust devils in Texas. *Monthly Weather Review*, 132(1), 209-224.

Bodine, D. J., Maruyama, T., Palmer, R. D., Fulton, C. J., Bluestein, H. B., and Lewellen, D. C. (2016). Sensitivity of tornado dynamics to soil debris loading. *Journal of the Atmospheric Sciences*, 73(7), 2783-2801.

Boughton, G. N. Henderston, D.J., Ginger, J.D., Homes, J.D., Walker, G.R., Leitch, C.J., Somerville, L.R., Frye, U., Jayasinghe, N.C., Kim, P.Y. (2012). Tropical Cyclone Yasi: structural damage to buildings. *Technical Report No. 57, Cyclone Testing Station*, James Cook University.

Burgers, J. M. (1948). A mathematical model illustrating the theory of turbulence. *Advances in Applied Mechanics* (Vol. 1). Elsevier, 171-199.

Burgess, D., Ortega, K., Stumpf, G., Garfield, G., Karstens, C., Meyer, T., Smith, B., Speheger, D., LaDue, J., Smith, R., and Marshall, T. (2014). 20 May 2013 Moore, Oklahoma, tornado: Damage survey and analysis. *Weather and Forecasting*, 29(5), 1229-1237.

Cannon, J. B., Barrett, M. E., and Peterson, C. J. (2015). The effect of species, size, failure mode, and fire-scarring on tree stability. *Forest Ecology and Management*, 356, 196-203.

Cannon, J. B., Hepinstall-Cymerman, J., Godfrey, C. M., and Peterson, C. J. (2016). Landscape-scale characteristics of forest tornado damage in mountainous terrain. *Landscape Ecology*, 31(9), 2097-2114.

Canny, J. (1986). A computational approach to edge detection. *IEEE Transactions on Pattern Analysis and Machine Intelligence*, (6), 679-698.

Cao, J., Tamura, Y., and Yoshida, A. (2012). Wind tunnel study on aerodynamic characteristics of shrubby specimens of three tree species. *Urban Forestry & Urban Greening*, 11(4), 465-476.

Carter, P. R., and Hudelson, K. D. (1988). Influence of simulated wind lodging on corn growth and grain yield. *Journal of Production Agriculture*, 1(4), 295-299.

Chehata, N., Orny, C., Boukir, S., Guyon, D., and Wigneron, J. P. (2014). Object-based change detection in wind storm-damaged forest using high-resolution multispectral images. *International Journal of Remote Sensing*, 35(13), 4758-4777.

Chen, G., and Lombardo, F. T. (2019). An analytical pattern-based method for estimation of a near-surface tornadic wind field. *Journal of Wind Engineering and Industrial Aerodynamics*, 194, 103999.

Cheng, F. H., Hsu, W. H., and Chen, M. Y. (1989). Recognition of handwritten Chinese characters by modified Hough transform techniques. *IEEE Transactions on Pattern Analysis and Machine Intelligence*, 11(4), 429-439.

Chien, C. L., and Tseng, D. C. (2011). Color image enhancement with exact HSI color model. *International Journal of Innovative Computing, Information and Control*, 7(12), 6691-6710.

Church, C., Snow, J. T., Baker, G. L., and Agee, E. M. (1979). Characteristics of tornado-like vortices as a function of swirl ratio: A laboratory investigation. *Journal of the Atmospheric Sciences*, 36(9), 1755-1776.

Church, C.R., Kosiba, K.A., Cleland, J.D., and Beer, C.P. (2004). The formation and intensification of supercritical tornado-like vortices – a laboratory study. In *Proceedings of the 22nd Conference on Severe Local Storms*, Hyannis, MA.

Cleugh, H. A., Miller, J. M., and Böhm, M. (1998). Direct mechanical effects of wind on crops. *Agroforestry Systems*, 41(1), 85-112.

COD, (2018). Canadian Upper Air Soundings. College of DuPage. https://weather.cod.edu/analysis/.

Coleman, T.F., and Li, Y. (1994). On the Convergence of Reflective Newton Methods for Large-Scale Nonlinear Minimization Subject to Bounds. *Mathematical Programming*, 67(2), 189-224.

Coleman, T.F., and Li, Y. (1996). An Interior, Trust Region Approach for Nonlinear Minimization Subject to Bounds. *SIAM Journal on Optimization*, 6, 418-445.

Cook, N. J. (1990). The Designer's Guide to Wind Loading of Building Structures, Part 2: Static structures. Building Research Establishment, London, UK.

Coutts, M. P. (1986). Components of tree stability in Sitka spruce on peaty gley soil. *Forestry*, 59(2), 173-197.

Cucchi, V., Meredieu, C., Stokes, A., Berthier, S., Bert, D., Najar, M., and Lastennet, R. (2004). Root anchorage of inner and edge trees in stands of Maritime pine (Pinus pinaster Ait.) growing in different podzolic soil conditions. *Trees*, 18(4), 460-466.

Curtis, R. O. (1967). Height-diameter and height-diameter-age equations for second-growth Douglas-fir. *Forest Science*, 13(4), 365-375.

Davies-Jones, R. P. (1982). Observational and theoretical aspects of tornadogenesis. *Intense Atmospheric Vortices*. Springer, 175-189.

Davies-Jones, R., and Kessler, E. (1974). Tornadoes. *Weather and Climate Modification*. John Wiley, 552–595.

Davies-Jones, R., Trapp, R. J., and Bluestein, H. B. (2001). Tornadoes and tornadic storms. *Severe Convective Storms* (No. 50). American Meteorological Society, 167-221.

Davies-Jones, R. P., and Wood, V. T. (2006). Simulated Doppler velocity signatures of evolving tornado-like vortices. *Journal of Atmospheric and Oceanic Technology*, 23(8), 1029-1048.

Dawkins, H. C. (1963). Crown diameters: their relation to bole diameter in tropical forest trees. *The Commonwealth Forestry Review*, 318-333.

Doswell III, C. A. (2003). A guide to F-scale damage assessment. *US Dept. of Commerce, NOAA/NWS*.

Doswell III, C. A., and Burgess, D. W. (1988). On some issues of United States tornado climatology. *Monthly Weather Review*, 116(2), 495-501.

Doviak, R. J., and Zrnić, D. S. (1993). Observation of winds, storms, and related phenomena. *Doppler Radar and Weather Observations*, 2, 280-385.

Dralle, K., and Rudemo, M. (1996). Stem number estimation by kernel smoothing of aerial photos. *Canadian Journal of Forest Research*, 26(7), 1228-1236.

Duda, R. O., and Hart, P. E. (1972). Use of the Hough transformation to detect lines and curves in pictures. *Communications of the ACM*, 15(1), 11-15.

Edelsbrunner, H., Kirkpatrick, D., and Seidel, R. (1983). On the shape of a set of points in the plane. *IEEE Transactions on Information Theory*, 29(4), 551-559.

Edelsbrunner, H., and Mücke, E. P. (1994). Three-dimensional alpha shapes. *ACM Transactions on Graphics*, 13(1), 43-72.

Edwards, R., LaDue, J. G., Ferree, J. T., Scharfenberg, K., Maier, C., and Coulbourne, W. L. (2013). Tornado intensity estimation: Past, present, and future. *Bulletin of the American Meteorological Society*, 94(5), 641-653.

Ellingwood, B. R., Rosowsky, D. V., Li, Y., and Kim, J. H. (2004). Fragility assessment of light-frame wood construction subjected to wind and earthquake hazards. *Journal of Structural Engineering*, 130(12), 1921-1930.

ESDU. (1989). Boundary walls, fences and hoardings: Mean and peak wind loads and overturning moments, Data Item 89050. ESDU (Engineering Sciences Data Unit) International, London, UK.

ESDU. (1991). Mean wind speeds over hills and other topography, Data Item 91043. ESDU (Engineering Sciences Data Unit) International, London, UK.

Eshelman, S., and Stanford, J. L. (1977). Tornadoes, funnel clouds and thunderstorm damage in Iowa during 1974. *Iowa State Journal of Research*, 51, 327-361.

Feldpausch, T. R., Banin, L., Phillips, O. L., Baker, T. R., Lewis, S. L., Quesada, C. A., Affum-Baffoe, K., Arets, E. J. M. M., Berry, N. J., Bird, M., Brondizio, E. S., de Camargo, P., Chave, J., Djagbletey, G., Domingues, T. F., Drescher, M., Fearnside, P. M., França, M. B., Fyllas, N. M., Lopez-Gonzalez, G., Hladik, A., Higuchi, N., Hunter, M. O., Iida, Y., Salim, K. A., Kassim, A. R., Keller, M., Kemp, J., King, D. A., Lovett, J. C., Marimon, B. S., Marimon-Junior, B. H., Lenza, E., Marshall, A. R., Metcalfe, D. J., Mitchard, E. T. A., Moran, E. F., Nelson, B. W., Nilus, R., Nogueira, E. M., Palace, M., Patiño, S., Peh, K. S.-H., Raventos, M. T., Reitsma, J. M., Saiz, G., Schrodt, F., Sonké, B., Taedoumg, H. E., Tan, S., White, L., Wöll, H., and Lloyd, J. (2011). Height-diameter allometry of tropical forest trees. *Biogeosciences*, 8(5), 1081-1106.

Folger, P. (2013). *Severe thunderstorms and tornadoes in the United States*. Congressional Research Service.

Forbes, G. S. (1998). Topographic influences on tornadoes in Pennsylvania. In *Proceedings of the 19th Conference on Severe Local Storms*, Minneapolis, MN.

Forbes, G. S., and Wakimoto, R. M. (1983). A concentrated outbreak of tornadoes, downbursts and microbursts, and implications regarding vortex classification. *Monthly Weather Review*, 111(1), 220-236.

Foster, D. R. (1988). Species and stand response to catastrophic wind in central New England, USA. *The Journal of Ecology*, 135-151.

Fu, K. S., and Mui, J. K. (1981). A survey on image segmentation. *Pattern Recognition*, 13(1), 3-16.

Fujita, T. T. (1981). Tornadoes and downbursts in the context of generalized planetary scales. *Journal of the Atmospheric Sciences*, 38(8), 1511-1534.

Fujita, T. T. (1989). The Teton-Yellowstone tornado of 21 July 1987. *Monthly Weather Review*, 117(9), 1913-1940.

Fujita, T. T. (1970). The Lubbock tornadoes: A study of suction spots. *Weatherwise*, 23(4), 161-173.

Fujita, T. T. (1993). Plainfield tornado of August 28, 1990. *The Tornado: Its Structure, Dynamics, Prediction and Hazards* (Vol. 79). American Geophysical Union, 1-17.

Gardiner, B., Berry, P., and Moulia, B. (2016). Wind impacts on plant growth, mechanics and damage. *Plant Science*, 245, 94-118.

Gillmeier, S., Sterling, M., Hemida, H., and Baker, C. J. (2018). A reflection on analytical tornado-like vortex flow field models. *Journal of Wind Engineering and Industrial Aerodynamics*, 174, 10-27.

Godfrey, C. M., and Peterson, C. J. (2017). Estimating enhanced Fujita scale levels based on forest damage severity. *Weather and Forecasting*, 32(1), 243-252.

Gold, S., White, E., Roeder, W., McAleenan, M., Kabban, C. S., and Ahner, D. (2020). Probabilistic Contingency Tables: An Improvement to Verify Probability Forecasts. *Weather and Forecasting*, 35(2), 609-621.

Guyer, J.L., and Moritz, M.L. (2003). On issues of tornado damage assessment and F-scale assignment in agricultural areas. In *Proceedings of 83rd AMS Annual Meeting Symposium on F-scale and Severe-Weather Damage Assessment*, Long Beach, CA.

Haan Jr, F. L., Sarkar, P. P., and Gallus, W. A. (2008). Design, construction and performance of a large tornado simulator for wind engineering applications. *Engineering Structures*, 30(4), 1146-1159.

Hall, F., and Brewer, R. D. (1959). A sequence of tornado damage patterns. *Monthly Weather Review*, 87, 207-216.

Hemery, G. E., Savill, P. S., and Pryor, S. N. (2005). Applications of the crown diameter–stem diameter relationship for different species of broadleaved trees. *Forest Ecology and Management*, 215(1-3), 285-294.

Hjelmfelt, M. R. (1988). Structure and life cycle of microburst outflows observed in Colorado. *Journal of Applied Meteorology*, 27(8), 900-927.

Hökkä, H. (1997). Height-diameter curves with random intercepts and slopes for trees growing on drained peatlands. *Forest Ecology and Management*, 97(1), 63-72.

Holland, G. J. (1980). An analytic model of the wind and pressure profiles in hurricanes. *Monthly Weather Review*, 108(8), 1212-1218.

Holland, G. J., Belanger, J. I., and Fritz, A. (2010). A revised model for radial profiles of hurricane winds. *Monthly Weather Review*, 138(12), 4393-4401.

Holland, A. P., Riordan, A. J., and Franklin, E. C. (2006). A simple model for simulating tornado damage in forests. *Journal of Applied Meteorology and Climatology*, 45(12), 1597-1611.

Holmes, J. D. (2015). *Wind loading of structures*. CRC press.

Holmes, J. D., and Oliver, S. E. (2000). An empirical model of a downburst. *Engineering Structures*, 22(9), 1167-1172.

IDOT. (2016). Standard specification for road and bridge construction. Illinois Department of Transportation, Springfield, IL.

Ishihara, T., Oh, S., and Tokuyama, Y. (2011). Numerical study on flow fields of tornado-like vortices using the LES turbulence model. *Journal of Wind Engineering and Industrial Aerodynamics*, 99(4), 239-248.

Joseph, G. M. D., Mohammadi, M., Sterling, M., Baker, C. J., Gillmeier, S. G., Soper, D., and Murray, J. (2020). Determination of crop dynamic and aerodynamic parameters for lodging prediction. *Journal of Wind Engineering and Industrial Aerodynamics*, 202, 104169.

Kane, B., and Smiley, E. T. (2006). Drag coefficients and crown area estimation of red maple. *Canadian Journal of Forest Research*, 36(8), 1951-1958.

Karstens, C. D. (2012). Observations and Laboratory Simulations of Tornadoes in Complex Topographical Regions. Doctoral dissertation, Iowa State University.

Karstens, C. D., Gallus Jr, W. A., Lee, B. D., and Finley, C. A. (2013). Analysis of tornado-induced tree fall using aerial photography from the Joplin, Missouri, and Tuscaloosa–Birmingham, Alabama, tornadoes of 2011. *Journal of Applied Meteorology and Climatology*, 52(5), 1049-1068.

Karstens, C. D., Samaras, T. M., Lee, B. D., Gallus Jr, W. A., and Finley, C. A. (2010). Near-ground pressure and wind measurements in tornadoes. *Monthly Weather Review*, 138(7), 2570-2588.

Key, T., Warner, T. A., McGraw, J. B., and Fajvan, M. A. (2001). A comparison of multispectral and multitemporal information in high spatial resolution imagery for classification of individual tree species in a temperate hardwood forest. *Remote Sensing of Environment*, 75(1), 100-112.

Knox, J. A., Rackley, J. A., Black, A. W., Gensini, V. A., Butler, M., Dunn, C., Gallo, T., Hunter, M.R., Lindsey, L., Phan, M., Scroggs, R., and Brustad, S. (2013). Tornado debris characteristics and trajectories during the 27 April 2011 super outbreak as determined using social media data. *Bulletin of the American Meteorological Society*, 94(9), 1371-1380.

Koizumi, A., Motoyama, J. I., Sawata, K., Sasaki, Y., and Hirai, T. (2010). Evaluation of drag coefficients of poplar-tree crowns by a field test method. *Journal of Wood Science*, 56(3), 189-193.

Koizumi, A., Shimizu, M., Sasaki, Y., and Hirai, T. (2016). In situ drag coefficient measurements for rooftop trees. *Journal of Wood Science*, 62(4), 363-369.

Kosiba, K., and Wurman, J. (2010). The three-dimensional axisymmetric wind field structure of the Spencer, South Dakota, 1998 tornado. *Journal of the Atmospheric Sciences*, 67(9), 3074-3083.

Kosiba, K. A., and Wurman, J. (2013). The three-dimensional structure and evolution of a tornado boundary layer. *Weather and Forecasting*, 28(6), 1552-1561.

Kuai, L., Haan Jr, F. L., Gallus Jr, W. A., and Sarkar, P. P. (2008). CFD simulations of the flow field of a laboratory-simulated tornado for parameter sensitivity studies and comparison with field measurements. *Wind and Structures*, 11(2), 75-96.

Kuligowski, E. D., Lombardo, F. T., Phan, L. T., Levitan, M. L., and Jorgensen, D. P. (2014). Final Report, National Institute of Standards and Technology (NIST) Technical Investigation of the May 22, 2011, Tornado in Joplin, Missouri, NIST NCSTAR-3, National Institute of Standards and Technology, Gaithersburg, MD.

Larsen, D. R. (2017). Simple taper: Taper equations for the field forester. In *Proceedings of the 20th Central Hardwood Forest Conference*, Columbia, MO.

Letchford, C. W. (2001). Wind loads on rectangular signboards and hoardings. *Journal of Wind Engineering and Industrial Aerodynamics*, 89(2), 135-151.

Lee, W. C., Jou, B. J. D., Chang, P. L., and Deng, S. M. (1999). Tropical cyclone kinematic structure retrieved from single-Doppler radar observations. Part I: Interpretation of Doppler velocity patterns and the GBVTD technique. *Monthly Weather Review*, 127(10), 2419-2439.

Lee, K. H., and Rosowsky, D. V. (2005). Fragility assessment for roof sheathing failure in high wind regions. *Engineering Structures*, 27(6), 857-868.

Lewellen, D. C., Lewellen, W. S., and Xia, J. (2000). The influence of a local swirl ratio on tornado intensification near the surface. *Journal of the Atmospheric Sciences*, 57(4), 527-544.

Lewellen, D. C., and Lewellen, W. S. (2007). Near-surface intensification of tornado vortices. *Journal of the Atmospheric Sciences*, 64(7), 2176-2194.

Lewellen, D. C. (2012). Effects of topography on tornado dynamics: A simulation study. In *Proceedings of the 26th Conference on Severe Local Storms*, Nashville, TN.

Lewellen, W. S. (1993). Tornado vortex theory. *The Tornado: Its Structure, Dynamics, Prediction and Hazards* (Vol. 79). American Geophysical Union, 19-39.

Lombardo, F. T. (2017). Engineering analysis of a full-scale high-resolution tornado wind speed record. *Journal of Structural Engineering*, 144(2), 04017212.

Lombardo, F. T., Roueche, D. B., and Prevatt, D. O. (2015). Comparison of two methods of near-surface wind speed estimation in the 22 May, 2011 Joplin, Missouri Tornado. *Journal of Wind Engineering and Industrial Aerodynamics*, 138, 87-97.

Mallinis, G., Koutsias, N., Tsakiri-Strati, M., and Karteris, M. (2008). Object-based classification using Quickbird imagery for delineating forest vegetation polygons in a Mediterranean test site. *ISPRS Journal of Photogrammetry and Remote Sensing*, 63(2), 237-250.

Mamoun, H. O., Zein, A. I., and Mugira, M. I. (2012). Modelling height-diameter relationships of selected economically important natural forests species. *Journal of Forest Products and Industries*, 2(1), 34-42.

Mamoun, H. O., Zein, A. I., and Mugira, M. (2013). Height-diameter prediction models for some utilitarian natural tree species. *Journal of Forest Products and Industries*, 2(2), 31-39.

MathWorks. (2019). Image Processing Toolbox User's Guide (R2019b), www.mathworks.com /help/pdf_doc/gads/gads_tb.pdf, Natick, MA.

Mayhead, G. J. (1973). Some drag coefficients for British forest trees derived from wind tunnel studies. *Agricultural Meteorology*, 12, 123-130.

Mayhead, G.J., Gardiner, J.B.H., and Durrant, D.W. (1975). A report on the physical properties of conifers in relation to plantation stability. Unpublished report. Forestry Commission, Northern Research Station. Edinburgh, UK.

McDonald, J. R., and Mehta, K. C. (2006). *A recommendation for an Enhanced Fujita scale (EF-Scale)*. Wind Science and Engineering Center, Texas Tech University.

McKee, G. W. (1964). A coefficient for computing leaf area in hybrid corn 1. *Agronomy Journa*l, 56(2), 240-241.

Ransom, J., and Endres, G. (2020). Corn growth and management quick guide. *NSDU, A-1173*, North Dakota State University, Fargo, ND.

Meng, Z., and Yao, D. (2014). Damage survey, radar, and environment analyses on the first-ever documented tornado in Beijing during the heavy rainfall event of 21 July 2012. *Weather and Forecasting*, 29(3), 702-724.

Middleton, S. E., Middleton, L., and Modafferi, S. (2013). Real-time crisis mapping of natural disasters using social media. *IEEE Intelligent Systems*, 29(2), 9-17.

Moore, J. R. (2000). Differences in maximum resistive bending moments of Pinus radiata trees grown on a range of soil types. *Forest Ecology and Management*, 135(1-3), 63-71.

Nasir, Z., and Bitsuamlak, G. T. (2018). Topographic effects on tornado-like vortex. *Wind and Structures*, 27(2), 123-136.

Natarajan, D., and Hangan, H. (2012). Large eddy simulations of translation and surface roughness effects on tornado-like vortices. *Journal of Wind Engineering and Industrial Aerodynamics*, 104, 577-584.

Nese, J. M., and Forbes, G. S. (1998). An updated tornado climatology of Pennsylvania: Methodology and uncertainties. *Journal of the Pennsylvania Academy of Science*, 113-124.

Nicoll, B. C., Gardiner, B. A., Rayner, B., and Peace, A. J. (2006). Anchorage of coniferous trees in relation to species, soil type, and rooting depth. *Canadian Journal of Forest Research*, 36(7), 1871-1883.

Nishijima, K., Maruyama, T., and Graf, M. (2012). A preliminary impact assessment of typhoon wind risk of residential buildings in Japan under future climate change. *Hydrological Research Letters*, 6, 23-28.

NOAA. (2020a). *Annual U.S. Killer Tornado Statistics*. Storm Prediction Center. https://www.spc.noaa.gov/climo/torn/fatalmap.php.

NOAA. (2020b). *Glossary of Forecast Verification Metrics*. National Weather Service. https://www.nws.noaa.gov/oh/rfcdev/docs/Glossary_Verification_Metrics.pdf.

NOAA. (2020c). *Monthly and Annual U.S. Tornado Summaries*. Storm Prediction Center. https://www.spc.noaa.gov/climo/torn/fatalmap.php.

NOAA. (2019). *State of the Climate: Tornadoes for Annual 2018*. National Centers for Environmental Information. https://www.ncdc.noaa.gov/sotc/tornadoes/201813.

Nolan, D. S. (2012). Three-dimensional instabilities in tornado-like vortices with secondary circulations. *Journal of Fluid Mechanics*, 711, 61.

Nolan, D. S. (2013). On the use of Doppler radar–derived wind fields to diagnose the secondary circulations of tornadoes. *Journal of the Atmospheric Sciences*, 70(4), 1160-1171.

Nolan, D. S., Dahl, N. A., Bryan, G. H., and Rotunno, R. (2017). Tornado vortex structure, intensity, and surface wind gusts in large-eddy simulations with fully developed turbulence. *Journal of the Atmospheric Sciences*, 74(5), 1573-1597.

Nowak, D. J. (1990). Height diameter relations of maple street trees. *Journal of Arboriculture*, 16(9), 231-235.

NWS. (2011). Tuscaloosa-Birmingham Tornado - April 27, 2011. National Weather Service. https://www.weather.gov/bmx/event_04272011tuscbirm.

NWS. (2016). Summary of September 9th Tornadoes in East Central Illinois. National Weather Service. https://www.weather.gov/ilx/09sep2016-survey.

NWS. (2017). Severe Weather Event Review for Tuesday February 28, 2017. National Weather Service. http://www.spc.noaa.gov/exper/archive/event.php?date=20170228.

NWS. (2018). July 19, 2018 Tornadoes - Bondurant, Marshalltown, Pella. National Weather Service. https://www.weather.gov/dmx/20180719_Tornadoes.

NWS. (2020). *The Enhanced Fujita Scale (EF Scale)*. National Weather Service. https://www.weather.gov/oun/efscale.

Pauley, R. L., and Snow, J. T. (1988). On the kinematics and dynamics of the 18 July 1986 Minneapolis tornado. *Monthly Weather Review*, 116(12), 2731-2736.

Peltola, H., and Kellomäki, S. (1993). A mechanistic model for calculating windthrow and stem breakage of Scots pines at stand age. *Silva Fennica*, 27(2), 99-111.

Peltola, H., Kellomäki, S., Hassinen, A., and Granander, M. (2000). Mechanical stability of Scots pine, Norway spruce and birch: an analysis of tree-pulling experiments in Finland. *Forest Ecology and Management*, 135(1-3), 143-153.

Peltola, H., Kellomäki, S., Väisänen, H., and Ikonen, V. P. (1999). A mechanistic model for assessing the risk of wind and snow damage to single trees and stands of Scots pine, Norway spruce, and birch. *Canadian Journal of Forest Research*, 29(6), 647-661.

Pennala, E. (1980). Lujuusopin perusteet (Principles for Strength Analysis), No. 407. Otakustantamo, Espoo, Finland.

Peper, P. J., McPherson, E. G., and Mori, S. M. (2001). Equations for predicting diameter, height, crown width, and leaf area of San Joaquin Valley street trees. *Journal of Arboriculture*, 27(6), 306-317.

Peterson, C. J. (2003). Factors influencing treefall risk in tornadoes in natural forests. In *Proceedings of Symposium on the F-Scale and Severe-Weather Damage Assessment*, Long Beach, CA.

Peterson, C. J. (2007). Consistent influence of tree diameter and species on damage in nine eastern North America tornado blowdowns. *Forest Ecology and Management*, 250(1-2), 96-108.

Peterson, C. J., and Claassen, V. (2013). An evaluation of the stability of Quercus lobata and Populus fremontii on river levees assessed using static winching tests. *Forestry*, 86(2), 201-209.

Peterson, R. E. (1992). Johannes Letzmann: A pioneer in the study of tornadoes. *Weather and Forecasting*, 7(1), 166-184.

Prevatt, D. O., van de Lindt, J. W., Back, E. W., Graettinger, A. J., Pei, S., Pei, S., Coulbourne, W., Gupta, R., James, D., and Agdas, D. (2012a). Making the case for improved structural

design: Tornado outbreaks of 2011. *Leadership and Management in Engineering*, 12(4), 254-270.

Prevatt, D. O., Roueche, D. B., van De Lindt, J. W., Pei, S., Dao, T., Coulbourne, W., Graettinger, A., Gupta, R., and Grau, D. (2012b). Building damage observations and EF classifications from the Tuscaloosa, AL, and Joplin, MO, Tornadoes. In *Proceeding of Structures Congress 2012*, Chicago, IL.

Radhika, S., Tamura, Y., and Matsui, M. (2012). Use of post-storm images for automated tornado-borne debris path identification using texture-wavelet analysis. *Journal of Wind Engineering and Industrial Aerodynamics*, 107, 202-213.

Radhika, S., Tamura, Y., and Matsui, M. (2015). Cyclone damage detection on building structures from pre-and post-satellite images using wavelet based pattern recognition. *Journal of Wind Engineering and Industrial Aerodynamics*, 136, 23-33.

Rankine, W. J. M. (1882). A manual of applied physics. Charles Griff and Co., London, UK.

Refan, M., and Hangan, H. (2018). Near surface experimental exploration of tornado vortices. *Journal of Wind Engineering and Industrial Aerodynamics*, 175, 120-135.

Refan, M., Hangan, H., Wurman, J., and Kosiba, K. (2017). Doppler radar-derived wind field of five tornado events with application to engineering simulations. *Engineering Structures*, 148, 509-521.

R.M. Young. (2020). Wind sensors & accessories. Retrieved September 9, 2020, from http://www.youngusa.com/products/1/.

Robertson, D., Smith, S., Gardunia, B., and Cook, D. (2014). An improved method for accurate phenotyping of corn stalk strength. *Crop Science*, 54(5), 2038-2044.

Robertson, D. J., Julias, M., Gardunia, B. W., Barten, T., and Cook, D. D. (2015). Corn stalk lodging: a forensic engineering approach provides insights into failure patterns and mechanisms. *Crop Science*, 55(6), 2833-2841.

Robertson, D. J., Julias, M., Lee, S. Y., and Cook, D. D. (2017). Maize stalk lodging: morphological determinants of stalk strength. *Crop Science*, 57(2), 926-934.

Rosowsky, D. V., and Ellingwood, B. R. (2002). Performance-based engineering of wood frame housing: Fragility analysis methodology. *Journal of Structural Engineering*, 128(1), 32-38.

Rosten, E., Porter, R., and Drummond, T. (2010). Faster and better: A machine learning approach to corner detection. *IEEE Transactions on Pattern Analysis and Machine Intelligence*, 32(1), 105-119.

Rott, N. (1958). On the viscous core of a line vortex. *Zeitschrift für angewandte Mathematik und Physik*, 9(5-6), 543-553.

Roueche, D. B., Lombardo, F. T., and Prevatt, D. O. (2017). Empirical approach to evaluating the tornado fragility of residential structures. *Journal of Structural Engineering*, 143(9), 04017123.

Roueche, D. B., Prevatt, D. O., and Lombardo, F. T. (2018). Epistemic uncertainties in fragility functions derived from post-disaster damage assessments. *ASCE-ASME Journal of Risk Uncertainty in Engineering System Part A: Civil Engineering*, 4(2), 04018015.

Roueche, D. B., and Prevatt, D. O. (2013). Residential damage patterns following the 2011 Tuscaloosa, AL and Joplin, MO tornadoes. *Journal of Disaster Research*, 8(6), 1061-1067.

Rudnicki, M., Mitchell, S. J., and Novak, M. D. (2004). Wind tunnel measurements of crown streamlining and drag relationships for three conifer species. *Canadian Journal of Forest Research*, 34(3), 666-676.

Ruel, J. C. (2000). Factors influencing windthrow in balsam fir forests: from landscape studies to individual tree studies. *Forest Ecology and Management*, 135(1-3), 169-178.

Satrio, M. A., Bodine, D. J., Reinhart, A. E., Maruyama, T., and Lombardo, F. T. (2020). Understanding How Complex Terrain Impacts Tornado Dynamics Using a Suite of High-Resolution Numerical Simulations. *Journal of the Atmospheric Sciences*, 77(10), 3277-3300.

Sills, D. M., Kopp, G. A., Elliott, L., Jaffe, A., Sutherland, E., Miller, C., Kunkel, J., Hong, E., Stevenson, S., and Wang, W. (2020). The Northern Tornadoes Project-Uncovering Canada's True Tornado Climatology. *Bulletin of the American Meteorological Society*, 1-54.

Sobel, I. (1978). Neighborhood coding of binary images for fast contour following and general binary array processing. *Computer Graphics and Image Processing*, 8(1), 127-135.

SPC. (2016). Tornado Watch 472. Storm Prediction Center. http://www.spc.noaa.gov/products/watch/2016/ww0472.html.

SPC. (2017). Severe Weather Event Review for Tuesday February 28, 2017. Storm Prediction Center. https://www.spc.noaa.gov/exper/archive/event.php?date=20170228.

SPC. (2018). Tornado Watch 285. Storm Prediction Center. https://www.spc.noaa.gov/products/watch/2018/ww0285.html.

Sterling, M., Baker, C. J., Berry, P. M., and Wade, A. (2003). An experimental investigation of the lodging of wheat. *Agricultural and Forest Meteorology*, 119(3-4), 149-165.

Sugumaran, R., Pavuluri, M. K., and Zerr, D. (2003). The use of high-resolution imagery for identification of urban climax forest species using traditional and rule-based classification approach. *IEEE Transactions on Geoscience and Remote Sensing*, 41(9), 1933-1939.

Sullivan, R. D. (1959). A two-cell vortex solution of the Navier-Stokes equations. *Journal of the Aerospace Sciences*, 26(11), 767-768.

Szantoi, Z., Malone, S., Escobedo, F., Misas, O., Smith, S., and Dewitt, B. (2012). A tool for rapid post-hurricane urban tree debris estimates using high resolution aerial imagery. *International Journal of Applied Earth Observation and Geoinformation*, 18, 548-556.

Tanamachi, R. L., Bluestein, H. B., Lee, W. C., Bell, M., and Pazmany, A. (2007). Ground-based velocity track display (GBVTD) analysis of W-band Doppler radar data in a tornado near Stockton, Kansas, on 15 May 1999. *Monthly Weather Review*, 135(3), 783-800.

Thelen, M. (2017). *Flattened corn fields can recover from wind damage*. Michigan Farm Bureau. https://www.michiganfarmnews.com/flattened-corn-fields-can-recover-from-wind-damage.

Ting, L., and Klein, R. (1991). Viscous vortical flows. *Lecture Notes in Physics* (Vol. 374). Springer.

Torre, V., and Poggio, T. A. (1986). On edge detection. *IEEE Transactions on Pattern Analysis and Machine Intelligence*, (2), 147-163.

Ukkusuri, S. V., Zhan, X., Sadri, A. M., and Ye, Q. (2014). Use of social media data to explore crisis informatics: Study of 2013 Oklahoma tornado. *Transportation Research Record*, 2459(1), 110-118.

Urmson, C., Anhalt, J., Bagnell, D., Baker, C., Bittner, R., Clark, M. N., Dolan, J., Duggins, D., Galatali, T., Geyer, C., Gittleman, M., Harbaugh, S., Hebert, M., Howard, T. M., Kolski, S., Kelly, A., Likhachev, M., McNaughton, M., Miller, N., Peterson, K., Pilnick, B., Rajkumar, R., Rybski, P., Salesky, B., Seo, Y., Singh, S., Snider, J., Stentz, A., Whittaker, W., Wolkowicki, Z., Ziglar, J., Bae, H., Brown, T., Demitrish, D., Litkouhi, B., Nickolaou, J., Sadekar, V., Zhang, W., Struble, J., Taylor, M., Darms, M., and Ferguson, D. (2008).

Autonomous driving in urban environments: Boss and the urban challenge. *Journal of Field Robotics*, 25(8), 425-466.

USDA. (2020). *CropScape and Cropland Data Layer*. National Agricultural Statistics Service. https://www.nass.usda.gov/Research_and_Science/Cropland/SARS1a.php.

van de Lindt, J. W., Pei, S., Dao, T., Graettinger, A., Prevatt, D. O., Gupta, R., and Coulbourne, W. (2013). Dual-objective-based tornado design philosophy. *Journal of Structural Engineering*, 139(2), 251-263.

Vollsinger, S., Mitchell, S. J., Byrne, K. E., Novak, M. D., and Rudnicki, M. (2005). Wind tunnel measurements of crown streamlining and drag relationships for several hardwood species. *Canadian Journal of Forest Research*, 35(5), 1238-1249.

Wakimoto, R. M., Wienhoff, Z., Bluestein, H. B., and Reif, D. (2018). The Dodge City tornadoes on 24 May 2016: Damage survey, photogrammetric analysis combined with mobile polarimetric radar data. *Monthly Weather Review*, 146(11), 3735-3771.

Wang, Y., Titus, S. J., and LeMay, V. M. (1998). Relationships between tree slenderness coefficients and tree or stand characteristics for major species in boreal mixedwood forests. *Canadian Journal of Forest Research*, 28(8), 1171-1183.

Wilson, J. D., Ward, D. P., Thurtell, G. W., and Kidd, G. E. (1982). Statistics of atmospheric turbulence within and above a corn canopy. *Boundary-Layer Meteorology*, 24(4), 495-519.

Wilson, J. W., and Wakimoto, R. M. (2001). The discovery of the downburst: TT Fujita's contribution. *Bulletin of the American Meteorological Society*, 82(1), 49-62.

Womble, J. A., Mehta, K. C., and Adams, B. J. (2007). Automated building damage assessment using remote-sensing imagery. In *Proceedings of Forensic Engineering Conference at Structures Congress 2007*, Long Beach, CA.

Womble, J. A., Wood, R. L., Smith, D. A., Louden, E. I., and Mohammadi, M. E. (2017). Reality capture for tornado damage to structures. In *Proceedings of Structures Congress 2017*, Denver, CO.

Womble, J. A., Wood, R. L., and Mohammadi, M. E. (2018). Multi-scale remote sensing of tornado effects. *Frontiers in Built Environment*, 4, 66.

Wood, V. T., and Brown, R. A. (2011). Simulated tornadic vortex signatures of tornado-like vortices having one-and two-celled structures. *Journal of Applied Meteorology and Climatology*, 50(11), 2338-2342.

Wood, V. T., and White, L. W. (2011). A new parametric model of vortex tangential-wind profiles: Development, testing, and verification. *Journal of the Atmospheric Sciences*, 68(5), 990-1006.

Wurman, J. (2002). The multiple-vortex structure of a tornado. *Weather and Forecasting*, 17(3), 473-505.

Wurman, J., and Alexander, C. R. (2005). The 30 May 1998 Spencer, South Dakota, storm. Part II: Comparison of observed damage and radar-derived winds in the tornadoes. *Monthly Weather Review*, 133(1), 97-119.

Wurman, J., and Gill, S. (2000). Finescale radar observations of the Dimmitt, Texas (2 June 1995), tornado. *Monthly Weather Review*, 128(7), 2135-2164.

Wurman, J., Kosiba, K., and Robinson, P. (2013). In situ, Doppler radar, and video observations of the interior structure of a tornado and the wind–damage relationship. *Bulletin of the American Meteorological Society*, 94(6), 835-846.

Wurman, J., Kosiba, K., Robinson, P., and Marshall, T. (2014). The role of multiple-vortex tornado structure in causing storm researcher fatalities. *Bulletin of the American Meteorological Society*, 95(1), 31-45.

Zhang, Z., Ma, S., Liu, H., and Gong, Y. (2009). An edge detection approach based on directional wavelet transform. *Computers & Mathematics with Applications,* 57(8), 1265-1271.